

NONLINEAR DYNAMIC ANALYSIS OF A DRIVETRAIN COMPOSED OF
CYLINDRICAL GEARS, STRAIGHT AND SPIRAL BEVEL GEARS

A THESIS SUBMITTED TO
THE GRADUATE SCHOOL OF NATURAL AND APPLIED SCIENCES
OF
MIDDLE EAST TECHNICAL UNIVERSITY

BY

ŞİAR DENİZ YAVUZ

IN PARTIAL FULFILLMENT OF THE REQUIREMENTS
FOR
THE DEGREE OF DOCTOR OF PHILOSOPHY
IN
MECHANICAL ENGINEERING

FEBRUARY 2018

Approval of the thesis:

**NONLINEAR DYNAMIC ANALYSIS OF A DRIVETRAIN COMPOSED
OF CYLINDRICAL GEARS, STRAIGHT AND SPIRAL BEVEL GEARS**

submitted by **ŞİAR DENİZ YAVUZ** in partial fulfillment of the requirements for
the degree of **Doctor of Philosophy in Mechanical Engineering Department,**
Middle East Technical University by,

Prof. Dr. Gülbin Dural Ünver
Dean, Graduate School of **Natural and Applied Sciences** _____

Prof. Dr. M. A. Sahir Arıkan
Head of Department, **Mechanical Engineering** _____

Assoc. Prof. Dr. Ender Ciğeroğlu
Supervisor, **Mechanical Engineering Dept., METU** _____

Assoc. Prof. Dr. Zihni Burçay Sarıbay
Co-Supervisor, **Turkish Aerospace Industries (TAI)** _____

Examining Committee Members:

Prof. Dr. Metin Akkök
Mechanical Engineering Dept., METU _____

Assoc. Prof. Dr. Ender Ciğeroğlu
Mechanical Engineering Dept., METU _____

Asst. Prof. Dr. Mehmet Bülent Özer
Mechanical Engineering Dept., METU _____

Assoc. Prof. Dr. S. Çağlar Başlamışlı
Mechanical Engineering Dept., Hacettepe University _____

Asst. Prof. Dr. Can U. Doğruer
Mechanical Engineering Dept., Hacettepe University _____

Date: 01.02.2018

I hereby declare that all information in this document has been obtained and presented in accordance with academic rules and ethical conduct. I also declare that, as required by these rules and conduct, I have fully cited and referenced all material and results that are not original to this work.

Name, Last name : Şiar Deniz YAVUZ

Signature :

ABSTRACT

NONLINEAR DYNAMIC ANALYSIS OF A DRIVETRAIN COMPOSED OF CYLINDRICAL GEARS, STRAIGHT AND SPIRAL BEVEL GEARS

Yavuz, Şiar Deniz

Ph.D., Department of Mechanical Engineering

Supervisor: Assoc. Prof. Dr. Ender Ciğeroğlu

Co-Supervisor: Assoc. Prof. Dr. Zihni Burçay Sarıbay

February 2018, 168 pages

A nonlinear dynamic model of a drivetrain composed of spur, helical and spiral bevel gears is proposed. Gear shafts are modeled by using Timoshenko beam finite element method and mesh models of gear pairs are used to couple them. Dynamic model includes the flexibilities of bearings as well. Gear backlash and time variation of mesh stiffness are incorporated into the mesh model. Harmonic Balance Method (HBM) with multiple harmonics is applied on the system of nonlinear differential equations in order to obtain a system of nonlinear algebraic equations. Since finite element modelling results in large number of nonlinear equations, receptance method and modal superposition method are introduced to forced response analysis of geared systems with nonlinearities in order to reduce computational effort. This makes it possible to use finite element models for gear shafts. In the calculation of Fourier coefficients, continuous-time Fourier transform, as opposed to the gear dynamics studies that utilize discrete Fourier transform, is used. Thus, convergence problems that arise when the number of nonlinear DOFs is large are avoided.

Moreover, analytical integration is employed for the calculation of Fourier coefficients rather than numerical integration in order to further reduce the computational time required. Nonlinear algebraic equations obtained are solved by utilizing Newton's method with arc-length continuation. The results obtained by HBM are verified by comparing them with those obtained by direct numerical integration, which are computationally demanding. Several parametric studies are performed and response of the system is investigated to demonstrate the effects of system parameters.

Keywords: Nonlinear gear dynamics, spiral bevel gear, time-varying mesh stiffness, static transmission error, Harmonic Balance Method with multiple harmonics

ÖZ

SİLİNDİRİK DİŞLİLER, DÜZ VE SİRAL KONİK DİŞLİLERDEN OLUŞAN BİR DİŞLİ KUTUSUNUN DOĞRUSAL OLMAYAN DİNAMİK ANALİZİ

Yavuz, Şiar Deniz

Doktora, Makina Mühendisliği Bölümü

Tez Yöneticisi: Doç. Dr. Ender Ciğeroğlu

Ortak Tez Yöneticisi: Doç. Dr. Zihni Burçay Sarıbay

Şubat 2018, 168 sayfa

Düz, helis ve spiral konik dişlilerden oluşan bir dişli sisteminin doğrusal olmayan dinamik modeli önerilmektedir. Dişli şaftları Timoshenko kiriş sonlu elemanlar metodu kullanılarak modellenmiştir ve bunları birleştirmek için dişli çiftlerinin kavrama modelleri kullanılmıştır. Dinamik model rulman esnekliklerini de içermektedir. Dişli boşluğu ve kavrama sıklığının zamanla değişimi kavrama modeline dahil edilmiştir. Doğrusal olmayan cebirsel denklem sistemini elde etmek için, doğrusal olmayan diferansiyel denklem sistemine çok harmonikli Harmonik Denge Yöntemi uygulanmıştır. Sonlu elemanlar modellemesi çok sayıda doğrusal olmayan denklemlerle sonuçlandığından, hesaplama çabasını azaltmak için doğrusal olmayan dişli sistemlerin zorlamalı yanıt analizlerine reseptans yöntemi ve modal süperpozisyon yöntemi getirilmiştir. Bu, dişli şaftları için sonlu elemanlar modelleri kullanmayı mümkün kılar. Fourier katsayılarının hesaplanmasında, kesikli Fourier dönüşümü kullanan dişli dinamiği çalışmalarının aksine sürekli-zamanlı Fourier

dönüşümü kullanılmıştır. Böylece, doğrusal olmayan serbestlik derecesi çok olduğunda ortaya çıkan yakınsama problemleri önlenir. Ayrıca, gereken hesaplama süresini daha da azaltmak için Fourier katsayılarının hesaplanmasında sayısal entegrasyon yerine analitik entegrasyon kullanılmıştır. Elde edilen doğrusal olmayan cebirsel denklemler yay uzunluğu sürekliliği ve Newton Yöntemi kullanılarak çözülmüştür. Harmonik Denge Yöntemi ile elde edilen sonuçlar, hesaplama açısından zorlu doğrudan sayısal entegrasyonla elde edilenlerle karşılaştırılarak doğrulanmıştır. Birçok parametrik çalışma yapılmıştır ve sistem parametrelerinin etkisini göstermek için sistemin yanıtı incelenmiştir.

Keywords: Doğrusal olmayan dişli dinamiği, spiral konik dişli, zamanla değişen kavrama sıklığı, statik aktarım hatası, çok harmonikli Harmonik Denge Yöntemi

*To My Wife,
Nazlı
&
To My Children
Emir & Zeynep*

ACKNOWLEDGEMENTS

I would like to thank my supervisor Assoc. Prof. Dr. Ender Ciğerođlu and my co-supervisor Assoc. Prof. Dr. Zihni Burçay Sarıbay for their supervision, help and guidance from the beginning to end of this dissertation.

I want to thank Prof. Dr. Metin Akkök and Assoc. Prof. Dr. S. Çađlar Bařlamıřlı for their guidance as members of thesis progress committee.

I want to thank my wife Nazlı for her endless support and encouragement throughout this study.

I would like to express my thanks to my son Emir for his patience when I was studying instead of playing together.

I would like to thank my daughter Zeynep for accelerating me with her birth.

TABLE OF CONTENTS

ABSTRACT	v
ÖZ.....	vii
ACKNOWLEDGEMENTS	x
TABLE OF CONTENTS	xi
LIST OF TABLES	xiv
LIST OF FIGURES.....	xv
LIST OF SYMBOLS	xix
CHAPTERS	
1 INTRODUCTION.....	1
1.1 Introduction	1
1.2 Literature Survey.....	5
1.3 Motivation, Scope and Objective.....	9
1.4 Dissertation Overview.....	11
2 NONLINEAR TIME-VARYING DYNAMIC ANALYSIS OF A MULTI-MESH SPUR GEAR TRAIN.....	13
2.1 Introduction	13
2.2 Dynamic Model Formulation.....	14
2.2.1 Physical System and Dynamic Model.....	14
2.2.2 Period-one dynamics	19
2.2.3 Loading Conditions and Mesh Phases	24
2.3 Results and Discussion.....	26

2.4 Conclusion.....	33
3 LINEAR DYNAMIC ANALYSIS OF A HELICAL GEARED SYSTEM ...	35
3.1 Dynamic Model Formulation	35
3.1.1 Physical System and Dynamic Model.....	35
3.1.2 Solution Method.....	43
3.2 Results and Discussion.....	44
4 NONLINEAR TIME-VARYING DYNAMIC ANALYSIS OF A SPIRAL BEVEL GEARED SYSTEM	53
4.1 Introduction	53
4.2 Dynamic Model Formulation	55
4.2.1 Physical System and Dynamic Model.....	55
4.2.2 Solution Method.....	64
4.2.2.1 Receptance Method	64
4.2.2.2 Multi-harmonics Harmonic Balance Method with Continuous- Time Fourier Transform.....	66
4.3 Results and Discussion.....	70
4.4 Conclusion.....	86
5 NONLINEAR DYNAMIC ANALYSIS OF A DRIVETRAIN INCLUDING SPUR, HELICAL AND SPIRAL BEVEL GEARS	89
5.1 Introduction	89
5.2 Dynamic Model Formulation	91
5.2.1 Physical System and Dynamic Model.....	91
5.2.2 Solution Method	100

5.2.2.1 Multi-term Harmonic Balance Method with Continuous-Time Fourier Transform	100
5.2.2.2 Modal Superposition Method.....	103
5.3 Results and Discussion.....	107
5.4 Conclusion.....	129
6 CONCLUSION AND FUTURE WORK.....	133
6.1 Conclusion.....	133
6.2 Future Work	137
REFERENCES.....	139
APPENDICES	
APPENDIX A PUBLISHED PAPERS DURING PHD	145
CURRICULUM VITAE	168

LIST OF TABLES

TABLES

Table 2.1 Parameters of the drivetrain	27
Table 3.1 Parameters of the helical gear system in countershaft arrangement shown in Fig. 3.4.....	46
Table 3.2 Comparison of the natural frequencies of the countershaft arrangement (Fig. 3.4).....	47
Table 3.3 Parameters of the helical gear system in idler and split-torque arrangements shown in Fig. 3.5.....	48
Table 3.4 Comparison of the natural frequencies of the idler arrangement (Fig. 3.5)	49
Table 3.5 Comparison of the natural frequencies of the split-torque arrangement (Fig. 3.5).....	50
Table 3.6 Parameters of the helical gear system in idler and split-torque arrangements shown in Fig. 3.6.....	51
Table 4.1 Parameters of the example system	71
Table 4.2 Comparison of natural frequencies of linear-time invariant system	72
Table 5.1 Parameters of the example drivetrain.....	109
Table 5.2 Comparison of natural frequencies of linear-time invariant system	112

LIST OF FIGURES

FIGURES

Fig. 1.1 Straight (left) and spiral (right) bevel gears [4]	2
Fig. 1.2 Zerol bevel gear [5].....	2
Fig. 1.3 Hypoid gear [6].....	2
Fig. 1.4 Collector stage of AW139 helicopter [7].....	4
Fig. 1.5 Main gearbox of Sikorsky CH-53K helicopter [8]	5
Fig. 2.1 Multi-mesh spur gear train considered in this study.....	15
Fig. 2.2 Dynamic model of the system.....	16
Fig. 2.3 Different loading conditions such as split-torque and idler arrangements	25
Fig. 2.4 Definition of the angle ψ	26
Fig. 2.5 rms values of the responses, $p_1(t)$ and $p_2(t)$ predicted by HBM and NI in the idler arrangement with even Z_2	28
Fig. 2.6 Mean components of the responses, $p_1(t)$ and $p_2(t)$ predicted by HBM and NI in the idler arrangement with even Z_2	28
Fig. 2.7 Comparison of rms value and mean component of the response $p_1(t)$ predicted by HBM and NI in the split-torque arrangement with even Z_2	31
Fig. 2.8 Effect of the out-of-phase relationship between the static transmission error and mesh stiffness	32
Fig. 2.9 Effect of loading conditions on dynamic response.....	33
Fig. 2.10 Effect of orientation angle on dynamic response of the split-torque arrangement with $Z_2 = 30$	34
Fig. 3.1 Mesh model of a helical gear pair.....	37
Fig. 3.2 Effective mesh point and LOA vector in a configuration where pinion rotates CCW and has left hand teeth.....	39

Fig. 3.3 Angle between the reference teeth of the gears mounted on the same shaft, β_j , and angle between the vectors directed to the effective mesh points, φ	44
Fig. 3.4 Countershaft arrangement used in the 1 st case study	45
Fig. 3.5 Idler and split-torque arrangements used in the 2 nd and 3 rd case studies ..	47
Fig. 3.6 Idler and split-torque arrangements used in the 4 th case study	50
Fig. 3.7 Forced responses of Gear 1 and Gear 2 in split-torque arrangement, Z_2 is even	52
Fig. 3.8 Effect of loading conditions on dynamic mesh forces	52
Fig. 4.1 Schematic of gear mesh model and finite element model for the spiral bevel gear train considered in this study	57
Fig. 4.2 Gear mesh model for a spiral bevel gear pair	59
Fig. 4.3 Effective mesh point and LOA vector	61
Fig. 4.4 Comparison of rms values of the responses predicted by HBM and NI for $T = 200 \text{ Nm}$ and $b = 20 \mu\text{m}$, (a) dynamic mesh force $F_m^{(rms)}$, (b) dynamic transmission error $\delta_d^{(rms)}$	73
Fig. 4.5 (a) Time history and (b) frequency spectrum of $F_m(t)$ at $\omega = 3968 \text{ Hz}$ obtained by NI	75
Fig. 4.6 Normalized amplitudes of the subharmonics with $1/4\omega$, $1/3\omega$ and $3/4\omega$ for both dynamic transmission error δ_d and dynamic mesh force F_m	76
Fig. 4.7 Frequency spectra, phase plane plots and Poincare map points (*) of dynamic transmission error δ_d obtained by NI	78
Fig. 4.8 Nonlinear characteristics of the spiral bevel gear train	79
Fig. 4.9 Fourier spectrum of $F_m(t)$ at super-harmonic resonance peaks obtained by NI, (a) $\omega \approx 1/2\omega_2 = 567 \text{ Hz}$ (b) $\omega \approx 1/3\omega_2 = 378 \text{ Hz}$	80
Fig. 4.10 Effect of number of harmonics employed in HBM	81
Fig. 4.11 Effect of static transmission error and parametric excitations	82
Fig. 4.12 Dynamic mesh force for $T = 200 \text{ Nm}$ and different backlash amounts ..	83

Fig. 4.13 Dynamic bearing forces $F_b^{(rms)}$ for the first bearing of the pinion shaft (Bearing A in Fig. 4.1)	84
Fig. 4.14 Effect of bearing stiffness coefficient, $k_{b\theta_x} = k_{b\theta_y}$, on the dynamic gear mesh force	84
Fig. 4.15 Comparison of coupled gear system model with torsional model.....	85
Fig. 5.1 The drivetrain considered in this study.....	92
Fig. 5.2 Numbering of the components in the drivetrain	93
Fig. 5.3 A generic mesh model that is applicable to all types of gears	95
Fig. 5.4 Schematic of gear mesh model and finite element model	96
Fig. 5.5 Orientation of the input spur pinion, α_{input} , and angle between the vectors directed to the effective mesh points, φ	108
Fig. 5.6 Angle between the reference teeth of the gears mounted on the same shaft, β_j , and angle between the vectors directed to the effective mesh points, φ	108
Fig. 5.7 Mesh stiffness and static transmission error, (a-b) 1 st mesh (spur gear) [58], (c-d) 2 nd mesh (spiral bevel gear) [69], (e-f) 3 rd mesh (helical gear) [58].....	110
Fig. 5.8 Comparison of rms values of the responses predicted by HBM and NI, (a) dynamic mesh force at 1 st mesh, $F_{m(1)}^{(rms)}$, (b) dynamic mesh force at 2 nd mesh, $F_{m(2)}^{(rms)}$, (c) dynamic mesh force at 3 rd mesh, $F_{m(3)}^{(rms)}$	113
Fig. 5.9 (a) Time trace and (b) frequency spectrum of $F_{m(1)}(t)$ at $\Omega_{input} = 10000$ rpm predicted by NI.....	115
Fig. 5.10 Nonlinear behavior of the drivetrain.....	116
Fig. 5.11 Amplitudes of the harmonics of dynamic mesh force, $F_{m(3)}(t)$, at the helical gear mesh (3 rd stage) obtained by HBM.....	117
Fig. 5.12 Effect of number of mode shapes utilized in modal superposition method (a) $F_{m(1)}^{(rms)}$, (b) $F_{m(2)}^{(rms)}$, (c) $F_{m(3)}^{(rms)}$	118

Fig. 5.13 Effect of harmonics employed in HBM (a) $F_{m(1)}^{(rms)}$, (b) $F_{m(2)}^{(rms)}$, (c) $F_{m(3)}^{(rms)}$	120
Fig. 5.14 Effect of the length of the third shaft on the dynamic gear mesh force, $F_{m(3)}^{(rms)}$, at the helical gear mesh (3 rd stage)	121
Fig. 5.15 Effect of the length of the third shaft on the dynamic gear mesh force, $F_{m(1)}^{(rms)}$, at the spur gear mesh (1 st stage).....	122
Fig. 5.16 Effect of the length of the third shaft on the dynamic gear mesh force, $F_{m(2)}^{(rms)}$, at the spiral bevel gear mesh (2 nd stage)	122
Fig. 5.17 Effect of gear hand configurations of helical gears on dynamic bearing forces, $F_b^{(rms)}$, of bearing 3B (shown in Fig. 5.2)	123
Fig. 5.18 Effect of orientation of input spur pinion, α_{input} , on dynamic bearing force, $F_{by}^{(rms)}$, of bearing 2A (shown in Fig. 5.2)	125
Fig. 5.19 Effect of orientation of input spur pinion, α_{input} , on dynamic bearing force, $F_{bz}^{(rms)}$, of bearing 2A (shown in Fig. 5.2)	125
Fig. 5.20 Effect of bearing stiffness coefficients, $k_{b\theta_x} = k_{b\theta_y}$, on $F_{m(3)}^{(rms)}$	126
Fig. 5.21 Effect of bearing stiffness coefficients, $k_{b\theta_x} = k_{b\theta_y}$, on the dynamic gear mesh force, $F_{m(1)}^{(rms)}$	127
Fig. 5.22 Effect of bearing stiffness coefficients, $k_{b\theta_x} = k_{b\theta_y}$, on the dynamic gear mesh force, $F_{m(2)}^{(rms)}$	127
Fig. 5.23 Effect of helix angle of input pinion (a) $F_{m(1)}^{(rms)}$, (b) $F_{m(2)}^{(rms)}$, (c) $F_{m(3)}^{(rms)}$	128

LIST OF SYMBOLS

b	half of gear backlash
c_m	mesh damping coefficient
\mathbf{C}	damping matrix
$\bar{\mathbf{C}}$	modal viscous damping matrix
e_m	static transmission error
f_n	nonlinear displacement functions
\mathbf{F}	external force vector
$\bar{\mathbf{F}}$	modal forcing vector
F_m	dynamic mesh force
\mathbf{F}_N	nonlinear restoring force vector
$\bar{\mathbf{F}}_N$	modal nonlinear restoring force vector
\mathbf{h}	transformation vector
h	arc-length equation
\mathbf{I}	identity matrix
ID	inner diameter of shaft segment
i	unit imaginary number
\mathbf{J}	Jacobian matrix
\mathbf{K}	stiffness matrix
k_m	mesh stiffness
L	length of shaft segment
\mathbf{n}	directional cosine vector of line of action
\mathbf{M}	mass matrix
n	directional cosine

OD	outer diameter of shaft segment
p	extended coordinate transformation vector
r	position vector of effective mesh point
R	residual vector
S	residual vector including arc-length equation
<i>S</i>	pinion/gear coordinate system
<i>S_s</i>	pinion/gear shaft coordinate system
T_σ	transformation matrix about coordinate σ
<i>T_{in}, T_{out}</i>	input and output torques
<i>t</i>	time
v	vector of unknowns
x	displacement vector
α	receptance matrix of linear system
<i>α</i>	phase angle
<i>β</i>	angle between reference teeth of gears mounted on the same shaft
<i>δ_d</i>	dynamic transmission error
<i>λ</i>	directional rotational radius
<i>θ</i>	rotational displacement
<i>θ_d</i>	angle between the <i>z</i> axes of <i>S_i</i> and <i>S_{si}</i>
<i>θ_o</i>	angle between the <i>x</i> axes of <i>S_i</i> and <i>S_{si}</i>
<i>ω</i>	frequency
<i>ζ_s</i>	damping ratio for shaft-bearing assembly
<i>φ_t</i>	transverse pressure angle
<i>ψ</i>	spiral/helix angle
<i>γ</i>	pitch angle
η	modal coefficient vector
Φ	mass normalized undamped modal matrix

Ω	diagonal matrix of squares of natural frequencies
Π	phase difference

Subscripts

b	bearing
i	pinion ($i = p$) and gear ($i = g$)
l	linear DOFs
n	nonlinear DOFs
s	shaft

Superscripts

r	harmonic index
rms	root-mean-square value
\cdot	derivative with respect to time

CHAPTER 1

INTRODUCTION

1.1 Introduction

Gears are used in numerous applications in order to transmit power between shafts. Therefore, extensive researches have been performed on conventional gears such as spur, helical and bevel gears. Spur and helical gears are classified as parallel axis gears, whereas bevel gears are called nonparallel axis gears. Teeth of spur gears are parallel to the rotation axis; therefore, they are the most common and simplest form of gears. Helical gears have teeth making an angle with the rotation axis, which provides a smoother operation with less noise. Furthermore, a helical gear pair can transmit a larger load compared to an equivalent spur gear. On the other hand, shafts are nonparallel in many applications and bevel gears are utilized for transmitting power between these shafts [1,2]. Bevel gears, which have teeth formed on conical surfaces, are classified by American Gear Manufacturers Association (AGMA) as follows [3]:

- ***Straight bevel gears:*** These are the simplest form of bevel gears, which is shown in Fig. 1.1. They have straight and tapered teeth, whose inward extension intersect in a common point at the axis of the gear. Therefore, they are the bevel counterpart of the spur gears. Straight bevel gears are recommended for the applications with pitch-line velocities up to 5 m/s due to the noise [1–3].



Fig. 1.1 Straight (left) and spiral (right) bevel gears [4]



Fig. 1.2 Zerol bevel gear [5]

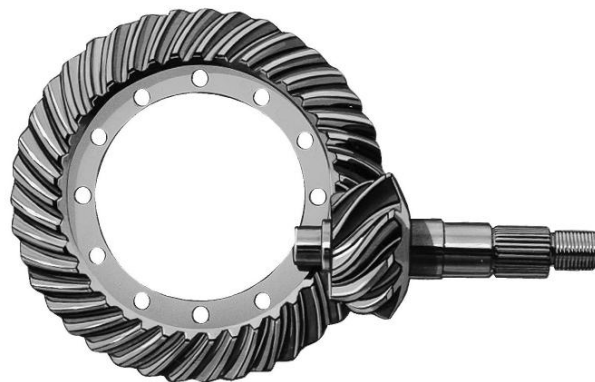


Fig. 1.3 Hypoid gear [6]

- ***Spiral bevel gears:*** These are the most complex form of bevel gears, which is shown in Fig. 1.1. They have curved and oblique teeth and so they are the bevel counterpart of the helical gears. As a result of considerable amount of overlapping tooth action, i.e. high contact ratio, power transmission with spiral bevel gears is quieter and smoother than transmission with straight bevel or Zerol bevel gears. Consequently, spiral bevel gears are utilized in high speed applications, where noise is a significant concern.
- ***Zerol bevel gears:*** These are special gears with curved teeth having a zero spiral angle, which is shown in Fig. 1.2. They can transmit more power with less noise compared to straight bevel gears. They produce the same thrust load on the bearings and have smooth operating characteristics. Moreover, manufacturing process of Zerol bevel gears is very similar to that of spiral bevel gears. They are widely used as accessory drives in high speed applications.
- ***Hypoid gears:*** As shown in Fig. 1.3, the axis of pinion has an offset with the axis of wheel, which is appropriate for some applications such as automotive differential requiring nonintersecting shafts. The meshing process in hypoid gears include both sliding and rolling, which is similar to that of worm gears. The hypoid gears with larger offsets are sometimes referred to by the name “spiroid gears”.

Among the all types, spiral bevel gears are mainly used in helicopter transmission system, which is illustrated in Fig. 1.4. In the shown stage of the transmission system of AW139 helicopters, the large diameter collector wheel combines the two input power supply branches, redirecting the drive about an almost vertical axis, coincident with the main rotor axis. Moreover, the tail rotor and accessory drives are connected to the collector wheel, which constitutes one of the main features of

the entire system [7]. Similarly, in Sikorsky CH-53K helicopter and Bell 525 helicopter, the first reduction stages, which transmit power from the engines to the main gearboxes, are comprised of spiral bevel gears. These spiral bevel gears are the fastest rotating components in these gearboxes and they are critical from dynamics perspective.

Gear vibration is an important consideration in drivetrain systems due to noise and durability problems. Dynamic mesh forces are much higher compared to static forces and these dynamic forces are transmitted to casing through bearings, which cause excessive noise. Moreover, alternating forces induced by vibration reduce fatigue lives of the driveline components. Therefore, a comprehensive investigation of gear dynamics is the key point in the design of a quiet and durable transmission system.



Fig. 1.4 Collector stage of AW139 helicopter [7]

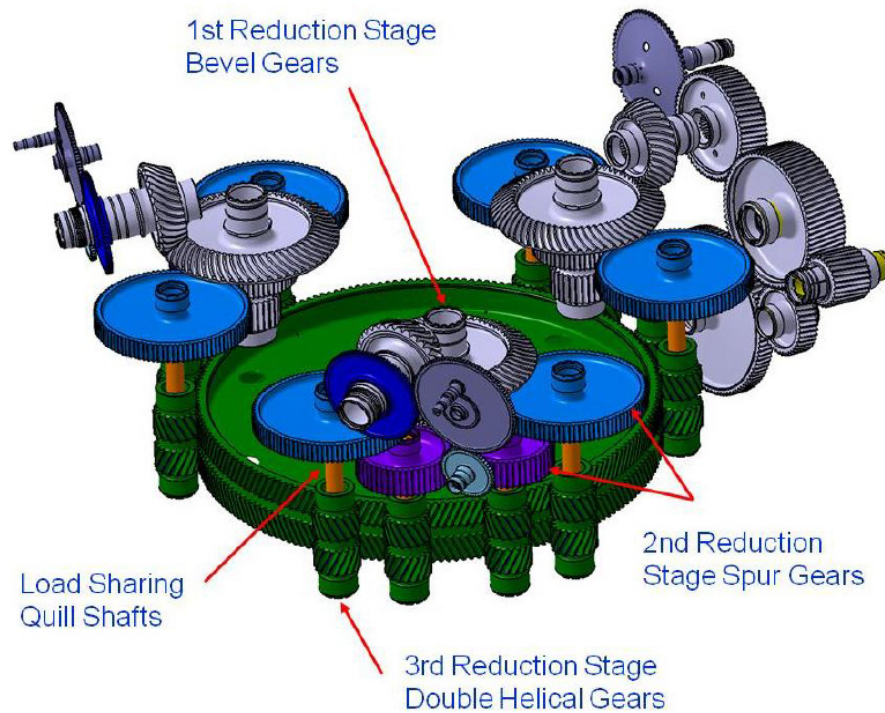


Fig. 1.5 Main gearbox of Sikorsky CH-53K helicopter [8]

1.2 Literature Survey

The literature about gears are categorized into many areas, such as gear tooth surface geometry, tooth contact, dynamics, stress and fracture, fatigue, wear, lubrication and tribology, manufacturing etc. However, the literature review performed in this dissertation is limited to gear dynamics related studies.

There are a large number of studies about gear dynamics in the literature and in the vast majority of these studies, parallel axis gears are considered. Mathematical models used in spur gear dynamics are reviewed in [9]. The models are classified into 5 groups as follows:

- 1) Simple Dynamic Factor Models, which are used by most of early studies in order to obtain a dynamic factor for the calculation of gear root stress.
- 2) Models with Tooth Stiffness, in which only the tooth stiffness is included by neglecting the flexibilities of shafts, bearings etc.
- 3) Models for Gear Dynamics, in which the stiffness of the other components, i.e. torsional flexibilities of shafts and lateral flexibilities of bearings, in addition to tooth stiffness are included.
- 4) Models for Geared Rotor Dynamics, in which transverse flexibilities of shafts are also considered.
- 5) Models for Torsional Vibrations, which neglect gear tooth stiffness and include torsional flexibilities of shafts. This models may be considered as pure torsional vibration problems, rather than gear dynamics problems.

A single degree-of-freedom (SDOF) nonlinear dynamic model of a spur gear pair is proposed in [10]. In that study, a computer program is developed in order to calculate the dynamic transmission error and dynamic mesh force by using loaded static transmission error. Time variation of mesh stiffness is also included in the model. Moreover, an SDOF nonlinear dynamic model with time invariant mesh stiffness for a spur gear pair is proposed in [11]. Two solution methods, i.e. direct time integration, and Harmonic Balance Method (HBM), are utilized in order to obtain the steady-state solutions, which are then compared to the experimental results. Nonlinear torsional dynamics of a spur gear pair are also analyzed in [12–14].

A 3-DOF nonlinear dynamic model with time invariant mesh stiffness is developed in [15]. Clearance-type nonlinearities of bearings as well as nonlinearities associated with backlash are included in the model. Later on, fluctuation of mesh stiffness is incorporated into the model in [16].

Considering torsional flexibilities of shafts and transverse flexibilities of bearings, a 6-DOF nonlinear time-varying (NTV) dynamic model for a spur gear train is presented in [17].

A finite element model of a drivetrain including spur gears on flexible bearings is developed in [18] in order to study the effect of bearing flexibility on the dynamics of the drivetrain. The shafts are modeled by using finite elements with 5-DOFs at each node (excluding axial motion). The parametric excitations caused by fluctuating mesh stiffness are considered as well. Furthermore, a NTV dynamic model of a gear train including shafts and bearings is presented in [19], where FEM is used to model the shafts. Then, clearance-type nonlinearity in bearings is incorporated into the model in [20,21].

Effects of clearance-type nonlinearity and parametric excitations on a mechanical oscillator with a piecewise-linear clearance function are studied in [22] and HBM is used for the calculation of the response. In [23], the study is extended to the investigation of subharmonic resonances in the response of the same system. Then, experimental results about the nonlinear dynamic behavior of the same system are presented in [24]. Similarly, considering external and parametric excitations, dynamic behavior, i.e., period-one and subharmonic motions, of a mechanical oscillator with a piecewise-nonlinear clearance function is studied in [25,26].

A 2-DOF NTV dynamic model of a two stage spur geared system composed of rigid shafts is presented in [27]. Furthermore, subharmonic motions of the same gear train are investigated in [28]. Then, the model is extended to consist of M shafts coupled by $M-1$ gear pairs and to include the torsional flexibilities of the shafts in [29]. Nonlinear dynamic models with fluctuating mesh stiffness are proposed in [30,31] for idler and counter-shaft arrangements of spur gears. A NTV dynamic model is proposed for a planetary gear set composed of spur gears in [32].

In the literature, there are also studies including friction in dynamic model. An analytical model incorporating sliding friction into the dynamic equations of a spur gear pair is developed in [33,34]. In [33], a linear time-varying (LTV) dynamic model is considered, whereas both LTV and NTV models are utilized in [34]. A 6-DOF NTV dynamic model of a spur gear pair, which includes a friction coefficient based on an elastohydrodynamic lubrication (EHL) formulation is proposed in [35] in order to study the influence of friction on dynamics. Influences of sliding friction on gear dynamics are also investigated in [36,37]. Moreover, a mathematical model is proposed in [38] for the calculation of frictional losses.

Several investigations are also conducted for helical gears. Considering shaft and bearings flexibilities, a linear time-invariant (LTI) dynamic model of a helical gear pair is presented in [39]. Shaft and bearing flexibilities are included in a linear time-invariant (LTI) dynamic model of a helical gear pair. A LTI dynamic model for a flexibly mounted drivetrain including three helical gears is proposed in [40] in order to examine the influence of mesh phasing on dynamics. Furthermore, a LTI dynamic model of a multi-mesh helical geared system is developed in [41], where FEM is used to model the shafts. A LTI dynamic model is proposed for a planetary gear set composed of helical gears in [42].

Even though there are many studies regarding the dynamics of parallel axis gears, research on bevel gear dynamics is limited. Initially, dynamics of a bevel geared system considering axial, torsional and transverse vibrations is investigated in [43,44], where mesh stiffness is not considered. An SDOF NTV dynamic model of a hypoid gear pair is developed in [45]. In that study, a new gear mesh model based on a tooth contact analysis by using Calyx commercial software is proposed. An 8-DOF NTV dynamic model including asymmetric mesh stiffness for a spiral bevel gear is proposed in [46]. Furthermore, a 14-DOF NTV dynamic model of a bevel gear train including a bevel gear pair, a load and an engine is developed in [47].

Moreover, time variation of bearing stiffness is incorporated into the same model in [48]. Then, FEM model of shafts is introduced in [49] for a LTI spiral bevel gear train in order to describe the shaft-bearing structural characteristics better. On the other hand, considering a friction coefficient based on EHL, a model is proposed in [50] in order to calculate the frictional losses. Moreover, the influence of friction on dynamics of hypoid and spiral bevel gears is investigated in [51].

1.3 Motivation, Scope and Objective

Analytical evaluation of the dynamics of gear pairs and also full drive train system is required to design a more silent and durable transmission system. Therefore, there are numerous gear dynamics related studies in the literature. It is seen from the literature that a single cylindrical gear pair, i.e., spur and helical gear, is considered in the vast majority of these studies. The studies about dynamics of bevel gears are limited due to complexity of tooth geometry, kinematics and meshing process of these types of gears. These studies mainly focus on gear pair; hence, supporting structures such as shafts and bearings are modeled by employing lumped stiffness and damping elements. Therefore, dynamic characteristics of shaft-bearing structures are not studied extensively. Moreover, the studies on multi-mesh gear systems are fewer compared to the ones on single gear pair systems in spite of the widespread use of multi-stage, multi-mesh drivetrains. Even, there is no known study that addresses nonlinear dynamics of a multi-stage, multi-mesh drivetrain including a bevel gear.

The main goal of this dissertation is to develop a nonlinear dynamic model of a multi-mesh, multi-stage drivetrain composed of both cylindrical gears and bevel gears. An accurate mesh model including both fluctuating mesh stiffness and backlash nonlinearity is aimed to be proposed. The dynamic model will combine the

Timoshenko beam FEM model of shaft-bearing structures with the mesh models of gear pairs. Therefore, dynamic characteristics of shaft-bearing structures will be studied as well.

Due to finite element modeling of shafts, a large number of nonlinear equations is obtained. Since the iterative solution of these equations is computationally demanding and an inefficient process, some nonlinear solution methods such as receptance method and modal superposition method will be introduced to the dynamic analysis of geared systems with nonlinearities in order to decrease the computational time. In the receptance method, the total DOFs are grouped into linear and nonlinear DOFs and only the nonlinear equations obtained from the nonlinear DOFs need to be solved [52,53]. Since only the DOFs associated with the gears contain nonlinearity, receptance method can be utilized in the dynamic response analysis of a drivetrain. However, if drivetrain consists of multiple gear pairs, receptance method will also result in a large number of nonlinear equations and large matrices will be involved in the solution procedure. Therefore, modal superposition method is to be introduced to the dynamic response analysis of multi-stage, multi-mesh gear systems. In modal superposition method, the response of the nonlinear system is estimated by modal superposition employing the mode shapes of the linear system. The number of resulting nonlinear equations depends on the number of modes utilized in the modal superposition; therefore, it is independent of the number of nonlinear DOFs, i.e., the number of gear meshes.

Both time domain simulation and frequency domain simulation by utilizing Harmonic Balance Method (HBM) will be performed. In HBM, nonlinear forces are represented by Fourier series approximation and it is an extensively used method in the dynamic response analysis of geared systems. However, discrete Fourier transform utilized in HBM causes some convergence problems in the solutions of systems with large number of nonlinear equations. Therefore, it is aimed to develop

a computationally efficient solution method and as opposed to gear dynamics studies that utilize discrete Fourier transform [27,28,54,55], continuous-time Fourier transform will be employed. It is also aimed to decrease the computational time by employing analytical integration rather than numerical integration for the calculation of Fourier coefficients. Furthermore, the method to be developed will be applicable to single and multiple harmonic forced response analysis. Finally, several parametric studies will be accomplished in order to examine the effects of a large number of design parameters on dynamics of geared systems. In these parametric studies, effects of shaft lengths, gear hand configurations, orientation angles of gears, backlash amount, bearing stiffness coefficients, helix angle etc. will be investigated.

1.4 Dissertation Overview

In the first chapter of this dissertation, a brief introduction, literature survey and motivation, scope and objective of this research are provided. In Chapter 2, nonlinear time-varying dynamic analysis of a multi-mesh spur gear train is presented in order to gain insight of gear dynamics. The interactions between the gear meshes such as mesh phasing are investigated for different loading conditions such as idler and split-torque arrangements. The effects of asymmetric positioning of the gears around the middle gear on the dynamic response are also studied. Chapter 3 describes the linear dynamic analysis of helical geared systems. The undamped natural frequencies of some drivetrain configurations, i.e., countershaft arrangement, split-torque and idler arrangements, obtained by Timoshenko beam finite element model (FEM) used in this study and by commercial gear analysis software MASTA are compared in order to verify the FEM developed in this study. In Chapter 4, considering both backlash nonlinearity and time-varying mesh stiffness, a nonlinear dynamic model of a spiral bevel gear train composed of two

flexible shafts is proposed. The mesh model of the gear pair is integrated into the Timoshenko beam FEM model of shaft-bearing structures. Furthermore, receptance method is introduced to the dynamic analysis of geared systems with nonlinearities in order to decrease the number of resulting nonlinear equations. Several case studies are performed and the effects of backlash amount and fluctuating mesh stiffness on dynamics are studied. In Chapter 5, a nonlinear time-varying dynamic model of a multi-stage, multi-mesh drivetrain composed of both cylindrical and bevel gears is presented. Since receptance method also results in a large number of nonlinear equations and large matrices are utilized in the solution, modal superposition method is employed. Thus, the number of nonlinear equations is proportional to the number of modes utilized in the modal superposition, rather than the number of DOFs associated with the nonlinear elements. Several parametric studies are accomplished in order to demonstrate the influences of a large number of design parameters on dynamics of multi-mesh, multi-stage geared system.

CHAPTER 2

NONLINEAR TIME-VARYING DYNAMIC ANALYSIS OF A MULTI-MESH SPUR GEAR TRAIN

2.1 Introduction

There are numerous gear dynamics related studies in the literature and in the vast majority of these studies, a single gear pair is considered. Numerous mathematical models are constructed and analytical and numerical solution methods are developed in those studies. The models including a spur gear pair are mostly nonlinear (piecewise-linear) due to backlash but differ in incorporating time variation of mesh stiffness. Some of these models are nonlinear time-invariant (NTI) [11], whereas the others are nonlinear time-varying (NTV) [13,16,22,23,35]. However, published experimental data [22–24] show that the dynamic behavior of a spur gear is nonlinear and time-varying. These single degree-of-freedom (DOF) models are extended to multiple DOFs nonlinear models of geared rotor-bearing systems [15,17,19,21]. Moreover, linear and time-invariant characteristics of helical gears are studied in [39–41].

The studies on multi-mesh gear systems are fewer than the ones on single gear pair systems in spite of the widespread use of multi-stage, multi-mesh drivetrains. NTV dynamic models of multi-mesh spur geared systems are developed in [27–29]. In those studies, Harmonic Balance Method (HBM) with multiple harmonics and discrete Fourier transform (DFT) are utilized to obtain period-1 and subharmonic responses. NTV dynamic models of two-stage spur gear trains in idler and counter-

shaft arrangements are presented in [30,31]. For planetary gear sets composed of spur and helical gears, NTV [32] and LTI [42] dynamic models are proposed, respectively.

A nonlinear time-varying dynamic model of a multi-mesh spur gear train is proposed in this study. Both backlash nonlinearity and mesh stiffness fluctuation are included in the model, which consists of three spur gears with one of the gears in mesh with the other two as shown in Fig. 2.1. Both static transmission error excitation and parametric excitations due to fluctuating mesh stiffness are considered. The multi-term HBM coupled with DFT and arc-length numerical continuation are employed to solve the equations of motion for periodic steady-state response. Direct numerical integration (NI), which is computationally demanding, is employed to validate the results obtained by HBM. Furthermore, the stability of the steady-state solutions is determined by utilizing Floquet theory. Dynamics of both split-torque and idler arrangements are studied. In the split-torque arrangement, the system is driven by the middle gear, whereas one of the end gears is the input and the other one is the output in the idler arrangement. The interaction between meshes such as phasing is investigated for each loading condition and the influence of mesh phasing on dynamics is discussed. The effects of asymmetric positioning of the gears around the middle gear on the dynamic response are also studied.

2.2 Dynamic Model Formulation

2.2.1 Physical System and Dynamic Model

The drivetrain illustrated in Fig. 2.1 is composed of three spur gears with rigid gear blanks mounted on rigid shaft-bearing assembly. The gear in the middle, gear-2, meshes with the other two gears, gear-1 and gear-3. The mesh coupling between the

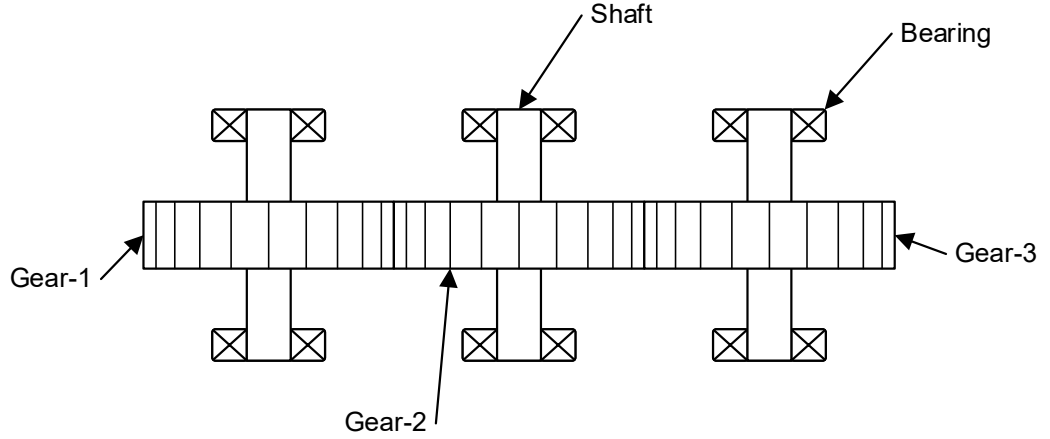


Fig. 2.1 Multi-mesh spur gear train considered in this study

gears, which is illustrated in Fig. 2.2, includes gear backlash, time-varying mesh stiffness, which acts as parametric excitation, and time-invariant mesh damping. The static transmission errors, $\bar{e}_1(\bar{t})$ and, $\bar{e}_2(\bar{t})$, excite the gear train as well. Gear mesh damping elements are also assumed not to be subjected to gear backlash nonlinearity.

In Fig. 2.2, torsional vibrations of each gear are considered where r_i denotes the base radius and I_i represents the polar mass moment of inertia of the i^{th} gear. Therefore, the system is modeled by a 3-DOFs semi-definite dynamic model with coordinates $\bar{\theta}_i$, ($i=1-3$).

The equations of motion of the drivetrain are expressed as follows

$$I_1 \ddot{\bar{\theta}}_1(\bar{t}) + r_1 \bar{c}_1 \left[r_1 \dot{\bar{\theta}}_1(\bar{t}) + r_2 \dot{\bar{\theta}}_2(\bar{t}) + \dot{\bar{e}}_1(\bar{t}) \right] + r_1 \bar{k}_1(\bar{t}) \bar{g}_1(\bar{t}) = \bar{T}_1, \quad (2.1)$$

$$I_2 \ddot{\bar{\theta}}_2(\bar{t}) + r_2 \bar{c}_1 \left[r_1 \dot{\bar{\theta}}_1(\bar{t}) + r_2 \dot{\bar{\theta}}_2(\bar{t}) + \dot{\bar{e}}_1(\bar{t}) \right] + r_2 \bar{k}_1(\bar{t}) \bar{g}_1(\bar{t}) + r_2 \bar{c}_2 \left[r_2 \dot{\bar{\theta}}_2(\bar{t}) + r_3 \dot{\bar{\theta}}_3(\bar{t}) + \dot{\bar{e}}_2(\bar{t}) \right] + r_2 \bar{k}_2(\bar{t}) \bar{g}_2(\bar{t}) = \bar{T}_2, \quad (2.2)$$

$$I_3 \ddot{\bar{\theta}}_3(\bar{t}) + r_3 \bar{c}_2 \left[r_2 \dot{\bar{\theta}}_2(\bar{t}) + r_3 \dot{\bar{\theta}}_3(\bar{t}) + \dot{\bar{e}}_2(\bar{t}) \right] + r_3 \bar{k}_2(\bar{t}) \bar{g}_2(\bar{t}) = \bar{T}_3, \quad (2.3)$$

where \bar{g}_1 and \bar{g}_2 are nonlinear displacement functions defined mathematically as

$$\bar{g}_1 = \begin{cases} \left[r_1 \bar{\theta}_1(\bar{t}) + r_2 \bar{\theta}_2(\bar{t}) + \bar{e}_1(\bar{t}) \right] - \bar{b}_1, & \left[r_1 \bar{\theta}_1(\bar{t}) + r_2 \bar{\theta}_2(\bar{t}) + \bar{e}_1(\bar{t}) \right] > \bar{b}_1 \\ 0, & \left| r_1 \bar{\theta}_1(\bar{t}) + r_2 \bar{\theta}_2(\bar{t}) + \bar{e}_1(\bar{t}) \right| \leq \bar{b}_1 \\ \left[r_1 \bar{\theta}_1(\bar{t}) + r_2 \bar{\theta}_2(\bar{t}) + \bar{e}_1(\bar{t}) \right] + \bar{b}_1, & \left[r_1 \bar{\theta}_1(\bar{t}) + r_2 \bar{\theta}_2(\bar{t}) + \bar{e}_1(\bar{t}) \right] < -\bar{b}_1 \end{cases}, \quad (2.4)$$

$$\bar{g}_2 = \begin{cases} \left[r_2 \bar{\theta}_2(\bar{t}) + r_3 \bar{\theta}_3(\bar{t}) + \bar{e}_2(\bar{t}) \right] - \bar{b}_2, & \left[r_2 \bar{\theta}_2(\bar{t}) + r_3 \bar{\theta}_3(\bar{t}) + \bar{e}_2(\bar{t}) \right] > \bar{b}_2 \\ 0, & \left| r_2 \bar{\theta}_2(\bar{t}) + r_3 \bar{\theta}_3(\bar{t}) + \bar{e}_2(\bar{t}) \right| \leq \bar{b}_2 \\ \left[r_2 \bar{\theta}_2(\bar{t}) + r_3 \bar{\theta}_3(\bar{t}) + \bar{e}_2(\bar{t}) \right] + \bar{b}_2, & \left[r_2 \bar{\theta}_2(\bar{t}) + r_3 \bar{\theta}_3(\bar{t}) + \bar{e}_2(\bar{t}) \right] < -\bar{b}_2 \end{cases}. \quad (2.5)$$

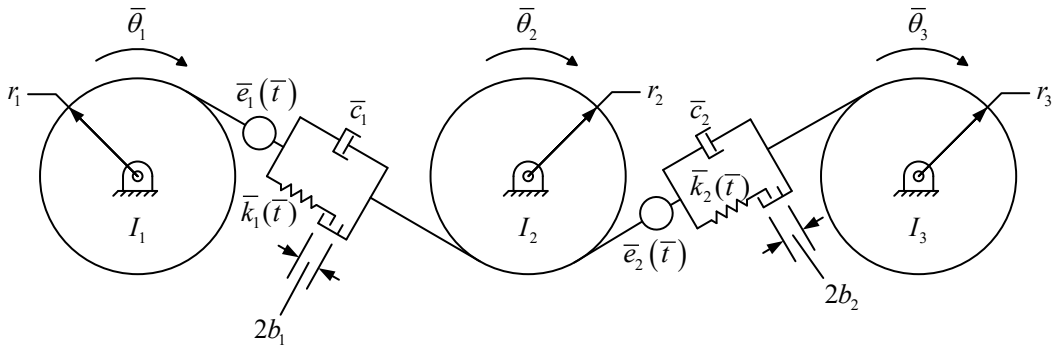


Fig. 2.2 Dynamic model of the system

The above 3-DOFs semi-definite system can be transformed to a 2-DOFs definite system by defining two new coordinates:

$$\bar{p}_1(\bar{t}) = r_1\bar{\theta}_1(\bar{t}) + r_2\bar{\theta}_2(\bar{t}) + \bar{e}_1(\bar{t}), \quad (2.6)$$

$$\bar{p}_2(\bar{t}) = r_2\bar{\theta}_2(\bar{t}) + r_3\bar{\theta}_3(\bar{t}) + \bar{e}_2(\bar{t}). \quad (2.7)$$

These new coordinates represent the relative mesh displacements, which are the combinations of the dynamic and static transmission errors. Using Eqs. (2.1)-(2.3), (2.6) and (2.7), the following new system of equations is obtained

$$\begin{aligned} \ddot{\bar{p}}_1(\bar{t}) + \bar{c}_1 \left[\frac{r_1^2}{I_1} + \frac{r_2^2}{I_2} \right] \dot{\bar{p}}_1(\bar{t}) + \bar{c}_2 \frac{r_2^2}{I_2} \dot{\bar{p}}_2(\bar{t}) + \bar{k}_1(\bar{t}) \left[\frac{r_1^2}{I_1} + \frac{r_2^2}{I_2} \right] \bar{g}_1(\bar{t}) \\ + \bar{k}_2(\bar{t}) \frac{r_2^2}{I_2} \bar{g}_2(\bar{t}) = \frac{r_1}{I_1} \bar{T}_1 + \frac{r_2}{I_2} \bar{T}_2 + \ddot{\bar{e}}_1(\bar{t}) \end{aligned}, \quad (2.8)$$

$$\begin{aligned} \ddot{\bar{p}}_2(\bar{t}) + \bar{c}_1 \frac{r_2^2}{I_2} \dot{\bar{p}}_1(\bar{t}) + \bar{c}_2 \left[\frac{r_2^2}{I_2} + \frac{r_3^2}{I_3} \right] \dot{\bar{p}}_2(\bar{t}) + \bar{k}_1(\bar{t}) \frac{r_2^2}{I_2} \bar{g}_1(\bar{t}) \\ + \bar{k}_2(\bar{t}) \left[\frac{r_2^2}{I_2} + \frac{r_3^2}{I_3} \right] \bar{g}_2(\bar{t}) = \frac{r_2}{I_2} \bar{T}_2 + \frac{r_3}{I_3} \bar{T}_3 + \ddot{\bar{e}}_2(\bar{t}) \end{aligned}. \quad (2.9)$$

In order to obtain the dimensionless equations of motion, the following transformations are applied:

$$m_1 = \frac{I_1 I_2}{r_1^2 I_2 + r_2^2 I_1}, \quad m_2 = \frac{I_2}{r_2^2}, \quad m_3 = \frac{I_2 I_3}{r_3^2 I_2 + r_2^2 I_3}, \quad (2.10)$$

$$k_1(\bar{t}) = \frac{\bar{k}_1(\bar{t})}{k_{1m}}, \quad k_2(\bar{t}) = \frac{\bar{k}_2(\bar{t})}{k_{2m}}, \quad (2.11)$$

$$\bar{\omega}_{11}^2 = \frac{k_{1m}}{m_1}, \quad \bar{\omega}_{12}^2 = \frac{k_{2m}}{m_2}, \quad \bar{\omega}_{21}^2 = \frac{k_{1m}}{m_2}, \quad \bar{\omega}_{22}^2 = \frac{k_{2m}}{m_3}, \quad (2.12)$$

$$\zeta_{11} = \frac{\bar{c}_1}{2m_1\bar{\omega}_{11}}, \quad \zeta_{12} = \frac{\bar{c}_2}{2m_2\bar{\omega}_{12}}, \quad \zeta_{21} = \frac{\bar{c}_1}{2m_2\bar{\omega}_{21}}, \quad \zeta_{22} = \frac{\bar{c}_2}{2m_3\bar{\omega}_{22}}, \quad (2.13)$$

where the mean components of the mesh stiffness functions, $\bar{k}_1(\bar{t})$ and $\bar{k}_2(\bar{t})$, are denoted by k_{1m} and k_{2m} , respectively. Here, $\zeta_{ij}(i, j = 1, 2)$ defines the damping ratio and $\bar{\omega}_{ij}(i, j = 1, 2)$ is the characteristic frequency. Moreover, $t = \bar{t}\omega_c$ is the dimensionless time, where ω_c is one of the characteristic frequencies. Dimensionless displacements are expressed as $p_i(\bar{t}) = \bar{p}_i(\bar{t})/b_c$, $e_i(\bar{t}) = \bar{e}_i(\bar{t})/b_c$ and $b_i = \bar{b}_i/b_c$ ($i = 1, 2$), where b_c denotes the characteristic length. Using these dimensionless parameters and letting $\omega_{ij} = \bar{\omega}_{ij}/\omega_c$ ($i, j = 1, 2$), the dimensionless equations of motion can be written as

$$\begin{aligned} \begin{Bmatrix} p_1''(t) \\ p_2''(t) \end{Bmatrix} + 2 \begin{bmatrix} \zeta_{11}\omega_{11} & \zeta_{12}\omega_{12} \\ \zeta_{21}\omega_{21} & \zeta_{22}\omega_{22} \end{bmatrix} \begin{Bmatrix} p_1'(t) \\ p_2'(t) \end{Bmatrix} \\ + \begin{bmatrix} \omega_{11}^2 k_1(t) & \omega_{12}^2 k_2(t) \\ \omega_{21}^2 k_1(t) & \omega_{22}^2 k_2(t) \end{bmatrix} \begin{Bmatrix} g_1(t) \\ g_2(t) \end{Bmatrix} = \begin{Bmatrix} F_m^{(1)} + e_1''(t) \\ F_m^{(2)} + e_2''(t) \end{Bmatrix}, \end{aligned} \quad (2.14)$$

where

$$g_i(t) = \begin{cases} p_i(t) - b_i, & p_i(t) > b_i \\ 0, & |p_i(t)| \leq b_i, \\ p_i(t) + b_i, & p_i(t) < -b_i \end{cases}, \quad i = 1, 2, \quad (2.15)$$

$$F_m^{(1)}(t) = \frac{1}{\omega_c^2 b_c} \left(\frac{r_1}{I_1} \bar{T}_1 + \frac{r_2}{I_2} \bar{T}_2 \right), \quad F_m^{(2)}(t) = \frac{1}{\omega_c^2 b_c} \left(\frac{r_2}{I_2} \bar{T}_2 + \frac{r_3}{I_3} \bar{T}_3 \right). \quad (2.16)$$

2.2.2 Period-one dynamics

The multi-harmonics Harmonic Balance Method in conjunction with discrete Fourier transform, which has been successfully employed in [22,23,27,28], is utilized to solve the dimensionless equations of motion for p_i ($i=1,2$). Since the static transmission errors and the time-varying parameters are assumed to be periodic, the solution can be expressed periodically as well [27]. This also implies that the nonlinear displacement functions $g_i(t)$ ($i=1,2$) can also be described periodically. The harmonic expressions for mesh stiffness and static transmission error are expressed as

$$k_i(t) = 1 + \sum_{a=1}^A \left[\kappa_{2a}^{(i)} \cos(a\Omega t) + \kappa_{2a+1}^{(i)} \sin(a\Omega t) \right], \quad (i=1,2), \quad (2.17)$$

$$e_i(t) = \sum_{j=1}^J \left[\varepsilon_{2j}^{(i)} \cos(j\Omega t) + \varepsilon_{2j+1}^{(i)} \sin(j\Omega t) \right], \quad (i=1,2). \quad (2.18)$$

The mean values of the static transmission errors are set to zero since only the second order derivatives of them are incorporated into the equations of motion (2.14) as parts of the excitation terms on the right hand side of the equation.

Given the periodic excitations of Eqs. (2.17)-(2.18), the steady-state solution is assumed as follows

$$p_i(t) = u_1^{(i)} + \sum_{r=1}^R \left[u_{2r}^{(i)} \cos(r\Omega t) + u_{2r+1}^{(i)} \sin(r\Omega t) \right], \quad (i=1,2), \quad (2.19)$$

which is differentiated as

$$p_i'(t) = \sum_{r=1}^R \left[-(r\Omega) u_{2r}^{(i)} \sin(r\Omega t) + (r\Omega) u_{2r+1}^{(i)} \cos(r\Omega t) \right], \quad (i=1,2), \quad (2.20)$$

$$p_i''(t) = -\sum_{r=1}^R \left[(r\Omega)^2 u_{2r}^{(i)} \cos(r\Omega t) + (r\Omega)^2 u_{2r+1}^{(i)} \sin(r\Omega t) \right], \quad (i=1,2). \quad (2.21)$$

Sampling N points in a mesh cycle, the time series of nonlinear restoring forces can be calculated as follows

$$F_k^{(i)}(t_n) = \omega_{i1}^2 k_1(t_n) g_1(t_n) + \omega_{i2}^2 k_2(t_n) g_2(t_n), \quad (i=1,2), \quad (2.22)$$

where $t_n = n\rho$ ($n = 0, 1, 2, \dots, N-1$). Here, $\rho = 2\pi/(N\Omega)$.

In order to utilize multi-harmonics HBM, the nonlinear restoring forces are represented by Fourier series as

$$F_k^{(i)}(t) = F_{k1}^{(i)} + \sum_{r=1}^R \left[F_{k(2r)}^{(i)} \cos(r\Omega t) + F_{k(2r+1)}^{(i)} \sin(r\Omega t) \right], \quad (i=1,2), \quad (2.23)$$

where the coefficients are calculated by employing discrete Fourier transform as ($r = 1, 2, \dots, R$)

$$F_{k1}^{(i)} = \frac{1}{N} \sum_{n=0}^{N-1} F_k^{(i)}, \quad (i=1,2), \quad (2.24)$$

$$F_{k(2r)}^{(i)} = \frac{2}{N} \sum_{n=0}^{N-1} F_k^{(i)} \cos\left(\frac{2\pi rn}{N}\right), \quad (i=1,2), \quad (2.25)$$

$$F_{k(2r+1)}^{(i)} = \frac{2}{N} \sum_{n=0}^{N-1} F_k^{(i)} \sin\left(\frac{2\pi rn}{N}\right), \quad (i=1,2). \quad (2.26)$$

Substituting Eqs. (2.18), (2.20)-(2.21), and (2.23) into Eq. (2.14) and equating the coefficients of the like harmonic terms, a total of $(4R+2)$ nonlinear algebraic equations are obtained with $(i=1,2)$ and $(r=1,2,\dots,R)$

$$S_1^{(i)} = F_{k1}^{(i)} - F_m^{(i)} = 0, \quad (2.27)$$

$$\begin{aligned} S_{2r}^{(i)} = & -(r\Omega)^2 u_{2r}^{(i)} + 2\zeta_{i1}\omega_{i1}(r\Omega)u_{2r+1}^{(1)} \\ & + 2\zeta_{i2}\omega_{i2}(r\Omega)u_{2r+1}^{(2)} + F_{k(2r)}^{(i)} + (r\Omega)^2 \varepsilon_{2r}^{(i)} = 0 \end{aligned} \quad (2.28)$$

$$\begin{aligned} S_{2r+1}^{(i)} = & -(r\Omega)^2 u_{2r+1}^{(i)} - 2\zeta_{i1}\omega_{i1}(r\Omega)u_{2r}^{(1)} \\ & - 2\zeta_{i2}\omega_{i2}(r\Omega)u_{2r}^{(2)} + F_{k(2r+1)}^{(i)} + (r\Omega)^2 \varepsilon_{2r+1}^{(i)} = 0 \end{aligned} \quad (2.29)$$

Finally, the solution vector $\mathbf{U} = [u_1^{(1)}, u_2^{(1)}, \dots, u_{2R}^{(1)}, u_{2R+1}^{(1)}, u_1^{(2)}, u_2^{(2)}, \dots, u_{2R}^{(2)}, u_{2R+1}^{(2)}]^T$ is determined by employing Newton's Method. In order to follow the solution path even around turning points, where the Jacobian becomes singular, arc-length continuation is employed. Details are given in Chapter 4.

The Floquet theory is used to determine the stability of the steady-state solutions $p_i, (i=1,2)$ obtained above. This is done by investigating the stability of the

perturbed solution $p_i + \Delta p_i, (i = 1, 2)$. The variational equation for the perturbation $\Delta p_i, (i = 1, 2)$ is

$$\begin{aligned} & \begin{Bmatrix} \Delta p_1''(t) \\ \Delta p_2''(t) \end{Bmatrix} + 2 \begin{bmatrix} \zeta_{11}\omega_{11} & \zeta_{12}\omega_{12} \\ \zeta_{21}\omega_{21} & \zeta_{22}\omega_{22} \end{bmatrix} \begin{Bmatrix} \Delta p_1'(t) \\ \Delta p_2'(t) \end{Bmatrix} \\ & + \begin{bmatrix} \omega_{11}^2 k_1(t) \phi_1(t) & \omega_{12}^2 k_2(t) \phi_2(t) \\ \omega_{21}^2 k_1(t) \phi_1(t) & \omega_{22}^2 k_2(t) \phi_2(t) \end{bmatrix} \begin{Bmatrix} \Delta p_1(t) \\ \Delta p_2(t) \end{Bmatrix} = \{0\} \end{aligned}, \quad (2.30)$$

where $\phi_i(t)$ represents the discontinuous separation function

$$\phi_i(t) = \begin{cases} 1, & |p_i(t)| > 1 \\ 0, & |p_i(t)| \leq 1 \end{cases}, \quad (i = 1, 2). \quad (2.31)$$

Eq. (2.30) is expressed in state-space form $\mathbf{P}'(t) = \mathbf{G}(t)\mathbf{P}(t)$ where $\mathbf{P}(t) = [\Delta p_1 \ \Delta p_2 \ \Delta p_1' \ \Delta p_2']^T$ is the state vector and $\mathbf{G}(t) = \mathbf{G}(t+T)$ is the periodic state matrix as

$$\mathbf{G}(t) = \begin{bmatrix} 0 & 0 & 1 & 0 \\ 0 & 0 & 0 & 1 \\ -\omega_{11}^2 k_1(t) \phi_1(t) & -\omega_{12}^2 k_2(t) \phi_2(t) & -2\zeta_{11}\omega_{11} & -2\zeta_{12}\omega_{12} \\ -\omega_{21}^2 k_1(t) \phi_1(t) & -\omega_{22}^2 k_2(t) \phi_2(t) & -2\zeta_{21}\omega_{21} & -2\zeta_{22}\omega_{22} \end{bmatrix}. \quad (2.32)$$

Then, a homogenous matrix equation, $\mathbf{z}'(t) = \mathbf{G}(t)\mathbf{z}(t)$, is obtained by employing Floquet theory and the solution of this homogenous matrix equation with the initial condition $\mathbf{z}(0) = \mathbf{I}_4$ results in the monodromy matrix, $\mathbf{M} = \mathbf{z}(T)$. The stability of

the solution is determined by investigating the eigenvalues of this matrix. Here \mathbf{I}_4 is 4×4 identity matrix [22].

\mathbf{M} can be computed with a method based on an assumed stepwise variation. $\mathbf{G}(t)$ is estimated as a series of step functions \mathbf{G}_n at N discrete time intervals $\tau = nh$ as follows

$$\mathbf{G}_n = \frac{1}{h} \int_{(n-1)h}^{nh} \mathbf{G}(\tau) d\tau, \quad (n = 1, 2, \dots, N). \quad (2.33)$$

If large number of time steps, N , is used, $\mathbf{G}(t)$ can be considered constant between two consecutive time steps and the integration is not needed. Between these two time instants, the following relation, where the exponential term is the state transition matrix, can be written

$$\mathbf{z}_{n+1} = e^{h\mathbf{G}_n} \mathbf{z}_n. \quad (2.34)$$

Then, the monodromy matrix is computed as the product of the individual transition matrices [56]:

$$\mathbf{z}_N = \prod_{n=0}^{N-1} e^{h\mathbf{G}_n} \mathbf{z}_0, \quad (2.35)$$

$$\mathbf{M} = \prod_{n=0}^{N-1} e^{h\mathbf{G}_n}. \quad (2.36)$$

Using Pade approximation or L^{th} order truncated Taylor series approximation as in [22] to calculate the matrix exponentiation above, monodromy matrix \mathbf{M} is

calculated. The solution is unstable when the amplitude of any of the eigenvalues λ_i of \mathbf{M} is larger than unity; otherwise the solution is stable [22,56].

2.2.3 Loading Conditions and Mesh Phases

Two different loading conditions as shown in Fig. 2.3 are considered here. In case-I, the system is driven by the middle gear (gear-2) and gears at the ends, gear-1 and gear-3, are outputs. This is known as split-torque arrangement. On the other hand, in case-II, gear-3 (output) is driven by gear-1 (input) through gear-2 (idler), which is idler arrangement. Therefore, the dynamic model shown in Fig. 2.2 is actually for idler arrangement but the same equations of motion can be obtained for split-torque arrangement by defining the same coordinates $\bar{p}_1(\bar{t})$ and $\bar{p}_2(\bar{t})$ as given in Eqs. (2.6) and (2.7). The static transmission errors for the two meshes in the system are defined as

$$e_1(t) = \sum_{j=1}^J E_j^{(1)} \sin(j\Omega t + \alpha_{1j}), \quad (2.37)$$

$$e_2(t) = \sum_{j=1}^J E_j^{(2)} \sin[j\Omega t + \alpha_{2j} + j\Pi], \quad (2.38)$$

where $E_j^{(i)}$ and α_{ij} are the j^{th} harmonic amplitude and phase angle of the i^{th} gear mesh, respectively. Assuming that the both gear meshes are subject to same flank modifications yields $\alpha_{1j} = \alpha_{2j}$ [40]. Therefore, the only phase difference between the meshes is Π , which is defined as

$$\Pi = Z_2(\psi + \gamma), \quad (2.39)$$

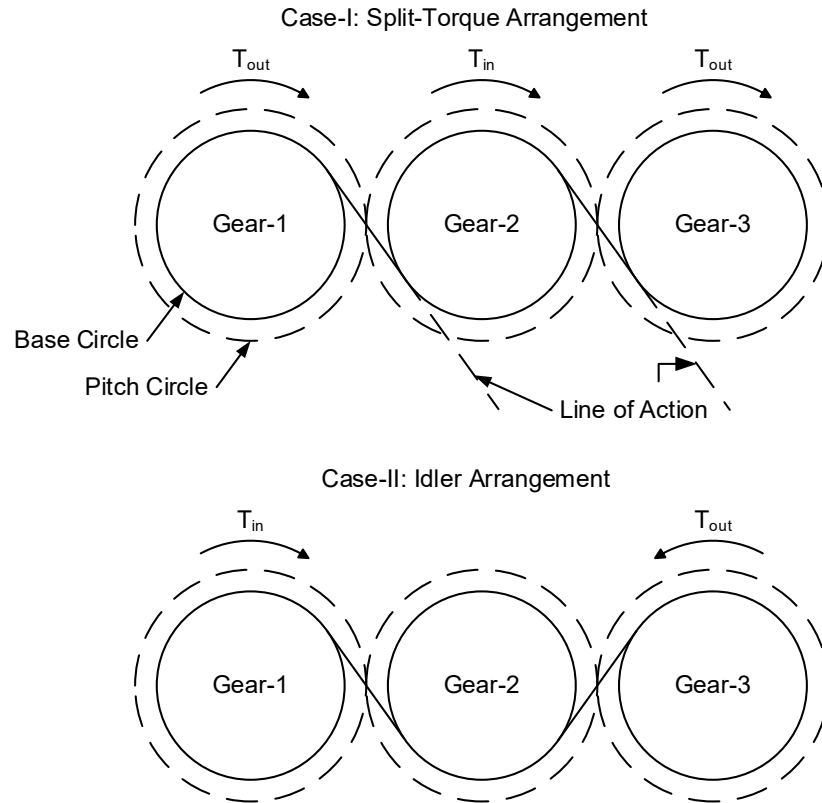


Fig. 2.3 Different loading conditions such as split-torque and idler arrangements

where Z_2 represents the number of teeth of gear-2 and ψ denotes the angle between the lines connecting the centers of the gears forming the meshes, which is shown in Fig. 2.4. γ is given as

$$\gamma = \begin{cases} 0, & \text{split-torque arrangement} \\ \pi/Z_2, & \text{idler arrangement} \end{cases} \quad (2.40)$$

The same phase relationship is also valid for the mesh stiffness. In addition, tooth deflection is maximum when the mesh stiffness is minimum. Similarly, the minimum tooth deflection corresponds to the maximum mesh stiffness. Thus, there

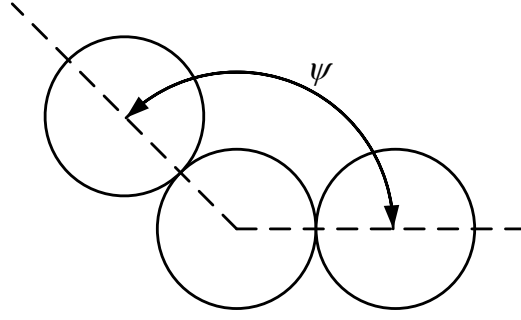


Fig. 2.4 Definition of the angle ψ

is an out-of-phase relationship between the mesh stiffness and the static transmission error of a gear mesh:

$$k_1(t) = K_0^{(1)} + \sum_{a=1}^A K_a^{(1)} \sin(a\Omega t + \alpha_{1j} + \pi), \quad (2.41)$$

$$k_2(t) = K_0^{(2)} + \sum_{a=1}^A K_a^{(2)} \sin(a\Omega t + \alpha_{1j} + \pi + a\Pi). \quad (2.42)$$

Definition of mesh stiffness k_i and static transmission error e_i can be converted to expressions that contain sine and cosine functions as in Eqs. (2.17) and (2.18).

2.3 Results and Discussion

A multi-mesh gear train composed of three identical spur gears with the parameters listed in Table 2.1 is considered as the example case. Only the first harmonics of the static transmission errors $e_i(t)$ ($i=1,2$) and the mesh stiffness functions

$k_i(t)$ ($i=1,2$) are considered in order to simplify the study. Furthermore, external torque values are taken as constant with no disturbances in the form of pulsations.

Firstly, the period-1 motion solutions found by HBM and direct numerical integration are compared. Fig. 2.5 shows the rms values of the displacement response in the idler arrangement, whereas the corresponding mean components are illustrated in Fig. 2.6. In the HBM solution, three harmonics are utilized ($R=3$ in Eq. (2.19)). The number of teeth of the middle gear Z_2 is taken as even, which results in a phase difference of π between the two meshes.

Table 2.1 Parameters of the drivetrain

Parameter	Numerical value
r_i , [m]	0.0423
Mass, [kg]	1.029
I_i , [kg m ²]	0.00136
k_{1m}, k_{2m} [N/m]	$6(10^8)$
c_1, c_2 [Ns/m]	3000
T_1, T_2, T_3 in idler arrangement [Nm]	100, 0, -100
T_1, T_2, T_3 in split-torque arrangement [Nm]	100, 200, 100
$K_1^{(1)}, K_1^{(2)}$	0.3
$E_1^{(1)}, E_1^{(2)}$	0.15
ψ	180°

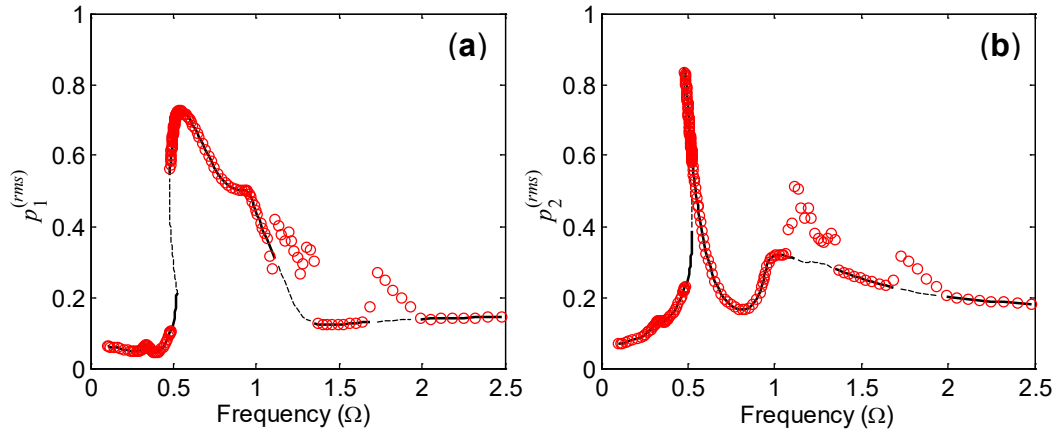


Fig. 2.5 rms values of the responses, $p_1(t)$ and $p_2(t)$ predicted by HBM and NI in the idler arrangement with even Z_2 . (—) Stable and (— —) unstable HBM solution, (\circ) NI solutions, (a) $p_1^{(rms)}$ (b) $p_2^{(rms)}$

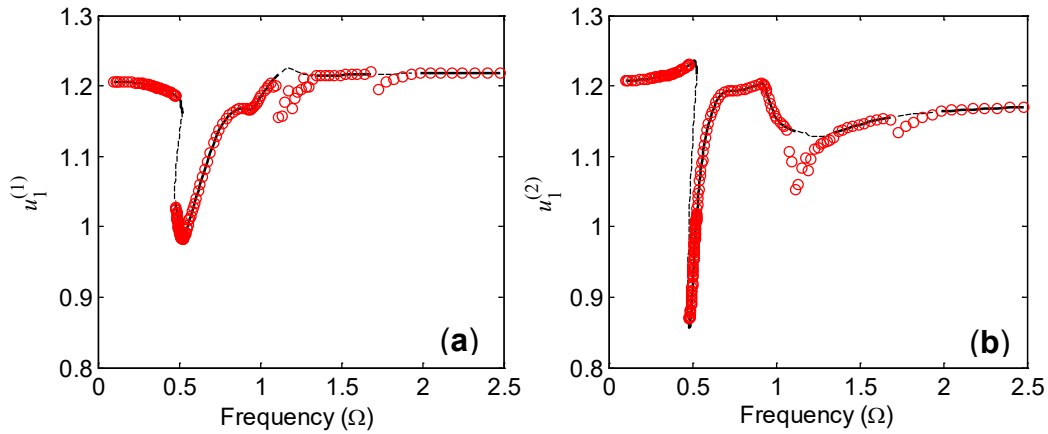


Fig. 2.6 Mean components of the responses, $p_1(t)$ and $p_2(t)$ predicted by HBM and NI in the idler arrangement with even Z_2 . (—) Stable and (— —) unstable HBM solution, (\circ) NI solutions, (a) $u_1^{(1)}$ (b) $u_1^{(2)}$

$b_c = 20 \mu\text{m}$ is used as the characteristic length, which implies that gears have a total of backlash. $\omega_c = 39667 \text{ rad/s}$, i.e. $\bar{\omega}_{11}$ given in Eq. (2.12), is considered as the characteristic frequency. With this characteristic frequency, the dimensionless undamped natural frequencies of the corresponding linear system are $\omega_{n1} = 0.71$ and $\omega_{n2} = 1.25$. The rms values are calculated as

$$p_i^{(rms)} = \left\{ \sum_{r=1}^R [A_r^{(i)}]^2 \right\}^{1/2}, \quad (2.43)$$

where $A_r^{(i)}$ is the amplitude of the r^{th} harmonic of $p_i(t)$ that can be defined as

$$A_r^{(i)} = \left\{ [u_{2r}^{(i)}]^2 + [u_{2r+1}^{(i)}]^2 \right\}. \quad (2.44)$$

In Fig. 2.5 and Fig. 2.6, stable and unstable HBM solutions are plotted with thick solid lines and thin dashed lines, respectively. It is observed that the solutions of the two methods are in very good agreement except around the unstable frequency ranges observed at $\Omega = [1.13 - 1.33]$ and $\Omega = [1.73 - 1.93]$. This shows the existence of subharmonic motions dictating these ranges, which corresponds to the parametric resonances due to the fluctuating mesh stiffness. While the NI solution can converge to these motions depending on the initial condition used, HBM cannot find these motions since the subharmonics are not included in the solutions assumed.

It is known from past studies [11,22,23] that spur gears can exhibit both single-sided (SSI) and double-sided (DSI) tooth impacts depending on the system parameters. Similar behaviors are also seen here in the results of both HBM and NI. Focusing on Fig. 2.5, the responses of the gear pairs are linear with no tooth impact in the low frequency range. As the frequency increases, $p_1^{(rms)}$ and $p_2^{(rms)}$ forced response curves

exhibit SSI, which is a softening-type nonlinear behavior due to tooth separation occurring near the primary resonance frequency, $\Omega = \omega_{n1}$. However, DSI, which is a hardening-type nonlinear behavior due to the additional impact with the preceding tooth, is not observed in the responses, since the amplitudes of the responses are smaller than the total amount of static deflection and backlash.

There is also a super-harmonic resonance peak at $\Omega \approx 0.5\omega_{n1} = 0.35$ due to the parametric excitation in Fig. 2.5. This peak can only be observed if sufficient number of harmonics is used in HBM. The nonlinear behavior is also obvious in Fig. 2.6. Mean amplitudes of $p_1(t)$ and $p_2(t)$ remain nearly constant in the case of no tooth separation. However, the values of $u_1^{(1)}$ and $u_1^{(2)}$ vary significantly in the case of tooth separation.

In Fig. 2.7, the response $p_1(t)$ of the split-torque arrangement obtained by HBM and NI is compared. Again, the number of teeth of gear-2 is even; hence, the two meshes are in phase. Due to the symmetry, the responses $p_1(t)$ and $p_2(t)$ are exactly the same; therefore, only $p_1(t)$ is shown here. The gear train in the split-torque arrangement exhibits nonlinear behavior as single-sided impact near the primary resonance frequency at $\Omega = \omega_{n2}$. Contrary to the idler arrangement, anti-resonance occurs near the primary resonance frequency at $\Omega = \omega_{n1}$ in the split-torque case. It is also clear in Fig. 2.7 that HBM and NI solutions again match very well. In this case, there are no frequency ranges which are dictated by subharmonic motions.

The influence of the out-of-phase relationship between the static transmission error and the mesh stiffness in the gear train with even Z_2 is shown in Fig. 2.8. Here, the combined response due to the static transmission error and parametric excitations is

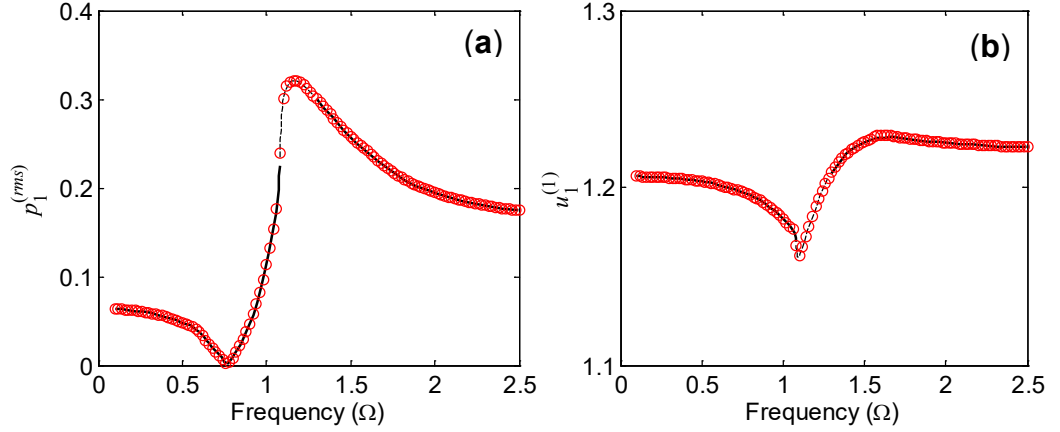


Fig. 2.7 Comparison of rms value and mean component of the response $p_1(t)$ predicted by HBM and NI in the split-torque arrangement with even Z_2 . (—) Stable and (— —) unstable HBM solution, (\circ) NI solutions, **(a)** $p_1^{(rms)}$ **(b)** $u_1^{(1)}$

compared with the responses of the system, where only one of the excitation sources exists. Split-torque arrangement is considered in Fig. 2.8(a) while Fig. 2.8(b) demonstrates the effect in idler case. Focusing on Fig. 2.8(a), each excitation alone forms a response peak at the same resonance frequency $\Omega = \omega_{n_2}$. However, the out-of-phase relationship results in a decrease in the combined response at the resonance frequencies. It is also noted in Fig. 2.8(a) that the super-harmonic resonance peak at $\Omega \approx 0.5 \omega_{n_2} = 0.62$ observed in the response curve of the only parametric excitation vanishes in the combined response. On the other hand, in the idler arrangement, the peak due to each excitation alone appears at different resonance frequency; hence, they do not affect each other significantly.

Fig. 2.9 compares the dynamic responses of four different loading conditions: (i) idler arrangement, $Z_2 = \text{even}$, (ii) idler arrangement, $Z_2 = \text{odd}$, (iii) split-torque

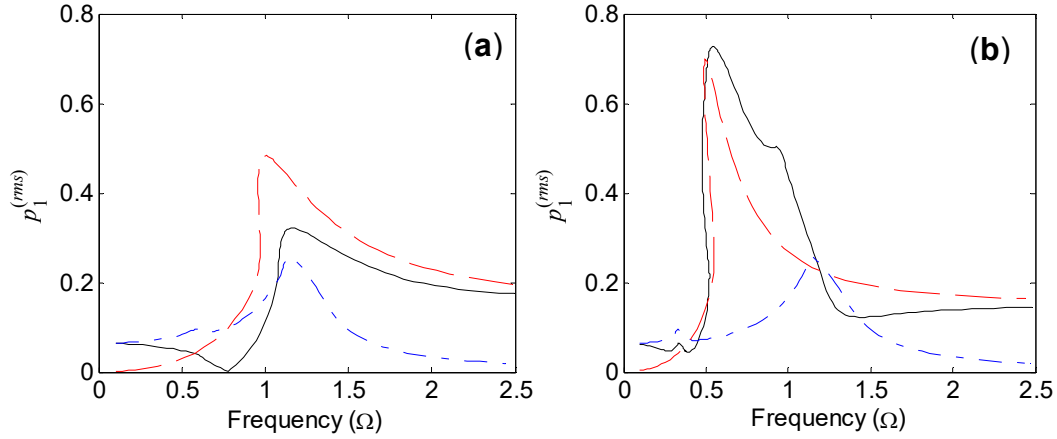


Fig. 2.8 Effect of the out-of-phase relationship between the static transmission error and mesh stiffness. Z_2 is even. (---) Response of the only parametric excitation (---) Response of the only static transmission error excitation (—) Combined response
(a) $p_1^{(rms)}$ in split-torque arrangement **(b)** $p_1^{(rms)}$ in idler arrangement

arrangement, $Z_2 = even$, (iv) split-torque arrangement, $Z_2 = odd$. As seen from Fig. 2.9, the split-torque arrangement excites the second mode shape at $\Omega = \omega_{n_2}$ when $Z_2 = even$ and the first mode shape at $\Omega = \omega_{n_1}$ when $Z_2 = odd$. Therefore, a shift in the frequency occurs due to the change of the excited mode shape. On the other hand, the idler arrangement has always two peaks at both resonance frequencies independent from the number of teeth of gear-2. The amplitudes of the peaks are affected significantly depending on the interaction between the static transmission errors and the mesh stiffness in terms of phasing.

Influence of the orientation angles of the end gears around the middle gear is illustrated in Fig. 2.10 for the split-torque arrangement with $Z_2 = 30$. The phase difference between the meshes are found as 0° , 90° and 180° by using Eq. (2.39) corresponding to the orientation angles of 180° , 135° and 90° , respectively. In the

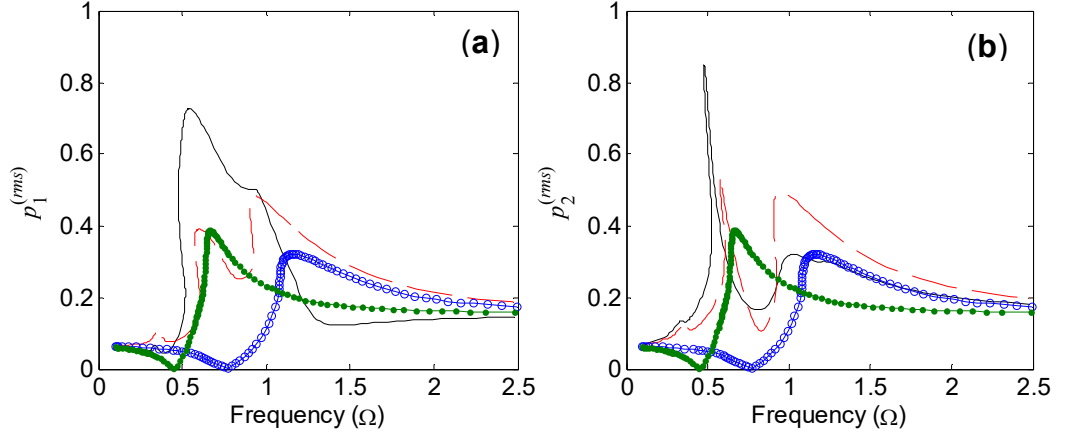


Fig. 2.9 Effect of loading conditions on dynamic response. (—) idler arrangement with even Z_2 (---) idler arrangement with odd Z_2 (—○—) split-torque arrangement with even Z_2 (—●—) split-torque arrangement with odd Z_2 (a) $p_1^{(rms)}$ (b) $p_2^{(rms)}$

configuration with $\psi = 180^\circ$, the peaks in the response curves of both meshes occur at the resonance frequency $\Omega = \omega_{n_2}$, while configuration with $\psi = 90^\circ$ triggers the first mode shape at $\Omega = \omega_{n_1}$. For $\psi = 135^\circ$, two distinct peaks exist in both $p_1^{(rms)}$ and $p_2^{(rms)}$. This agrees with the results of the linear time-invariant model of multi-mesh helical gear train studied in [40].

2.4 Conclusion

A nonlinear time-varying dynamic model for a multi-mesh spur gear train consisting of three gears and three shafts is formulated in this study. Harmonic balance method is employed in order to solve the resulting dimensionless equations of motion for steady-state response. Fourier coefficients are calculated by utilizing discrete

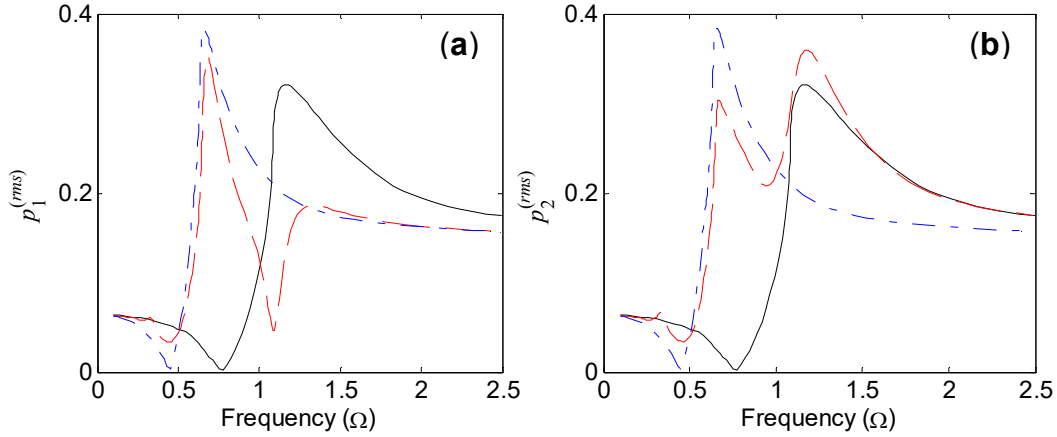


Fig. 2.10 Effect of orientation angle on dynamic response of the split-torque arrangement with $Z_2 = 30$. (—) $\psi = 180^\circ$ (---) $\psi = 135^\circ$ (- · - ·) $\psi = 90^\circ$ (a) $p_1^{(rms)}$ (b) $p_2^{(rms)}$

Fourier transform. Direct numerical integration (NI), which is computationally demanding, is employed to validate the results obtained by HBM. Furthermore, the stability of the solutions is determined by utilizing Floquet theory. It is seen from the results that the multi-mesh gear train exhibits nonlinear behavior as single-sided impact with the given system parameters. Double-sided tooth impacts including both tooth separations and back collisions are not observed. NI solutions also show the existence of the subharmonic motions near the frequencies corresponding to the parametric resonances.

The interaction between the static transmission error and parametric excitations is analyzed by considering the phasing between them. It is shown that the number of teeth of gear-2 has a significant effect on the dynamic response since it directly determines the phase angle between the meshes. Dynamic response is also influenced greatly by the positions of the end gears. Therefore, optimization of these parameters in the design may reduce vibration and noise.

CHAPTER 3

LINEAR DYNAMIC ANALYSIS OF A HELICAL GEARED SYSTEM

3.1 Dynamic Model Formulation

3.1.1 Physical System and Dynamic Model

Gears can lose contact due to backlash if dynamic mesh force exceeds static force transmitted. This cause tooth separations and back collisions of gears with a strongly nonlinear dynamic behavior. However, such nonlinear behaviors are not observed for moderately and heavily loaded helical geared systems, while gear backlash has significant influence on dynamics of spur gears. Furthermore, in contrast with spur gears, parametric resonances due to fluctuating mesh stiffness are not observed in dynamics of high contact ratio helical gears [39–41]. Therefore, in this research, a linear time-invariant (LTI) dynamic model of helical gears is developed. The gear shafts are modeled by using finite element formulation. Here, Timoshenko beam formulation is employed since shear deformations and rotary inertia are expected to be significant due to the use of stub shafts. The mass and stiffness effects of gear blanks are included in the shaft sections by using beam elements rather than lumping at a node. The bearings supporting the gear shafts are represented by linear and torsional springs. Clearance nonlinearity of bearings is neglected, which is a valid assumption for preloaded rolling element bearings [57]. Moreover, stiffness fluctuations of bearings are disregarded.

The mass matrix, \mathbf{M}_{sn} , and stiffness matrix, \mathbf{K}_{sn} , of each shaft n ($n = 1, 2, \dots, N$) are calculated by assembling the mass and stiffness matrices of Timoshenko beam elements. Complete mass matrix and shaft stiffness matrix of the drivetrain are then assembled as $\mathbf{M}_s = \text{Diag}[\mathbf{M}_{s1}, \mathbf{M}_{s2}, \dots, \mathbf{M}_{sN}]$ and $\mathbf{K}_s = \text{Diag}[\mathbf{K}_{s1}, \mathbf{K}_{s2}, \dots, \mathbf{K}_{sN}]$, respectively. Considering that each node has 6 DOFs and the shaft n is modeled by using a total of m_n beam elements, the dimension of both matrices is q where $q = 6 \cdot \sum_{n=1}^N (m_n + 1)$ is the total number of DOFs of the gear train.

Similarly, the complete bearing stiffness matrix of a gear train including a total of n_b bearings is assembled as $\mathbf{K}_b = \text{Diag}[\dots \mathbf{K}_{b1} \dots \mathbf{K}_{b2} \dots \mathbf{K}_{bn_b} \dots]$, where $\mathbf{K}_{bi} = \text{Diag}[k_{bxi}, k_{byi}, k_{bzi}, k_{b\theta_x i}, k_{b\theta_y i}, k_{b\theta_z i}]$ ($i = 1$ to n_b) is the stiffness matrix of the i^{th} bearing and k_{bxi} to $k_{b\theta_z i}$ are the stiffness values in the indicated directions. In the overall bearing stiffness matrix, \mathbf{K}_b , each individual bearing stiffness is located according to the node number where the bearing is attached. The remaining elements in \mathbf{K}_b are zero.

Fig. 3.1 illustrates a three-dimensional mesh model of a helical gear pair. The gears are connected to each other by a time-invariant mesh stiffness extending in the direction of tooth normal, i.e. along the line of action (LOA), which is determined by the helix angle, ψ . Static transmission error in the mesh coupling, which is connected in series to the mesh spring, excites the system. These parameters, i.e., mesh stiffness, static transmission error and LOA, are assumed to remain unchanged under dynamic conditions and a single point mesh model consisting of an effective mesh point and a constant LOA vector for a single spring element is used.

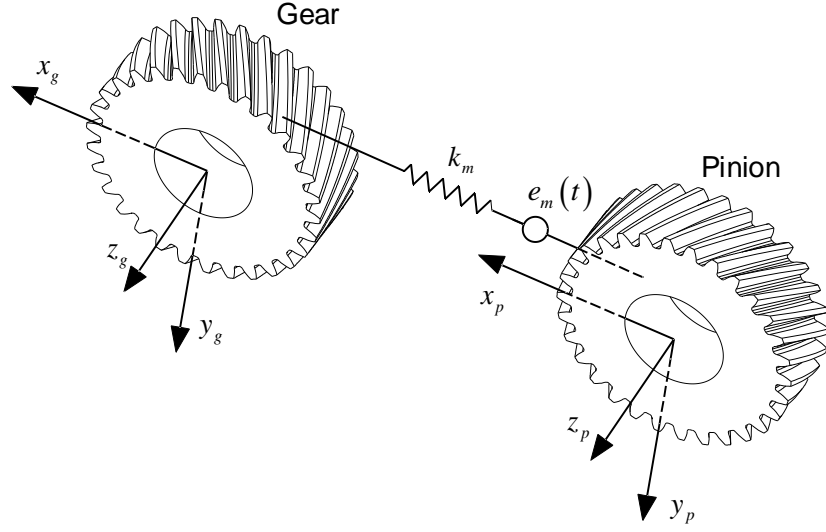


Fig. 3.1 Mesh model of a helical gear pair

Since the mesh node of each gear has 3 translational and 3 rotational DOFs as illustrated in Fig. 3.1, each mesh coupling between the shafts are defined by a total of 12 DOFs. Since some shafts have multiple gears forming multiple mesh couplings with the other shafts, the generalized coordinates are expressed relative to the local reference frames of gear shafts, S_{si} ($i = p, g$) rather than those of gears, S_i ($i = p, g$). Thus, the displacement vectors of the mesh nodes are expressed as $\mathbf{x}_{si} = (x_{si} \ y_{si} \ z_{si} \ \theta_{xsi} \ \theta_{ysi} \ \theta_{zsi})^T$ ($i = p, g$).

The dynamic transmission error is defined along the LOA as

$$\delta_d = \mathbf{h}_p^T \mathbf{x}_{sp} - \mathbf{h}_g^T \mathbf{x}_{sg}, \quad (3.1)$$

where \mathbf{h}_i ($i = p, g$) is the transformation vector, consisting of the directional cosines and directional rotation radii between the LOA and generalized coordinates, i.e., the

respective coordinates of pinion or gear shaft. Transformation vectors can be expressed as

$$\mathbf{h}_i = (n_{ix} \quad n_{iy} \quad n_{iz} \quad \lambda_{ix} \quad \lambda_{iy} \quad \lambda_{iz})^T \quad (i = p, g). \quad (3.2)$$

The directional rotation radii, λ , can be written as

$$\lambda_{ix} = \mathbf{n}_i \cdot (\mathbf{u}_{xi} \times \mathbf{r}_i) \quad (i = p, g), \quad (3.3)$$

$$\lambda_{iy} = \mathbf{n}_i \cdot (\mathbf{u}_{yi} \times \mathbf{r}_i) \quad (i = p, g), \quad (3.4)$$

$$\lambda_{iz} = \mathbf{n}_i \cdot (\mathbf{u}_{zi} \times \mathbf{r}_i) \quad (i = p, g), \quad (3.5)$$

where $\mathbf{n}_i = (n_{ix} \quad n_{iy} \quad n_{iz})^T$ is the directional cosine vector of LOA and $\mathbf{r}_i = (x_{im} \quad y_{im} \quad z_{im})^T$ represents the position vector of the effective mesh point. Moreover, $\mathbf{u}_{xi} = (1 \quad 0 \quad 0)^T$, $\mathbf{u}_{yi} = (0 \quad 1 \quad 0)^T$ and $\mathbf{u}_{zi} = (0 \quad 0 \quad 1)^T$ are the trio of unit vectors for coordinate system $S_{si}(i = p, g)$. In all the above equations, subscript $i = p, g$ indicates that the quantity is expressed in the local reference frame of the pinion or gear shaft, respectively. In this study, the effective mesh point is assumed to be the point of tangency of two pitch circles, i.e., pitch point, at the middle of the facewidth as shown in Fig. 3.2. Thus, the position vector of the effective mesh point is written as $\mathbf{r}_p = (r_{pm}^p \quad 0 \quad 0)^T$ and $\mathbf{r}_g = (-r_{pm}^g \quad 0 \quad 0)^T$ in the local reference frames of the pinion, S_p , and gear, S_g , respectively, where $r_{pm}^i (i = p, g)$ is the pitch radius. Furthermore, \mathbf{n}_i and $\mathbf{r}_i (i = p, g)$ can be expressed in $S_{si}(i = p, g)$ with a series of coordinate transformation as follows

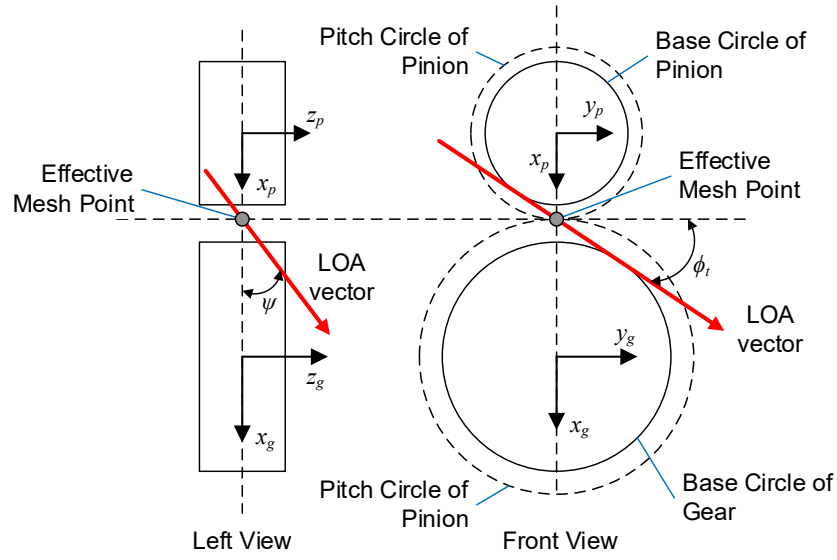


Fig. 3.2 Effective mesh point and LOA vector in a configuration where pinion rotates CCW and has left hand teeth

$$\mathbf{n}_i = \mathbf{T}_x(\theta_{di})\mathbf{T}_z(\theta_{oi})\mathbf{T}_z(\phi_t)\mathbf{T}_x(-\psi) \begin{Bmatrix} 0 \\ 1 \\ 0 \end{Bmatrix} \quad (i = p, g), \quad (3.6)$$

$$\mathbf{r}_i = \mathbf{T}_x(\theta_{di})\mathbf{T}_z(\theta_{oi}) \begin{Bmatrix} r_{pm}^i \\ 0 \\ 0 \end{Bmatrix} \quad (i = p, g), \quad (3.7)$$

where \mathbf{T}_σ ($\sigma = x, y, z$) denotes the transformation matrix about coordinate σ . Here, ϕ_t and ψ are the transverse pressure angle and helix angle of the gear pair, respectively. Moreover, based on the hand and the rotation direction of the driver gear (pinion), ϕ_t , and ψ are defined as follows

$$\phi_t = \begin{cases} \phi_t, & \text{if pinion rotates counterclockwise } (+z_p) \\ \pi - \phi_t, & \text{if pinion rotates clockwise } (-z_p) \end{cases}, \quad (3.8)$$

$$\psi = \begin{cases} \psi, & \text{if pinion rotates CCW and has left hand teeth} \\ -\psi, & \text{if pinion rotates CCW and has right hand teeth} \\ -\psi, & \text{if pinion rotates CW and has left hand teeth} \\ \psi, & \text{if pinion rotates CW and has right hand teeth} \end{cases}. \quad (3.9)$$

Two more angles, namely θ_{oi} and θ_{di} ($i = p, g$), are defined to transform the LOA vector from the local reference frames of gears, S_i ($i = p, g$), to the local reference frames of gear shafts, S_{si} ($i = p, g$). θ_{oi} represents the angle between the x axes of S_i and S_{si} , whereas θ_{di} denotes the angle between the z axes of S_i and S_{si} .

The dynamic mesh force, F_m , along the LOA is written as

$$F_m(t) = k_m (\delta_d(t) - e_m(t)). \quad (3.10)$$

The equation of motion of the whole geared system can be expressed as

$$\mathbf{M}\ddot{\mathbf{x}}(t) + \mathbf{C}\dot{\mathbf{x}}(t) + \mathbf{K}\mathbf{x}(t) = \mathbf{F}(t), \quad (3.11)$$

where $\mathbf{x}(t)$ is the displacement vector and $\mathbf{F}(t)$ is the overall external forcing vector including the external torques and static transmission error excitations as follows

$$\mathbf{F}(t) = \mathbf{F}_m + \mathbf{F}_a(t). \quad (3.12)$$

Here, \mathbf{F}_m and $\mathbf{F}_a(t)$ are the mean and alternating components of the forcing vector, which can be calculated as follows

$$\mathbf{F}_m = \left(\cdots \overbrace{\left(\begin{array}{cccccc} 0 & 0 & 0 & 0 & 0 & T_{in} \end{array} \right)}^{\text{Input Gear Node}} \cdots \overbrace{\left(\begin{array}{cccccc} 0 & 0 & 0 & 0 & 0 & -T_{out} \end{array} \right)}^{\text{Output Gear Node}} \cdots \right)^T, \quad (3.13)$$

$$\mathbf{F}_a(t) = \sum_{q=1}^{N_m} k_{m(q)} e_{m(q)} \mathbf{p}_q. \quad (3.14)$$

In the mean component of the external force vector, \mathbf{F}_m , the input and output torque values are located according to the node numbers associated with the input and output gears, respectively. The only nonzero elements of this vector are the ones related to rotation of input and output gears about z axis. The remaining elements in \mathbf{F}_m are zero. Assuming that the torque values are constant, only internal vibratory excitation, i.e., static transmission error, is considered.

The stiffness matrix of the whole geared system, \mathbf{K} , is calculated as $\mathbf{K} = \mathbf{K}_s + \mathbf{K}_b + \mathbf{K}_m$ where the mesh stiffness matrix, \mathbf{K}_m , is calculated as follows

$$\mathbf{K}_m = \sum_{q=1}^{N_m} k_{m(q)} \mathbf{p}_q \mathbf{p}_q^T, \quad (3.15)$$

where $k_{m(q)}$ denotes the mesh stiffness of the q^{th} gear mesh and \mathbf{p}_q represents the extended coordinate transformation vector for the q^{th} gear mesh obtained by locating the individual transformation vectors, $\mathbf{h}_i (i = p, g)$, in a null vector, whose length is equal to the number of total DOFs, according to the node numbers of pinion and gear forming the mesh:

$$\mathbf{p} = \left(\dots \mathbf{h}_p^T \dots - \mathbf{h}_g^T \dots \right)^T. \quad (3.16)$$

Furthermore, a set of damping ratio ζ_s is used for the shaft-bearing assembly in this study.

There are phase differences between gear meshes in multi-mesh, multi-stage geared systems. The static transmission error at q^{th} mesh in the system can be defined periodically as

$$e_{m(q)}(t) = \sum_{r=1}^R E_{m(q)}^r \sin(r\omega_q t + \alpha_q^r + r\Pi_q), \quad (3.17)$$

where $E_{m(q)}^r$ and α_q^r are the r^{th} harmonic amplitude and phase angle of the static transmission error at the q^{th} mesh, respectively. ω_q denotes the gear mesh frequency of the q^{th} mesh. Assuming that all the gear meshes are subject to same flank modifications yields $\alpha_1^r = \alpha_2^r = \dots = \alpha_q^r$. The other phase angle Π_q represents the phase difference between $e_{m(q)}(t)$ and $e_{m(1)}(t)$ where $\Pi_1 = 0$. Therefore, Π_q ($q = 2$ to N_m) can be defined as

$$\Pi_q = \sum_{j=2}^q \bar{\Pi}_j, \quad (3.18)$$

where $\bar{\Pi}_j$ denotes the phase difference between $e_{m(j)}(t)$ and the previous static transmission error $e_{m(j-1)}(t)$ and it can be calculated as

$$\bar{\Pi}_j = Z(\varphi_j - \beta_j) + \pi, \quad (3.19)$$

where Z is the number of teeth of the driver gear in the j^{th} mesh and φ_j denotes the angle between the vectors directed to the effective mesh points of j^{th} and $(j-1)^{\text{th}}$ meshes (see Fig. 3.3). β_j represents the angle between the reference teeth of the gears mounted on the same shaft, which is shown in Fig. 3.3. On the other hand, for systems that consist of three gears forming two meshes, i.e., idler and split-torque arrangements;

$$\beta_j = \begin{cases} 0, & \text{idler arrangement} \\ \pi/Z, & \text{split-torque arrangement} \end{cases} \quad (3.20)$$

3.1.2 Solution Method

Natural frequencies ω_s and mode shapes ϕ_s are obtained by the solution of the eigenvalue problem corresponding to (3.11), i.e., $\mathbf{K}\Phi = \omega^2\mathbf{M}\Phi$, where s is the modal index. The system response to the force vector defined by (3.12) is the sum of the mean, \mathbf{x}_m , and alternating components, $\mathbf{x}_a(t)$, of the response. The alternating component is calculated by utilizing Modal Summation Technique.

$$\mathbf{x}(t) = \mathbf{x}_m + \mathbf{x}_a(t), \quad (3.21)$$

$$\mathbf{x}_a(t) = \sum_{q=1}^{N_m} \sum_{r=1}^R \sum_{s=1}^S \left\{ \frac{\phi_s \phi_s^T}{\omega_s^2 - r^2 \omega_q^2 + 2i\zeta_s \omega_s \omega_q} \times k_{m(q)} \mathbf{p}_q \left[E_{m(q)}^r \sin(r\omega_q t + \alpha_q^r + r\Pi_q) \right] \right\}, \quad (3.22)$$

$$\mathbf{x}_m = \mathbf{K}^{-1} \mathbf{F}_m, \quad (3.23)$$

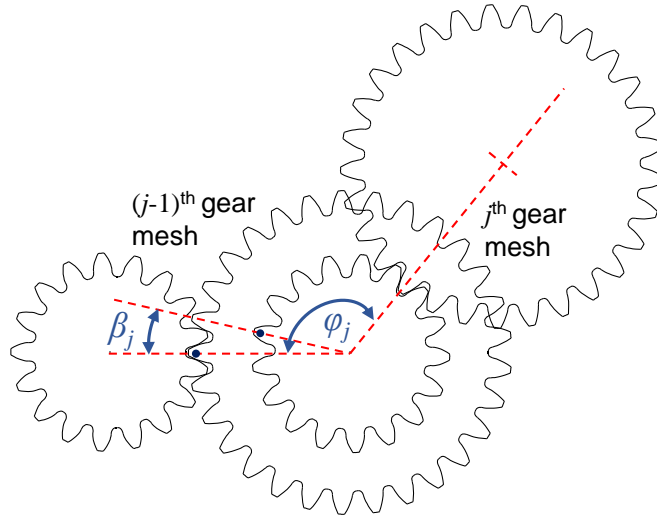


Fig. 3.3 Angle between the reference teeth of the gears mounted on the same shaft, β_j , and angle between the vectors directed to the effective mesh points, φ

where i denotes the unit imaginary number. Then, the dynamic response of the gear nodes, \mathbf{x}_{si} ($i = p, g$), are extracted from the total displacement vector, $\mathbf{x}(t)$ for the calculations of the dynamic transmission error and dynamic mesh force along the LOA given by (3.1) and (3.10), respectively.

3.2 Results and Discussion

Three case studies are accomplished to compare the natural frequencies and mode shapes obtained by Timoshenko beam FEM model developed in this study and by gear analysis software MASTA [58]. In the 1st case study, a drivetrain composed of helical gears in a countershaft arrangement as illustrated in Fig. 3.4 is considered. The parameters of the drivetrain are given in Table 3.1 and the undamped natural frequencies are listed in Table 3.2. It can be concluded that the finite element

modeling of shaft-bearing assembly including the gear blanks and the mesh couplings is accomplished in very good agreement with MASTA.

As the 2nd and 3rd case studies, three gears forming two meshes are used in idler and split-torque arrangements, respectively, which are illustrated in Fig. 3.5. The system parameters are given in Table 3.3. In split-torque arrangement, the gear train is driven by the middle gear (gear 2) and gears at the ends, gear 1 and gear 3, are outputs. On the other hand, the gear 3 (output gear) is driven by gear 1 (input gear) through gear 2 (idler gear) in idler arrangement. The natural frequencies of the drivetrain in idler and split-torque arrangements are listed in Table 3.4 and Table 3.5, respectively. The results obtained by Timoshenko beam FEM used in this study and by MASTA agree very well with each other.

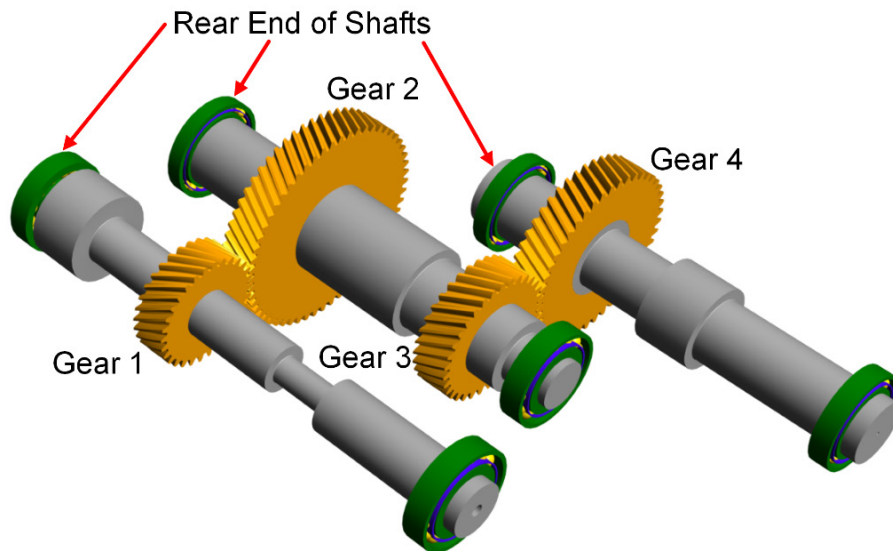


Fig. 3.4 Countershaft arrangement used in the 1st case study

Table 3.1 Parameters of the helical gear system in countershaft arrangement shown in Fig. 3.4

<i>Shaft Parameters</i>									
Segment	Shaft 1			Shaft 2			Shaft 3		
	OD	ID	L	OD	ID	L	OD	ID	L
1	40	0	30	60	10	30	55	18	75
2	75	0	30	60	20	70	65	18	30
3	75	10	15	75	20	140	49	18	30
4	40	10	190	60	20	30	49	3	30
5	23	10	50	60	0	60	68	3	45
6	45	10	135	40	0	40	51	3	140

<i>Gear Parameters</i>				
	Gear 1	Gear 2	Gear 3	Gear 4
Number of teeth	30	57	33	45
Helix angle (°)	30	30	25	25
Normal pressure angle (°)	17.5	17.5	20	20
Pitch diameter (mm)	90.07	171.13	101.95	139.03
Face width (mm)	30	30	30	30
Hand	Left	Right	Left	Right
Locations (mm) ^a	170	125	290	90
T (Nm)	250	0	0	-647.73

<i>Bearing Parameters</i>						
	Shaft 1		Shaft 2		Shaft 3	
	B1	B2	B1	B2	B1	B2
Locations (mm) ^a	15	430	10	355	20	330
k_b (N/m, Nm/rad)						

<i>Gear Mesh Parameters</i>		
	Mesh 1	Mesh 2
$k_{m(q)}$ (N/m)	540.2e6	524.3e6
$E_{m(q)}^1$ (μm)	0.5	0.5

^a Distance from the rear end of the corresponding shaft

Table 3.2 Comparison of the natural frequencies of the countershaft arrangement (Fig. 3.4)

Undamped Natural Frequencies			
n	Timoshenko beam FEM (Hz)	MASTA Solution (Hz)	Difference (%)
1	0.0	0.0	0.0
2	487.6	491.1	-0.70
3	604.1	607.4	-0.54
4	689.8	693.6	-0.56
5	710.1	714.6	-0.62
6	746.7	750.1	-0.46
7	770.0	771.1	-0.15
8	889.0	893.8	-0.53
9	954.4	956.1	-0.17
10	1096.6	1099.8	-0.30
11	1298.8	1303.0	-0.32
12	1380.8	1384.0	-0.23
13	1464.9	1467.1	-0.15
14	1532.1	1537.6	-0.35
15	1574.5	1581.9	-0.47
16	1636.3	1644.7	-0.51

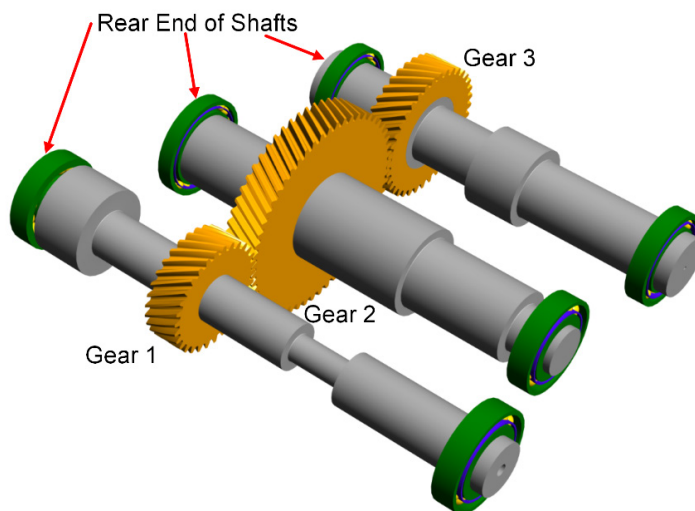


Fig. 3.5 Idler and split-torque arrangements used in the 2nd and 3rd case studies

Table 3.3 Parameters of the helical gear system in idler and split-torque arrangements shown in Fig. 3.5

<i>Shaft Parameters</i>									
Segment	Shaft 1			Shaft 2			Shaft 3		
	OD	ID	L	OD	ID	L	OD	ID	L
1	40	0	30	60	10	30	55	18	75
2	75	0	30	60	20	70	65	18	30
3	75	10	15	75	20	140	49	18	30
4	40	10	190	60	20	30	49	3	30
5	23	10	50	60	0	60	68	3	45
6	45	10	135	40	0	40	51	3	140

<i>Gear Parameters</i>			
	Gear 1	Gear 2	Gear 3
Number of teeth	30	57	37
Helix angle (°)	30	30	30
Normal pressure angle (°)	17.5	17.5	17.5
Pitch diameter (mm)	90.07	171.13	111.08
Face width (mm)	30	30	30
Hand	Left	Right	Left
Locations (mm) ^a	170	125	90
T in idler arrangement (Nm)	200	0	-246.7
T in split-torque arrangement (Nm)	-52.5	200	-65.1

<i>Bearing Parameters</i>						
	Shaft 1		Shaft 2		Shaft 3	
	B1	B2	B1	B2	B1	B2
Locations (mm) ^a	15	430	10	355	20	330
\mathbf{k}_b (N/m, Nm/rad)	Diag[$2.7(10^8)$, $2(10^8)$, $1.7(10^8)$, $0.788(10^6)$, $1.272(10^6)$, 0]					

<i>Gear Mesh Parameters</i>		
	Mesh 1	Mesh 2
$k_{m(q)}$ (N/m)	540.7e6	472.6e6
$E_{m(q)}^1$ (μm)	0.5	0.5

^a Distance from the rear end of the corresponding shaft

Table 3.4 Comparison of the natural frequencies of the idler arrangement (Fig. 3.5)

Undamped Natural Frequencies			
n	Timoshenko beam FEM (Hz)	MASTA Solution (Hz)	Difference (%)
1	0.0	0.0	0.0
2	487.4	495.1	-1.57
3	629.1	632.5	-0.54
4	691.3	700.9	-1.36
5	745.0	751.3	-0.84
6	780.5	780.8	-0.04
7	832.3	830.9	0.17
8	987.8	979.8	0.82
9	1025.3	1031.4	-0.59
10	1097.2	1098.9	-0.15
11	1379.8	1379.5	0.02
12	1460.0	1452.4	0.52
13	1529.6	1527.4	0.14
14	1549.3	1560.1	-0.69
15	1642.6	1655.2	-0.76
16	1732.7	1759.7	-1.53

The forced response of a helical geared system shown in Fig. 3.6 is plotted in Fig. 3.7 and Fig. 3.8. The parameters of the system are taken from [40] and given in Table 3.6. In Fig. 3.7, the root-mean-square (rms) values of the displacements of gear 1 and gear 2 in split-torque arrangement is shown, whereas Fig. 3.8 illustrates the effect of loading condition on dynamics. In Fig. 3.7, the responses of gear 1 and gear 3 are identical since the system in split-torque arrangement is symmetric. Similarly, the displacement, y_2 , is zero due to the symmetry. However, this behavior changes significantly when the idler arrangement is considered.

Table 3.5 Comparison of the natural frequencies of the split-torque arrangement (Fig. 3.5)

Undamped Natural Frequencies			
n	Timoshenko beam FEM (Hz)	MASTA Solution (Hz)	Difference (%)
1	0.0	0.0	0.0
2	487.3	483.1	-0.07
3	628.5	628.1	-0.65
4	697.5	697.2	0.26
5	748.5	748.0	-1.20
6	774.0	773.3	-0.33
7	833.3	829.5	0.12
8	987.8	987.4	0.80
9	1025.3	1025.9	-0.60
10	1094.3	1095.2	-0.58
11	1371.0	1378.2	-0.91
12	1445.9	1430.7	-1.21
13	1523.0	1518.8	-0.80
14	1548.4	1534.5	-0.58
15	1647.2	1683.6	0.09
16	1745.1	1746.0	-0.19

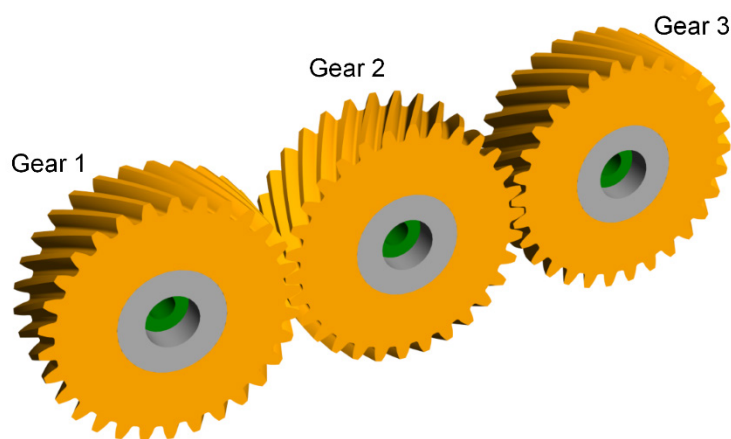


Fig. 3.6 Idler and split-torque arrangements used in the 4th case study

Table 3.6 Parameters of the helical gear system in idler and split-torque arrangements shown in Fig. 3.6

<i>Gear Parameters</i>			
	Gear 1	Gear 2	Gear 3
Mass (kg)	30	30	30
J , Polar mass moment of inertia (kgm^2)	0.0116	0.0116	0.0116
I , Mass moment of inertia (kgm^2)	0.0058	0.0058	0.0058
Base radius (mm)	75	75	75
Helix angle ($^\circ$)	30	30	30
Normal pressure angle ($^\circ$)	17.5	17.5	17.5
Face width (mm)	30	30	30
Hand	Left	Right	Left
<i>Bearing Parameters</i>			
\mathbf{k}_b (N/m, Nm/rad)	<i>Diag</i> $[2.7(10^8), 2(10^8), 1.7(10^8), 0.788(10^6), 1.272(10^6), 0]$		
<i>Gear Mesh Parameters</i>			
	Mesh 1	Mesh 2	
$k_{m(q)}$ (N/m)	200e6	200e6	
$E_{m(q)}^1$ (μm)	1	1	
Damping ratio ζ	0.03		

Fig. 3.8 compares the dynamic responses of four different conditions: (i) idler arrangement, $Z_2 = \text{even}$, (ii) idler arrangement, $Z_2 = \text{odd}$, (iii) split-torque arrangement, , (iv) split-torque arrangement, $Z_2 = \text{odd}$. Depending on the loading condition and the number of teeth of the middle gear (gear 2), the phase angle between the gear meshes changes. In the cases of (i) and (iv), the phase difference between the meshes is π and ϕ_1 ($\omega_{11} \cong 2100$ Hz) is excited, whereas the phase difference between the meshes is 0 and ϕ_2 ($\omega_{12} \cong 2600$ Hz) is excited in the cases of (ii) and (iii). Therefore, a shift in the frequency response occurs due to the change of the excited mode shape. The results obtained are very similar to those of [40].

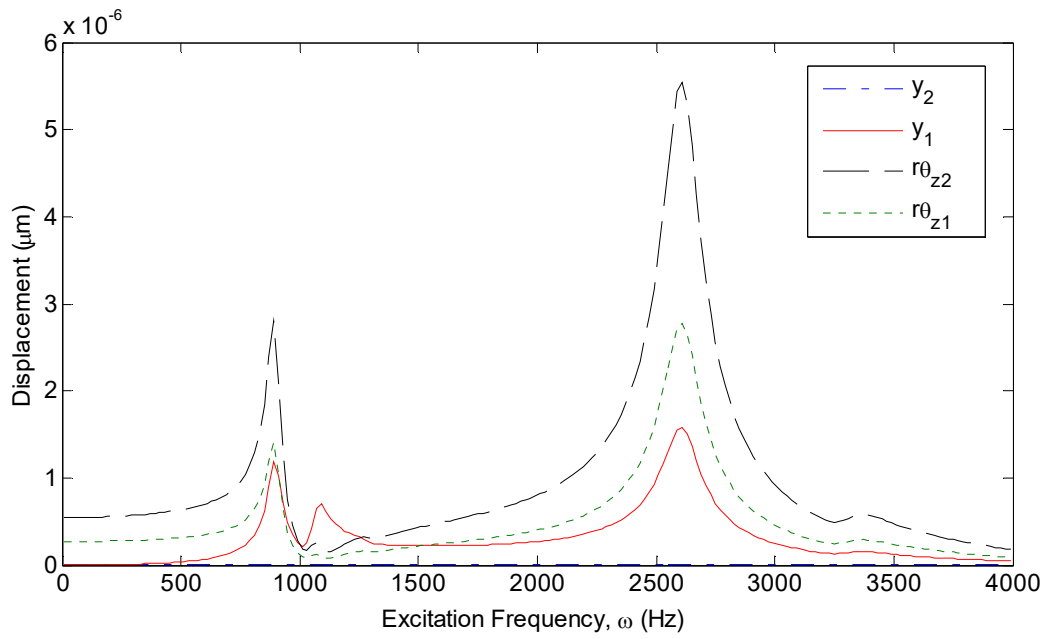


Fig. 3.7 Forced responses of Gear 1 and Gear 2 in split-torque arrangement, Z_2 is even

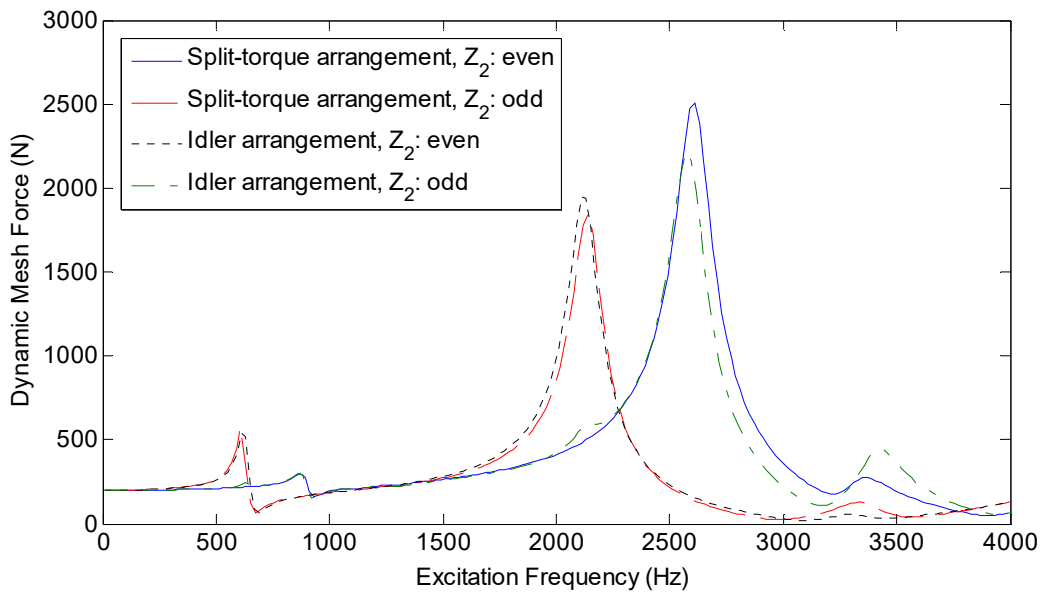


Fig. 3.8 Effect of loading conditions on dynamic mesh forces

CHAPTER 4

NONLINEAR TIME-VARYING DYNAMIC ANALYSIS OF A SPIRAL BEVEL GEARED SYSTEM

4.1 Introduction

Dynamics of cylindrical gears are extensively studied in the literature. A large number of mathematical models are proposed, and both numerical and analytical methods of solution are presented in these studies. Most of the dynamic models available in literature for a spur gear pair include clearance-type nonlinearity due to gear backlash; however, the fluctuating stiffness of gear mesh is considered differently. These models can be classified in two groups as nonlinear time-varying (NTV) [13,16,22,23,35], and nonlinear time-invariant (NTI) [11]. Furthermore, nonlinear multi-degree-of-freedom (MDOFs) models of geared rotor-bearing systems are studied in [15,17,19,21]. Linear time-invariant (LTI) dynamic models for helical gears are proposed in [39–41]. NTV dynamics of two-stage spur gear systems are studied in [27,28,55], in which the responses are obtained by utilizing Harmonic Balance Method (HBM) with multiple harmonics by using discrete Fourier transform (DFT). NTV dynamic models of two-stage spur geared systems in idler and counter-shaft arrangements are presented in [30,31]. Moreover, NTV [32] and LTI [42] dynamic models are developed for planetary gears formed by spur and helical gears, respectively.

Although dynamics of cylindrical gears has been studied extensively, limited publications on dynamics of bevel gears can be found in the literature due to their

complex tooth geometry and meshing process. A mesh model is proposed in [59] based on the tooth geometry of a spiral bevel gear. Nonlinear dynamics of bevel and hypoid gear systems are studied in [45,54] and the influences of time-varying parameters on dynamics are investigated. Furthermore, a MDOF dynamic model of a spiral bevel gear system is proposed in [60] and authors investigate the influences of the system parameters on dynamics. Since the lumped parameter models used cannot accurately represent the structural characteristics of shaft-bearing assembly, an enhanced equivalent lumped parameter synthesis and a finite element model are proposed in [49] for a LTI spiral bevel gear train. Moreover, considering the flexibilities of shafts and bearings, a NTI dynamic model of a spiral bevel gear system is proposed in [61].

Most of the previous studies about spiral bevel gear systems include linear time-invariant dynamic models. Therefore, a nonlinear time-varying dynamic model of a drivetrain composed of a spiral bevel gear pair including shafts and bearings is developed in this study. A three-dimensional discrete mesh model of a spiral bevel gear pair is integrated into the finite element (FE) model of shafts and bearings as shown in Fig. 4.1. Both parametric excitation caused by fluctuation of gear mesh stiffness and excitation due to static transmission error are considered. Since the resulting nonlinear system has many DOFs, receptance method [52,53,62] is employed which decreases the number of nonlinear equations. Utilizing receptance method, it is possible to model gear shafts by using finite element method without increasing the number of nonlinear equations, which reduces the computational time drastically, and hence, the shaft-bearing dynamic characteristics can be easily taken into account. Utilizing HBM with multiple harmonics, the system of nonlinear differential equations of the gear train are transformed to a system of nonlinear algebraic equations. In order to determine Fourier coefficients required in the HBM, continuous-time Fourier transform is used, as opposed to the gear dynamics studies [22,23,27,28,54,55,61] that utilize discrete Fourier transform. Thus, the

convergence problems encountered when the number of nonlinear DOFs is large are avoided. Moreover, analytical integration rather than numerical integration is employed for the calculation of Fourier coefficients which decreases the computational time further. Obtained nonlinear algebraic equations of the gear train are solved by Newton's method with arc-length continuation. Direct numerical integration (NI), which is computationally demanding, is employed to verify the results obtained by HBM. In direct numerical integration, computational cost increases significantly as the size of the system increases. Frequency domain methods are preferred for the determination of steady state response due to their significant computational savings. This computational efficiency with respect to time domain methods increases as the size of the system gets larger; therefore, HBM is used in this study. Dynamic bearing forces are also calculated to demonstrate that gear backlash nonlinearity affects the bearing forces, which are important in the selection of bearings. Several case studies are performed and the effects of backlash amount, fluctuation of gear mesh stiffness and variation of bearing stiffness on system response are investigated. Comparison of dynamic responses of coupled gear system model and gear torsional model shows that gear torsional model is inadequate for the analysis of dynamic response of a spiral bevel gear system and coupling has significant effect on dynamic response when stiffness of shafts and bearings are comparable to mesh stiffness.

4.2 Dynamic Model Formulation

4.2.1 Physical System and Dynamic Model

The drivetrain considered in this study is composed of a spiral bevel gear pair including gear shafts and bearings on the shafts as shown in Fig. 4.1. A finite element (FE) formulation is utilized to model the gear shafts. Since the shafts used

in bevel geared systems are stub, Timoshenko beam formulation is employed. The mass and stiffness effects of gear blanks are included in the shaft sections by using beam elements rather than lumping at a node. In other words, the outer diameter of the shaft beam element follows the gear cone as shown in Fig. 4.1. Linear and torsional springs are used in order to represent the bearings supporting the gear shafts. Clearance nonlinearity of bearings is neglected, since preloaded rolling element bearings [57] are considered in this study. Furthermore, time variation of bearing stiffness is disregarded.

Element mass and stiffness matrices are assembled to calculate the mass matrix, \mathbf{M}_{sn} , and stiffness matrix, \mathbf{K}_{sn} , of the n^{th} shaft ($n = 1, 2$). Complete mass and stiffness matrices of the drivetrain shafts are then assembled as $\mathbf{M}_s = \text{Diag}[\mathbf{M}_{s1}, \mathbf{M}_{s2}]$ and $\mathbf{K}_s = \text{Diag}[\mathbf{K}_{s1}, \mathbf{K}_{s2}]$, respectively. The size of these symmetric matrices is $q \times q$, where q is the total number of DOFs of the system. It can be calculated as $q = 6 \cdot \sum_{n=1}^2 (m_n + 1)$, where m_n is the number of beam elements used in modeling the n^{th} shaft. It should be noted that tapering effects of the gear cones are considered by using multiple nodes associated with the gear blanks in the Timoshenko beam finite element model as shown in Fig. 4.1. Rigid links are used to connect the effective mesh nodes, which are coincident for pinion and gear, to the cone nodes of the gear and pinion.

The total bearing stiffness matrix of a drivetrain including a total of n_b bearings is assembled as $\mathbf{K}_b = \text{Diag}[\cdots \mathbf{K}_{b1} \cdots \mathbf{K}_{b\ell} \cdots \mathbf{K}_{bn_b} \cdots]$, where $\mathbf{K}_{b\ell} = \text{Diag}[k_{bx\ell}, k_{by\ell}, k_{bz\ell}, k_{b\theta_x\ell}, k_{b\theta_y\ell}, k_{b\theta_z\ell}]$ ($\ell = 1$ to n_b) and $k_{bx\ell}$ to $k_{b\theta_z\ell}$ are the stiffness of the ℓ^{th} bearing in the indicated directions. In the overall bearing stiffness matrix, \mathbf{K}_b , each individual bearing stiffness is located according to the node

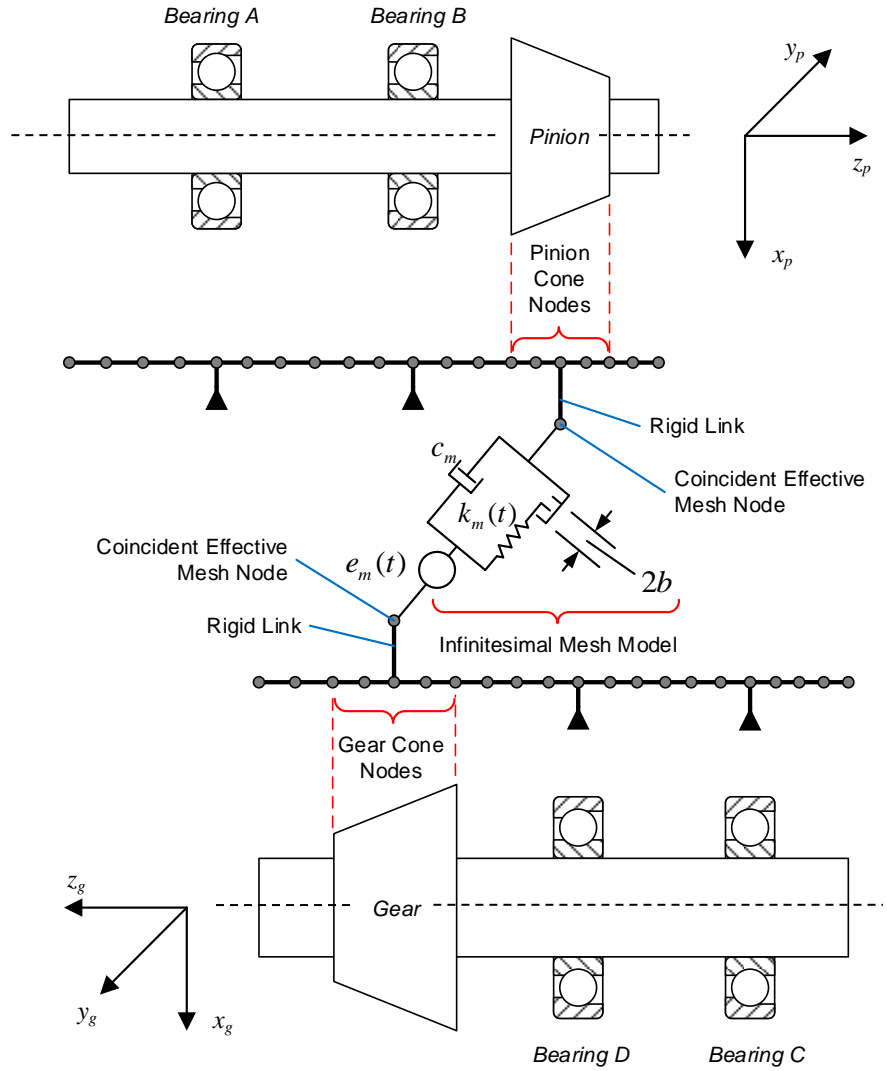


Fig. 4.1 Schematic of gear mesh model and finite element model for the spiral bevel gear train considered in this study

number where the bearing is attached. The remaining elements in \mathbf{K}_b are zero. Thus, the stiffness matrix of the whole FE model can be expressed as $\mathbf{K} = \mathbf{K}_s + \mathbf{K}_b$. Furthermore, Rayleigh damping is assumed for the shaft-bearing assembly for simplicity; hence, the damping matrix is expressed as $\mathbf{C} = \beta \mathbf{K}$ where β represents the Rayleigh damping coefficient.

A three-dimensional dynamic model of a spiral bevel gear pair is given in Fig. 4.2. The mesh coupling between the pinion and the gear consists of fluctuating mesh stiffness resulting in parametric type of excitation, viscous mesh damping and gear backlash extending along the direction of tooth normal, i.e., line of action (LOA). Unlike parallel axis gears, mesh stiffness, mesh point and direction of LOA, which are the parameters characterizing a gear mesh, change considerably for a spiral bevel gear pair in a meshing cycle. However, time variation of mesh stiffness has much more significant influence on bevel gear dynamics compared to that of mesh vector [47]. Moreover, the system model is large and the study focuses not only on the gears but also on the shaft-bearing assembly. Therefore, a mesh model composed of a time-varying mesh stiffness, an effective mesh point and a constant LOA vector is used. The mesh parameters are also assumed to be constant under dynamic conditions. Furthermore, static transmission error in the gear mesh coupling shown in Fig. 4.2 is the other excitation source for the drivetrain. It should be noted that backlash nonlinearity is assumed to be ineffective on mesh damping element.

As shown in Fig. 4.2, the pinion and gear have both translational and rotational degrees of freedom. Considering that the mesh node of each gear has 6 DOFs, the mesh coupling between the shafts is defined by a total of 12 DOFs. The displacement vectors of the gears are defined as $\mathbf{x}_i = (x_i \ y_i \ z_i \ \theta_{xi} \ \theta_{yi} \ \theta_{zi})^T$ in each local reference frame S_i located at the centroid of pinion or gear and $i = p, g$ represents pinion and gear, respectively.

The dynamic transmission error is defined as follows

$$\delta_d = \mathbf{h}_p^T \mathbf{x}_p - \mathbf{h}_g^T \mathbf{x}_g, \quad (4.1)$$

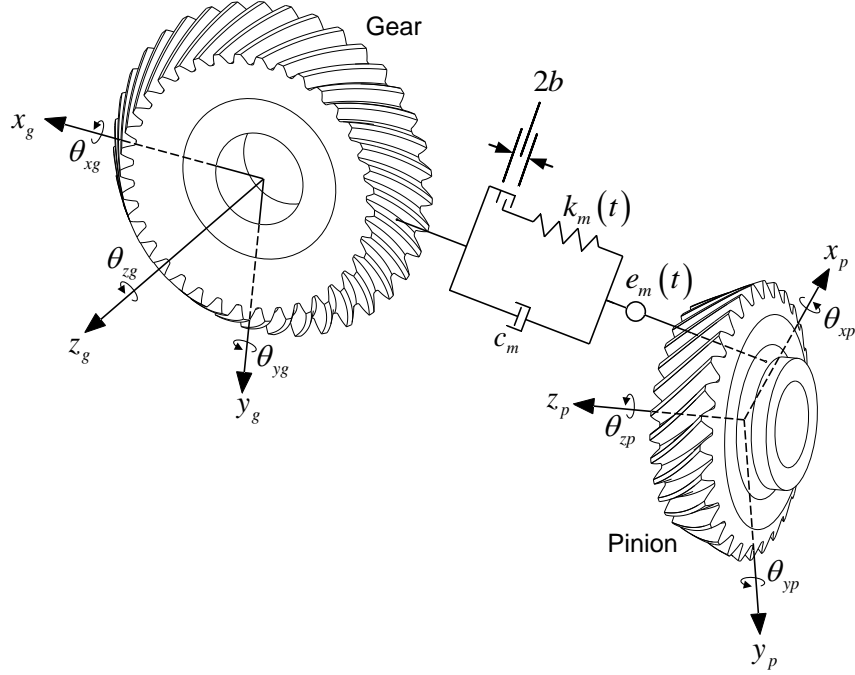


Fig. 4.2 Gear mesh model for a spiral bevel gear pair

where \mathbf{h}_i denotes the transformation vector between the line of action and local reference frames of pinion or gear, which can be written as

$$\mathbf{h}_i = (n_{ix} \quad n_{iy} \quad n_{iz} \quad \lambda_{ix} \quad \lambda_{iy} \quad \lambda_{iz})^T. \quad (4.2)$$

Here, $\mathbf{n}_i = (n_{ix} \quad n_{iy} \quad n_{iz})^T$ represents the directional cosine vector of line of action and $\boldsymbol{\lambda} = (\lambda_{ix} \quad \lambda_{iy} \quad \lambda_{iz})^T$ is the directional rotation radii, which can be expressed as

$$\lambda_{ix} = \mathbf{n}_i \cdot (\mathbf{u}_{xi} \times \mathbf{r}_i), \quad (4.3)$$

$$\lambda_{iy} = \mathbf{n}_i \cdot (\mathbf{u}_{yi} \times \mathbf{r}_i), \quad (4.4)$$

$$\lambda_{iz} = \mathbf{n}_i \cdot (\mathbf{u}_{zi} \times \mathbf{r}_i), \quad (4.5)$$

where $\mathbf{r}_i = (x_{im} \ y_{im} \ z_{im})^T$ represents the position vector of the mesh point, and $\mathbf{u}_{xi} = (1 \ 0 \ 0)^T$, $\mathbf{u}_{yi} = (0 \ 1 \ 0)^T$ and $\mathbf{u}_{zi} = (0 \ 0 \ 1)^T$ are the trio of unit vectors for the coordinate system S_i . In all the above equations, subscript $i = p, g$ designates that the parameter is expressed in the coordinate system of the pinion or the gear, respectively. In this study, the effective mesh point is assumed to be on the intersection line of the pitch cones of the pinion and gear at mean cone distance from the apex as shown in Fig. 4.3. Therefore, the effective mesh point is on the pitch radius at mean cone distance, r_{pm} , and the corresponding position vectors can be expressed as $\mathbf{r}_p = (r_{pm}^p \ 0 \ 0)^T$ and $\mathbf{r}_g = (-r_{pm}^g \ 0 \ 0)^T$, respectively, in the local coordinate systems of the pinion, S_p , and the gear, S_g . Moreover, $\mathbf{n}_i (i = p, g)$ can be calculated with a series of coordinate transformation as follows

$$\mathbf{n}_i = \mathbf{T}_y(\gamma_i) \mathbf{T}_z(\phi_i) \mathbf{T}_x(-\psi) \begin{Bmatrix} 0 \\ 1 \\ 0 \end{Bmatrix}, \quad (4.6)$$

where \mathbf{T}_x , \mathbf{T}_y and \mathbf{T}_z are the transformation matrices about x , y and z axes, respectively. Here, ϕ_i and ψ are the transverse pressure angle and spiral angle of the gear pair, respectively. Based on the hand and rotation direction of the pinion, these angles are modified as follows:

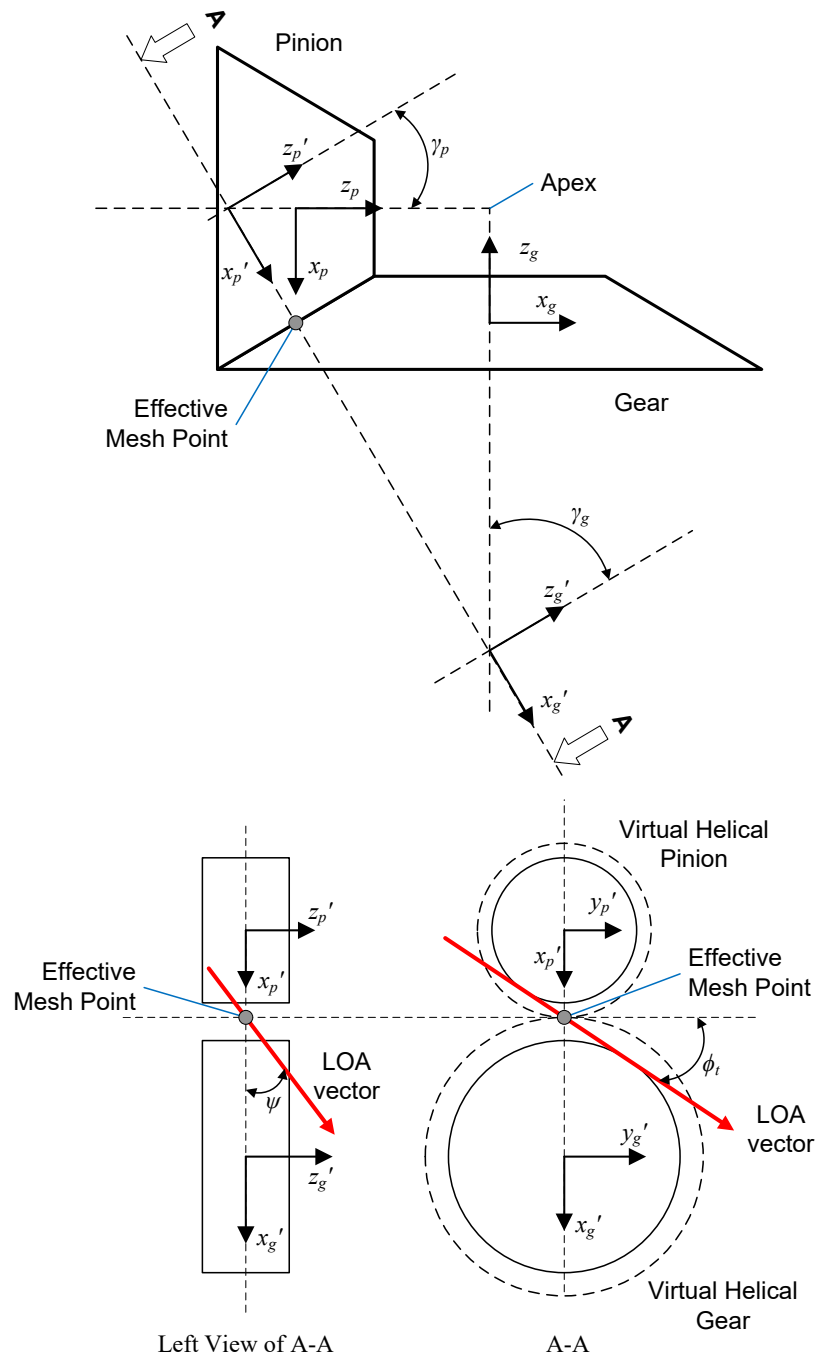


Fig. 4.3 Effective mesh point and LOA vector

$$\phi_t = \begin{cases} \phi_t, & \text{if pinion rotates counterclockwise } (+z_p) \\ \pi - \phi_t, & \text{if pinion rotates clockwise } (-z_p) \end{cases}, \quad (4.7)$$

$$\psi = \begin{cases} \psi, & \text{if pinion rotates CCW and has left hand teeth} \\ -\psi, & \text{if pinion rotates CCW and has right hand teeth} \\ -\psi, & \text{if pinion rotates CW and has left hand teeth} \\ \psi, & \text{if pinion rotates CW and has right hand teeth} \end{cases}. \quad (4.8)$$

Moreover, γ_p represents the pitch angle of the pinion, whereas γ_g is the negative of the pitch angle of the gear.

It is noted that S'_i ($i = p, g$) is an intermediate coordinate system used in the transformation of directional cosine vector of LOA and it is also shown in Fig. 4.3 for clarity.

Considering backlash nonlinearity, dynamic mesh force, F_m , along the line of action can be written as

$$F_m(t) = k_m(t) f_n(\delta_d(t) - e_m(t)) + c_m(\dot{\delta}_d(t) - \dot{e}_m(t)). \quad (4.9)$$

Here $f_n(\delta_d(t) - e_m(t))$ is the nonlinear displacement function which is defined as

$$f_n(\delta_d(t) - e_m(t)) = \begin{cases} \delta_d(t) - e_m(t) - b, & \delta_d(t) - e_m(t) > b \\ 0, & |\delta_d(t) - e_m(t)| \leq b \\ \delta_d(t) - e_m(t) + b, & \delta_d(t) - e_m(t) < -b \end{cases}, \quad (4.10)$$

where $2b$ is the total gear backlash. Reordering displacement vector \mathbf{x} such that the nonlinear DOFs, i.e. DOFs associated with mesh nodes, are located at the bottom, the equation of motion of the complete drivetrain is expressed as follows

$$\mathbf{M}\ddot{\mathbf{x}}(t) + \mathbf{C}\dot{\mathbf{x}}(t) + \mathbf{K}\mathbf{x}(t) + \mathbf{F}_{Nl}(t) = \mathbf{F}(t), \quad (4.11)$$

$$\mathbf{x} = \begin{pmatrix} \mathbf{x}_l \\ \dots \\ \mathbf{x}_n \end{pmatrix}, \quad (4.12)$$

$$\mathbf{F}_{Nl} = \begin{pmatrix} \mathbf{0} \\ \dots \\ \mathbf{F}_N \end{pmatrix}, \quad (4.13)$$

where \mathbf{x}_n is the nonlinear DOFs which correspond to mesh nodes in this study and \mathbf{x}_l corresponds to all other nodes. Here, $\mathbf{F}(t)$ denotes the external forcing vector consisting of the torques T_p and T_g acting on the pinion and gear as follows

$$\begin{aligned} \mathbf{F}(t) &= \mathbf{F} \\ &= \left(0 \quad \dots \quad 0 \quad \left(0 \quad 0 \quad 0 \quad 0 \quad 0 \quad T_p \right) \quad \left(0 \quad 0 \quad 0 \quad 0 \quad 0 \quad -T_g \right) \right)^T. \end{aligned} \quad (4.14)$$

Torque values are assumed to be constant in this study; therefore, only static transmission error excitation is taken into account. Consequently, the only nonzero components in the forcing vector are the components associated with rotations of the pinion and the gear about z axis. The overall nonlinear restoring force vector, \mathbf{F}_{Nl} , has nonzero elements only for the mesh nodes. Due to nonlinearity, the mesh coupling parameters k_m and c_m are not included in the overall stiffness and damping

matrices of the drivetrain. Instead, they are included in the nonlinear restoring force vector, $\mathbf{F}_N(t)$, through the dynamic mesh force given by Eq. (4.9) as follows

$$\mathbf{F}_N(t) = F_m(t) \mathbf{p}, \quad (4.15)$$

where \mathbf{p} is the combined form of the coordinate transformation vectors as

$$\mathbf{p} = \begin{pmatrix} \mathbf{h}_p^T & -\mathbf{h}_g^T \end{pmatrix}^T. \quad (4.16)$$

4.2.2 Solution Method

4.2.2.1 Receptance Method

For systems with many DOFs, the large number of nonlinear equations causes several numerical difficulties and significant increase in computational time. For systems where the number of nonlinear DOFs is much less than the total number of DOFs, receptance method, details of which are given in [52,53], can be used. For the spiral bevel gear system defined by Eq. (4.11), only the DOFs associated with bevel gears, i.e. mesh nodes, contain nonlinearity. If these DOFs are grouped, the equation of motion in case of multi-harmonic solution can be written as

$$\left[\mathbf{K} - (r\omega)^2 \mathbf{M} + ir\omega \mathbf{C} \right] \begin{Bmatrix} \mathbf{x}_l^r \\ \mathbf{x}_n^r \end{Bmatrix} + \begin{Bmatrix} \mathbf{0} \\ \mathbf{F}_N^r(\mathbf{x}_n) \end{Bmatrix} = \begin{Bmatrix} \mathbf{F}_l^r \\ \mathbf{F}_n^r \end{Bmatrix}, \quad (4.17)$$

where the linear and nonlinear DOFs are designated by subscripts l and n , respectively. Here, i represents the unit imaginary number and $r = 0, 1, 2, \dots, N_h$ is the harmonic index.

Multiplying both sides of Eq. (4.17) by the receptance matrix of the linear system, i.e. $\mathbf{a}(r\omega) = [\mathbf{K} - (r\omega)^2 \mathbf{M} + ir\omega \mathbf{C}]^{-1}$, the following result is obtained

$$\begin{aligned} \begin{Bmatrix} \mathbf{x}_l^r \\ \mathbf{x}_n^r \end{Bmatrix} + \begin{bmatrix} \mathbf{a}_{ll}(r\omega) & \mathbf{a}_{ln}(r\omega) \\ \mathbf{a}_{nl}(r\omega) & \mathbf{a}_{nn}(r\omega) \end{bmatrix} \begin{Bmatrix} \mathbf{0} \\ \mathbf{F}_N^r(\mathbf{x}_n) \end{Bmatrix} - \begin{bmatrix} \mathbf{a}_{ll}(r\omega) & \mathbf{a}_{ln}(r\omega) \\ \mathbf{a}_{nl}(r\omega) & \mathbf{a}_{nn}(r\omega) \end{bmatrix} \begin{Bmatrix} \mathbf{F}_l^r \\ \mathbf{F}_n^r \end{Bmatrix} \\ = \mathbf{0} \quad (r = 0, 1, 2, \dots, N_h) \end{aligned} \quad (4.18)$$

Partitioning Eq. (4.18), the following nonlinear and linear equation sets are obtained

$$\begin{aligned} \mathbf{x}_n^r + \mathbf{a}_{nn}(r\omega) \mathbf{F}_N^r(\mathbf{x}_n) - \mathbf{a}_{nl}(r\omega) \mathbf{F}_l^r - \mathbf{a}_{nn}(r\omega) \mathbf{F}_n^r = \mathbf{0} \\ (r = 0, 1, 2, \dots, N_h), \end{aligned} \quad (4.19)$$

$$\mathbf{x}_l^r = \mathbf{a}_{ll}(r\omega) \mathbf{F}_l^r + \mathbf{a}_{ln}(r\omega) (\mathbf{F}_n^r - \mathbf{F}_N^r(\mathbf{x}_n)) \quad (r = 0, 1, 2, \dots, N_h). \quad (4.20)$$

Only unknowns in Eq. (4.19) are the nonlinear DOFs; hence, it can be solved iteratively to obtain $\mathbf{x}_n(t)$, which decreases the computational time significantly due to the considerable decrease in the number of nonlinear equations. After determining $\mathbf{x}_n(t)$, dynamic transmission error $\delta_d(t)$, dynamic mesh force $F_m(t)$ and nonlinear restoring force $\mathbf{F}_N(t)$ can be calculated by using Eqs. (4.1), (4.9) and (4.15), respectively. Using the known value of $\mathbf{F}_N(\mathbf{x}_n)$, response of linear DOFs \mathbf{x}_l can be obtained by solving Eq. (4.20).

Therefore, with the use of receptance method, it is possible to model gear shafts by using finite element method without increasing the number of nonlinear equations and effects of shaft and bearing parameters can be easily studied.

4.2.2.2 Multi-harmonics Harmonic Balance Method with Continuous-Time Fourier Transform

The multi-term Harmonic Balance Method is utilized in this study in order to obtain the system of nonlinear algebraic equations given by Eq (4.19). Continuous-time Fourier transform is employed to obtain the Fourier coefficients required in the HBM. Since static transmission error excitation and time-varying mesh stiffness are assumed to be periodic, the solution of the nonlinear system can as also be expressed periodically [27]. As a result of this, the nonlinear displacement function, $f_n(\delta_d(t) - e_m(t))$, is also periodic. Therefore, the mesh stiffness $k_m(t)$, static transmission error $e_m(t)$ and its time derivative $\dot{e}_m(t)$ are represented in Fourier series as

$$k_m(t) = \kappa_0 + \sum_{a=1}^A [\kappa_{ca} \cos(a\omega t) + \kappa_{sa} \sin(a\omega t)], \quad (4.21)$$

$$e_m(t) = \sum_{j=1}^J [\varepsilon_{cj} \cos(j\omega t) + \varepsilon_{sj} \sin(j\omega t)], \quad (4.22)$$

$$\dot{e}_m(t) = \sum_{j=1}^J [-(j\omega)\varepsilon_{cj} \sin(j\omega t) + (j\omega)\varepsilon_{sj} \cos(j\omega t)]. \quad (4.23)$$

Displacement and velocity of the drivetrain can be expressed periodically as

$$\mathbf{x}_n(t) = \mathbf{u}_0 + \sum_{r=1}^{N_h} [\mathbf{u}_{cr} \cos(r\omega t) + \mathbf{u}_{sr} \sin(r\omega t)], \quad (4.24)$$

$$\dot{\mathbf{x}}_n(t) = \sum_{r=1}^{N_h} [-(r\omega)\mathbf{u}_{cr} \sin(r\omega t) + (r\omega)\mathbf{u}_{sr} \cos(r\omega t)]. \quad (4.25)$$

Furthermore, dynamic mesh force, $F_m(t)$, given by Eq. (4.9) can be expressed periodically as

$$F_m(t) = F_m^0 + \sum_{r=1}^{N_h} [F_m^{cr} \cos(r\omega t) + F_m^{sr} \sin(r\omega t)]. \quad (4.26)$$

In the above expressions, subscript or superscript c and s represent the Fourier coefficients corresponding to cosine and sine terms, respectively. In literature on gear dynamics [22,23,27,28,54,55], discrete Fourier transform is used in order to calculate Fourier coefficients of dynamic mesh force, $F_m(t)$. Since the nonlinear displacement function is a discontinuous function, the exact time of discontinuities must be determined to calculate the nonlinear forces and the corresponding Fourier integrals accurately. The error in the integral calculations changes depending on the time step used in the discretization. When the time point is away from the actual discontinuity, the nonlinear solver considers this as an error in the solution and tries to correct it. This results in no convergence or, at best, increases the number of iterations to converge. In order to prevent this issue, very small time steps can be used in discrete Fourier transform, which improves the accuracy slightly, but increases the computational effort drastically. Therefore, continuous-time Fourier transform is used in this study instead of DFT. Fourier coefficients required can be calculated as follows ($r = 1, 2, \dots, N_h$)

$$F_m^0 = \frac{\omega}{2\pi} \int_0^{2\pi/\omega} F_m(t) dt, \quad (4.27)$$

$$F_m^{cr} = \frac{\omega}{\pi} \int_0^{2\pi/\omega} F_m(t) \cos(r\omega t) dt, \quad (4.28)$$

$$F_m^{sr} = \frac{\omega}{\pi} \int_0^{2\pi/\omega} F_m(t) \sin(r\omega t) dt. \quad (4.29)$$

Moreover, the above integrals are computed analytically, rather than numerically, which decreases the computational time significantly.

Fourier coefficients of the nonlinear restoring force, $\mathbf{F}_N(t)$, are determined by using the combined coordinate transformation vector \mathbf{p} given by Eq. (4.16) as

$$\mathbf{F}_N(t) = \mathbf{F}_N^0 + \sum_{r=1}^{N_h} [\mathbf{F}_N^{cr} \cos(r\omega t) + \mathbf{F}_N^{sr} \sin(r\omega t)], \quad (4.30)$$

where,

$$\mathbf{F}_N^0 = F_m^0 \mathbf{p}, \quad \mathbf{F}_N^{cr} = F_m^{cr} \mathbf{p}, \quad \mathbf{F}_N^{sr} = F_m^{sr} \mathbf{p}. \quad (4.31)$$

Substituting Eqs. (4.24) and (4.30) into Eq. (4.19) and balancing the harmonic terms, the following system of nonlinear algebraic equations is obtained

$$\mathbf{R}_0(\mathbf{u}) = \mathbf{u}_0 + \boldsymbol{\alpha}_{nn}(0) \mathbf{F}_N^0 - [\boldsymbol{\alpha}_{nl}(0) \quad \boldsymbol{\alpha}_{mm}(0)] \begin{Bmatrix} \mathbf{F}_l^0 \\ \mathbf{F}_n^0 \end{Bmatrix}, \quad (4.32)$$

$$\begin{aligned} \mathbf{R}_r(\mathbf{u}) = & (\mathbf{u}_{sr} + i\mathbf{u}_{cr}) + \boldsymbol{\alpha}_{nm}(r\omega)(\mathbf{F}_N^{sr} + i\mathbf{F}_N^{cr}) \\ & - [\boldsymbol{\alpha}_{nl}(r\omega) \quad \boldsymbol{\alpha}_{nn}(r\omega)] \begin{Bmatrix} \mathbf{F}_l^{sr} + i\mathbf{F}_l^{cr} \\ \mathbf{F}_n^{sr} + i\mathbf{F}_n^{cr} \end{Bmatrix}, \end{aligned} \quad (4.33)$$

for $r = 1, 2, \dots, N_h$. Eq. (4.32) is a set of real equations obtained by balancing of bias terms, whereas Eq. (4.33) is a set of complex equations where the real and imaginary parts represent the sine component and the cosine component of the r^{th} harmonic, respectively. Consequently, response of the system can be calculated by solving a total of $12 \times (2N_h + 1)$ real nonlinear equations.

The nonlinear equation set given by Eqs. (4.32) and (4.33) is solved by Newton's Method for the unknown displacement vector $\mathbf{u} = (\mathbf{u}_0 \quad \mathbf{u}_{c1} \quad \mathbf{u}_{s1} \quad \mathbf{u}_{c2} \quad \mathbf{u}_{s2} \quad \dots \quad \mathbf{u}_{cN_h} \quad \mathbf{u}_{sN_h})^T$. However, convergence problems arise around the turning points, where the solution path reverses its direction, since the Jacobian matrix becomes singular. This problem is solved by using a new continuation parameter, i.e. replacing frequency with arc-length, which also makes it possible to trace the solution path when it changes its direction. However, as a result of this change, the vector of unknowns is expanded to $\mathbf{v} = (\mathbf{u}^T \quad \omega)^T$. The new continuation parameter, s , is defined as the radius of a hypothetical n -dimensional sphere having its center located at the previous converged solution. Therefore, the solution of the new system of nonlinear equations is located on the surface of this n -dimensional sphere, defined by $s^2 = \Delta\mathbf{v}_k^T \times \Delta\mathbf{v}_k$, by introducing the following residual equation [63–65]

$$h(\mathbf{v}_k) = \Delta\mathbf{v}_k^T \times \Delta\mathbf{v}_k - s^2 = 0, \quad (4.34)$$

$$\Delta\mathbf{v}_k = \mathbf{v}_k - \mathbf{v}_{k-1}. \quad (4.35)$$

Here \mathbf{v}_{k-1} is the last converged solution and \mathbf{v}_k is the k^{th} , current, solution point. Adding this new residual equation given by Eq. (4.34) to $\mathbf{R}(\mathbf{u})$, the new system of nonlinear algebraic equations is obtained as $\mathbf{S}(\mathbf{v}) = \left(\mathbf{R}(\mathbf{u})^T \quad h(\mathbf{v}) \right)^T$. Therefore, a single step of Newton's iteration is obtained as follows

$$\mathbf{v}_k^{(m)} = \mathbf{v}_k^{(m-1)} - \mathbf{J}(\mathbf{v}_k^{(m-1)})^{-1} \mathbf{S}(\mathbf{v}_k^{(m-1)}), \quad (4.36)$$

where $\mathbf{v}_k^{(m)}$ is the m^{th} iterative solution based on the $(m-1)^{\text{th}}$ iteration and $\mathbf{J}(\mathbf{v}_k^{(m-1)})$ represents the Jacobian matrix of \mathbf{S} calculated at the $(m-1)^{\text{th}}$ iteration for the k^{th} solution point. Newton's iteration defined in Eq. (4.36) is repeated until the norm of vector $\mathbf{S}(\mathbf{v}_k^{(m)})$ falls below a specified error tolerance. The solution of the corresponding linear system is used as the initial guess for the first solution point; whereas, for other solution points, since the Jacobian at the previous solution point is available, tangent predictor is used to estimate the initial guess.

4.3 Results and Discussion

Parameters of the example spiral bevel gear train considered in this study is given in Table 4.1. Since the static transmission error $e_m(t)$ depends on the micro geometry and manufacturing, it can be adjusted by tooth profile modifications. Furthermore, one of the main objectives of a gear design is to obtain a static transmission error having a form of sinusoidal-like. Therefore, the first harmonic is always dominant and it can be used to represent the total static transmission error. However, the harmonic content of the mesh stiffness, $k_m(t)$, is mainly affected by

the operating contact ratio. Similarly, the first harmonic is again dominant especially for medium-to-heavy load range in spiral bevel gear systems. Consequently, the first harmonics of the static transmission error, $e_m(t)$, and mesh stiffness, $k_m(t)$, are considered in this study. Moreover, external torques applied are considered to be constant.

Table 4.1 Parameters of the example system

<i>Shaft Parameters</i>				
	Pinion		Gear	
Outer diameter (mm)	55		70	
Inner diameter (mm)	40		50	
Length (mm)	202		234	
β	3(10 ⁻⁶)		3(10 ⁻⁶)	
<i>Gear Parameters</i>				
	Pinion		Gear	
Number of teeth	31		39	
Spiral angle (°)	30		30	
Normal pressure angle (°)	20		20	
Pitch angle (°)	38.48		51.52	
Pitch radius (mm)	65.1		81.9	
Face width (mm)	34		34	
Hand	Left		Right	
Locations (mm) ^a	172		209	
T (Nm)	200		251.61	
<i>Bearing Parameters</i>				
	Pinion		Gear	
	Bearing A	Bearing B	Bearing C	Bearing D
Locations (mm) ^a	42	127	74	144
\mathbf{k}_b (N/m, Nm/rad)	$Diag[2(10^9), 2(10^9), 1(10^9), 1(10^6), 1(10^6), 0]$			
<i>Gear Mesh Parameters</i>				
$\kappa_0, \kappa_{c1}, \kappa_{s1}$ (N/m)	3(10 ⁸), 0, -0.9(10 ⁸)			
c_m (Ns/m)	1500			
$\varepsilon_{c1}, \varepsilon_{s1}$ (μm)	0, 10			
b (μm)	20			

^a Distance from the rear end of the corresponding shaft

Table 4.2 Comparison of natural frequencies of linear-time invariant system

Undamped Natural Frequencies				
n	Timoshenko beam FEM (Hz)	ANSYS® Solution (Hz)	Difference (%)	Mode Shape
1	0.0	0.0	0.00	Rigid Body, $\theta_{z_p}, \theta_{z_g}$
2	1133.8	1135.9	-0.19	Coupled mode including torsional motion, $\theta_{z_p}, \theta_{z_g}$, bending of pinion shaft in x_p and y_p directions, bending of gear shaft in x_g and y_g directions
3	1492.5	1524.8	-2.12	Bending of gear shaft in x_g and y_g directions
4	1744.4	1779.6	-1.98	Coupled mode including torsional motion, $\theta_{z_p}, \theta_{z_g}$, bending of pinion shaft in x_p and y_p directions, bending of gear shaft in x_g and y_g directions
5	1953.7	1999.0	-2.26	Bending of pinion shaft in x_p and y_p directions
6	2950.5	2947.4	0.10	Translation of gear shaft in z_g direction Torsional motion of pinion shaft, θ_{z_p}
7	3056.8	3085.4	-0.93	Coupled mode including torsional motion, $\theta_{z_p}, \theta_{z_g}$, translation of pinion shaft in z_p direction, bending of pinion shaft in x_p and y_p directions, bending of gear shaft in x_g and y_g directions
8	3700.9	3650.2	1.39	Bending of gear shaft in x_g and y_g directions
9	3704.7	3650.8	1.48	Translation of pinion shaft in z_p direction, bending of gear shaft in x_g and y_g directions
10	3933.2	3928.2	0.13	Coupled mode including torsional motion, $\theta_{z_p}, \theta_{z_g}$, translation of pinion shaft in z_p direction, bending of pinion shaft in x_p and y_p directions, bending of gear shaft in x_g and y_g directions

Firstly, the undamped natural frequencies of the linear time-invariant gear train obtained by using the Timoshenko beam finite element model (FEM) given in this study and by commercial FE software ANSYS® [66] are given in Table 4.2. It is seen from the table that the results agree with each other very well. Therefore, the FE modeling of the shaft-bearing assembly with the mesh coupling and including the gear blanks is accomplished in agreement with the FE software.

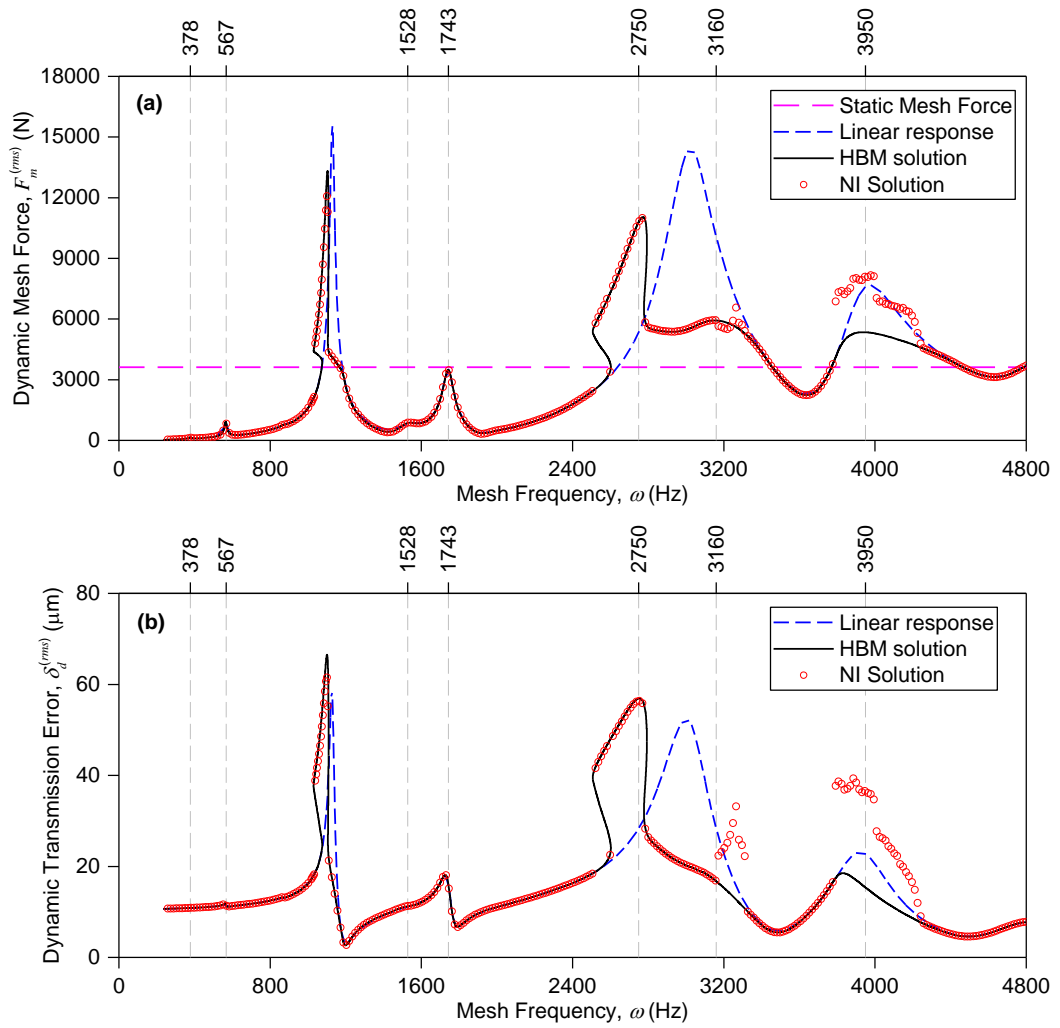


Fig. 4.4 Comparison of rms values of the responses predicted by HBM and NI for $T = 200 \text{ Nm}$ and $b = 20 \mu\text{m}$, (a) dynamic mesh force $F_m^{(rms)}$, (b) dynamic transmission error $\delta_d^{(rms)}$

Comparison of the steady state solutions obtained by HBM utilizing three harmonics ($R = 3$) and direct numerical integration (NI) are given in Fig. 4.4. The root-mean-square (rms) of the dynamic mesh force is calculated as follows:

$$F_m^{(rms)} = \left\{ \sum_{r=1}^R \left(\frac{A_r}{\sqrt{2}} \right)^2 \right\}^{1/2}, \quad (4.37)$$

where A_r is the amplitude of the r^{th} harmonic of $F_m(t)$ that can be defined as

$$A_r = \sqrt{(F_m^{cr})^2 + (F_m^{sr})^2}. \quad (4.38)$$

The rms of the dynamic transmission error is calculated similarly. Linear response of the drivetrain is given in Fig. 4.4 as well. The resonance peaks observed at $\omega = 1134$ Hz, $\omega = 1743$ Hz, $\omega = 3059$ Hz and $\omega = 3984$ Hz for the linear response occur when the gear mesh frequency is equal to the 2nd, the 4th, the 7th and the 10th natural frequencies of the linear gear train, respectively. The gear pair exhibits coupled axial-transverse-rotational motions in all of these natural frequencies as indicated by the definition of mode shapes given in Table 4.2.

It can be seen from Fig. 4.4 that solutions obtained by HBM agree well with direct NI solutions except around the resonance peaks observed at $\omega \cong 3160$ Hz and $\omega \cong 3950$ Hz (shown by vertical dashed lines). This indicates the existence of subharmonic motions around these resonance frequencies as illustrated in Fig. 4.5, which shows the time history and frequency spectrum of the steady-state portion of the response at $\omega = 3968$ Hz obtained by NI. In addition to the fundamental harmonic, for this frequency, it is observed that the subharmonics having the frequencies of 1/4 and 3/4 of the mesh frequency dominates the response. NI can predict subharmonic motions; whereas, since the assumed solution does not include subharmonics, HBM cannot predict them.

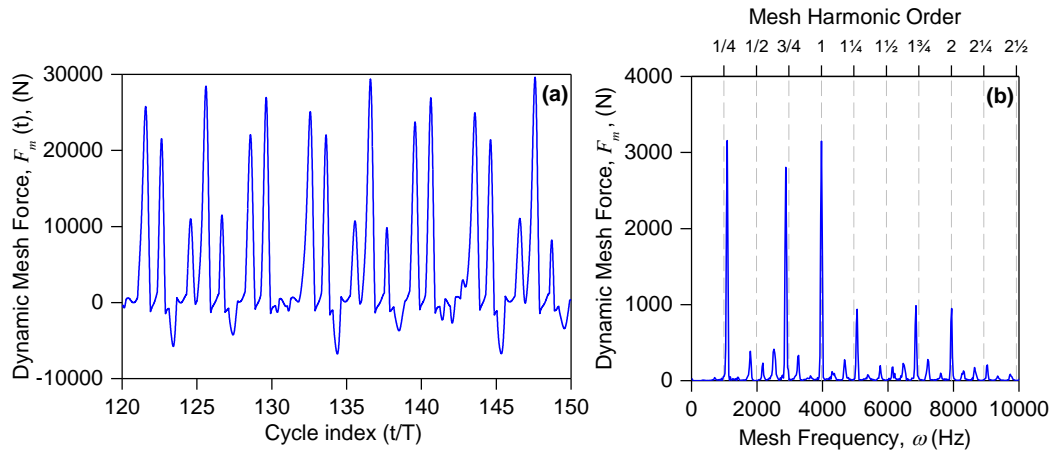


Fig. 4.5 (a) Time history and (b) frequency spectrum of $F_m(t)$ at $\omega = 3968\text{Hz}$ obtained by NI

The subharmonic contents of the responses in the form of both dynamic mesh force and dynamic transmission error obtained by NI are investigated in Fig. 4.6, which shows the normalized amplitudes of the subharmonics with respect to the amplitude of the fundamental harmonic at $1/4\omega$, $1/3\omega$ and $3/4\omega$ frequencies. The existence of subharmonics are obvious in the vicinity of excitation frequencies of $\omega \cong 1500\text{ Hz}$, $\omega \cong 3300\text{ Hz}$ and $\omega \cong 4000\text{ Hz}$ (shown by vertical dashed lines). The subharmonic motion around $\omega \approx 4/3\omega_2 \cong 1500\text{ Hz}$ are characterized by the subharmonic component with the frequency $3/4\omega$ and around this frequency, the amplitudes of the subharmonics in the dynamic mesh force are larger compared to the amplitudes of the subharmonics in the dynamic transmission error. However, it can be concluded from Fig. 4.4 that, since the amplitudes of the responses in the vicinity of $\omega \cong 1500\text{ Hz}$ are small, the subharmonics in NI solutions do not cause an inconsistency with the solutions of HBM.

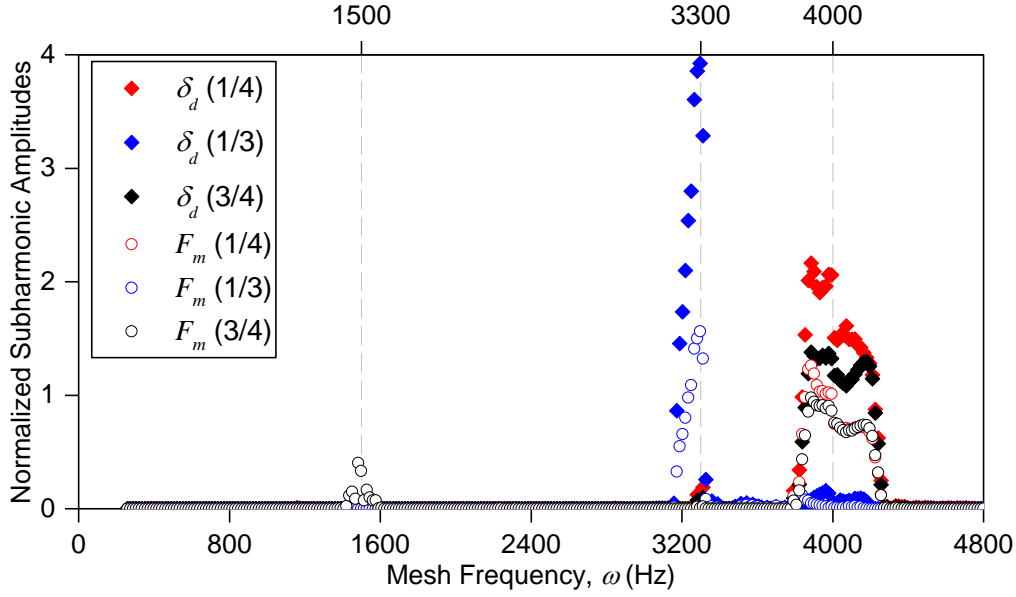


Fig. 4.6 Normalized amplitudes of the subharmonics with $1/4\omega$, $1/3\omega$ and $3/4\omega$ for both dynamic transmission error δ_d and dynamic mesh force F_m

On the other hand, subharmonic content of the response is more significant around $\omega \cong 3300\text{ Hz}$ and $\omega \cong 4000\text{ Hz}$, since these frequency ranges coincide with other resonance peaks at the natural frequencies of ω_7 and ω_{10} (see Fig. 4.4). This is the main cause of the inconsistency between NI and HBM solutions in these frequency ranges. It is also noted that contrary to the case in the vicinity of $\omega \cong 1500\text{ Hz}$, the amplitudes of the subharmonics in the dynamic transmission error are larger than the amplitudes of the subharmonics in the dynamic mesh force in later two frequency ranges. The spectral content of the response in the vicinity of $\omega \approx 3\omega_2 \cong 3300\text{ Hz}$ is clearly dominated by the subharmonic component with the frequency $1/3\omega$, whereas two distinct subharmonic components with the frequencies of $1/4\omega$ and $3/4\omega$ are dominant in the spectral content of the response around $\omega \approx 4\omega_2 \approx 4/3\omega_7 \cong 4000\text{ Hz}$. In general, a subharmonic motion observed at $\omega \approx r_1/r_2 \omega_n$ is governed by the subharmonic component with the frequency of

(r_2/r_1) of the excitation frequency or in this case mesh frequency. Furthermore, the examples of different nonlinear behaviors, i.e. period-1 motion, period-3 subharmonic motion, long-period subharmonic motion and chaotic motion, are illustrated in Fig. 4.7, which shows the frequency spectra and corresponding phase plane plots including Poincare map points of dynamic transmission error δ_d at different mesh frequencies. Poincare map points are the displacement-velocity points calculated at time instants with intervals of $1T$. In the phase plane plots of period-1 motion and period-3 subharmonic motion, there are 1 and 3 Poincare map points, respectively, indicating that these are $1T$ and $3T$ motions. On the other hand, the number of Poincare map points are much more in the cases of long-period subharmonic motion and chaotic motion. The frequency spectrum of chaotic motion also has a broadband content.

It is known from past studies [45,54,59,60], that spiral bevel gears exhibit nonlinear behaviors such as single-sided tooth impact (SSI) and double-sided tooth impact (DSI). These nonlinear behaviors can also be observed here in the NI and HBM solutions. It is obvious in Fig. 4.8 that the response of the gear pair is linear at the frequencies around $\omega = 900$ Hz. As the frequency increases to $\omega = 1075$ Hz, SSI begins to emerge. Due to softening effect of tooth separation, the forced response curve takes a sharp turn towards left with decreasing frequency and advances along the same path as the frequency decreases from $\omega = 1075$ Hz to $\omega = 1030$ Hz. At this point, the gear pair begins to exhibit DSI, in which impact with the preceding tooth occurs following the tooth separation. Because of the hardening behavior of DSI compared to SSI, the response veers right towards the higher frequency and begins to increase in amplitude. The response reaches the peak amplitude at $\omega = 1104$ Hz and then the amplitude begins to decrease as DSI type nonlinear behavior continues. Then, the response changes back to SSI and subsequently becomes linear as the frequency increases further. Similar SSI and DSI type nonlinear behaviors are also seen in the vicinity of the resonance peak observed at $\omega \cong 2750$ Hz (see Fig. 4.4).

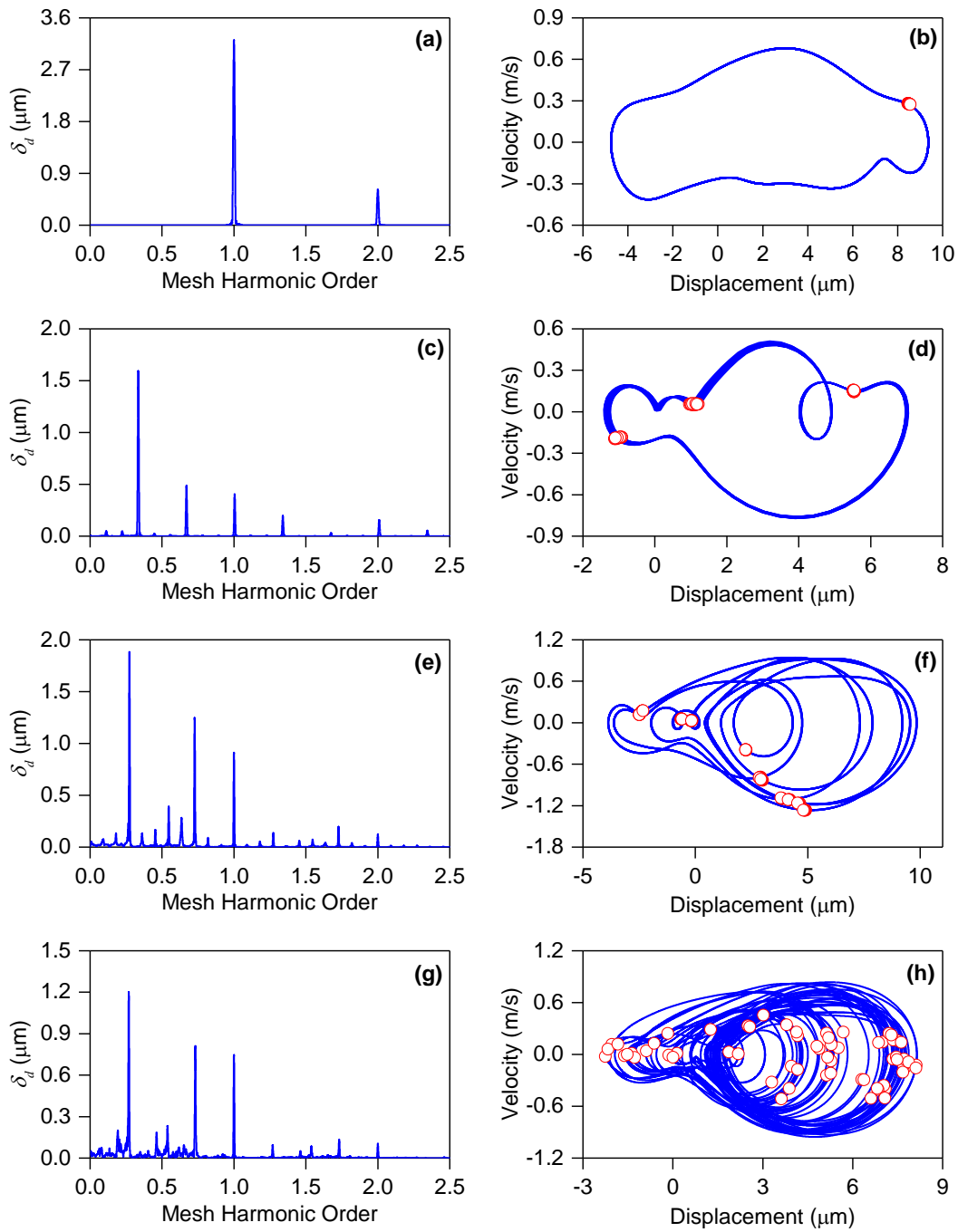


Fig. 4.7 Frequency spectra, phase plane plots and Poincaré map points (○) of dynamic transmission error δ_d obtained by NI **(a-b)** period-1 motion at $\omega = 1064$ Hz **(c-d)** period-3 subharmonic motion at $\omega = 3281$ Hz **(e-f)** long-period subharmonic motion at $\omega = 3978$ Hz **(g-h)** chaotic motion at $\omega = 4071$ Hz

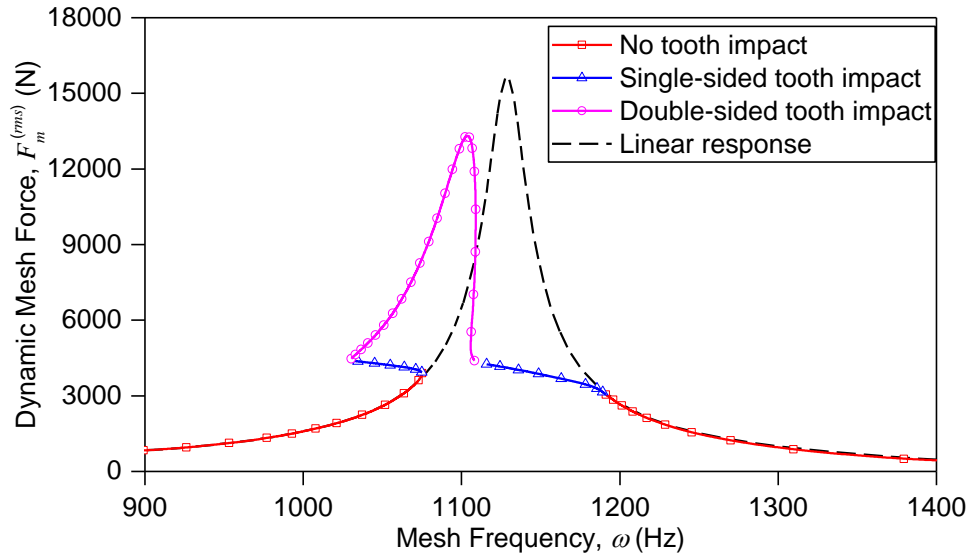


Fig. 4.8 Nonlinear characteristics of the spiral bevel gear train

Studying Fig. 4.4 further, the gear pair exhibits SSI type nonlinear behavior around the resonance peaks observed at $\omega \cong 3160$ Hz and $\omega \cong 3950$ Hz. However, the response amplitudes in the vicinity of these peaks are less than the total amount of backlash and static deflection; hence, impact with the preceding tooth, i.e. DSI, cannot occur. Furthermore, it is clear in Fig. 4.4 that the amplitude of the resonance peak observed at $\omega = 1743$ Hz is small compared to the static mesh force (dashed horizontal line in Fig. 4.4); hence, the gear pair behaves linearly around this peak. Moreover, there are super-harmonic resonance peaks at $\omega \approx 1/2 \omega_2 = 567$ Hz and $\omega \approx 1/2 \omega_7 = 1528$ Hz. A very small super-harmonic peak is also evident at $\omega \approx 1/3 \omega_2 = 378$ Hz. These peaks can only be obtained by utilizing adequate number of harmonics in HBM. Fourier spectrums of the dynamic mesh force at $\omega \approx 1/2 \omega_2 = 567$ Hz and $\omega \approx 1/3 \omega_2 = 378$ Hz obtained from NI are shown in Fig. 4.9. In general, a super-harmonic resonance peak observed at $\omega \approx 1/r \omega_n$ is governed by the r^{th} harmonic of the response.

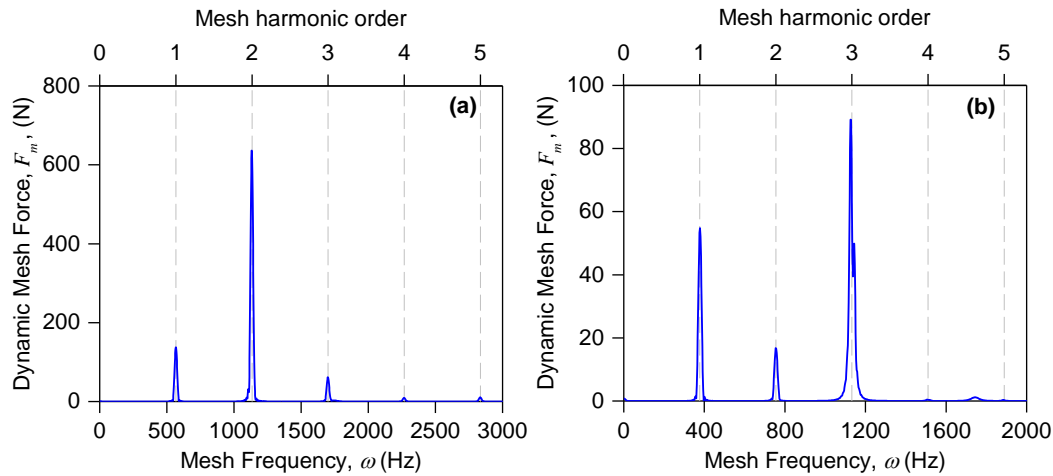


Fig. 4.9 Fourier spectrum of $F_m(t)$ at super-harmonic resonance peaks obtained by NI, (a) $\omega \approx 1/2 \omega_2 = 567$ Hz (b) $\omega \approx 1/3 \omega_2 = 378$ Hz

The effect of the number of harmonics retained in HBM on the dynamic mesh force is presented in Fig. 4.10. It can be seen that the results obtained by utilizing two or three harmonics in the solution agree well with each other. On the other hand, the results obtained by using single-harmonic deviates from the multi-harmonic solutions significantly in the frequency ranges where separation occurs, since the nonlinear characteristics cannot be captured accurately by a single-harmonic solution. Moreover, single-harmonic solution cannot predict any of the super-harmonic resonance peaks observed at $\omega \approx 1/2 \omega_2 = 567$ Hz, $\omega \approx 1/2 \omega_7 = 1528$ Hz and $\omega \approx 1/2 \omega_{10} = 1967$ Hz (shown by vertical dashed lines), since these resonance peaks are governed by the 2nd harmonic of the response.

Fig. 4.11 shows the influence of parametric excitation caused by fluctuating stiffness of gear mesh and static transmission error excitation. The combined response, where both excitations exist, is compared to the responses due to each individual excitation. When the only excitation source is the static transmission error $e_m(t)$, the system is

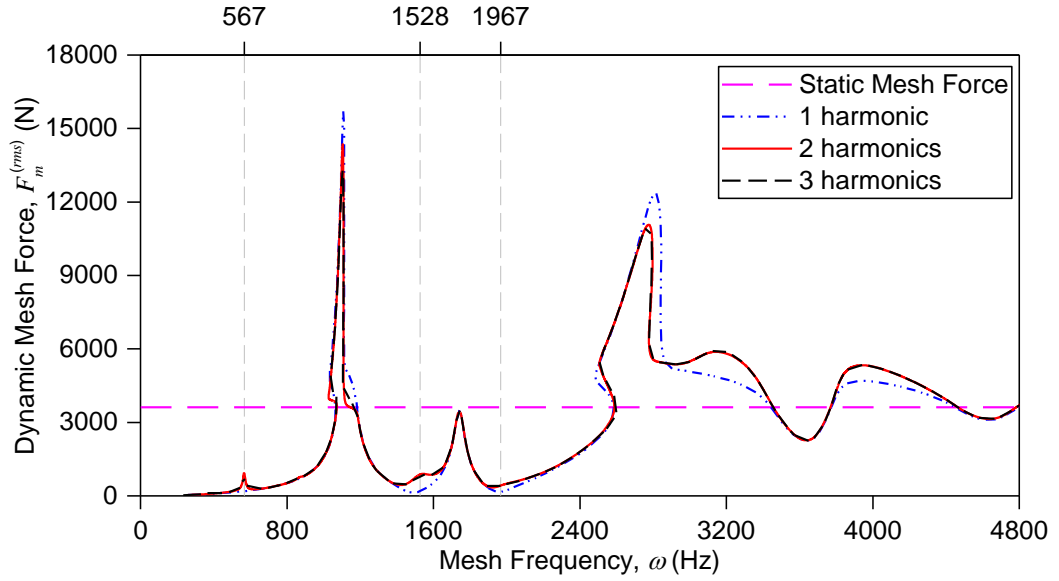


Fig. 4.10 Effect of number of harmonics employed in HBM

nonlinear time-invariant. However, the combined response represents a nonlinear time-varying system. In Fig. 4.11, it can be seen that the super-harmonic resonance peaks observed at $\omega \approx 1/2 \omega_2 = 567$ Hz and $\omega \approx 1/2 \omega_7 = 1528$ Hz (shown by vertical dashed lines) in the combined response are due to the parametric excitation. Moreover, the parametric excitation increases the response amplitude of the corresponding NTI system in the entire frequency range. The single-sided impact type nonlinear behavior observed at $\omega \cong 2750$ Hz in the response curve of the corresponding NTI system changes to double-sided impact type in the combined response.

The effect of backlash amount is given in Fig. 4.12. Since both SSI and DSI are observed in the vicinity of the first resonance peak when $T = 200$ Nm, the response around this peak is addressed in the figure. As the backlash is increased from $b = 20 \mu\text{m}$ to $b = 40 \mu\text{m}$, SSI range increases while the DSI range decreases. A

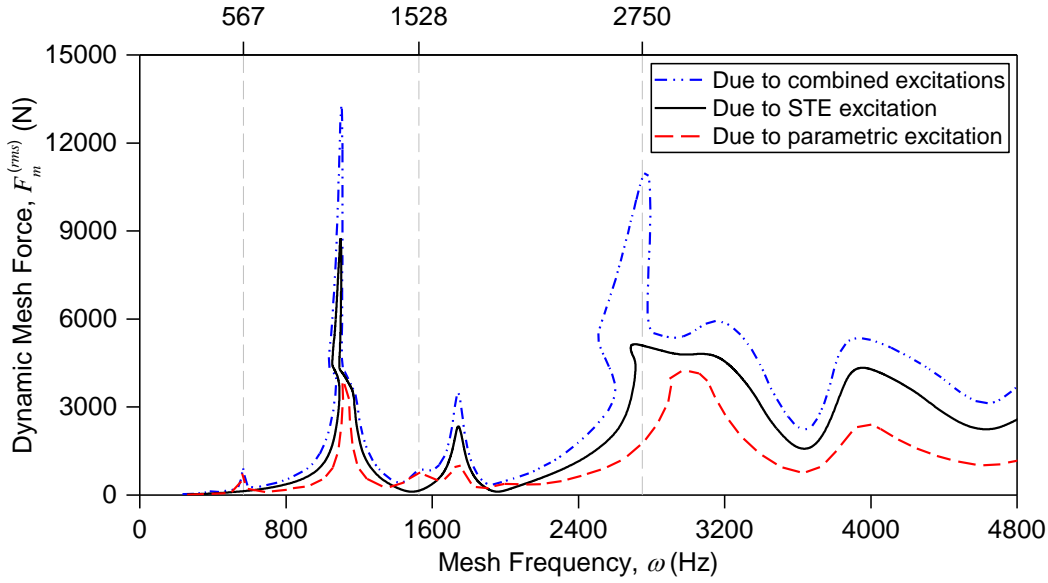


Fig. 4.11 Effect of static transmission error and parametric excitations

further increase in backlash from $b = 40 \mu\text{m}$ to $b = 60 \mu\text{m}$ cause DSI to disappear, since the response amplitude becomes smaller compared to the total amount of backlash and static deflection; hence, SSI dominates the nonlinear response. A further increase in backlash does not affect the nonlinear response any more since DSI cannot occur.

The components of the dynamic bearing forces $F_b^{(rms)}$ for the first bearing of the pinion shaft (Bearing A in Fig. 4.1) are given in Fig. 4.13. Here, each force component can be calculated by the multiplication of the corresponding component of the bearing stiffness and the amplitude of the response of the bearing location in the corresponding direction. It is seen from the figure that gear backlash causes similar nonlinear behaviors in the bearing forces. It should be noted that after $\omega = 2400 \text{ Hz}$, the axial component of the bearing force increases significantly compared to the radial components which decreases the bearing lives considerably. This is because the 7th, the 9th and the 10th modes occurring in this high frequency

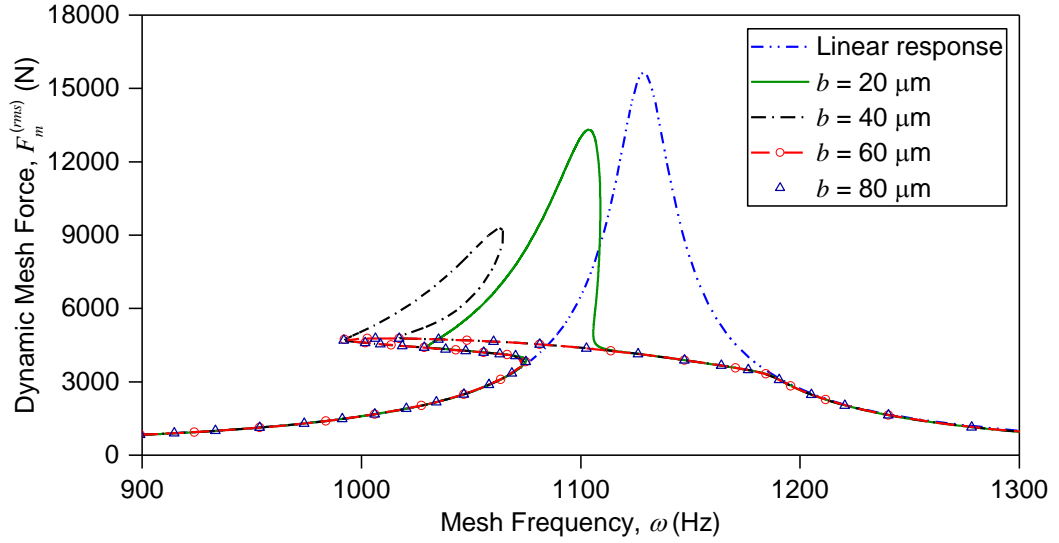


Fig. 4.12 Dynamic mesh force for $T = 200$ Nm and different backlash amounts

range are more associated with the axial motion of the pinion shaft compared to the radial motions as indicated by the definition of mode shapes given in Table 4.2.

In order to investigate the effect of bearing stiffness, the bending stiffness coefficients of all bearings in the system, $k_{b\theta_x} = k_{b\theta_y}$, are changed equally. Fig. 4.14 shows the change in the dynamic mesh force as a function of $k_{b\theta_x} = k_{b\theta_y}$. It is seen from the figure that resonance peaks shift to the right when $k_{b\theta_x} = k_{b\theta_y}$ is increased. Moreover, the amplitudes of the peaks are affected in different way; that is, some peak amplitudes increase while the others decrease with increasing bending stiffness coefficients of the bearings. The change in peak amplitude affects the nonlinearity of the response as well. As the stiffness coefficient is increased to $k_{b\theta_x} = k_{b\theta_y} = 1 \times 10^7$ Nm/rad, DSI disappears in the vicinity of the resonance peak at $\omega \cong 3200$ Hz and the gear pair exhibits only SSI. Therefore, if the operating frequency range of the bevel gear system is above 1600 Hz, increased bearing stiffness decreases the dynamic mesh force and gives better results compared to other cases.

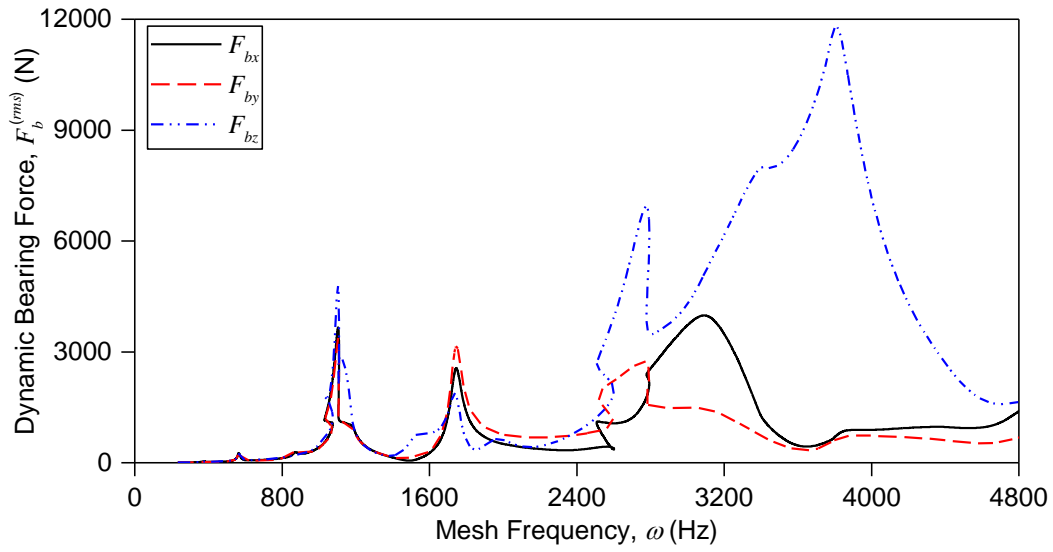


Fig. 4.13 Dynamic bearing forces $F_b^{(rms)}$ for the first bearing of the pinion shaft (Bearing A in Fig. 4.1)

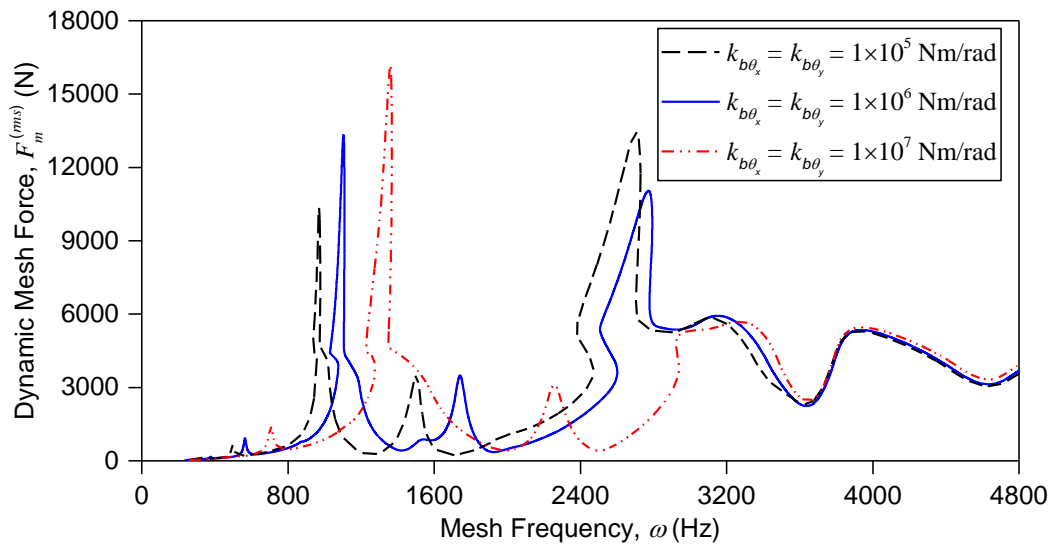


Fig. 4.14 Effect of bearing stiffness coefficient, $k_{b\theta_x} = k_{b\theta_y}$, on the dynamic gear mesh force

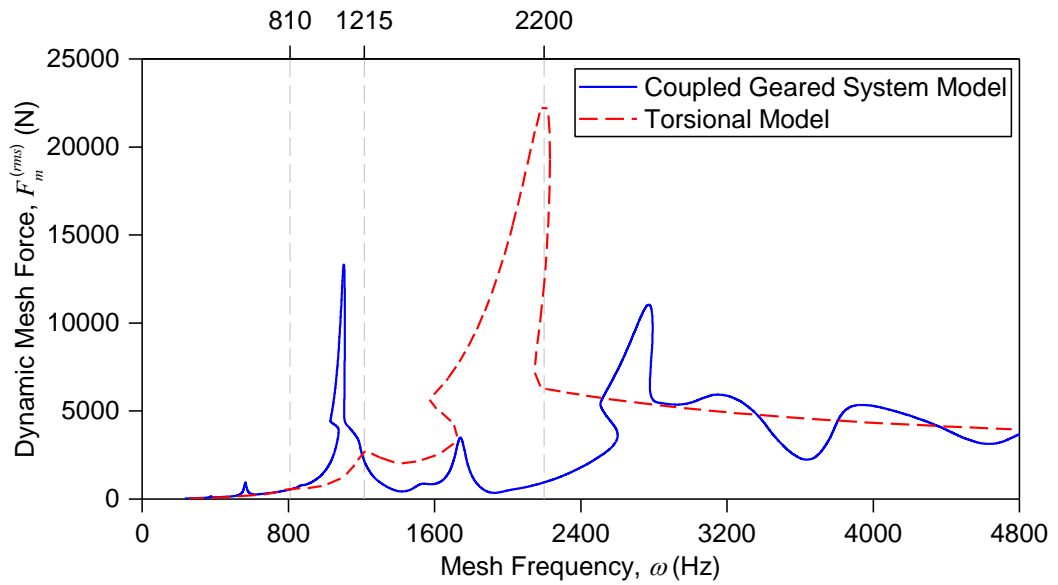


Fig. 4.15 Comparison of coupled gear system model with torsional model

In Fig. 4.15, the dynamic response of the coupled gear system considered in this study is compared with that of gear torsional model in order to investigate the effect of coupling on system dynamics. The gear torsional model is generated from the coupled dynamic model developed in this study by considering the shafts and bearings as rigid. The resulting torsional model is a two DOFs semi-definite system with a rigid body mode. The second mode of this system is the contraction/expansion of the mesh spring by the rotational motions of the gears, θ_{zi} ($i = p, g$) and the corresponding linear system exhibit this mode at a natural frequency of $\omega_n = 2430$ Hz, which is verified by ANSYS[®] as well. Both SSI and DSI type nonlinear behaviors are observed around the corresponding resonance peak observed at $\omega_n = 2200$ Hz. Moreover, there are super-harmonic resonance peaks in the response of the gear torsional model at $\omega \approx 1/2 \omega_n = 1215$ Hz and $\omega \approx 1/3 \omega_n = 810$ Hz. It is evident in the figure that the dynamic responses of the two

models are totally different, which shows the significant influence of the coupling on dynamic response. Consequently, gear torsional model is inadequate for the investigation of the dynamics of a spiral bevel gear system when the stiffness of shaft-bearing structures is comparable to mesh stiffness.

4.4 Conclusion

In this study, a nonlinear time-varying dynamic model of a spiral bevel gear system is developed. The mesh model of the gear pair is integrated into the Timoshenko beam finite element (FE) model of shafts supported by bearings. Natural frequencies of the linear system obtained by the developed Timoshenko beam FE model and commercial FE software, ANSYS® agree well with each other, which ensures the quality of the FEM used in the study. FE shaft models obtained are coupled with each other by the nonlinear backlash elements including mesh stiffness. The resulting number of nonlinear equations, which is very large due to the finite element modelling of the shafts, is considerably reduced by the use of receptance method. Therefore, solving only the equations related to the DOFs associated with the gear pair, where the nonlinear elements are attached, are sufficient for the shaft-bearing dynamic characteristics to be taken into account.

Applying HBM with multiple harmonics on the nonlinear differential equations of the gear train a system of nonlinear algebraic equations is obtained. Continuous-time Fourier transform is used in the calculation of Fourier coefficients, as opposed to gear dynamics studies that utilize discrete Fourier transform. Utilizing continuous-time Fourier transform, the possible convergence problems for the large nonlinear systems can be avoided. Furthermore, in order to decrease the computational time, analytical integration is employed for the calculation of Fourier coefficients. Obtained system of nonlinear algebraic equations is solved by

Newton's method utilizing arc-length continuation. Moreover, solution of the nonlinear differential equations is also obtained by direct numerical integration. Solutions obtained by HBM and NI agree well with each other except around some resonance peaks, where the spectral content of the response is dominated by subharmonics, which are not included in the HBM solution.

Several case studies are performed and it is observed from the results that both single-sided and double-sided tooth impact type nonlinear behaviors emerge for the gear pair under investigation. Furthermore, NI solutions indicate the existence of subharmonic motions at $\omega \approx r_1/r_2 \omega_n$, whose spectral content is dominated by the subharmonic component with the frequency of (r_2/r_1) of the excitation frequency. The influence of parametric excitation is as well studied in the study. The parametric excitation causes super-harmonic resonance peaks governed by the r^{th} harmonic of the response at frequencies $\omega \approx \omega_n/r$. Furthermore, the response level of a NTV system is larger compared to the response level of the corresponding NTI system. Therefore, the parametric excitation due to fluctuating stiffness of the gear mesh increases the severity of the nonlinearity. The effect of backlash amount is also investigated. It is observed that tooth separations and tooth impacts are possible, especially for lightly-loaded cases, for which the amount of backlash is critical. Moreover, dynamic bearing forces are calculated to demonstrate that gear backlash nonlinearity also affects the bearing forces which are important in the selection of bearings and determination of lives of the bearings used. It is also observed that bearing stiffness affects the amplitudes and frequencies of the resonance peaks considerably. The change in the response amplitude cause the nonlinear behavior of the gear pair to change as well. It is observed that increased bearing stiffness is useful in decreasing dynamic mesh force for an operating frequency greater than 1600Hz for the case study considered. Finally, the responses of the coupled gear system model and torsional model are compared and the result shows that the

coupling has a significant influence on the response of a spiral bevel gear system which needs to be considered in modeling.

CHAPTER 5

NONLINEAR DYNAMIC ANALYSIS OF A DRIVETRAIN INCLUDING SPUR, HELICAL AND SPIRAL BEVEL GEARS

5.1 Introduction

The vast majority of studies about gear dynamics in the literature focus on single gear pairs and several dynamic models and corresponding solution methods are proposed in these studies. On the other hand, studies on multi-stage, multi-mesh drive trains are limited in spite of their widespread use. Dynamics of two stage spur geared systems are studied in [27,28,55], where authors develop dynamic models including fluctuating mesh stiffness and backlash nonlinearity and employ Harmonic Balance Method (HBM) with discrete Fourier transform (DFT) to solve the resulting equations of motion for period-1 and subharmonic responses. Similar nonlinear dynamic models with fluctuating mesh stiffness are proposed in [30,31] for idler and counter-shaft arrangements of spur gears. Considering linear dynamic models with time-invariant mesh stiffness, idler and split-torque arrangements for multi-mesh helical gear trains are studied in [40], whereas counter-shaft arrangement is investigated in [41].

There are a few published studies on dynamics of bevel gears and they are all limited to a single gear pair. Using a mesh model in accordance with the gear tooth geometry, dynamics of bevel and hypoid gear systems are studied in [59]. Then, time-varying mesh parameters and backlash nonlinearity are included in the dynamic model and authors employ HBM [54] and direct numerical integration [45]

to obtain dynamic responses. In addition, a multi-degree-of-freedom (MDOF) lumped parameters dynamic model of a hypoid gear train developed in [60] is solved by employing direct numerical integration. A linear dynamic model of a spiral bevel gear train with time-invariant mesh stiffness is presented in [49], where finite element modeling is employed to describe the shaft-bearing structural characteristics better. More recently, Yavuz et al. [61] propose an MDOF nonlinear dynamic model of a spiral bevel gear train, which combines the Timoshenko beam FEM model of shaft-bearing assembly with the mesh model of the gear pair.

Since there is no known study that addresses a nonlinear dynamic model of a multi-stage, multi-mesh drivetrain including a bevel gear, a nonlinear dynamic model of a drivetrain composed of both cylindrical gears and bevel gears (Fig. 5.1) are proposed in this study. In the dynamic model, FEM models of shafts are coupled with each other by the mesh models of gear pairs, which include backlash nonlinearity and fluctuating mesh stiffness. Parametric excitation caused by fluctuating mesh stiffness is considered as well as static transmission error. Since the resulting nonlinear system has many degrees of freedom (DOFs), the forced response analysis is performed in modal domain where the resulting differential equations of motion are transformed to a set of nonlinear algebraic equations by using multi-harmonics HBM in conjunction with continuous-time Fourier transform and modal superposition. Hence, the number of nonlinear equations is proportional to the number of modes utilized in the modal superposition, rather than the number of DOFs associated with the nonlinearity. Consequently, this approach can be employed to obtain the dynamic responses of multi-mesh geared systems without increasing the number of nonlinear equations, which drastically decreases the computational time, and thus it is possible to model gear shafts by using finite element method for shaft-bearing dynamic characteristics to be easily taken into account. In contrast with gear dynamics studies that utilize discrete Fourier transform [27,28,54,55,61], using continuous-time Fourier transform, the

convergence problems encountered in the solution of systems with large number of nonlinear equations are avoided. Furthermore, the computational time is decreased further by employing analytical integration rather than numerical integration for the calculation of Fourier coefficients. The resulting system of nonlinear algebraic equations is solved by utilizing Newton's method with arc-length continuation. A much more computationally demanding method, i.e. direct numerical integration, is utilized to validate the solutions obtained by HBM. Since computational cost in time domain methods such as direct numerical integration increases considerably as the number of nonlinear equations increases, a frequency domain method, i.e. HBM, is utilized in this study. Several parametric studies are accomplished in order to examine the influences of a large number of design parameters on dynamics of multi-mesh, multi-stage geared system.

5.2 Dynamic Model Formulation

5.2.1 Physical System and Dynamic Model

The gear train shown in Fig. 5.1 and Fig. 5.2 is comprised of spur, helical and spiral bevel gears with shafts supported by bearings. Timoshenko beam finite element method (FEM) is used to model the gear shafts. The outer diameters of the gear shafts follow the gear blanks in order to incorporate them into the FEM model; thus, the stiffness and mass effects of the gear blanks are considered as well. Multiple nodes are used to model the spiral bevel gear cones in order to consider the tapering effects of them. The bearing stiffnesses, which are assumed to be time-invariant, are also included in the FEM model. Clearance-type nonlinearity is disregarded in the bearings, which is reasonable for preloaded bearings [57].

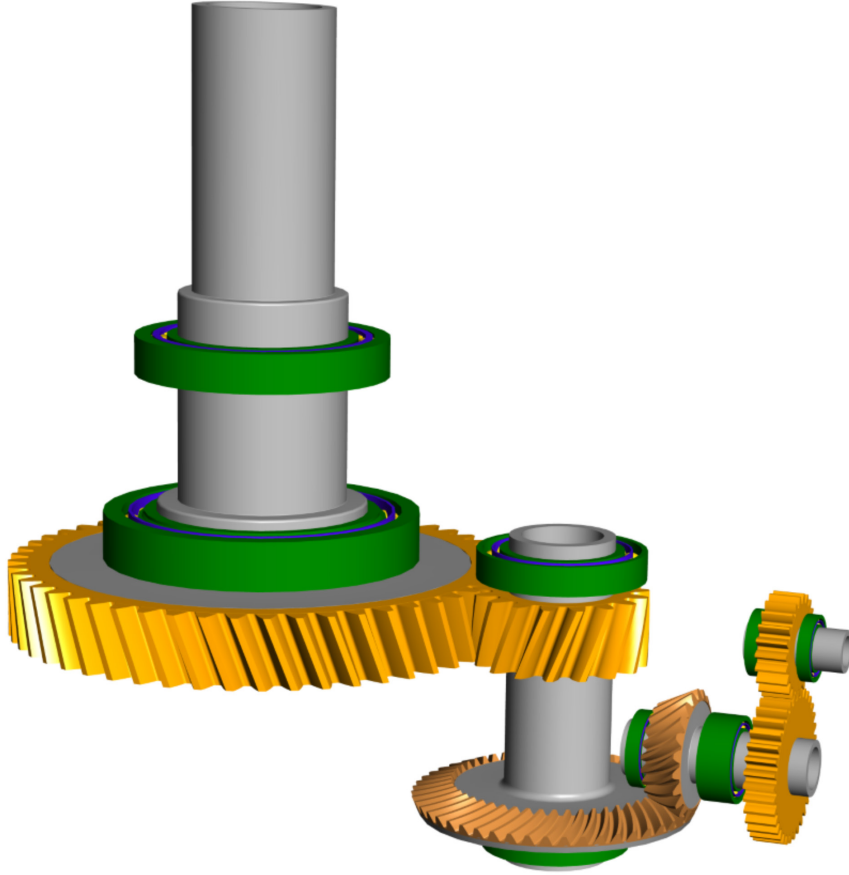


Fig. 5.1 The drivetrain considered in this study

The mass matrix, \mathbf{M}_{sn} , and stiffness matrix, \mathbf{K}_{sn} , of each shaft n ($n = 1, 2, \dots, N$) are calculated by assembling the mass and stiffness matrices of Timoshenko beam elements. Then, complete mass and shaft stiffness matrices of the gear train are obtained as $\mathbf{M}_s = \text{Diag}[\mathbf{M}_{s1}, \mathbf{M}_{s2}, \dots, \mathbf{M}_{sN}]$ and $\mathbf{K}_s = \text{Diag}[\mathbf{K}_{s1}, \mathbf{K}_{s2}, \dots, \mathbf{K}_{sN}]$, respectively. Considering that each node has 6 DOFs and the shaft n is modeled by using a total of m_n beam elements, the dimension of both matrices is $q \times q$ where $q = 6 \cdot \sum_{n=1}^N (m_n + 1)$ is the total number of DOFs of the gear train.

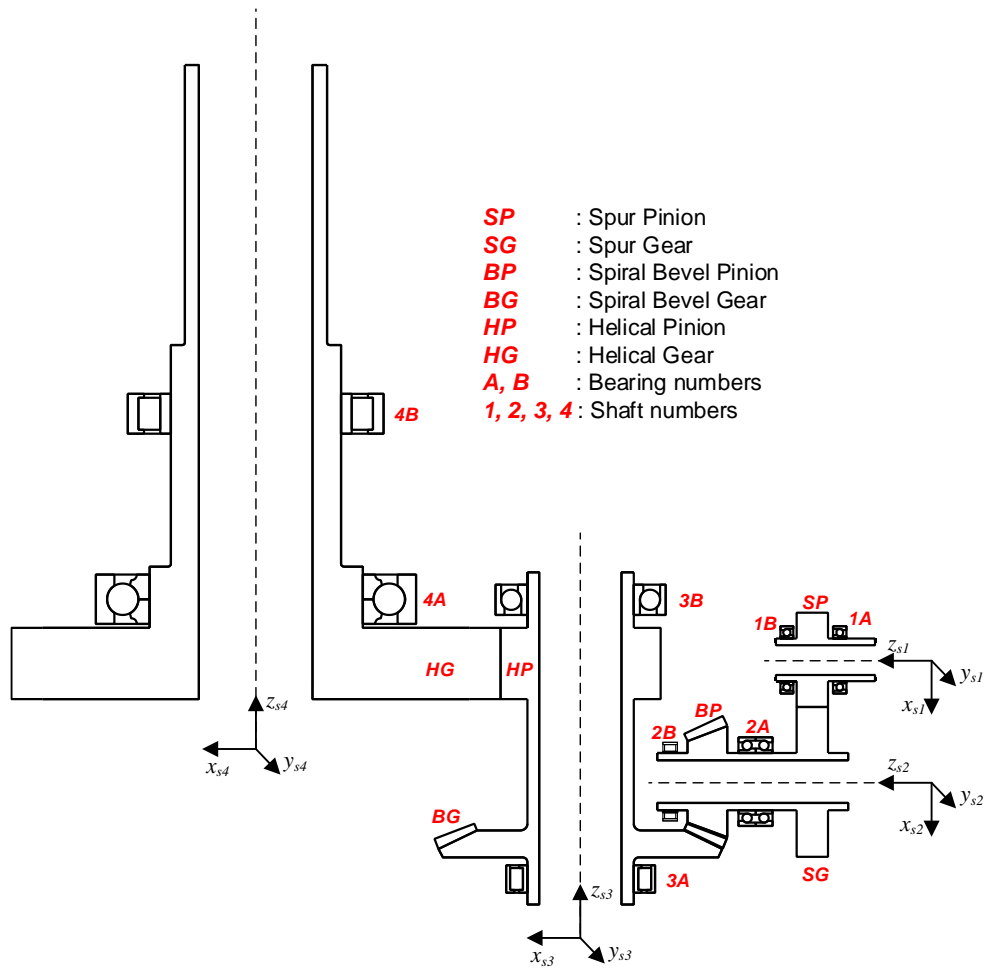


Fig. 5.2 Numbering of the components in the drivetrain

For a drivetrain supported by a total of n_b bearings, the complete bearing stiffness matrix is assembled as $\mathbf{K}_b = \text{Diag} [\cdots \mathbf{K}_{b1} \cdots \mathbf{K}_{b2} \cdots \mathbf{K}_{bn_b} \cdots]$, where $\mathbf{K}_{bi} = \text{Diag} [k_{bxi}, k_{byi}, k_{bzi}, k_{b\theta_x i}, k_{b\theta_y i}, k_{b\theta_z i}]$ ($i = 1$ to n_b) is the stiffness matrix of the i^{th} bearing and k_{bxi} to $k_{b\theta_z i}$ are the stiffness values in the designated directions. The stiffness matrix of each individual bearing is located in the complete bearing stiffness matrix, \mathbf{K}_b , in accordance with the node number to which the corresponding bearing is attached and the remaining elements of \mathbf{K}_b are zero.

Consequently, the overall stiffness matrix of whole FEM model is obtained as $\mathbf{K} = \mathbf{K}_s + \mathbf{K}_b$. Furthermore, a set of damping ratio ζ_s is used for the shaft-bearing assembly.

A generic mesh model, which is applicable to all types of gears in the drivetrain considered in this study, i.e., spur, helical and spiral bevel gears, is formulated. The mesh model is illustrated in Fig. 5.3, which shows a three-dimensional dynamic model of a spiral bevel gear pair. The gears are connected to each other by a time-varying mesh stiffness and a time-invariant mesh damping in the direction of tooth normal, i.e., along the line of action (LOA). Moreover, a displacement excitation in the form of static transmission error is connected in series with the stiffness and damping elements in the same direction. There is also backlash between the gears, which causes nonlinearity in the dynamics of the system. Since time variation of mesh vector parameters, i.e., LOA vector and the position of mesh point, is much smaller compared to time variation of mesh stiffness [47], a constant LOA vector with an effective mesh point is utilized. The mesh couplings for spur and helical gears are exactly the same as the one for spiral bevel gear shown in the figure. The effective mesh nodes in the three-dimensional discrete mesh model, which are coincident for pinion and gear, are connected to the Timoshenko beam finite element model of shaft-bearing structures by using rigid links as shown in Fig. 5.4.

Since the mesh node of each gear has 3 translational and 3 rotational DOFs as illustrated in Fig. 5.3, a total of 12 DOFs defines the mesh coupling. Since some shafts have multiple gears forming multiple mesh couplings with the other shafts, the generalized coordinates are expressed relative to the local reference frames of the gear shafts, $S_{si} (i = p, g)$ rather than the local reference frames of the gears, $S_i (i = p, g)$. Thus, the displacement vectors of the mesh nodes can be written as

$$\mathbf{x}_{si} = \begin{pmatrix} x_{si} & y_{si} & z_{si} & \theta_{xsi} & \theta_{ysi} & \theta_{zsi} \end{pmatrix}^T (i = p, g).$$

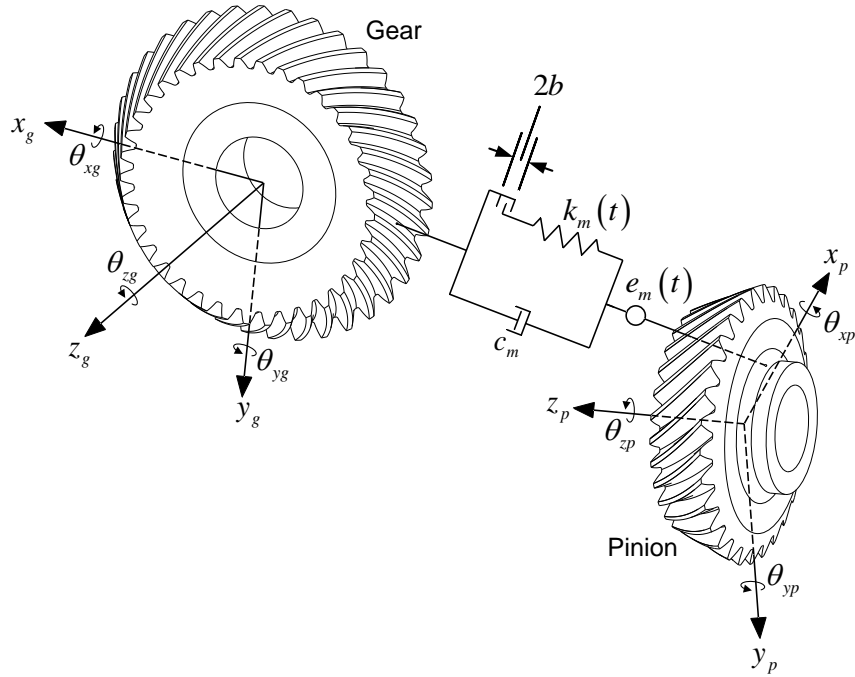


Fig. 5.3 A generic mesh model that is applicable to all types of gears

Transforming the displacement vectors of the mesh nodes to the LOA direction by using the coordinate transformation vectors, $\mathbf{h}_i (i = p, g)$, the relative dynamic displacement along the LOA, i.e. the dynamic transmission error, is expressed as follows

$$\delta_d = \mathbf{h}_p^T \mathbf{x}_{sp} - \mathbf{h}_g^T \mathbf{x}_{sg}. \quad (5.1)$$

The transformation vectors composed of the directional rotation radii and the directional cosines between the generalized coordinates and LOA can be written as

$$\mathbf{h}_i = (n_{ix} \quad n_{iy} \quad n_{iz} \quad \lambda_{ix} \quad \lambda_{iy} \quad \lambda_{iz})^T \quad (i = p, g). \quad (5.2)$$

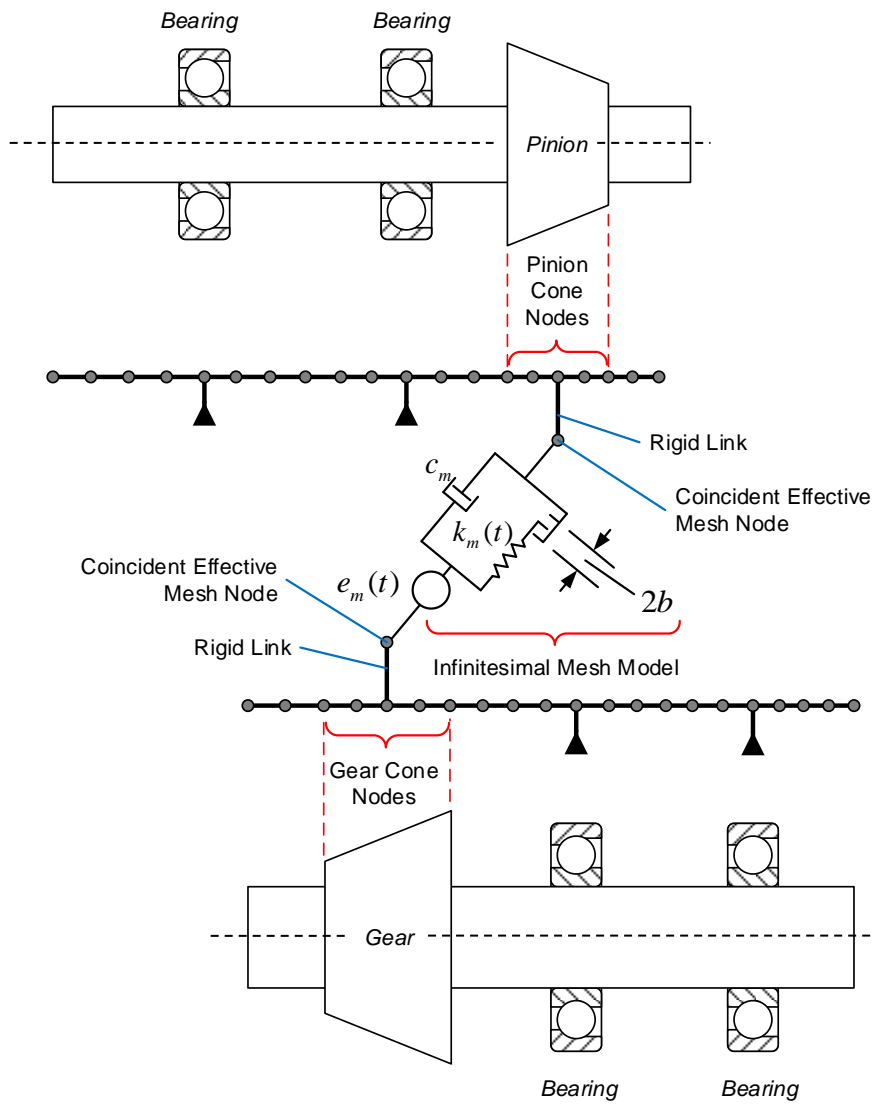


Fig. 5.4 Schematic of gear mesh model and finite element model

The directional rotation radii, λ , can be written as

$$\lambda_{ix} = \mathbf{n}_i \cdot (\mathbf{u}_{xi} \times \mathbf{r}_i) \quad (i = p, g), \quad (5.3)$$

$$\lambda_{iy} = \mathbf{n}_i \cdot (\mathbf{u}_{yi} \times \mathbf{r}_i) \quad (i = p, g), \quad (5.4)$$

$$\lambda_{iz} = \mathbf{n}_i \cdot (\mathbf{u}_{zi} \times \mathbf{r}_i) \quad (i = p, g), \quad (5.5)$$

where $\mathbf{n}_i = (n_{ix} \ n_{iy} \ n_{iz})^T$ represents the directional cosine vector of LOA and $\mathbf{r}_i = (x_{im} \ y_{im} \ z_{im})^T$ denotes the position vector of the effective mesh point. Moreover, $\mathbf{u}_{xi} = (1 \ 0 \ 0)^T$, $\mathbf{u}_{yi} = (0 \ 1 \ 0)^T$ and $\mathbf{u}_{zi} = (0 \ 0 \ 1)^T$ are the unit vectors for coordinate system $S_{si} (i = p, g)$. The effective mesh point of a bevel gear pair is considered to be the intersection point of the pitch cones of the pinion and the gear at mean cone distance from the apex as shown in Fig. 4.3. Thus, the position vector of the effective mesh point is written as $\mathbf{r}_p = (r_{pm}^p \ 0 \ 0)^T$ and $\mathbf{r}_g = (-r_{pm}^g \ 0 \ 0)^T$ in the local reference frames of the pinion, S_p , and the gear, S_g , respectively, where $r_{pm}^i (i = p, g)$ is the pitch radius at mean cone distance. Similarly, the effective mesh point of a cylindrical gear pair is assumed to be the point of tangency of two pitch circles, i.e., pitch point, at the middle of the facewidth as illustrated in Fig. 3.2. Furthermore, \mathbf{n}_i and $\mathbf{r}_i (i = p, g)$ can be expressed in $S_{si} (i = p, g)$ with a series of coordinate transformation as follows

$$\mathbf{n}_i = \mathbf{T}_x(\theta_{di}) \mathbf{T}_z(\theta_{oi}) \mathbf{T}_y(\gamma_i) \mathbf{T}_z(\phi_i) \mathbf{T}_x(-\psi) \begin{Bmatrix} 0 \\ 1 \\ 0 \end{Bmatrix} \quad (i = p, g), \quad (5.6)$$

$$\mathbf{r}_i = \mathbf{T}_x(\theta_{di}) \mathbf{T}_z(\theta_{oi}) \begin{Bmatrix} r_{pm}^i \\ 0 \\ 0 \end{Bmatrix} \quad (i = p, g), \quad (5.7)$$

where $\mathbf{T}_\sigma (\sigma = x, y, z)$ denotes the transformation matrix about coordinate σ . Spiral/helix angle, ψ , and transverse pressure angle, ϕ_t , of the gear pair can be defined depending on the hand and rotation direction of the pinion as follows:

$$\psi = \begin{cases} \psi, & \text{if pinion rotates CCW and has left hand teeth} \\ -\psi, & \text{if pinion rotates CCW and has right hand teeth} \\ -\psi, & \text{if pinion rotates CW and has left hand teeth} \\ \psi, & \text{if pinion rotates CW and has right hand teeth} \end{cases}, \quad (5.8)$$

$$\phi_t = \begin{cases} \phi_t, & \text{if pinion rotates counterclockwise } (+z_p) \\ \pi - \phi_t, & \text{if pinion rotates clockwise } (-z_p) \end{cases}. \quad (5.9)$$

In Eq. (5.6), γ_p denotes the pitch angle of the pinion, whereas γ_g represents the negative of the pitch angle of the gear.

Moreover, two more angles, namely θ_{oi} and θ_{di} ($i = p, g$), are defined to transform the LOA vector from the local reference frames of gears, S_i ($i = p, g$), to the local reference frames of gear shafts, S_{si} ($i = p, g$). θ_{oi} is the angle between the x axes of S_i and S_{si} , whereas θ_{di} denotes the angle between the z axes of S_i and S_{si} . It should be noted that pitch angle, γ , and spiral/helix angle, ψ , are 0 for a cylindrical gear and a spur gear, respectively.

Considering backlash nonlinearity, the dynamic mesh force, F_m , along the LOA can be written as

$$F_m(t) = k_m(t) f_n(\delta_d(t) - e_m(t)) + c_m(\dot{\delta}_d(t) - \dot{e}_m(t)), \quad (5.10)$$

where the nonlinear displacement function, $f_n(\delta_d(t) - e_m(t))$, is defined as

$$f_n(\delta_d(t) - e_m(t)) = \begin{cases} \delta_d(t) - e_m(t) - b, & \delta_d(t) - e_m(t) > b \\ 0, & |\delta_d(t) - e_m(t)| \leq b \\ \delta_d(t) - e_m(t) + b, & \delta_d(t) - e_m(t) < -b \end{cases} \quad (5.11)$$

Here, b is the half of the gear backlash. The equation of motion of the whole gear train can be expressed as

$$\mathbf{M}\ddot{\mathbf{x}}(t) + \mathbf{C}\dot{\mathbf{x}}(t) + \mathbf{K}\mathbf{x}(t) + \mathbf{F}_N(t) = \mathbf{F}(t), \quad (5.12)$$

where $\mathbf{F}(t)$ represents the external force vector consisting of the external torques as follows

$$\mathbf{F}(t) = \mathbf{F} = \left(\dots \overbrace{\left(\begin{array}{cccccc} 0 & 0 & 0 & 0 & 0 & T_{in} \end{array} \right)}^{\text{Input Gear Node}} \dots \overbrace{\left(\begin{array}{cccccc} 0 & 0 & 0 & 0 & 0 & -T_{out} \end{array} \right)}^{\text{Output Gear Node}} \dots \right)^T \quad (5.13)$$

In the external force vector, $\mathbf{F}(t)$, the input and output torque values, which are assumed to be constant, are located according to the node numbers related with the input and output gears, respectively, and only the vector elements associated with the rotation of input and output gears about z axis are nonzero. The complete damping and stiffness matrices of the system does not include the mesh damping c_m and mesh stiffness k_m , respectively, due to the backlash nonlinearity. These mesh parameters are included in the equations of motion through the nonlinear restoring force vector, $\mathbf{F}_N(t)$, which is obtained from the dynamic mesh force as follows

$$\mathbf{F}_N(t) = \sum_{q=1}^{N_m} F_{m(q)}(t) \mathbf{p}_q, \quad (5.14)$$

where N_m represents the number of gear meshes in the drivetrain, $F_{m(q)}(t)$ is the dynamic mesh force corresponding to the q^{th} gear mesh and \mathbf{p}_q is the extended coordinate transformation vector for the q^{th} gear mesh obtained by locating the individual transformation vectors, $\mathbf{h}_i (i = p, g)$, in a null vector, whose length is equal to the number of total DOFs, according to the node numbers of pinion and gear forming the mesh:

$$\mathbf{p} = (\cdots \mathbf{h}_p^T \cdots - \mathbf{h}_g^T \cdots)^T. \quad (5.15)$$

5.2.2 Solution Method

5.2.2.1 Multi-term Harmonic Balance Method with Continuous-Time Fourier Transform

Harmonic Balance Method with multiple harmonics is employed to solve the equation of motion given by Eq. (5.12). Time-varying parameters such as static transmission error and mesh stiffness in a single gear pair system are assumed to be periodic with the mesh frequency, which can be calculated by the multiplication of the rotational speed of a gear in the mesh with the number of teeth of the same gear. Therefore, the response is as well periodic with the mesh frequency. However, since the drivetrain considered in this study includes multiple gear meshes with distinct mesh frequencies, the response is usually expected to be periodic with the common period of all the mesh excitations. For a drivetrain including a total of N_m gear

meshes, the common period can be defined as an integer multiple of all the mesh periods, according to $T = z_j T_j$ ($j = 1, 2, \dots, N_m$). Moreover, the number of harmonics employed in the response should not be less than $\max(z_1, z_2, \dots, z_{N_m})$ [31]. On the other hand, since the excitations that are periodic with different mesh frequencies emerge at different mesh locations of the drivetrain, dynamic response of any region in the drivetrain is mainly governed by one of these excitations while another region is dominated by another excitation. Therefore, all the excitations can be considered separately and the response can be expressed in such a Fourier series that it includes the fundamental and super-harmonic terms of each mesh frequency, ω_j ($j = 1, 2, \dots, N_m$), as follows

$$\mathbf{x}(t) = \text{Im} \left(\sum_{j=1}^{N_m} \sum_{r=0}^{N_{h,j}} \mathbf{X}_j^r e^{ir\omega_j t} \right), \quad (5.16)$$

where i denotes the unit imaginary number and Im represents the imaginary part. The response consists of the bias terms \mathbf{X}_j^0 , fundamental harmonic and super-harmonic terms, \mathbf{X}_j^r ($j = 1, 2, \dots, N_m$ & $r = 1, 2, \dots, N_{h,j}$). Here, \mathbf{X}_j^r is the complex amplitude vector of the harmonic with the frequency $r\omega_j$ and $N_{h,j}$ denotes the number of harmonics with the frequencies of integer multiples of the j^{th} gear mesh frequency. Moreover, based on the assumption that the response and so the nonlinear displacement function $f_n(\delta_d(t) - e_m(t))$ is periodic, the dynamic mesh force $F_{m(q)}(t)$ ($q = 1, 2, \dots, N_m$) at the q^{th} mesh can be described periodically as follows

$$F_{m(q)}(t) = \text{Im} \left(\sum_{j=1}^{N_m} \sum_{r=0}^{N_{h,j}} F_{m(q),j}^r e^{ir\omega_j t} \right). \quad (5.17)$$

For the nonlinear displacement function given by Eq. (5.11), it is required to determine the exact time of discontinuities for the accurate calculation of Fourier coefficients. A time point that is not very close to the actual discontinuity makes the nonlinear solver not to converge or, at best, to perform more iterations for convergence. This problem is tried to be avoided by using a very small time step in discrete Fourier transform, which provides only a slight improvement in accuracy, but increases the computational time considerably. For this reason, continuous-time Fourier transform is preferred rather than DFT in this study in order to calculate the Fourier coefficients. Accordingly, Fourier coefficients of the dynamic mesh force are calculated as follows $((j = 1, 2, \dots, N_m), (r = 1, 2, \dots, N_{h,j}))$

$$F_{m(q),j}^0 = \frac{1}{T} \int_0^T F_{m(q)}(t) dt, \quad (5.18)$$

$$F_{m(q),j}^r = \frac{2i}{T} \int_0^T F_{m(q)}(t) e^{-ir\omega_j t} dt. \quad (5.19)$$

It should be noted that the period, T , in Eqs. (5.18) and (5.19) is the common period for all gear meshes in the system according to $T = z_j T_j$ ($j = 1, 2, \dots, N_m$). Furthermore, the above integrals are computed analytically, rather than numerically, which decreases the computational time significantly.

Utilizing the extended coordinate transformation vector \mathbf{p} given in Eq. (5.15), Fourier coefficients of the nonlinear restoring force vector, $\mathbf{F}_N(t)$, can be calculated as follow

$$\mathbf{F}_N(t) = \text{Im} \left(\sum_{j=1}^{N_m} \sum_{r=0}^{N_{h,j}} \mathbf{F}_{N,j}^r e^{ir\omega_j t} \right), \quad (5.20)$$

where,

$$\mathbf{F}_{N,j}^r = \sum_{q=1}^{N_m} F_{m(q),j}^r \mathbf{p}_q \quad (j = 1, 2, \dots, N_m \text{ \& } r = 0, 1, 2, \dots, N_{h,j}). \quad (5.21)$$

Substituting Eqs. (5.16) and (5.20) into Eq. (5.12) and balancing the harmonic terms, the following set of nonlinear algebraic equations is obtained for $j = 1, 2, \dots, N_m$ and $r = 0, 1, 2, \dots, N_{h,j}$

$$\left[-(r\omega_j)^2 \mathbf{M} + i(r\omega_j) \mathbf{C} + \mathbf{K} \right] \mathbf{X}_j^r + \mathbf{F}_{N,j}^r = \mathbf{F}_j^r. \quad (5.22)$$

5.2.2.2 Modal Superposition Method

In the dynamic analysis of systems with many DOFs, the large number of nonlinear equations causes several numerical difficulties and significant increase in computational time. For systems where the number of nonlinear DOFs is much smaller than the total number of DOFs, receptance method, details of which are given in [52,62], can be employed. Using receptance method, the number of nonlinear equations can be decreased to the number of nonlinear DOFs multiplied by the number of harmonics. For geared systems, only the DOFs associated with gears, i.e., mesh nodes, contain nonlinearity. However, if the drivetrain consists of multiple gear pairs, which is the case in this study, receptance method will also result in a large number of nonlinear equations and large matrices will be involved in the solution procedure. Therefore, it is not convenient to use receptance method for dynamic response analysis of multi-stage, multi-mesh gear trains.

On the other hand, Kuran and Özgüven [67] studied on the calculation of the dynamic response of some MDOF nonlinear structures by employing modal superposition method. Later, Cigeroglu et al. [68] developed a modal superposition method for the dynamic analysis of bladed-disk systems and they [53] also extended the work to include multi-harmonic solution. In this study, modal superposition method is introduced to the dynamic analysis of multi-mesh drivetrains. In this approach, the response of the nonlinear system is estimated by modal superposition using the modes of the linear system. The number of resulting nonlinear equations depends on the number of modes utilized in the modal superposition; therefore, it is independent of the number of nonlinear DOFs, i.e., the number of gear meshes. Consequently, the modal superposition method is more appropriate for the dynamic analysis of multi-mesh drivetrains.

In order to transform the system of nonlinear algebraic equations given by Eq. (5.22) to modal coordinates, the following coordinate transformation is defined

$$\mathbf{X}_{(n \times 1)} = \mathbf{\Phi}_{(n \times m)} \boldsymbol{\eta}_{(m \times 1)}, \quad (5.23)$$

where $\boldsymbol{\eta}$ denotes the modal coefficient vector and $\mathbf{\Phi}$ represents the mass normalized undamped modal matrix obtained by the solution of the eigenvalue problem, i.e., $\mathbf{K}\mathbf{\Phi} = \omega^2 \mathbf{M}\mathbf{\Phi}$. Here, m and n represent the number of modes employed and the number of DOFs, respectively. It is noted that the number of modes, m , should be selected accordingly by considering the frequency range where the solution is searched. Consequently, using the orthogonality of mode shapes, the coordinate transformation yields the following set of nonlinear algebraic equations for $j = 1, 2, \dots, N_m$ and $r = 0, 1, 2, \dots, N_{h,j}$

$$\left[-(r\omega_j)^2 \mathbf{I} + i(r\omega_j) \bar{\mathbf{C}} + \bar{\mathbf{\Omega}} \right] \boldsymbol{\eta}_j^r + \bar{\mathbf{F}}_{N,j}^r = \bar{\mathbf{F}}_j^r, \quad (5.24)$$

where $\mathbf{\Omega}$ represents the diagonal matrix including the squares of natural frequencies, \mathbf{I} denotes the identity matrix and $\bar{\mathbf{C}} = \mathbf{\Phi}^T \mathbf{C} \mathbf{\Phi}$ represents the modal viscous damping matrix, which is diagonal in the case of proportional damping. Moreover, $\bar{\mathbf{F}}_N = \mathbf{\Phi}^T \mathbf{F}_N$ and $\bar{\mathbf{F}} = \mathbf{\Phi}^T \mathbf{F}$ are the modal nonlinear restoring force and the modal forcing vector, respectively.

A residual vector for all harmonics including the bias term can be written as follows ($j = 1, 2, \dots, N_m$ & $r = 1, 2, \dots, N_{h,j}$)

$$\mathbf{R}^0(\boldsymbol{\eta}) = \mathbf{\Omega} \boldsymbol{\eta}^0 + \bar{\mathbf{F}}_N^0 - \bar{\mathbf{F}}^0 = 0, \quad (5.25)$$

$$\mathbf{R}_j^r(\boldsymbol{\eta}) = \left[-(r\omega_j)^2 \mathbf{I} + i(r\omega_j) \bar{\mathbf{C}} + \mathbf{\Omega} \right] \boldsymbol{\eta}_j^r + \bar{\mathbf{F}}_{N,j}^r - \bar{\mathbf{F}}_j^r = 0. \quad (5.26)$$

Eq. (5.25) is a real equation set including the bias terms, whereas Eq. (5.26) is a set of complex equations regarding the r^{th} harmonic of the j^{th} gear mesh frequency. Therefore, a total of $m \times \left(2 \times \left(\sum_{j=1}^{N_m} N_{h,j} \right) + 1 \right)$ real nonlinear equations are solved in order to determine the dynamic response of the drivetrain under investigation.

The system of nonlinear equations is solved by using Newton's Method for the unknown modal coefficient vector,

$$\boldsymbol{\eta} = \left(\boldsymbol{\eta}^0 \quad \boldsymbol{\eta}_1^1 \quad \dots \quad \boldsymbol{\eta}_1^{N_{h,1}} \quad \boldsymbol{\eta}_2^1 \quad \dots \quad \boldsymbol{\eta}_2^{N_{h,2}} \quad \dots \quad \boldsymbol{\eta}_{N_m}^1 \quad \dots \quad \boldsymbol{\eta}_{N_m}^{N_{h,N_m}} \right)^T.$$

Furthermore, arc-length continuation is employed in order to trace the solution path even it changes its direction. Details of Newton's method with arc-length continuation can be found in [63–65]. The initial guess for the first solution point is obtained from the solution of the corresponding linear drivetrain. Then, the initial guess for the subsequent

solution points are estimated by using tangent predictor since the Jacobian at the previous solution point is available.

There are phase differences between gear meshes in multi-mesh, multi-stage geared systems. The static transmission error at the q^{th} mesh in the system can be defined in Fourier series form as

$$e_{m(q)}(t) = \sum_{l=1}^L E_{m(q)}^l \sin(l\omega_q t + \alpha_q^l + l\Pi_q), \quad (5.27)$$

where $E_{m(q)}^l$ and α_q^l represent the l^{th} harmonic amplitude and phase angle of the static transmission error at the q^{th} mesh, respectively. ω_q denotes the gear mesh frequency of the q^{th} mesh. Considering that all the gear meshes have the same tooth profile modifications results in $\alpha_1^l = \alpha_2^l = \dots = \alpha_q^l$. The other phase angle Π_q represents the phase difference between $e_{m(q)}(t)$ and $e_{m(1)}(t)$ where $\Pi_1 = 0$. Π_q ($q = 2$ to N_m) can be defined as

$$\Pi_q = \sum_{j=2}^q \bar{\Pi}_j, \quad (5.28)$$

where $\bar{\Pi}_q$ is the phase difference between $e_{m(q)}(t)$ and the previous excitation $e_{m(q-1)}(t)$ and it can be calculated as

$$\bar{\Pi}_j = Z(\varphi_j - \beta_j) + \pi, \quad (5.29)$$

where Z represents the number of teeth of the driver gear in the j^{th} mesh and φ_j is the angle between the vectors directed to the effective mesh points of j^{th} and $(j-1)^{\text{th}}$ meshes (see Fig. 5.5 and Fig. 5.6). β_j represents the angle between the reference teeth of the gears mounted on the same shaft, which is shown in Fig. 5.6.

The mesh stiffness functions of the gear meshes have the same phase relationship with each other. Furthermore, the mesh stiffness and static transmission error of each individual gear mesh are considered to be out-of-phase. The mesh stiffness at the q^{th} mesh in the system is written in Fourier series form as follows

$$k_{m(q)}(t) = K_{m(q)}^0 + \sum_{h=1}^H K_{m(q)}^h \sin(h\omega_q t + \alpha_q^h + h\Pi_q + \pi), \quad (5.30)$$

where $K_{m(q)}^0$ and $K_{m(q)}^h$ are the mean value and h^{th} harmonic amplitude of the mesh stiffness of the q^{th} mesh, respectively.

5.3 Results and Discussion

A drivetrain composed of spur, helical and spiral bevel gears having the parameters given in Table 5.1 is considered as the example case. Since intentional modifications of tooth profiles make it possible to adjust the static transmission error, only the first harmonics of the static transmission error functions for all gear meshes are considered in this study. The spectral content of the mesh stiffness mainly depends on the operating contact ratio and the first harmonic is usually dominant especially for medium-to-heavy load range. Therefore, the mesh stiffness functions for all gear meshes are assumed to consist of only the first harmonics in this study. The mesh stiffness and static transmission errors for the gear meshes are shown in Fig. 5.7. Moreover, external torque values are assumed to be constant.

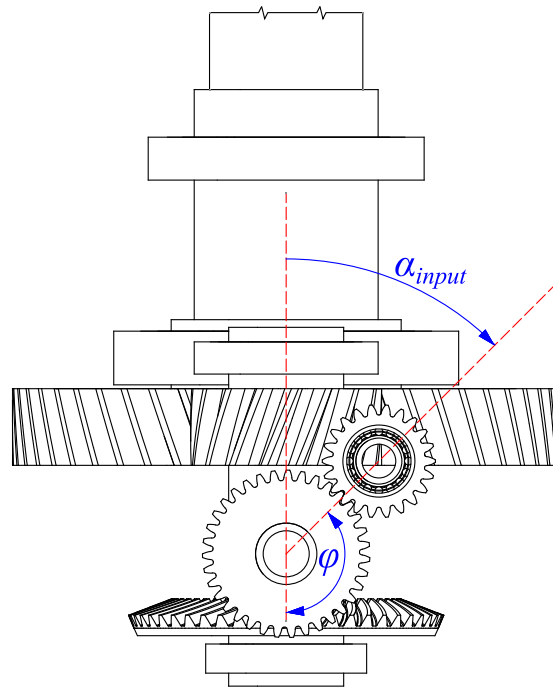


Fig. 5.5 Orientation of the input spur pinion, α_{input} , and angle between the vectors directed to the effective mesh points, φ

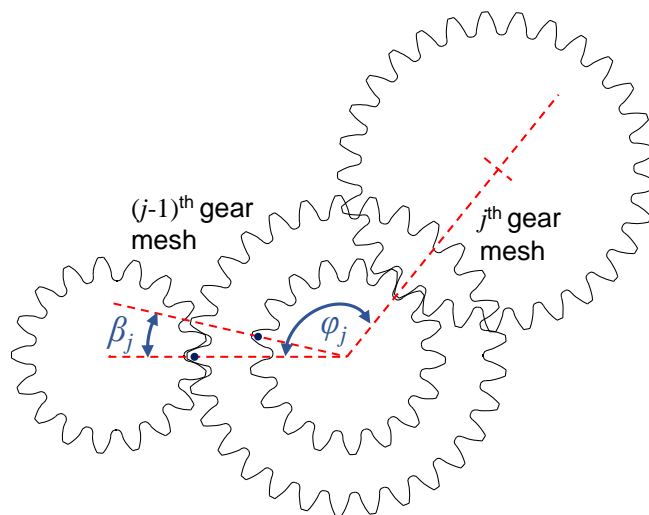


Fig. 5.6 Angle between the reference teeth of the gears mounted on the same shaft, β_j , and angle between the vectors directed to the effective mesh points, φ

Table 5.1 Parameters of the example drivetrain

<i>Shaft Parameters</i>												
Segment	Shaft 1			Shaft 2			Shaft 3			Shaft 4		
	OD	ID	L	OD	ID	L	OD	ID	L	OD	ID	L
1	30	22	70	40	30	135	75	58	234	150	80	95
2										120	80	150
3										100	80	200
Damping ratio ζ							0.04					
<i>Gear Parameters</i>												
	Spur Pinion	Spur Gear	Bevel Pinion	Bevel Gear	Helical Pinion	Helical Gear						
Number of teeth	22	35	21	51	17	52						
Helix/Spiral angle (°)	0	0	27	27	20	20						
Normal pressure angle (°)	20	20	20	20	20	20						
Pitch angle (°)	0	0	22.38	67.62	0	0						
Pitch diameter (mm)	66	105	84	204	112.55	344.26						
Face width (mm)	22	22	30	30	50	50						
Hand	-	-	Left	Right	Right	Left						
Locations (mm) ^a	44	24	100	50	169	25						
T (Nm)	70	0	0	0	0	-827.27						
<i>Bearing Parameters</i>												
	Shaft 1		Shaft 2		Shaft 3		Shaft 4					
	B1	B2	B1	B2	B1	B2	B1	B2				
Locations (mm) ^a	25	62	64	124	18	214	70	200				
\mathbf{k}_b (N/m, Nm/rad)	$Diag[2(10^9), 2(10^9), 1(10^9), 1(10^6), 1(10^6), 0]$											
<i>Gear Mesh Parameters</i>												
	Mesh 1		Mesh 2		Mesh 3							
$K_{m(q)}^0, K_{m(q)}^1$ (N/m)	290e6, 91e6		310e6, 44e6		750e6, 35e6							
c_m (Ns/m)	2900		3100		7500							
$E_{m(q)}^1$ (μm)	15		9		3							
b (μm)	40		40		40							

^a Distance from the end of shaft in the positive z direction of local shaft coordinate system (Fig. 5.2)

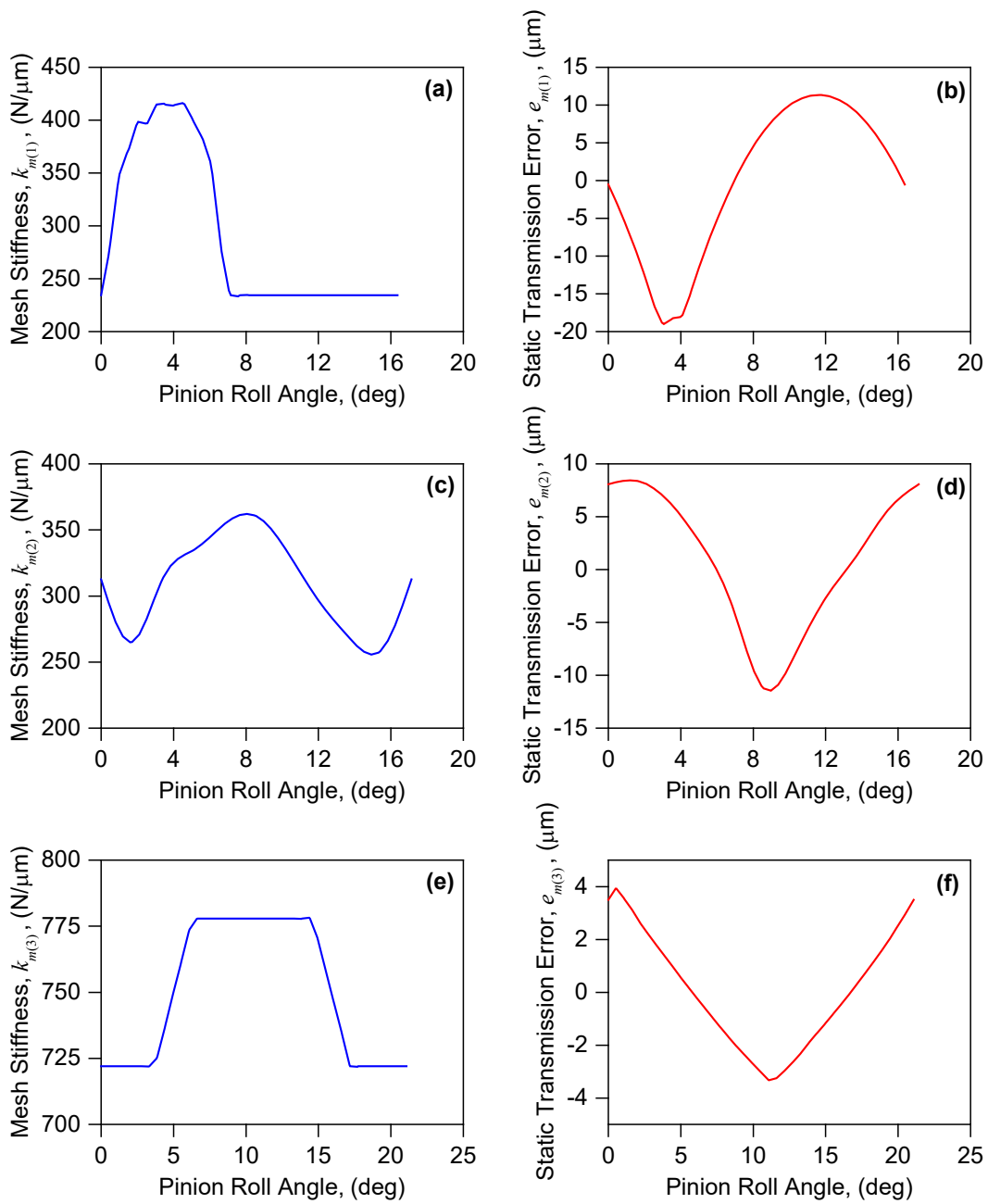


Fig. 5.7 Mesh stiffness and static transmission error, **(a-b)** 1st mesh (spur gear) [58], **(c-d)** 2nd mesh (spiral bevel gear) [69], **(e-f)** 3rd mesh (helical gear) [58]

The interactions between the two gear meshes depend on the ratio of the mesh frequencies. An integer mesh frequency ratio results in significant mesh interactions, whereas there are minimal mesh interactions in the case of a mesh frequency ratio that is not an integer [31]. Accordingly, the number of teeth of the gears in this study are determined so that the mesh frequencies, ω_1, ω_2 and ω_3 , are proportional to 5, 3 and 1, respectively, in order to have strong interactions between the meshes. With the number of teeth determined and $\beta_j = 0$ ($j = 2, 3$), the phase differences between the meshes are calculated as 0 so that all the meshes are in phase.

Firstly, the undamped natural frequencies of the corresponding linear time-invariant system obtained by the Timoshenko beam FEM model used in this study are compared with those obtained by commercial FEM software ANSYS® [66] in Table 5.2. The results demonstrates that the finite element modeling of shaft-bearing assembly including the gear blanks and the mesh couplings is achieved in very good agreement with the finite element software.

The steady-state solutions obtained by HBM utilizing two harmonics for each mesh frequency ($N_{h,j} = 2, j = 1, 2, 3$) are then compared with the solutions obtained by direct numerical integration (NI). Considering that the minimum gear mesh frequency, ω_3 , is the reference frequency, ω , a total of six harmonics with the frequencies $\omega, 2\omega, 3\omega, 5\omega, 6\omega$ and 10ω are utilized in HBM. Fig. 5.8 gives the comparison of the root-mean-square (rms) values of the responses in the form of dynamic mesh force, which are calculated as follows:

$$F_{m(q)}^{(rms)} = \left\{ \sum_{j=1}^{N_m} \sum_{r=1}^{N_{h,j}} \left(\frac{F_{m(q),j}^r}{\sqrt{2}} \right)^2 \right\}^{1/2}, \quad (q = 1, 2, 3), \quad (5.31)$$

where $F_{m(q),j}^r$ is the amplitude of the harmonic of the dynamic mesh force, $F_{m(q)}(t)$, at the q^{th} gear mesh with the frequency $r\omega_j$ given by Eq. (5.19).

Table 5.2 Comparison of natural frequencies of linear-time invariant system

Undamped Natural Frequencies			
n	Timoshenko beam FEM (Hz)	ANSYS® Solution (Hz)	Difference (%)
1	0.0	0.0	0.0
2	551.0	554.3	-0.59
3	611.0	619.6	-1.39
4	763.4	761.6	0.23
5	994.3	994.4	0.00
6	1141.4	1162.1	-1.78
7	1147.8	1167.4	-1.68
8	1615.2	1602.8	0.77
9	1744.2	1742.6	0.09
10	1779.7	1778.1	0.09
11	1817.4	1827.0	-0.52
12	1904.2	1900.6	0.19
13	2506.3	2521.4	-0.60
14	2561.9	2566.0	-0.16
15	2776.9	2793.2	-0.58
16	2923.3	2923.3	0.00
17	3802.8	3780.8	0.58
18	3860.0	3828.1	0.83
19	3875.3	3844.1	0.81
20	4002	3999	0.09

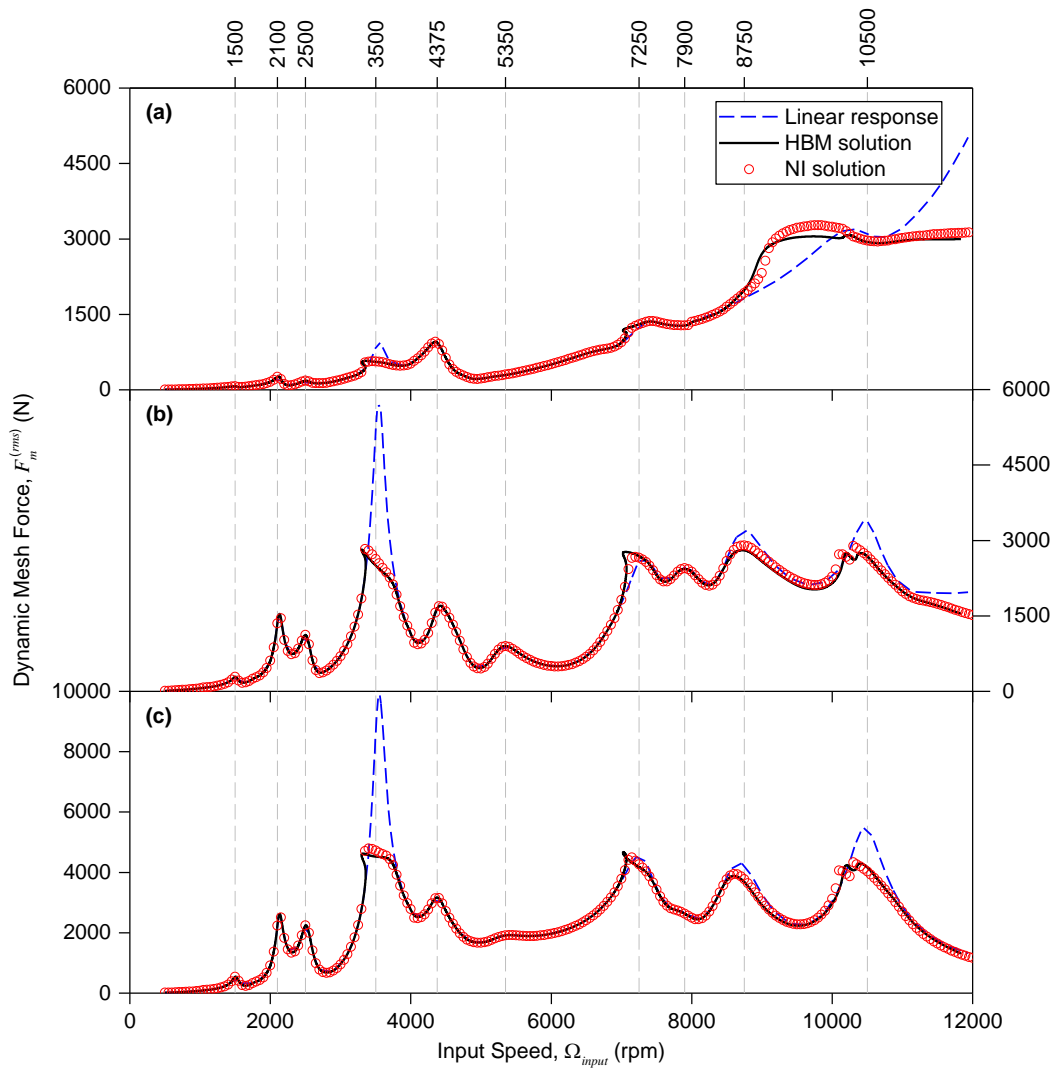


Fig. 5.8 Comparison of rms values of the responses predicted by HBM and NI, **(a)** dynamic mesh force at 1st mesh, $F_{m(1)}^{(rms)}$, **(b)** dynamic mesh force at 2nd mesh, $F_{m(2)}^{(rms)}$, **(c)** dynamic mesh force at 3rd mesh, $F_{m(3)}^{(rms)}$

The linear response of the geared system is also plotted in Fig. 5.8. The resonance peaks observed at $\Omega_{input} = 1500$ rpm, $\Omega_{input} = 2100$ rpm and $\Omega_{input} = 4375$ rpm (shown by vertical dashed lines) in the linear response occur when the gear mesh

frequency of the 1st mesh, ω_{m1} , is equal to the 2nd, the 4th and the 8th natural frequencies of the corresponding linear system, respectively. Furthermore, the 2nd gear mesh excites the 2nd, the 4th, the 7th, the 8th, the 9th and the 12th mode shapes of the corresponding linear system around the resonance peaks observed at $\Omega_{input} = 2500$ rpm, $\Omega_{input} = 3500$ rpm, $\Omega_{input} = 5350$ rpm, $\Omega_{input} = 7250$ rpm, $\Omega_{input} = 7900$ rpm and $\Omega_{input} = 8750$ rpm, respectively. Finally, the 4th natural frequency of the linear drivetrain is excited by the 3rd gear mesh around the resonance peak observed at $\Omega_{input} = 10500$ rpm occur.

It can be observed from Fig. 5.8 that HBM and NI solutions are in very good agreement except the input speed range between 9000 rpm and 12000 rpm. In this speed range, although dynamic mesh force results at the 2nd and the 3rd gear meshes obtained by HBM and NI agree well, there is a discrepancy between the solutions of two methods for the dynamic mesh force at the 1st gear mesh. This indicates the lack of some harmonics that should be included in the HBM solutions assumed. It is illustrated in Fig. 5.9, which shows the time trace and frequency spectrum of the steady-state portion of the dynamic mesh force at the 1st gear mesh, $F_{m(1)}(t)$, at $\Omega_{input} = 10000$ rpm obtained by NI. The spectral content of the response contains some other harmonics, i.e., 7th, 8th and 15th harmonics, with enough amplitudes to cause discrepancy. Since these harmonics are not included in the assumed solutions, HBM solutions deviate from the solutions obtained by NI.

It is known from past studies that spur [10,11,22,55] and spiral bevel gears [45,54,59–61] can exhibit both single-sided tooth impact (SSI) and double-sided tooth impact (DSI) type nonlinear behaviors depending on the system parameters. On the other hand, dynamic behavior of moderately and heavily loaded helical gears are linear since the static transmission error and parametric excitations due to mesh stiffness fluctuations are relatively small for helical gears [40,41]. However, since

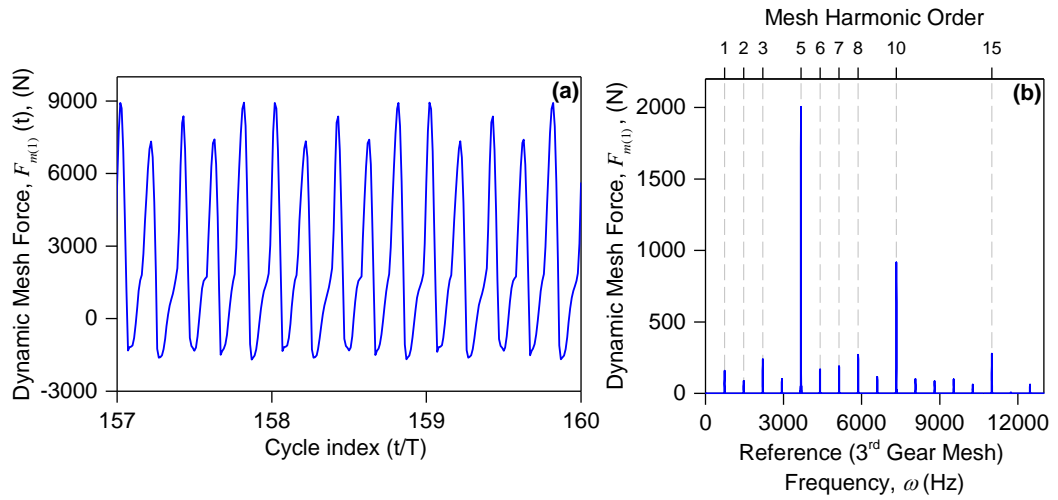


Fig. 5.9 (a) Time trace and (b) frequency spectrum of $F_{m(1)}(t)$ at $\Omega_{input} = 10000$ rpm predicted by NI

there is no known study that propose a dynamic model of a multi-mesh, multi-stage drivetrain consisting of spur, helical and spiral bevel gears, the effect of interactions between different types of gear meshes on dynamic behavior is an unknown. In this study, similar nonlinear responses are seen in both HBM and NI solutions even at the helical gear mesh, which shows the strong interaction between the gear meshes. Focusing on Fig. 5.10, the responses of all the gear pairs are linear with no tooth impacts in the low frequency range. As the input speed increases to $\Omega_{input} = 3358$ rpm, 3rd gear mesh (helical gear pair) begins to exhibit SSI. Tooth separation causes a softening effect in this nonlinear behavior; hence, all the response curves veer left towards the lower frequency range and follow the same path as the speed decreases to $\Omega_{input} = 3299$ rpm. Just before this input speed, tooth separation begins to occur at the 2nd gear mesh (spiral bevel gear pair), too. Then, the response curves take sharp turns towards the right and SSI type nonlinear behaviors at the 2nd and 3rd gear meshes continue. As the input speed increases further, firstly the response at the 2nd

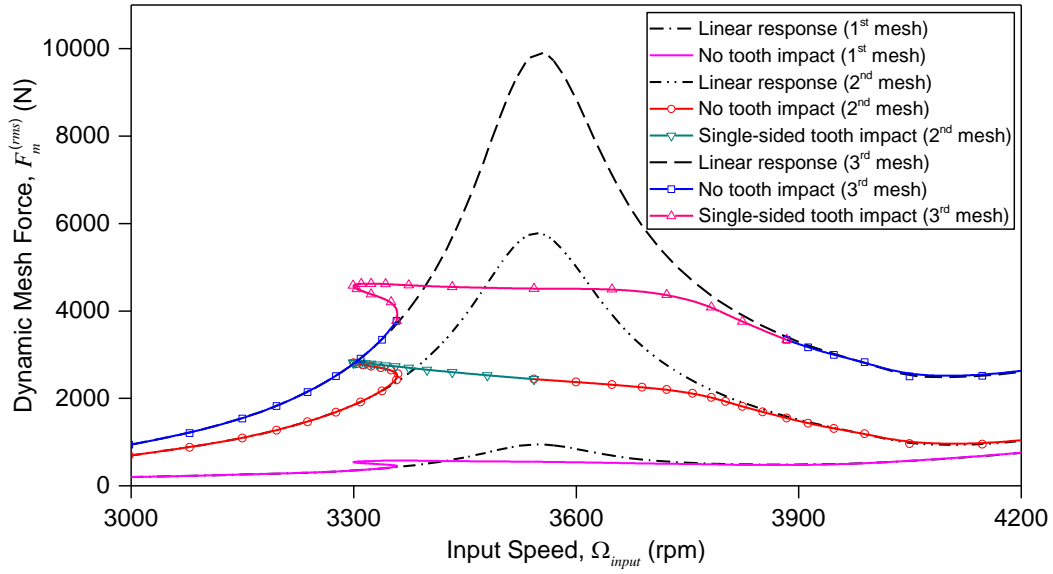


Fig. 5.10 Nonlinear behavior of the drivetrain

gear mesh (at $\Omega_{input} = 3543$ rpm) and then the response at the 3rd gear mesh becomes linear (at $\Omega_{input} = 3884$ rpm). On the other hand, DSI, which includes both tooth separation and impact with the preceding tooth, does not emerge since the backlash amount used in the analysis is large enough to avoid back collision. It should also be noted in Fig. 5.10 that tooth separations or back collisions do not occur at the 1st gear mesh (spur gear pair).

The strong interaction between the gear meshes is illustrated in Fig. 5.11, which shows the amplitudes of the harmonics of dynamic mesh force, $F_m(t)$, at the helical gear mesh (3rd stage) obtained by HBM. It is obvious from the figure that the tooth separations at the helical gear pair in this speed range are mainly due to the vibration induced by the larger static transmission error and parametric excitations consisting of the harmonic with the frequency of 3ω at the spiral bevel gear pair.

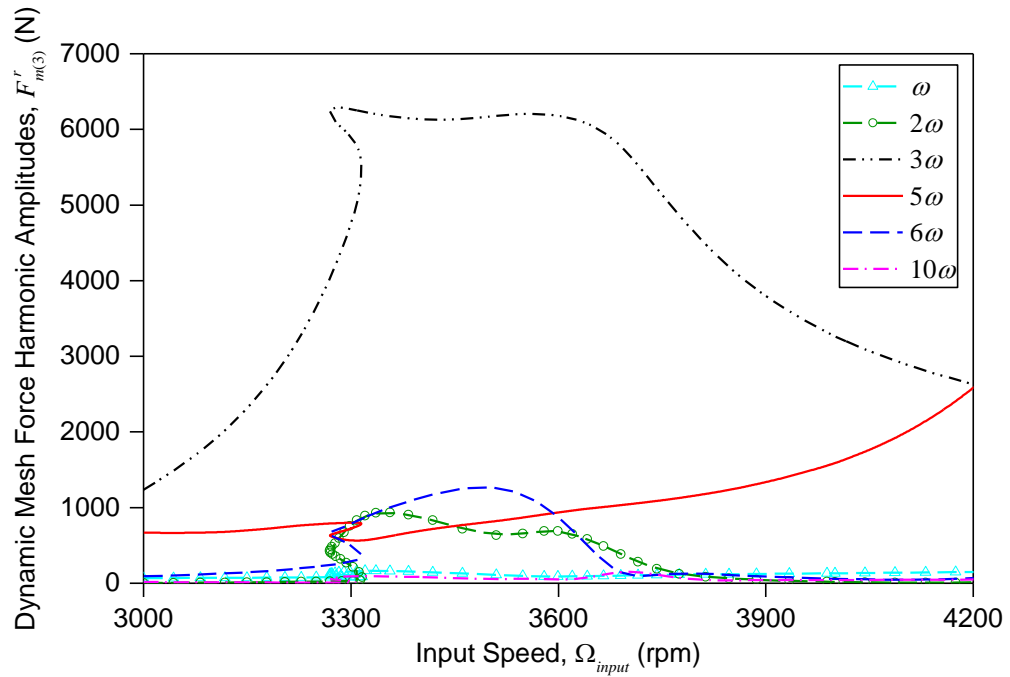


Fig. 5.11 Amplitudes of the harmonics of dynamic mesh force, $F_{m(3)}^r(t)$, at the helical gear mesh (3rd stage) obtained by HBM

Investigating Fig. 5.8 further, SSI also emerges in the vicinity of the other resonance peaks observed at $\Omega_{input} = 7250$ rpm, $\Omega_{input} = 8750$ rpm and $\Omega_{input} = 10500$ rpm (shown by vertical dashed lines). Furthermore, after $\Omega_{input} = 8500$ rpm, the response curve obtained by HBM for the 1st gear mesh begins to deviate significantly from the linear response curve. In this high speed range, the dynamic mesh force at the 1st gear mesh exceeds the static mesh force transmitted; hence, tooth separations occur there. It is also seen from Fig. 5.8 that the responses around the resonance peaks observed at $\Omega_{input} = 1500$ rpm, $\Omega_{input} = 2100$ rpm, $\Omega_{input} = 2500$ rpm, $\Omega_{input} = 4375$ rpm and $\Omega_{input} = 5350$ rpm are completely linear since static mesh forces at all the gear meshes are larger compared to the corresponding dynamic mesh forces. Moreover, there are so many resonance peaks in the responses caused by the

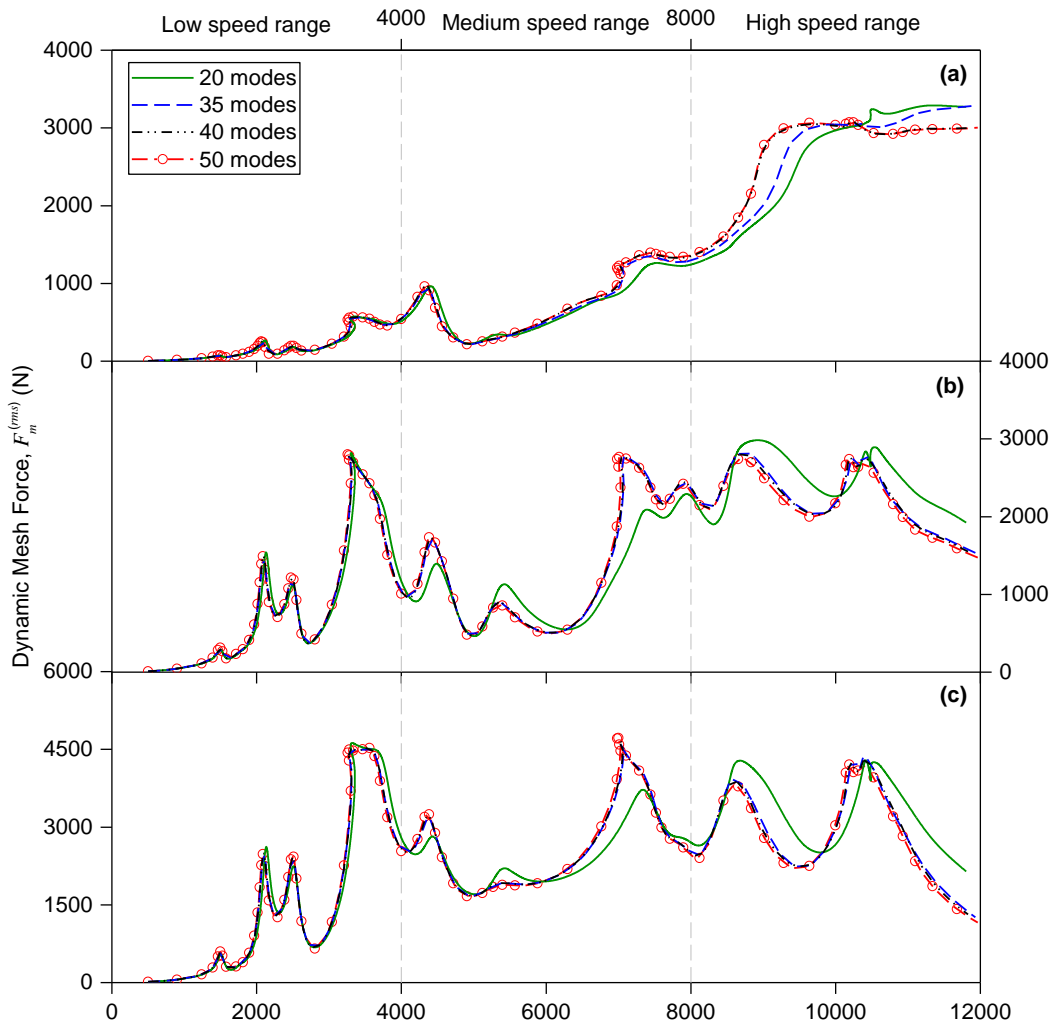


Fig. 5.12 Effect of number of mode shapes utilized in modal superposition method **(a)** $F_{m(1)}^{(rms)}$, **(b)** $F_{m(2)}^{(rms)}$, **(c)** $F_{m(3)}^{(rms)}$

excitations at the gear meshes that super-harmonic resonance peaks, which are common in parametrically excited systems, are not clearly observed here.

The effect of number of mode shapes utilized in the modal superposition method is given in Fig. 5.12. It can be concluded from the figure that the number of modes required in the forced response analysis mainly depends on the frequency range

where the solution is searched. In the low input speed range, i.e., 0-4000 rpm, the responses obtained by utilizing first 20 modes and 50 modes of the corresponding linear system are nearly same; hence, it can be concluded that 20 modes are sufficient to predict the responses quite accurately in this speed range. On the other hand, in the medium speed range, i.e., 4000-8000 rpm, the results obtained by employing the first 35 modes agree well with the results obtained by including the first 50 modes of the linear system. Finally, in the high speed range, i.e., 8000-12000 rpm, the responses at the 2nd and 3rd gear meshes can be accurately predicted by utilizing the first 35 modes, whereas minimum 40 modes are required to obtain the exact response at the 1st gear mesh. Consequently, in this study, the responses are obtained in both HBM and NI by utilizing the first 20, 35 and 40 modes of the linear system in the low, medium and high speed ranges, respectively. Thus, computational time is improved significantly compared to the case in which 40 modes are utilized for the all speed ranges.

The influence of set of harmonics employed in HBM on the response is shown in Fig. 5.13, which compares four different sets of harmonics: (i) five harmonics with the fundamental frequency of ω , (ii) fundamental harmonics of the mesh frequencies, (iii) two harmonics for each mesh frequency, (iv) three harmonics for each mesh frequency. The first case represents the common period rule, according to which the response is periodic with the common period of all the mesh excitations. The common period in this study is $2\pi/\omega$ where ω is the minimum frequency that satisfies $\omega = \omega_j/z_j$ ($j=1,2,3$) and ω_j is the mesh frequency of j^{th} mesh, and the number of harmonics used in the response should not be less than $\max(z_1, z_2, z_3) = 5$. The other three cases are associated with the mesh frequencies and their super-harmonics. It is observed from the figure that the results obtained by using two or three harmonics for each mesh frequency agree well with the results obtained by NI. However, the results obtained by using only fundamental harmonics of the mesh frequencies in the solution deviates from multi-harmonic solutions

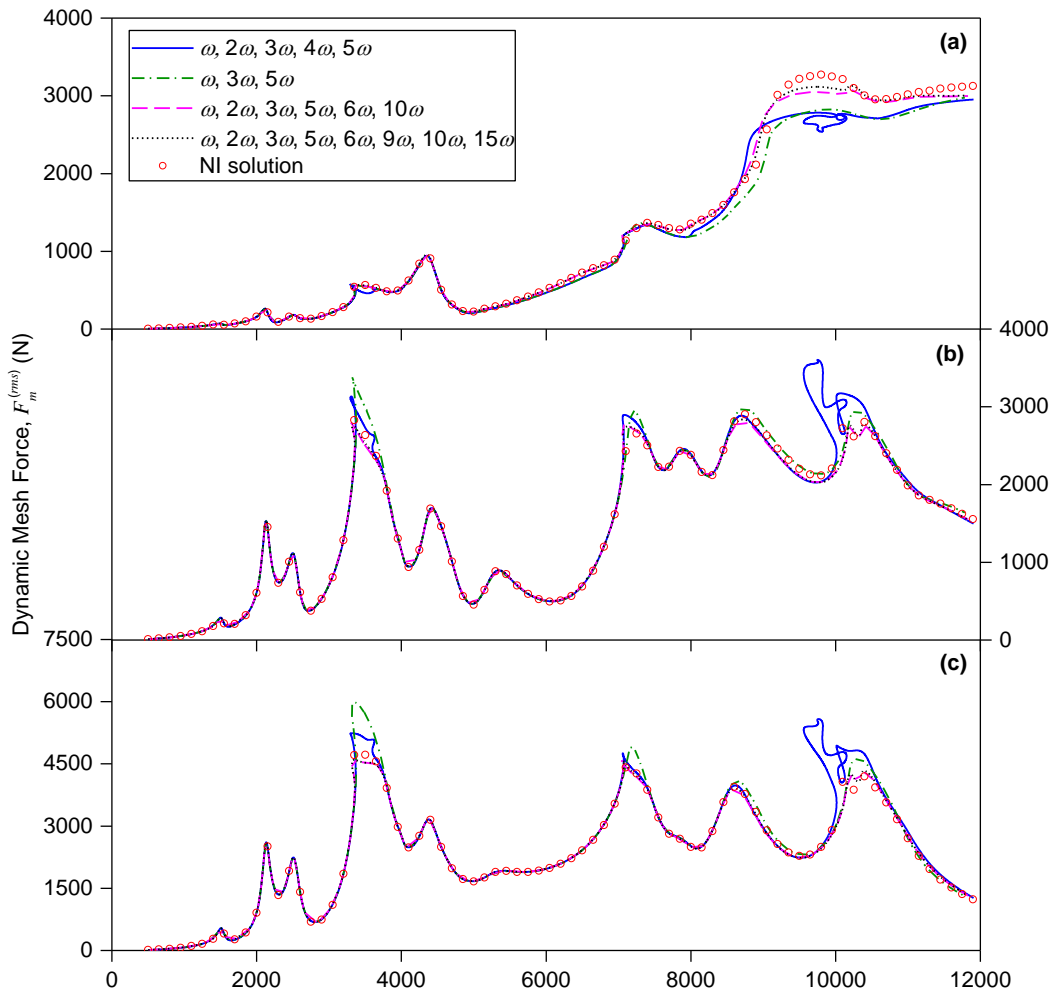


Fig. 5.13 Effect of harmonics employed in HBM (a) $F_{m(1)}^{(rms)}$, (b) $F_{m(2)}^{(rms)}$, (c) $F_{m(3)}^{(rms)}$

significantly in the frequency ranges where separation occurs, since the nonlinear characteristics cannot be captured accurately using single-harmonic. Similarly, there are some inconsistencies in the nonlinear response ranges between the results obtained by utilizing five harmonics with the fundamental frequency of ω and NI compared to the results of the other three cases. Especially, in the vicinity of the resonance peak observed at $\Omega_{input} = 10500$ rpm, some complex nonlinear behaviors, which NI does not predict, begin to emerge in the solution of the first case.

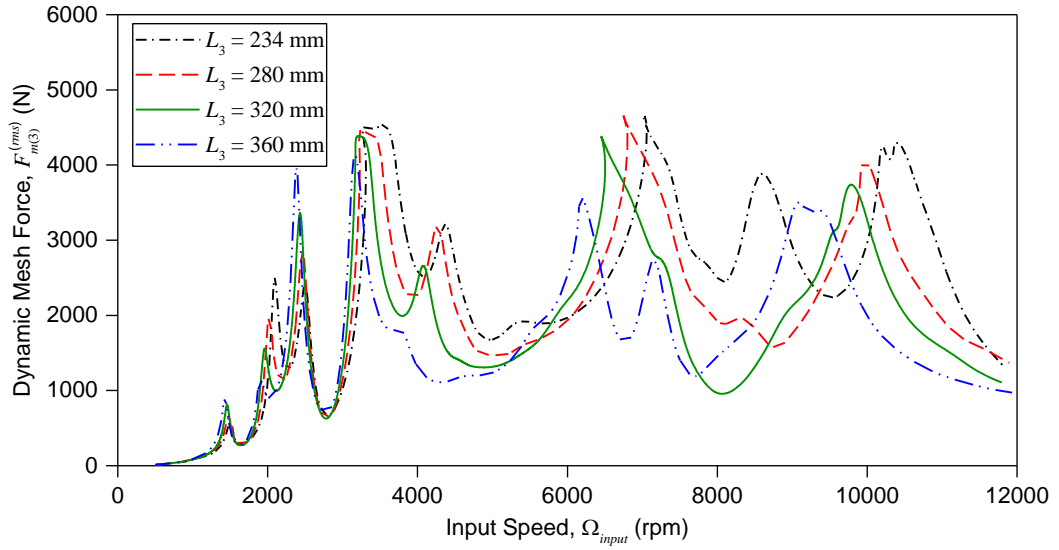


Fig. 5.14 Effect of the length of the third shaft on the dynamic gear mesh force, $F_{m(3)}^{(rms)}$, at the helical gear mesh (3rd stage)

Fig. 5.14 shows the influence of the length of the third shaft, which carries the bevel gear and helical pinion, on dynamic gear mesh force. The length of the shaft is changed incrementally from 234 mm to 360 mm by increasing the length of each shaft segment proportionally. It is evident in the figure that the increase in L_3 causes the resonance peaks to shift to the left, demonstrating that the corresponding natural frequencies decrease. Furthermore, the amplitudes of some peaks increase while those of the others decrease with increasing L_3 . Depending on the change in the peak amplitude, the effect of the nonlinearity around the corresponding peak changes as well. The same effects are observed on the responses of the other gear meshes, $F_{m(1)}^{(rms)}$ and $F_{m(2)}^{(rms)}$, which are shown in Fig. 5.15 and Fig. 5.16, respectively.

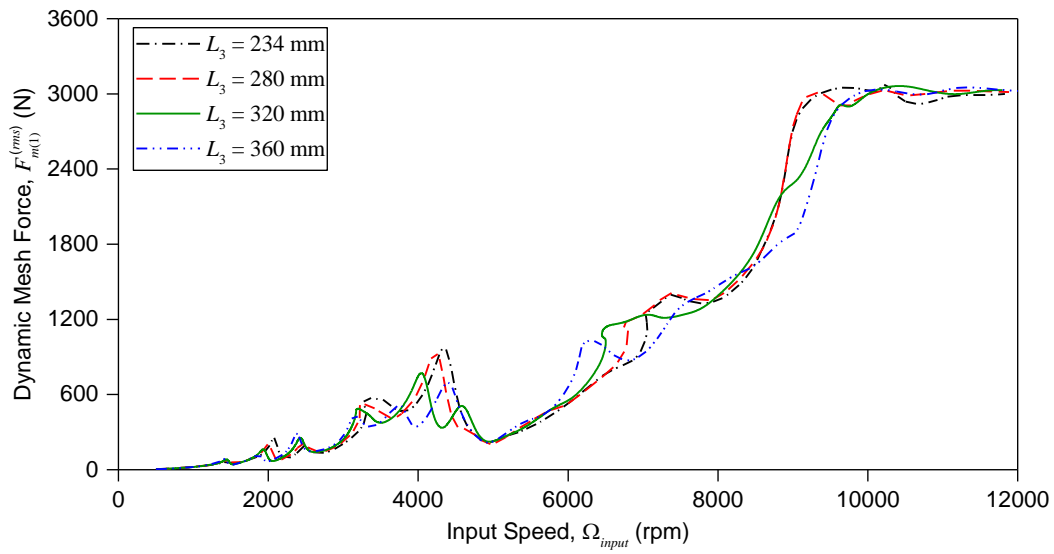


Fig. 5.15 Effect of the length of the third shaft on the dynamic gear mesh force, $F_{m(1)}^{(rms)}$, at the spur gear mesh (1st stage)

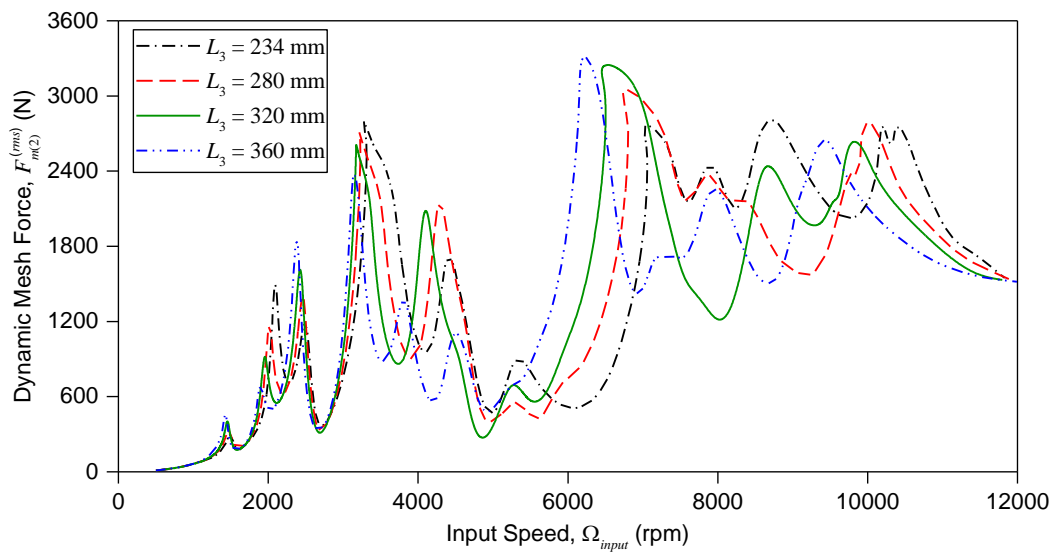


Fig. 5.16 Effect of the length of the third shaft on the dynamic gear mesh force, $F_{m(2)}^{(rms)}$, at the spiral bevel gear mesh (2nd stage)

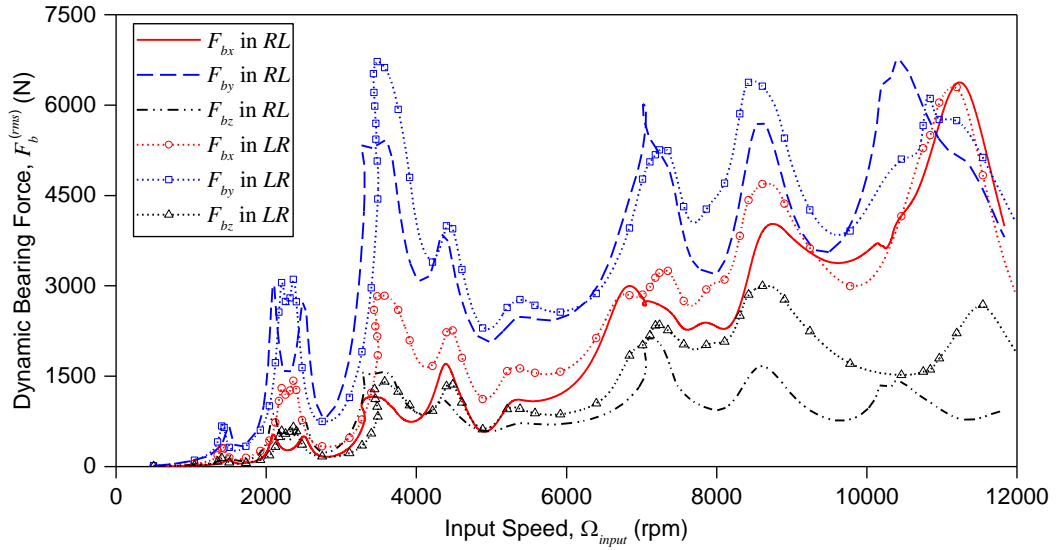


Fig. 5.17 Effect of gear hand configurations of helical gears on dynamic bearing forces, $F_b^{(rms)}$, of bearing 3B (shown in Fig. 5.2)

The effect of the hand of the helical gears on the dynamic bearing forces, $F_b^{(rms)}$, are illustrated in Fig. 5.17. Here, each force component is calculated by the multiplication of the corresponding component of the bearing stiffness and the amplitude of the response of the bearing location in the corresponding direction. The hands of the helical gears considered here are *RL* and *LR*. For instance, *RL* denotes a right-hand helical pinion and left-hand helical gear. In Fig. 5.17, the effect of the gear hand on the resonance peak amplitudes of F_{bx} , F_{by} and F_{bz} of the bearing 3B is quite significant. Furthermore, the alteration in the gear hand configurations cause some changes in the natural frequencies of the drivetrain. Similarly, the amplitudes of the bending moments, $F_{b\theta_x}$ and $F_{b\theta_y}$, of the same bearing is affected significantly by the hand of the gears as well. Moreover, the dynamic forces of the bearings 3A, 4A and 4B is very sensitive to the gear hand configurations, whereas the dynamic forces of the other bearings is not affected considerably. For brevity, the results of

the other bearings are not given here. It is also noted that the hand of the spiral bevel gears are held as *LR* in this analysis since the concave flank of the spiral bevel pinion is the drive side in a normal operation. An alteration in the gear hand configurations of the spiral bevel gears requires the rotation directions of the gears to be reversed. It is observed that the response of the geared system having *RL* and *LR* configurations for the spiral bevel and helical gears, respectively, is exactly the same as that of the geared system with *LR* and *RL* configurations for the bevel and helical gears, whose rotation directions are reversed. This is also not shown here for brevity.

Fig. 5.18 illustrates the change in the dynamic bearing force, $F_{by}^{(rms)}$, of the bearing 2A as a function of the orientation of the input spur pinion, α_{input} (see Fig. 5.5). Here, α_{input} is varied from -51.43 to 102.86 degrees incrementally. The particular α_{input} values are chosen such that the phase angles between the gear meshes are not influenced by α_{input} according to Eq. (5.28). It is observed from the figure that the resonance peak amplitudes of F_{by} of the bearing 2A change significantly, whereas the natural frequencies change slightly. F_{by} reaches its maximum when $\alpha_{input} = 0$ deg and its minimum when $\alpha_{input} = 102.86$ deg. Similarly, F_{bx} is also influenced significantly. On the other hand, F_{bz} is not affected considerably by α_{input} , which is shown in Fig. 5.19. The similar effects are also observed at the bearings 1A, 1B and 2B while the remaining bearings are influenced very slightly by the orientation of the input spur pinion. These observations are not shown here for brevity.

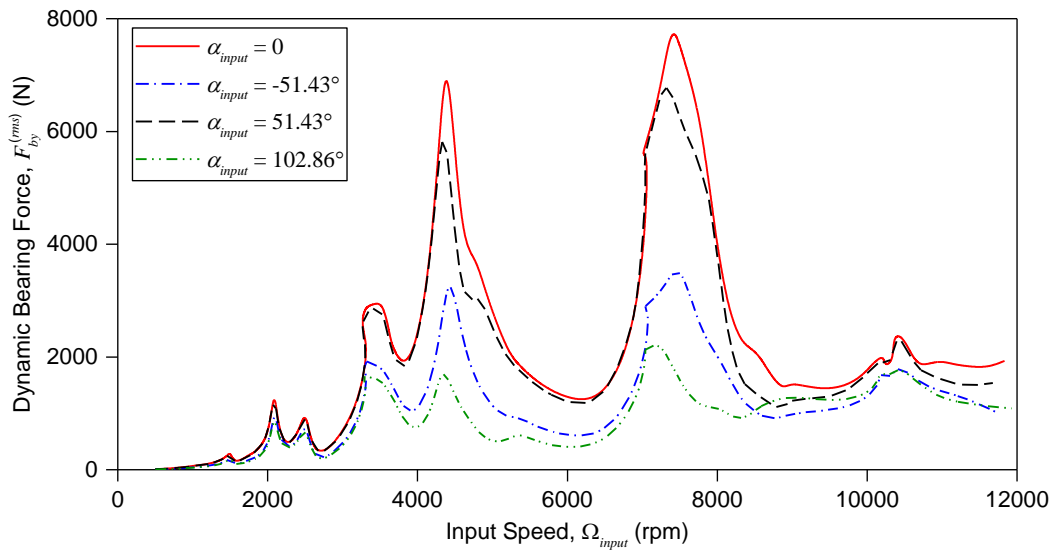


Fig. 5.18 Effect of orientation of input spur pinion, α_{input} , on dynamic bearing force, $F_{by}^{(rms)}$, of bearing 2A (shown in Fig. 5.2)

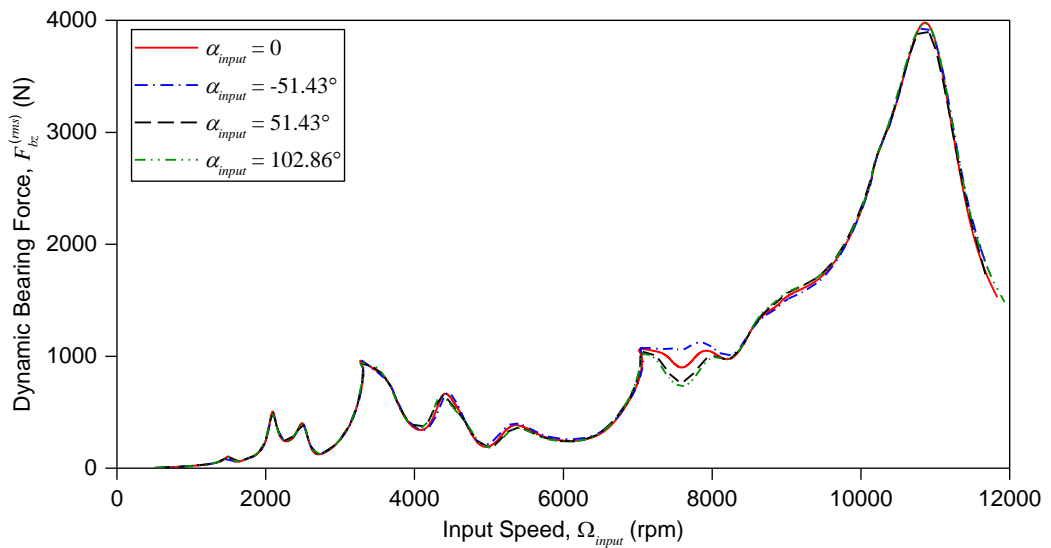


Fig. 5.19 Effect of orientation of input spur pinion, α_{input} , on dynamic bearing force, $F_{bz}^{(rms)}$, of bearing 2A (shown in Fig. 5.2)

Fig. 5.20 shows the change in the dynamic mesh force at the 3rd mesh, $F_{m(3)}^{(rms)}$, when the bending stiffness coefficients of all bearings in the system, $k_{b\theta_x} = k_{b\theta_y}$, are changed equally. It can be noticed that the increase in $k_{b\theta_x} = k_{b\theta_y}$ causes the resonance frequencies to shift to the right. Moreover, the peak amplitudes are influenced differently; that is, some peak amplitudes decrease, whereas the others increase with increasing $k_{b\theta_x} = k_{b\theta_y}$. The nonlinearity of the response are affected by the change in the peak amplitude as well. The same effects are also observed on the dynamic responses of the other gear meshes, $F_{m(1)}^{(rms)}$ and $F_{m(2)}^{(rms)}$, which are shown in Fig. 5.21 and Fig. 5.22, respectively. On the other hand, while the amplitudes of the dynamic bearing forces in the axial and radial directions are not very sensitive to the value of $k_{b\theta_x} = k_{b\theta_y}$, the amplitudes of the dynamic bending moments at the bearings, $M_{bx} = k_{b\theta_x} \theta_{bx}$ and $M_{by} = k_{b\theta_y} \theta_{by}$ are affected drastically. The dynamic bearing forces are not shown here for brevity.

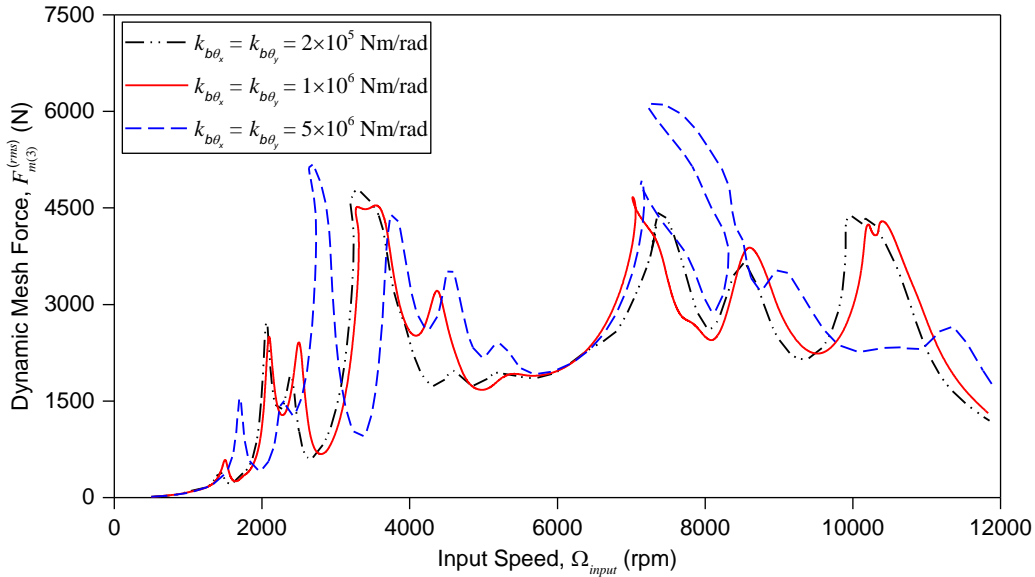


Fig. 5.20 Effect of bearing stiffness coefficients, $k_{b\theta_x} = k_{b\theta_y}$, on $F_{m(3)}^{(rms)}$

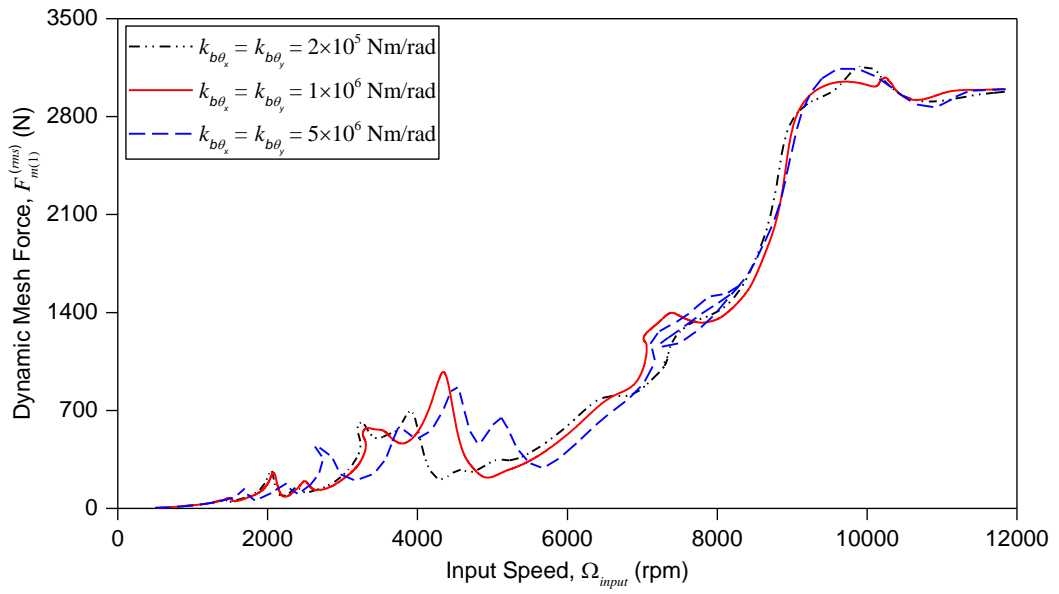


Fig. 5.21 Effect of bearing stiffness coefficients, $k_{b\theta_x} = k_{b\theta_y}$, on the dynamic gear mesh force, $F_{m(1)}^{(rms)}$

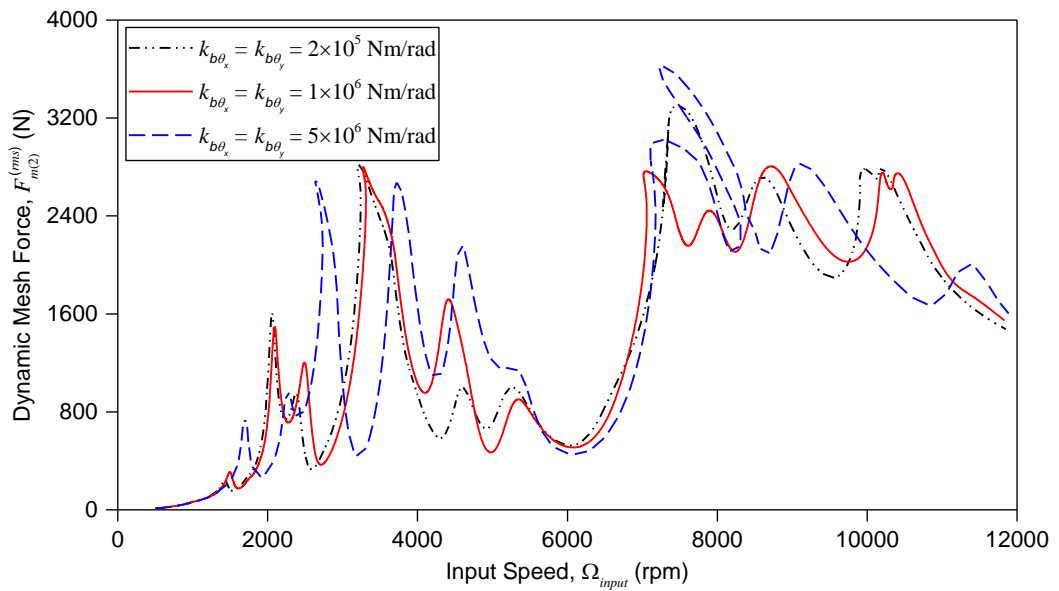


Fig. 5.22 Effect of bearing stiffness coefficients, $k_{b\theta_x} = k_{b\theta_y}$, on the dynamic gear mesh force, $F_{m(2)}^{(rms)}$

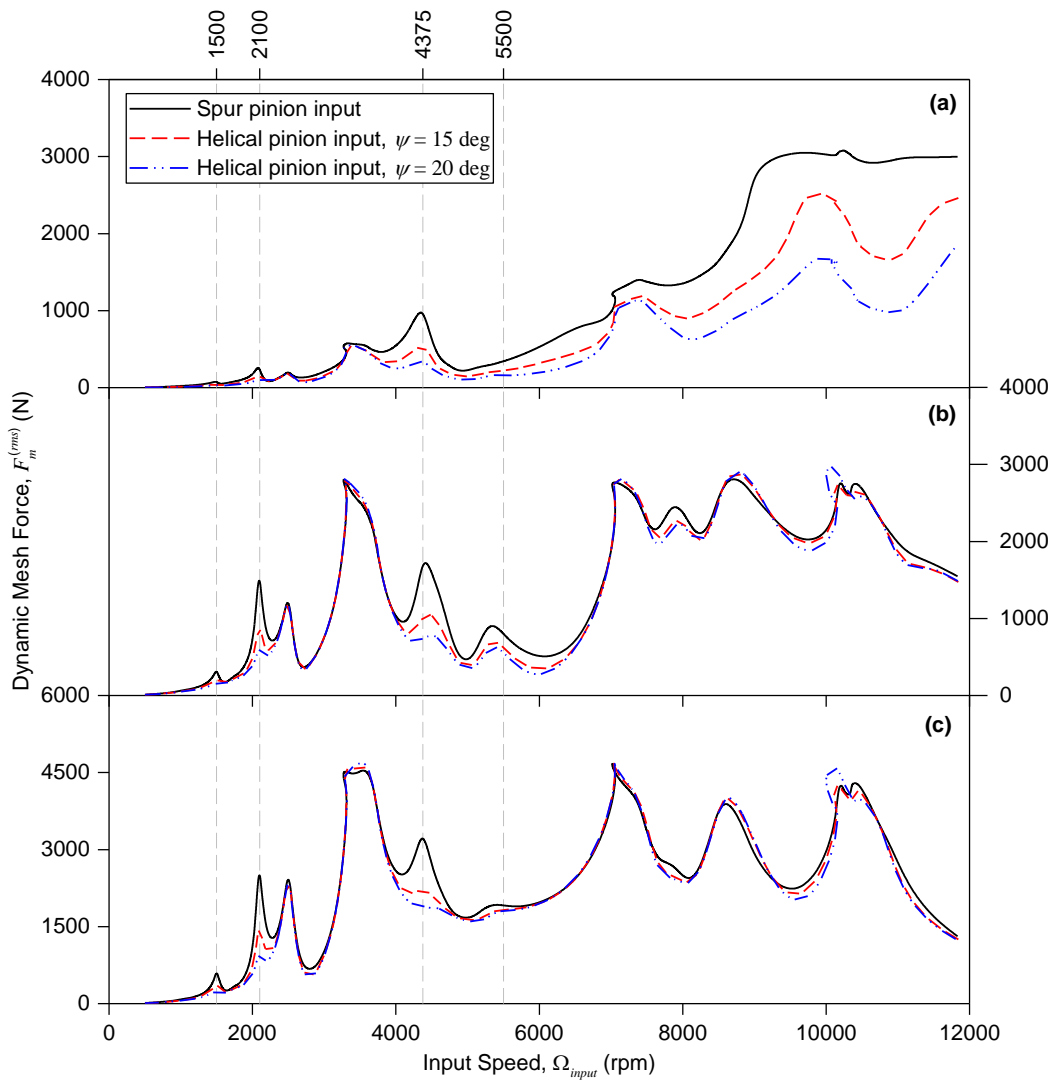


Fig. 5.23 Effect of helix angle of input pinion (a) $F_{m(1)}^{(rms)}$, (b) $F_{m(2)}^{(rms)}$, (c) $F_{m(3)}^{(rms)}$

Fig. 5.23 compares the dynamic mesh forces for the cases when the input pinion is a spur gear or a helical gear with increasing helix angle. Static transmission error and fluctuation of mesh stiffness for a helical gear are smaller compared to the ones for a spur gear of the same size. As helix angle is increased, these mesh parameters decrease more. Accordingly, the alternating components of the mesh stiffness

parameters are $91\text{e}6$, $56\text{e}6$ and $18\text{e}6$ N/m (31%, 19% and 6% of the mean values of the corresponding mesh stiffness parameters) for the input spur pinion, helical pinion with $\psi = 15$ deg and helical pinion with $\psi = 20$ deg, respectively. The respective static transmission errors are 15, 8 and 5 μm for the three cases. Consequently, as the helix angle of the input pinion is increased from 0 (spur pinion) to 20 deg., the amplitudes of the resonance peaks observed at $\Omega_{input} = 1500$ rpm, $\Omega_{input} = 2100$ rpm and $\Omega_{input} = 4375$ rpm (shown by vertical dashed lines) decrease since the static transmission error and parametric excitations at the 1st gear mesh, which cause these peaks, decrease. The other resonance peaks of $F_{m(2)}^{(rms)}$ and $F_{m(3)}^{(rms)}$ are affected very slightly. Furthermore, the dynamic mesh force at the 1st gear mesh, $F_{m(1)}^{(rms)}$ decreases significantly after $\Omega_{input} = 5500$ rpm.

5.4 Conclusion

A nonlinear time-varying dynamic model of a multi-stage, multi-mesh drivetrain composed of spur, helical and spiral bevel gears is formulated in this study. Flexibilities of shafts and bearings are included in the dynamic model by the use of finite element modeling. FEM model of shafts are coupled with each other by the mesh model of gear pairs including backlash nonlinearity and fluctuating mesh stiffness. Natural frequencies of the corresponding linear time-invariant system obtained by the developed Timoshenko beam finite element model and commercial finite element software, ANSYS[®], are in very good agreement, which ensures the quality of the FEM utilized in this study. The resulting nonlinear differential equations of motion are transformed to a set of nonlinear algebraic equations by utilizing Harmonic Balance Method (HBM) with multiple harmonics. In contrast with gear dynamics studies using discrete Fourier transform, continuous-time Fourier transform is employed in this study to calculate the Fourier coefficients

required in the HBM. Thus, the convergence problems that arise when the number of nonlinear equations is large are avoided. Furthermore, in order to decrease the computational time, analytical integration is employed rather than numerical integration for the calculation of Fourier coefficients. Since the resulting number of nonlinear algebraic equations is very large due to the finite element modeling of the shafts, these equations are transformed to modal coordinates by using modal superposition method. Thus, the number of nonlinear equations is proportional to the number of modes utilized in the modal superposition, rather than the number of DOFs associated with the nonlinear elements. Consequently, the proposed method decreases the computational time significantly in the dynamic analysis of multi-stage, multi-mesh drivetrains and makes it possible to model gear shafts by using FEM. The resulting nonlinear algebraic equations are solved by the use of Newton's method with arc-length continuation. Direct numerical integration (NI), i.e. a much more computationally demanding method, is used to validate the solutions obtained by HBM and the comparison shows that the solutions obtained by the two methods agree well with each other. It is observed from the results that single-sided tooth impacts occur in the multi-mesh drivetrain under investigation, whereas double-sided tooth impacts do not emerge since the backlash amount used in the analysis is large enough to avoid back collision.

The results show that the strong interactions between the gear meshes cause tooth separations even at the helical gear pair, even though the previous gear dynamics studies claim that the dynamic behavior of helical gears are linear. Moreover, it is observed that the number of modes required in the modal superposition mainly depends on the frequency range where the solution is searched. It is also observed that the results obtained by employing two or three harmonics for each mesh frequency in HBM agree better with the results obtained by NI compared to the results obtained by utilizing the harmonics of the minimum frequency which corresponds to the common period of all the mesh excitations. Several parametric

studies are as well performed and the results in the form of dynamic mesh forces and dynamic bearing forces indicate that a large number of design parameters affects the dynamic behavior of multi-mesh, multi-stage geared system in different levels and ways.

CHAPTER 6

CONCLUSION AND FUTURE WORK

6.1 Conclusion

Vibration and noise are important concerns in drivetrain systems since they are the main cause of fatigue failures of the driveline components. Therefore, analytical evaluation of the dynamics of gear pairs and also full drive train system is vital to design a more silent and durable transmission system. The main goal of this dissertation is to develop a nonlinear dynamic model of a multi-mesh, multi-stage drivetrain composed of both cylindrical gears and bevel gears and to help transmission product design by studying the effect of system parameters on dynamics. In order to achieve this, the following dynamic models are developed:

- Nonlinear time-varying dynamic model of a multi-mesh spur gear train,
- Linear time-invariant dynamic model of a helical geared system,
- Nonlinear time-varying dynamic model of a spiral bevel geared system,
- Nonlinear time-varying dynamic model of a complete drivetrain composed of a spur gear, a helical gear and a spiral bevel gear.

At the first stage of this research, a nonlinear time-varying dynamic model for a multi-mesh spur gear train consisting of three gears and three shafts is formulated. The three DOFs semi-definite system is converted to a two DOFs definite system by defining the relative gear mesh displacements as generalized coordinates. The equations of motion are transformed to dimensionless form. The resulting

dimensionless equations of motion are converted to a set of nonlinear algebraic equations by using multi-term Harmonic Balance Method (HBM) in conjunction with discrete Fourier transform. Then, this set of nonlinear algebraic equations is solved by Newton's method with arc-length continuation. A much more computationally demanding method, i.e. direct numerical integration (NI), is utilized to validate the solutions obtained by HBM. Floquet theory is employed in order to determine the stability of steady-state solutions. It is observed from the results that the multi-mesh gear train exhibits single-sided tooth impact, which is a softening-type nonlinear behavior due to tooth separation. Subharmonic motions are also observed near the frequencies corresponding to the parametric resonances. It is also noted that the number of teeth of the middle gear has a significant effect on dynamic response since it directly determines the phase angle between the gear meshes. Similarly, positions of end gears affect dynamic response considerably.

Tooth separation and back collisions of gears with a strongly nonlinear dynamic behavior are not observed for moderately and heavily loaded helical geared systems. Similarly, mesh stiffness fluctuations of helical gears are much smaller compared to those of spur gears. Therefore, a linear, time-invariant dynamic model of helical gears are presented in Chapter 3. Shaft-bearing structures are modeled by employing Timoshenko beam finite elements and they are coupled with a three-dimensional discrete mesh model. The undamped natural frequencies of some drivetrain configurations, i.e., countershaft arrangement, split-torque and idler arrangements, obtained by Timoshenko beam finite element model (FEM) developed in this study are compared with those obtained by commercial gear analysis software MASTA in order to validate the FEM used. The forced response of an example multi-mesh helical geared system is also obtained and the effect of loading condition on dynamic response is investigated. A shift in the frequency response is observed depending on the phase angle between the gear meshes. The finite element model developed is used in the subsequent chapters.

Considering both backlash nonlinearity and time-varying mesh stiffness, a nonlinear dynamic model of a spiral bevel geared system is considered in Chapter 4. The mesh model of the gear pair is integrated into the Timoshenko beam FEM model of shafts. Both static transmission error excitation and parametric excitations due to fluctuating mesh stiffness are considered. Natural frequencies of the linear system obtained from the developed Timoshenko beam finite element model and commercial finite element software, ANSYS[®], are compared and a good agreement is observed, which ensures the quality of the FEM used in the study. Since the number of resulting nonlinear equations is very large due to the finite element modeling of the shafts, receptance method is introduced to the forced response analysis of geared systems with nonlinearities. In the receptance method, the total DOFs are divided into linear and nonlinear DOFs and only the nonlinear equations related to the DOFs associated with the gear pair, where the nonlinear elements are attached, need to be solved. Thus, it is possible to model gear shafts by using finite element method without increasing the number of nonlinear equations, which drastically decreases the computational time required, and the shaft-bearing dynamic characteristics can be easily taken into account. The resulting nonlinear differential equations are transformed to a nonlinear system of algebraic equations by using multi-term HBM coupled with continuous-time Fourier transform, as opposed to the gear dynamics studies [22,23,27,28,54,55] that utilize discrete Fourier transform. Utilizing continuous-time Fourier transform, the possible convergence problems for the large nonlinear systems can be avoided. Moreover, analytical integration rather than numerical integration is employed for the calculation of Fourier coefficients in order to decrease the computational time. Then, the resulting nonlinear system of algebraic equations is solved by utilizing Newton's method with arc-length continuation.

The results of HBM are verified by comparing them with the results of NI. It is obvious from the results that the solutions obtained by both methods are in good agreement. Several case studies performed show that spiral bevel gear pairs exhibit nonlinear behavior as single-sided and double-sided tooth impacts depending on the system parameters. Subharmonic motions are observed in the solutions obtained by NI. It is also clear in the results that parametric excitations due to fluctuating mesh stiffness increase the response level of the system and severity of nonlinearity. Some super-harmonic resonance peaks due to the parametric excitation are also observed. The effect of backlash amount is studied and it should be noted that there is a potential of loss of contact and tooth impact for lightly loaded cases, for which the gear backlash is the critical factor. It is also clear from the dynamic bearing force results that backlash nonlinearity also affects the bearing forces which are important in the selection of bearings and determination of lives of the bearings used.

Finally, a nonlinear time-varying dynamic model of a multi-mesh, multi-stage drivetrain composed of both cylindrical gears and bevel gears are proposed in Chapter 5. Again, Timoshenko beam finite element modeling is used for shaft-bearing structures. Since the drivetrain consists of multiple gear pairs, receptance method results in a large number of nonlinear equations and large matrices are involved in the solution procedure. Therefore, modal superposition method is introduced to the forced response analysis of multi-stage, multi-mesh gear systems. In this approach, the response of the nonlinear system is approximated by modal superposition using the mode shapes of the linear system. The number of resulting nonlinear equations depends on the number of mode shapes utilized; therefore, it is independent of the number of nonlinear DOFs, i.e., the number of gear meshes. Using multi-term Harmonic Balance Method coupled with continuous-time Fourier transform, the resulting differential equations of motion are transformed to a nonlinear system of algebraic equations. Again, the computational time is decreased considerably by employing analytical integration rather than numerical integration

for the calculation of Fourier coefficients. The resulting nonlinear system of algebraic equations is solved by utilizing Newton's method with arc-length continuation. The results obtained by HBM are compared with those obtained by direct numerical integration and they agree well with each other. Similar nonlinear behaviors are observed in the multi-mesh geared system. The results show that the strong interactions between the gear meshes cause tooth separations even at the helical gear pair, even though the previous gear dynamics studies claim that the dynamic behavior of helical gears are linear. The number of mode shapes required in the modal expansion mainly depends on the frequency range where the solution is searched. It is also noted that the results obtained by employing two or three harmonics for each mesh frequency in HBM agree better with the results obtained by NI compared to the results obtained by utilizing the harmonics of the minimum frequency which corresponds to the common period of all the mesh excitations. Several parametric studies are as well performed and the results in the form of dynamic mesh forces and dynamic bearing forces indicate that a large number of design parameters affects the dynamic behavior of multi-mesh, multi-stage geared system in different levels and ways.

6.2 Future Work

As a future work, based on exact gear geometry, mesh parameters such as mesh stiffness and static transmission error can be generated especially for spiral bevel gear. This reduces the dependency on commercial software. Furthermore, fatigue evaluations of gears based on the output of this research can be developed. The mesh model used in this study can also be extended to include friction based on an elastohydrodynamic lubrication (EHL) formulation in order to study the influence of friction on system dynamics. Moreover, mesh damping model can be improved further and the effect of mesh damping on system dynamics can be investigated.

REFERENCES

- [1] Drago, R. J., 1988, *Fundamentals of Gear Design*, Butterworth Publishers, Stoneham, MA.
- [2] Shigley, J. E., Mischke, C. R., and Budynas, R. G., 2003, *Mechanical Engineering Design*, McGraw-Hill, New York, NY.
- [3] American Gear Manufacturers Association, 2007, *Bevel and Hypoid Gear Geometry*.
- [4] Nice, K., 2000, "How Gears Work" [Online]. Available: <https://science.howstuffworks.com/transport/engines-equipment/gear.htm>. [Accessed: 04-Feb-2018].
- [5] Divedi, H., 2015, "Types of Bevel Gears" [Online]. Available: <http://www.hkdivedi.com/2015/12/types-of-bevel-gears.html>. [Accessed: 04-Feb-2018].
- [6] 2018, "KHK Hypoid Gears" [Online]. Available: <https://www.medital.com/products/hypoid-gears>. [Accessed: 04-Feb-2018].
- [7] Gasparini, G., Motta, N., and Straulino, G., "The ' 035 ' Main GearBox : Strong , Light , Reliable and Silent Heart of the AW139 Helicopter."
- [8] Gmirya, Y., Alulis, M., Palcic, P., and Leigh, L., 2011, "Design and Development of a Modern Transmission : Baseline Configuration of the CH-53K Drive System," 67th Annual Forum of the American Helicopter Society, Virginia Beach, VA.
- [9] Özgüven, H. N., and Houser, D. R., 1988, "Mathematical Models Used in Gear Dynamics—A Review," *J. Sound Vib.*, **121**(3), pp. 383–411.
- [10] Özgüven, H. N., and Houser, D. R., 1988, "Dynamic Analysis of High Speed Gears By Using Loaded Static Transmission Error," *J. Sound Vib.*, **125**(1), pp. 71–83.
- [11] Kahraman, A., and Singh, R., 1990, "Non-linear Dynamics of a Spur Gear Pair," *J. Sound Vib.*, **142**(1), pp. 49–75.
- [12] Amabili, M., and Rivola, A., 1997, "Dynamic Analysis of Spur Gear Pairs:

Steady-State Response and Stability of the SDOF Model with Time-Varying Meshing Damping,” *Mech. Syst. Signal Process.*, **11**(3), pp. 375–390.

- [13] Shen, Y., Yang, S., and Liu, X., 2006, “Nonlinear dynamics of a spur gear pair with time-varying stiffness and backlash based on incremental harmonic balance method,” *Int. J. Mech. Sci.*, **48**, pp. 1256–1263.
- [14] Farshidianfar, A., Moeenfard, H., and Rafsanjani, A., 2008, “Frequency response calculation of non-linear torsional vibration in gear systems,” *Proc. Inst. Mech. Eng. Part K J. Multi-body Dyn.*, **222**(1), pp. 49–60.
- [15] Kahraman, A., and Singh, R., 1991, “Non-linear Dynamics of a Geared Rotor-Bearing System with Multiple Clearances,” *J. Sound Vib.*, **144**(3), pp. 469–506.
- [16] Kahraman, A., and Singh, R., 1991, “Interactions Between Time-Varying Mesh Stiffness and Clearance Non-linearities in a Geared System,” *J. Sound Vib.*, **146**(1), pp. 135–156.
- [17] Özgüven, H. N., 1991, “A Non-Linear Mathematical Model for Dynamic Analysis of Spur Gears Including Shaft and Bearing Dynamics,” *J. Sound Vib.*, **145**(2), pp. 239–260.
- [18] Kahraman, A., Özgüven, H. N., Houser, D. R., and Zakrajsek, J. J., 1992, “Dynamic Analysis of Geared Rotors by Finite Elements,” *J. Mech. Des.*, **114**(September), pp. 507–514.
- [19] Maliha, R., Doğruer, C. U., and Ozguven, H. N., 2004, “Nonlinear Dynamic Modeling of Gear-Shaft-Disk-Bearing Systems Using Finite Elements and Describing Functions,” *J. Mech. Des.*, **126**, pp. 534–541.
- [20] Gürkan, N. E., 2005, “Non-linear Mathematical Modeling of Gear Rotor Bearing Systems Including Bearing Clearance,” Middle East Technical University, M.S. Thesis.
- [21] Gürkan, N. E., and Ozguven, H. N., 2007, “Interactions Between Backlash and Bearing Clearance Nonlinearity in Geared Flexible Rotors,” *Proceedings of IDETC/PTG 2007 ASME International Design Engineering Technical Conferences and ASME International Power Transmission and Gearing Conference*, Las Vegas, Nevada.
- [22] Kahraman, A., and Blankenship, G. W., 1995, “Steady state forced response of a mechanical oscillator with combined parametric excitation and clearance type non-linearity,” *J. Sound Vib.*, **185**(5), pp. 743–765.

- [23] Kahraman, A., and Blankenship, G. W., 1996, "Interactions Between Commensurate Parametric and Forcing Excitations in a System with Clearance," *J. Sound Vib.*, **194**(3), pp. 317–336.
- [24] Kahraman, A., and Blankenship, G. W., 1997, "Experiments on Nonlinear Dynamic Behavior of an Oscillator With Clearance and Periodically Time-Varying Parameters," *J. Appl. Mech.*, **64**, pp. 217–226.
- [25] Ma, Q., and Kahraman, A., 2005, "Period-one motions of a mechanical oscillator with periodically time-varying, piecewise-nonlinear stiffness," *J. Sound Vib.*, **284**, pp. 893–914.
- [26] Ma, Q., and Kahraman, A., 2006, "Subharmonic resonances of a mechanical oscillator with periodically time-varying, piecewise-nonlinear stiffness," *J. Sound Vib.*, **294**(3), pp. 624–636.
- [27] Al-shyyab, A., and Kahraman, A., 2005, "Non-linear dynamic analysis of a multi-mesh gear train using multi-term harmonic balance method: period-one motions," *J. Sound Vib.*, **284**, pp. 151–172.
- [28] Al-shyyab, A., and Kahraman, A., 2005, "Non-linear dynamic analysis of a multi-mesh gear train using multi-term harmonic balance method: subharmonic motions," *J. Sound Vib.*, **279**, pp. 417–451.
- [29] Al-Shhyab, A., and Kahraman, A., 2007, "A Nonlinear Torsional Dynamic Model of Multi-Mesh Gear Trains Having Flexible Shafts," *JJMIE*, **1**(1), pp. 31–41.
- [30] Liu, G., and Parker, R. G., 2008, "Nonlinear dynamics of idler gear systems," *Nonlinear Dyn.*, **53**(4), pp. 345–367.
- [31] Liu, G., and Parker, R. G., 2012, "Nonlinear, parametrically excited dynamics of two-stage spur gear trains with mesh stiffness fluctuation," *Proc. Inst. Mech. Eng. Part C J. Mech. Eng. Sci.*, **226**(8), pp. 1939–1957.
- [32] Al-shyyab, A., and Kahraman, A., 2007, "A non-linear dynamic model for planetary gear sets," *Proc. Inst. Mech. Eng. Part K J. Multi-body Dyn.*, **221**(4), pp. 567–576.
- [33] Vaishya, M., and Singh, R., 2001, "Analysis of Periodically Varying Gear Mesh Systems With Coulomb Friction Using Floquet Theory," *J. Sound Vib.*, **243**(3), pp. 525–545.
- [34] Vaishya, M., and Singh, R., 2001, "Sliding Friction-Induced Non-linearity and Parametric Effects in Gear Dynamics," *J. Sound Vib.*, **248**(4), pp. 671–

- [35] Kahraman, A., Lim, J., and Ding, H., 2007, "A Dynamic Model of a Spur Gear Pair with Friction," 12th IFToMM World Congress, Besançon, France.
- [36] He, S., Gunda, R., and Singh, R., 2007, "Effect of sliding friction on the dynamics of spur gear pair with realistic time-varying stiffness," *J. Sound Vib.*, **301**(3–5), pp. 927–949.
- [37] Liu, G., and Parker, R. G., 2009, "Impact of tooth friction and its bending effect on gear dynamics," *J. Sound Vib.*, **320**(4–5), pp. 1039–1063.
- [38] Xu, H., Kahraman, A., Anderson, N. E., and Maddock, D. G., 2007, "Prediction of Mechanical Efficiency of Parallel-Axis Gear Pairs," *J. Mech. Des.*, **129**(1), pp. 58–68.
- [39] Kahraman, A., 1993, "Effect of Axial Vibrations on the Dynamics of a Helical Gear Pair," *J. Vib. Acoust.*, **115**, pp. 33–39.
- [40] Kahraman, A., 1994, "Dynamic Analysis of a Multi-Mesh Helical Gear Train," *J. Mech. Des.*, **116**, pp. 706–712.
- [41] Kubur, M., Kahraman, A., Zini, D. M., and Kienzle, K., 2004, "Dynamic Analysis of a Multi-Shaft Helical Gear Transmission by Finite Elements: Model and Experiment," *J. Vib. Acoust.*, **126**(3), pp. 398–406.
- [42] Sondkar, P., and Kahraman, A., 2013, "A dynamic model of a double-helical planetary gear set," *Mech. Mach. Theory*, **70**, pp. 157–174.
- [43] Li, M., Hu, H. Y., Jiang, P. L., and Yu, L., 2002, "Coupled Axial–Lateral–Torsional Dynamics of a Rotor–Bearing System Geared By Spur Bevel Gears," *J. Sound Vib.*, **254**(3), pp. 427–446.
- [44] Li, M., and Hu, H. Y., 2003, "Dynamic Analysis of a Spiral Bevel-Geared Rotor-Bearing System," *J. Sound Vib.*, **259**(3), pp. 605–624.
- [45] Wang, J., Lim, T. C., and Li, M., 2007, "Dynamics of a hypoid gear pair considering the effects of time-varying mesh parameters and backlash nonlinearity," *J. Sound Vib.*, **308**, pp. 302–329.
- [46] Yinong, L., Guiyan, L., and Ling, Z., 2010, "Influence of Asymmetric Mesh Stiffness on Dynamics of Spiral Bevel Gear Transmission System," *Math. Probl. Eng.*, **2010**, pp. 1–13.
- [47] Peng, T., 2010, "Coupled Multi-body Dynamic and Vibration Analysis of

Hypoid and Bevel Geared Rotor System. Dissertation, University of Cincinnati.”

- [48] Yang, J., 2012, “Nonlinear Dynamics of Driveline Systems with Hypoid Gear Pair,” University of Cincinnati, PhD. Dissertation.
- [49] Hua, X., Lim, T. C., Peng, T., and Wali, W. E., 2012, “Dynamic Analysis of Spiral Bevel Geared Rotor Systems Applying Finite Elements and Enhanced Lumped Parameters,” *Int. J. Automot. Technol.*, **13**(1), pp. 97–107.
- [50] Xu, H., and Kahraman, A., 2007, “Prediction of friction-related power losses of hypoid gear pairs,” *Proc. Inst. Mech. Eng. Part K J. Multi-body Dyn.*, **221**(3), pp. 387–400.
- [51] Feng, Z., Wang, S., Lim, T. C., and Peng, T., 2011, “Enhanced friction model for high-speed right-angle gear dynamics,” *J. Mech. Sci. Technol.*, **25**(11), pp. 2741–2753.
- [52] Menq, C.-H., Griffin, J. H., and Bielak, J., 1986, “The influence of microslip on vibratory response, Part II: A comparison with experimental results,” *J. Sound Vib.*, **107**(2), pp. 295–307.
- [53] Cigeroglu, E., An, N., and Menq, C.-H., 2009, “Forced Response Prediction of Constrained and Unconstrained Structures Coupled Through Frictional Contacts,” *J. Eng. Gas Turbines Power*, **131**(2), pp. 22505-22505–11.
- [54] Yang, J., Peng, T., and Lim, T. C., 2011, “An enhanced multi-term harmonic balance solution for nonlinear period-one dynamic motions in right-angle gear pairs,” *Nonlinear Dyn.*, **67**(2), pp. 1053–1065.
- [55] Yavuz, S. D., Saribay, Z. B., and Cigeroglu, E., 2016, “Nonlinear Time-Varying Dynamic Analysis of a Multi-Mesh Spur Gear Train,” *Dynamics of Coupled Structures, Volume 4. Conference Proceedings of the Society for Experimental Mechanics Series*, M. Allen, R. Mayes, and D. Rixen, eds., Springer, Cham.
- [56] Cardona, A., Lerusse, A., and Geradin, M., 1998, “Fast Fourier nonlinear vibration analysis,” *Comput. Mech.*, **22**, pp. 128–142.
- [57] Lim, T. C., and Singh, R., 1990, “Vibration Transmission Through Rolling Element Bearings, Part I: Bearing Stiffness Formulation,” *J. Sound Vib.*, **139**(2), pp. 179–199.
- [58] SMT (Smart Manufacturing Technology), “MASTA, Release 2014 5.4.3 x64,.”

- [59] Cheng, Y., and Lim, T. C., 2001, “Vibration Analysis of Hypoid Transmissions Applying an Exact Geometry-Based Gear Mesh Theory,” *J. Sound Vib.*, **240**(3), pp. 519–543.
- [60] Peng, T., and Lim, T. C., 2007, “Coupled multi-body dynamic and vibration analysis of high-speed hypoid geared rotor system,” *Proc. SAE Noise and Vibration Conf. and Exposition*, St. Charles, Illinois, USA.
- [61] Yavuz, S. D., Saribay, Z. B., and Cigeroglu, E., 2017, “Nonlinear Dynamic Analysis of a Spiral Bevel Geared System,” *Rotating Machinery, Hybrid Test Methods, Vibro-Acoustics & Laser Vibrometry*, Volume 8. Conference Proceedings of the Society for Experimental Mechanics Series, D. Di Maio, and P. Castellini, eds., Springer, Cham.
- [62] Menq, C. H., Griffin, J. H., and Bielak, J., 1986, “The Forced Response of Shrouded Fan Stages,” *J. Vib. Acoust. Stress. Reliab. Des.*, **108**(1), pp. 50–55.
- [63] Cigeroglu, E., and Samandari, H., 2012, “Nonlinear free vibration of double walled carbon nanotubes by using describing function method with multiple trial functions,” *Phys. E Low-dimensional Syst. Nanostructures*, **46**, pp. 160–173.
- [64] Yümer, M. E., Ciğeroglu, E., and Özgüven, H. N., 2010, “Non-Linear Forced Response Analysis of Mistuned Bladed Disk Assemblies,” *ASME. Turbo Expo: Power for Land, Sea, and Air*, Volume 6: Structures and Dynamics, Parts A and B, Glasgow, UK.
- [65] Von Groll, G., and Ewins, D. J., 2001, “The Harmonic Balance Method With Arc-Length Continuation in Rotor/Stator Contact Problems,” *J. Sound Vib.*, **241**(2), pp. 223–233.
- [66] “ANSYS Multiphysics, Release14.5.”
- [67] Kuran, B., and Özgüven, H. N., 1996, “a Modal Superposition Method for Non-Linear Structures,” *J. Sound Vib.*, **189**(3), pp. 315–339.
- [68] Cigeroglu, E., An, N., and Menq, C.-H., 2007, “A microslip friction model with normal load variation induced by normal motion,” *Nonlinear Dyn.*, **50**(3), pp. 609–626.
- [69] Vijayakar, S. M., 2003, “CALYX, Advanced Numerical Solutions LLC.”

APPENDIX A

PUBLISHED PAPERS DURING PHD

Chapter 30 Nonlinear Time-Varying Dynamic Analysis of a Multi-Mesh Spur Gear Train

Siar Deniz Yavuz, Zihni Burcay Saribay, and Ender Cigeroglu

Abstract The nonlinear dynamics of a multi-mesh spur gear train is considered in this study. The gear train consists of three spur gears, with one of the gears in mesh with the other two. Dynamic model includes gear backlash in the form of clearance-type displacement functions and time variation of gear mesh stiffness. The system is reduced to a two-degree-of-freedom definite model by using the relative gear mesh displacements as the coordinates. The equations of motion are solved for periodic steady-state response by using Harmonic Balance Method (HBM). The accuracy of the HBM solutions is demonstrated by comparing them to direct numerical integration solutions. Floquet theory is applied to determine the stability of the steady-state solutions. Two different loading conditions, where the system is driven by the middle gear and driven by one of the end gears, are considered. Phase difference between the two gear meshes is determined under each loading condition and natural modes are predicted for each loading condition. The forced response due to the combination of parametric excitation and static transmission error excitation is obtained and effects of loading conditions and asymmetric positioning on the response are explored.

Keywords Nonlinear gear dynamics • Multi-mesh spur gear train • Mesh phasing • Time-varying mesh stiffness • Multi-term harmonic balance method

Nomenclature

b	Half of gear backlash
c	Damping coefficient
e	Static transmission error
g	Nonlinear displacement functions
F	External force
G	Periodic state matrix
I	Polar mass moment of inertia
J	Jacobian matrix
k	Mesh stiffness
M	Monodromy matrix
m	Equivalent mass
p	Relative gear mesh displacement
Δp	Perturbation of relative gear mesh displacement
r	Gear base radius
S	Nonlinear algebraic equations in matrix form

S.D. Yavuz
Department of Mechanical Engineering, Middle East Technical University, Universiteler Mahallesi, Dumlupinar Bulvarı No:1,
06800 Cankaya, Ankara, Turkey

Turkish Aerospace Industries, Inc. (TAI), Fethiye Mahallesi Havacilik Bulvarı No:17, 06980 Kazan, Ankara, Turkey

Z.B.Saribay
Turkish Aerospace Industries, Inc. (TAI), Fethiye Mahallesi Havacilik Bulvarı No:17, 06980 Kazan, Ankara, Turkey

E. Cigeroglu (✉)
Department of Mechanical Engineering, Middle East Technical University, Universiteler Mahallesi, Dumlupinar Bulvarı No:1,
06800 Cankaya, Ankara, Turkey
e-mail: ender@metu.edu.tr

© The Society for Experimental Mechanics, Inc. 2016
M. Allen et al. (eds.), *Dynamics of Coupled Structures, Volume 4*, Conference Proceedings of the Society
for Experimental Mechanics Series, DOI 10.1007/978-3-319-29763-7_30

309

Yavuz, S. D., Saribay, Z. B., and Cigeroglu, E., 2016, "Nonlinear Time-Varying Dynamic Analysis of a Multi-Mesh Spur Gear Train," *Dynamics of Coupled Structures, Volume 4*. Conference Proceedings of the Society for Experimental Mechanics Series, M. Allen, R. Mayes, and D. Rixen, eds., Springer, Cham.

T	Torque
t	Time
\mathbf{U}	Solution vector
u	Gear mesh displacement harmonic amplitude
Z	Number of teeth
\mathbf{z}	Perturbation state vector
α	Phase of static transmission error harmonic
ρ	Discrete time interval
ϕ	Discontinuous separation function
θ	Rotational displacement
Π	Phase difference between meshes
Ω	Dimensionless frequency
ω	Characteristic frequency
ζ	Damping ratio
ψ	Angle between the lines connecting the centers of the gears
γ	Constant angle in mesh phasing calculation

Subscripts

a	Alternating component
i	Mesh index
m	Mean component

Superscripts

i	Mesh index
rms	Root-mean-square value
T	Matrix transpose
\cdot	Derivative with respect to time
$\dot{}$	Derivative with respect to dimensionless time
-	Dimensional quantities

30.1 Introduction

Gear vibration is an important consideration in drive-train systems due to noise and durability problems. Under dynamic conditions, gear systems produce much higher gear mesh forces than static forces transmitted. These high frequency dynamic forces must be supported by the bearings and are eventually transmitted to the housing to act as the main excitations for gear related noise. Furthermore, alternating forces induced by the vibration reduce fatigue life of the driveline components. Therefore, a better understanding of the gear system dynamics is vital in order to design more silent and durable transmission.

There are a large number of gear dynamics related studies in the literature and in the vast majority of these studies, a single gear pair is considered. Numerous mathematical models are constructed and analytical and numerical solution methods are developed in those studies. The models including a spur gear pair are mostly nonlinear (piecewise-linear) due to backlash but differ in incorporating time variation of mesh stiffness. Some of these models are nonlinear time-invariant (NTI) [1], whereas the others are nonlinear time-varying (NTV) [2–6]. However, published experimental data [3, 4, 7] show that the dynamic behavior of a spur gear pair can only be described by a NTV model. These single-degree-of-freedom (DOF) models are extended to multiple DOFs nonlinear models of geared rotor-bearing systems [8–11]. Moreover, linear and time-invariant characteristics of helical gears are studied in [12–14].

The studies on multi-mesh gear systems are fewer than the ones on single gear pair systems even though most practical systems use multi-mesh, multi-stage gear trains. Nonlinear time-varying dynamic models of multi-mesh spur gear trains are

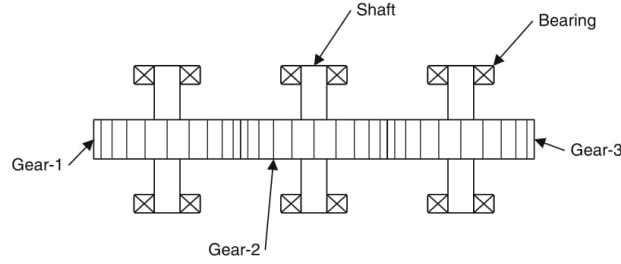


Fig. 30.1 Multi-mesh spur gear train considered in this study

developed in [15–17]. In those studies, a multi-term Harmonic Balance Method (HBM) is used in conjunction with discrete Fourier Transform (DFT) to obtain period-1 and subharmonic responses. Authors examined the nonlinear, parametrically excited dynamics of idler and two-stage counter-shaft configurations of spur gears in [18, 19]. NTV [20] and LTI [21] dynamic models are also proposed for planetary gear sets composed of spur and helical gears, respectively.

In this study, considering both backlash nonlinearity and time-varying mesh stiffness, a nonlinear dynamic model of a multi-mesh gear train is considered. The model consists of three spur gears with one of the gears in mesh with the other two as shown in Fig. 30.1. Both static transmission error excitation and parametric excitation due to time variation of mesh stiffness are considered. The multi-term HBM coupled with DFT and arc-length numerical continuation method are applied to solve the equation of motions for periodic steady-state response. The results of HBM are validated by comparing them to direct numerical integration solutions, which are computationally more intensive. Furthermore, the stability of the steady-state solutions is determined by the use of Floquet theory. Dynamics of both split-torque and idler arrangements are studied. In the split-torque arrangement, the system is driven by the middle gear, whereas one of the end gears is the input and the other one is the output in the idler arrangement. The interaction between meshes such as phasing is investigated for each loading condition and the influence of mesh phasing on the dynamic response is discussed. The effects of asymmetric positioning of the gears around the middle gear on the dynamic response are also studied.

30.2 Dynamic Model Formulation

30.2.1 Physical System and Dynamic Model

The geared system considered in this study, Fig. 30.1, consists of three spur gears with rigid gear blanks mounted on rigid bearings and shafts. The gear in the middle, gear-2, meshes with the other two gears, gear-1 and gear-3. The mesh coupling between the gears includes gear backlash, time-varying mesh stiffness, which acts as parametric excitation, and time-invariant mesh damping. The system is also excited by the static transmission errors, $\bar{e}_1(\bar{t})$ and $\bar{e}_2(\bar{t})$ which are connected in series to the stiffness and damping elements as shown in Fig. 30.2. Gear mesh damping elements are also assumed not to be subjected to gear backlash nonlinearity.

In Fig. 30.2, torsional vibrations of each gear are considered where I_i is the polar mass moment of inertia and r_i is the base radius of the i^{th} gear. Therefore, the system can be represented by a three-degrees-of-freedom semi-definite dynamic model with coordinates $\bar{\theta}_i$, ($i = 1 - 3$). The equations of motion of this system can be obtained as follows

$$I_1 \ddot{\bar{\theta}}_1(\bar{t}) + r_1 \bar{c}_1 \left[r_1 \dot{\bar{\theta}}_1(\bar{t}) + r_2 \dot{\bar{\theta}}_2(\bar{t}) + \dot{\bar{e}}_1(\bar{t}) \right] + r_1 \bar{k}_1(\bar{t}) \bar{g}_1(\bar{t}) = \bar{T}_1, \quad (30.1a)$$

$$I_2 \ddot{\bar{\theta}}_2(\bar{t}) + r_2 \bar{c}_1 \left[r_1 \dot{\bar{\theta}}_1(\bar{t}) + r_2 \dot{\bar{\theta}}_2(\bar{t}) + \dot{\bar{e}}_1(\bar{t}) \right] + r_2 \bar{k}_1(\bar{t}) \bar{g}_1(\bar{t}) + r_2 \bar{c}_2 \left[r_2 \dot{\bar{\theta}}_2(\bar{t}) + r_3 \dot{\bar{\theta}}_3(\bar{t}) + \dot{\bar{e}}_2(\bar{t}) \right] + r_2 \bar{k}_2(\bar{t}) \bar{g}_2(\bar{t}) = \bar{T}_2, \quad (30.1b)$$

$$I_3 \ddot{\bar{\theta}}_3(\bar{t}) + r_3 \bar{c}_2 \left[r_2 \dot{\bar{\theta}}_2(\bar{t}) + r_3 \dot{\bar{\theta}}_3(\bar{t}) + \dot{\bar{e}}_2(\bar{t}) \right] + r_3 \bar{k}_2(\bar{t}) \bar{g}_2(\bar{t}) = \bar{T}_3, \quad (30.1c)$$

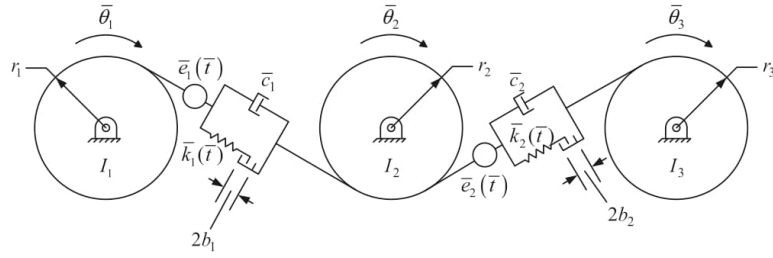


Fig. 30.2 Dynamic model of the system

where \bar{g}_1 and \bar{g}_2 are nonlinear displacement functions defined mathematically as

$$\bar{g}_1 = \begin{cases} \left[r_1\bar{\theta}_1(\bar{t}) + r_2\bar{\theta}_2(\bar{t}) + \bar{e}_1(\bar{t}) \right] - \bar{b}_1, & \left[r_1\bar{\theta}_1(\bar{t}) + r_2\bar{\theta}_2(\bar{t}) + \bar{e}_1(\bar{t}) \right] > \bar{b}_1 \\ 0, & \left[r_1\bar{\theta}_1(\bar{t}) + r_2\bar{\theta}_2(\bar{t}) + \bar{e}_1(\bar{t}) \right] \leq \bar{b}_1 \\ \left[r_1\bar{\theta}_1(\bar{t}) + r_2\bar{\theta}_2(\bar{t}) + \bar{e}_1(\bar{t}) \right] + \bar{b}_1, & \left[r_1\bar{\theta}_1(\bar{t}) + r_2\bar{\theta}_2(\bar{t}) + \bar{e}_1(\bar{t}) \right] < -\bar{b}_1 \end{cases}, \quad (30.2a)$$

$$\bar{g}_2 = \begin{cases} \left[r_2\bar{\theta}_2(\bar{t}) + r_3\bar{\theta}_3(\bar{t}) + \bar{e}_2(\bar{t}) \right] - \bar{b}_2, & \left[r_2\bar{\theta}_2(\bar{t}) + r_3\bar{\theta}_3(\bar{t}) + \bar{e}_2(\bar{t}) \right] > \bar{b}_2 \\ 0, & \left[r_2\bar{\theta}_2(\bar{t}) + r_3\bar{\theta}_3(\bar{t}) + \bar{e}_2(\bar{t}) \right] \leq \bar{b}_2 \\ \left[r_2\bar{\theta}_2(\bar{t}) + r_3\bar{\theta}_3(\bar{t}) + \bar{e}_2(\bar{t}) \right] + \bar{b}_2, & \left[r_2\bar{\theta}_2(\bar{t}) + r_3\bar{\theta}_3(\bar{t}) + \bar{e}_2(\bar{t}) \right] < -\bar{b}_2 \end{cases}. \quad (30.2b)$$

The above three-degrees-of-freedom semi-definite system can be reduced to a two-degrees-of-freedom definite system by defining the following two new coordinates:

$$\bar{p}_1(\bar{t}) = r_1\bar{\theta}_1(\bar{t}) + r_2\bar{\theta}_2(\bar{t}) + \bar{e}_1(\bar{t}), \quad (30.3a)$$

$$\bar{p}_2(\bar{t}) = r_2\bar{\theta}_2(\bar{t}) + r_3\bar{\theta}_3(\bar{t}) + \bar{e}_2(\bar{t}). \quad (30.3b)$$

These new coordinates represent the relative gear mesh displacements, which are the combinations of the dynamic and static transmission errors. Using Eqs. (30.1)–(30.3), the following new system of equations is obtained

$$\ddot{\bar{p}}_1(\bar{t}) + \bar{c}_1 \left[\frac{r_1^2}{I_1} + \frac{r_2^2}{I_2} \right] \dot{\bar{p}}_1(\bar{t}) + \bar{c}_2 \frac{r_2^2}{I_2} \dot{\bar{p}}_2(\bar{t}) + \bar{k}_1(\bar{t}) \left[\frac{r_1^2}{I_1} + \frac{r_2^2}{I_2} \right] \bar{g}_1(\bar{t}) + \bar{k}_2(\bar{t}) \frac{r_2^2}{I_2} \bar{g}_2(\bar{t}) = \frac{r_1}{I_1} \bar{T}_1 + \frac{r_2}{I_2} \bar{T}_2 + \ddot{\bar{e}}_1(\bar{t}), \quad (30.4a)$$

$$\ddot{\bar{p}}_2(\bar{t}) + \bar{c}_1 \frac{r_2^2}{I_2} \dot{\bar{p}}_1(\bar{t}) + \bar{c}_2 \left[\frac{r_2^2}{I_2} + \frac{r_3^2}{I_3} \right] \dot{\bar{p}}_2(\bar{t}) + \bar{k}_1(\bar{t}) \frac{r_2^2}{I_2} \bar{g}_1(\bar{t}) + \bar{k}_2(\bar{t}) \left[\frac{r_2^2}{I_2} + \frac{r_3^2}{I_3} \right] \bar{g}_2(\bar{t}) = \frac{r_2}{I_2} \bar{T}_2 + \frac{r_3}{I_3} \bar{T}_3 + \ddot{\bar{e}}_2(\bar{t}). \quad (30.4b)$$

In order to obtain the dimensionless equations of motion, the following transformations are applied:

$$m_1 = \frac{I_1 I_2}{r_1^2 I_2 + r_2^2 I_1}, \quad m_2 = \frac{I_2}{r_2^2}, \quad m_3 = \frac{I_2 I_3}{r_3^2 I_2 + r_2^2 I_3}, \quad (30.5a-c)$$

$$k_1(\bar{t}) = \frac{\bar{k}_1(\bar{t})}{k_{1m}}, \quad k_2(\bar{t}) = \frac{\bar{k}_2(\bar{t})}{k_{2m}}, \quad (30.5d,e)$$

$$\bar{\omega}_{11}^2 = \frac{k_{1m}}{m_1}, \quad \bar{\omega}_{12}^2 = \frac{k_{2m}}{m_2}, \quad \bar{\omega}_{21}^2 = \frac{k_{1m}}{m_2}, \quad \bar{\omega}_{22}^2 = \frac{k_{2m}}{m_3}, \quad (30.5f-i)$$

$$\zeta_{11} = \frac{\bar{c}_1}{2m_1\bar{\omega}_{11}}, \quad \zeta_{12} = \frac{\bar{c}_2}{2m_2\bar{\omega}_{12}}, \quad \zeta_{21} = \frac{\bar{c}_1}{2m_2\bar{\omega}_{21}}, \quad \zeta_{22} = \frac{\bar{c}_2}{2m_3\bar{\omega}_{22}}, \quad (30.5j-m)$$

where k_{1m} and k_{2m} are the mean components of $\bar{k}_1(\bar{t})$ and $\bar{k}_2(\bar{t})$, respectively, $\bar{\omega}_{ij}$ ($i, j = 1, 2$) is the characteristic frequency, and ζ_{ij} ($i, j = 1, 2$) defines the damping of the system. Moreover, a dimensionless time parameter is obtained by setting $t = \bar{t}\omega_c$, where ω_c is one of the characteristic frequencies. Also, dimensionless displacements are defined as $p_i(\bar{t}) = \bar{p}_i(\bar{t})/b_c$, $e_i(\bar{t}) = \bar{e}_i(\bar{t})/b_c$, and $b_i = \bar{b}_i/b_c$ ($i = 1, 2$) by employing a characteristic length b_c . Using these dimensionless parameters and letting $\omega_{ij} = \bar{\omega}_{ij}/\omega_c$ ($i, j = 1, 2$), the following dimensionless equations of motion are obtained:

$$\begin{cases} p_1''(t) \\ p_2''(t) \end{cases} + 2 \begin{bmatrix} \zeta_{11}\omega_{11} & \zeta_{12}\omega_{12} \\ \zeta_{21}\omega_{21} & \zeta_{22}\omega_{22} \end{bmatrix} \begin{cases} p_1'(t) \\ p_2'(t) \end{cases} + \begin{bmatrix} \omega_{11}^2 k_1(t) & \omega_{12}^2 k_2(t) \\ \omega_{21}^2 k_1(t) & \omega_{22}^2 k_2(t) \end{bmatrix} \begin{cases} g_1(t) \\ g_2(t) \end{cases} = \begin{cases} F_m^{(1)} + e_1''(t) \\ F_m^{(2)} + e_2''(t) \end{cases}, \quad (30.6a)$$

where

$$g_i(t) = \begin{cases} p_i(t) - b_i, & p_i(t) > b_i \\ 0, & |p_i(t)| \leq b_i \\ p_i(t) + b_i, & p_i(t) < -b_i \end{cases}, \quad i = 1, 2, \quad (30.6b)$$

$$F_m^{(1)}(t) = \frac{1}{\omega_c^2 b_c} \left(\frac{r_1 \bar{T}_1}{I_1} + \frac{r_2 \bar{T}_2}{I_2} \right), \quad F_m^{(2)}(t) = \frac{1}{\omega_c^2 b_c} \left(\frac{r_2 \bar{T}_2}{I_2} + \frac{r_3 \bar{T}_3}{I_3} \right). \quad (30.6c)$$

30.2.2 Period-One Dynamics

The multi-term harmonic balance method coupled with discrete Fourier Transform process and the numerical continuation method, which has been successfully applied in [3, 4, 15, 16], is used in this study to solve the dimensionless equations of motion for p_i ($i = 1, 2$). The solution is periodic based on the assumption that both excitations and time-varying parameters are periodic [15]. This also implies that the nonlinear displacement functions $g_i(t)$ ($i = 1, 2$) can also be described periodically. The harmonic expression for mesh stiffness and static transmission error can be written as

$$k_i(t) = 1 + \sum_{a=1}^A \left[\kappa_{2a}^{(i)} \cos(a\Omega t) + \kappa_{2a+1}^{(i)} \sin(a\Omega t) \right], \quad (i = 1, 2), \quad (30.7a)$$

$$e_i(t) = \sum_{j=1}^J \left[\varepsilon_{2j}^{(i)} \cos(j\Omega t) + \varepsilon_{2j+1}^{(i)} \sin(j\Omega t) \right], \quad (i = 1, 2). \quad (30.7b)$$

The mean values of the static transmission errors are set to zero since only the second order derivatives of them are included in the equations of motion (30.6a) as parts of the excitation terms on the right hand side of the equation.

Given the periodic excitations of Eqs. (30.7a, 30.7b), the steady-state solution is assumed to be of the form

$$p_i(t) = u_1^{(i)} + \sum_{r=1}^R \left[u_{2r}^{(i)} \cos(r\Omega t) + u_{2r+1}^{(i)} \sin(r\Omega t) \right], \quad (i = 1, 2), \quad (30.8)$$

which can be differentiated to yield

$$p_i'(t) = \sum_{r=1}^R \left[-(r\Omega) u_{2r}^{(i)} \sin(r\Omega t) + (r\Omega) u_{2r+1}^{(i)} \cos(r\Omega t) \right], \quad (i = 1, 2), \quad (30.9a)$$

$$p_i''(t) = -\sum_{r=1}^R \left[(r\Omega)^2 u_{2r}^{(i)} \cos(r\Omega t) + (r\Omega)^2 u_{2r+1}^{(i)} \sin(r\Omega t) \right], \quad (i = 1, 2). \quad (30.9b)$$

Then, the time series of nonlinear restoring forces can be obtained by sampling N points within one fundamental mesh period. Here, N must be larger than $2R$ where R is the highest harmonics of the solution in order to avoid aliasing errors. Hence, the time series of the nonlinear restoring forces are

$$F_k^{(i)}(t_n) = \omega_{i1}^2 k_1(t_n) g_1(t_n) + \omega_{i2}^2 k_2(t_n) g_2(t_n), \quad (i = 1, 2), \quad (30.10)$$

where $t_n = n\rho$ ($n = 0, 1, 2, \dots, N-1$). Here, $\rho = 2\pi / (N\Omega)$.

In order to use multi-term HBM, the nonlinear restoring forces must be represented by Fourier series as

$$F_k^{(i)}(t) = F_{k1}^{(i)} + \sum_{r=1}^R \left[F_{k(2r)}^{(i)} \cos(r\Omega t) + F_{k(2r+1)}^{(i)} \sin(r\Omega t) \right], \quad (i = 1, 2), \quad (30.11)$$

where the coefficients can be calculated using the discrete Fourier Transform as ($r = 1, 2, \dots, R$)

$$F_{k1}^{(i)} = \frac{1}{N} \sum_{n=0}^{N-1} F_k^{(i)}, \quad (i = 1, 2), \quad (30.12a)$$

$$F_{k(2r)}^{(i)} = \frac{2}{N} \sum_{n=0}^{N-1} F_k^{(i)} \cos\left(\frac{2\pi rn}{N}\right), \quad (i = 1, 2), \quad (30.12b)$$

$$F_{k(2r+1)}^{(i)} = \frac{2}{N} \sum_{n=0}^{N-1} F_k^{(i)} \sin\left(\frac{2\pi rn}{N}\right), \quad (i = 1, 2). \quad (30.12c)$$

Substituting Eqs. (30.7b), (30.9a, 30.9b), and (30.11) into Eq. (30.6a) and equating the coefficients of the like harmonic terms, a set of $(4R + 2)$ nonlinear algebraic equations are obtained with ($i = 1, 2$) and ($r = 1, 2, \dots, R$)

$$S_1^{(i)} = F_{k1}^{(i)} - F_m^{(i)}, \quad (30.13a)$$

$$S_{2r}^{(i)} = -(r\Omega)^2 u_{2r}^{(i)} + 2\zeta_{i1}\omega_{i1}(r\Omega)u_{2r+1}^{(1)} + 2\zeta_{i2}\omega_{i2}(r\Omega)u_{2r+1}^{(2)} + F_{k(2r)}^{(i)} + (r\Omega)^2 \varepsilon_{2r}^{(i)}, \quad (30.13b)$$

$$S_{2r+1}^{(i)} = -(r\Omega)^2 u_{2r+1}^{(i)} - 2\zeta_{i1}\omega_{i1}(r\Omega)u_{2r}^{(1)} - 2\zeta_{i2}\omega_{i2}(r\Omega)u_{2r}^{(2)} + F_{k(2r+1)}^{(i)} + (r\Omega)^2 \varepsilon_{2r+1}^{(i)}. \quad (30.13c)$$

Finally, the solution vector $\mathbf{U} = [u_1^{(1)}, u_2^{(1)}, \dots, u_{2R}^{(1)}, u_{2R+1}^{(1)}, u_1^{(2)}, u_2^{(2)}, \dots, u_{2R}^{(2)}, u_{2R+1}^{(2)}]^T$ is determined by using Newton's Method with arc length continuation. Newton's method can be applied as follows

$$\mathbf{U}^{(m)} = \mathbf{U}^{(m-1)} - (\mathbf{J}^{-1})^{(m-1)} \mathbf{S}^{(m-1)}, \quad (30.14)$$

where $\mathbf{U}^{(m)}$ is the m^{th} iterative solution based on the $(m-1)^{\text{th}}$ solution and $(\mathbf{J}^{-1})^{(m-1)}$ is the inverse of the Jacobian matrix of the vector function \mathbf{S} estimated at the previous point $(m-1)$. The iteration procedure described by Eq. (30.14) is repeated until the vector norm of $\mathbf{S}^{(m)}$ is below a predefined error limit for that excitation frequency. Furthermore, arc-length continuation method is used in the solution and a new parameter, arc-length, which is the radius of a hypothetical sphere in which the next solution point will be searched, is chosen as the continuation parameter instead of the frequency in order to follow the solution path even at the turning points. Details of Newton's method with arc-length continuation can be found in [22–24].

The Floquet theory is used to determine the stability of the steady state solutions p_i , ($i = 1, 2$) obtained above. This is done by examining the stability of the perturbed solution $p_i + \Delta p_i$, ($i = 1, 2$). The variational equation for the perturbation Δp_i , ($i = 1, 2$) is

$$\begin{Bmatrix} \Delta p_1''(t) \\ \Delta p_2''(t) \end{Bmatrix} + 2 \begin{bmatrix} \zeta_{11}\omega_{11} & \zeta_{12}\omega_{12} \\ \zeta_{21}\omega_{21} & \zeta_{22}\omega_{22} \end{bmatrix} \begin{Bmatrix} \Delta p_1'(t) \\ \Delta p_2'(t) \end{Bmatrix} + \begin{bmatrix} \omega_{11}^2 k_1(t)\phi_1(t) & \omega_{12}^2 k_2(t)\phi_2(t) \\ \omega_{21}^2 k_1(t)\phi_1(t) & \omega_{22}^2 k_2(t)\phi_2(t) \end{bmatrix} \begin{Bmatrix} \Delta p_1(t) \\ \Delta p_2(t) \end{Bmatrix} = \{0\}, \quad (30.15)$$

where $\phi_i(t)$ is a discontinuous separation function

$$\phi_i(t) = \begin{cases} 1, & |p_i(t)| > 1 \\ 0, & |p_i(t)| \leq 1 \end{cases}, \quad (i = 1, 2). \quad (30.16)$$

Equation (30.15) can be written in state-space form $\mathbf{z}'(t) = \mathbf{G}(t)\mathbf{z}(t)$ where $\mathbf{z}(t) = [\Delta p_1 \Delta p_2 \Delta p'_1 \Delta p'_2]^T$ is the state vector and $\mathbf{G}(t) = \mathbf{G}(t+T)$ is the periodic state matrix given by

$$\mathbf{G}(t) = \begin{bmatrix} 0 & 0 & 1 & 0 \\ 0 & 0 & 0 & 1 \\ -\omega_{11}^2 k_1(t) \phi_1(t) & -\omega_{12}^2 k_2(t) \phi_2(t) & -2\zeta_{11} \omega_{11} & -2\zeta_{12} \omega_{12} \\ -\omega_{21}^2 k_1(t) \phi_1(t) & -\omega_{22}^2 k_2(t) \phi_2(t) & -2\zeta_{21} \omega_{21} & -2\zeta_{22} \omega_{22} \end{bmatrix}. \quad (30.17)$$

Then, the monodromy matrix, $\mathbf{M} = \mathbf{z}(T)$ is defined as the state transition matrix at the end of one analysis period, which is obtained by solving the homogenous matrix equation $\mathbf{z}'(t) = \mathbf{G}(t)\mathbf{z}(t)$ given initial condition $\mathbf{z}(0) = \mathbf{I}_4$, and the stability of the perturbed solution and consequently the stability of the corresponding solution are determined by examining the eigenvalues of this matrix. Here \mathbf{I}_4 is 4x4 identity matrix [3].

\mathbf{M} can be computed with a method that is based on an assumed stepwise variation of the state transition matrix. The state matrix $\mathbf{G}(t)$ is approximated as a series of step functions \mathbf{G}_n at N discrete time intervals $\tau = nh$ as follows

$$\mathbf{G}_n = \frac{1}{h} \int_{(n-1)h}^{nh} \mathbf{G}(\tau) d\tau, \quad (n = 1, 2, \dots, N). \quad (30.18)$$

If large number of time steps, N , is used, $\mathbf{G}(t)$ can be considered constant between two consecutive time steps and the integration is not needed. Between these two time instants, the following relation, where the exponential term is the state transition matrix, can be written

$$\mathbf{z}_{n+1} = e^{h\mathbf{G}_n} \mathbf{z}_n. \quad (30.19)$$

Then, the monodromy matrix is computed as the product of the individual transition matrices [25]:

$$\mathbf{z}_N = \prod_{n=0}^{N-1} e^{h\mathbf{G}_n} \mathbf{z}_0, \quad (30.20a)$$

$$\mathbf{M} = \prod_{n=0}^{N-1} e^{h\mathbf{G}_n}. \quad (30.20b)$$

Using Pade approximation or L^{th} order truncated Taylor series approximation as in [3] to calculate the matrix exponentiation above, monodromy matrix \mathbf{M} is calculated. The solution is considered unstable when the modulus of any of the four eigenvalues λ_i of \mathbf{M} is greater than unity; otherwise the solution is stable [3, 25].

30.2.3 Loading Conditions and Mesh Phases

Two different loading conditions as shown in Fig. 30.3 are considered here. In case-I, the system is driven by the middle gear (gear-2) and gears at the ends, gear-1 and gear-3, are outputs. This is known as split-torque arrangement. On the other hand, in case-II, gear-3 (output) is driven by gear-1 (input) through gear-2 (idler), which is idler arrangement. Therefore, the dynamic model shown in Fig. 30.2 is actually for idler arrangement but the same equations of motion can be obtained for split-torque arrangement by defining the same coordinates $\bar{p}_1(\bar{t})$ and $\bar{p}_2(\bar{t})$ as given in Eqs. (30.3a) and (30.3b).

The static transmission errors for the two meshes in the system are defined as

$$e_1(t) = \sum_{j=1}^J E_j^{(1)} \sin(j\Omega t + \alpha_{1j}), \quad (30.21a)$$

$$e_2(t) = \sum_{j=1}^J E_j^{(2)} \sin[j\Omega t + \alpha_{2j} + j\Pi], \quad (30.21b)$$

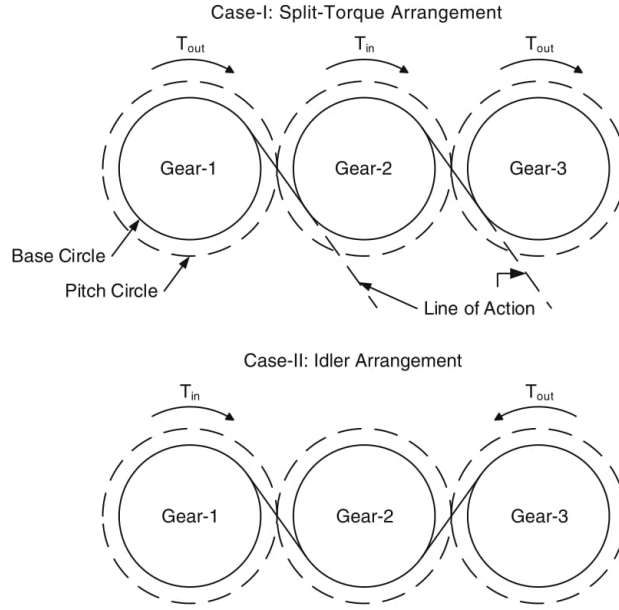
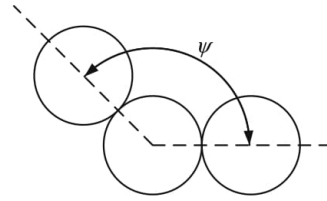


Fig. 30.3 Different loading conditions such as split-torque and idler arrangements

Fig. 30.4 Definition of the angle ψ



where $E_j^{(i)}$ and α_{ij} are the j^{th} harmonic amplitude and phase angle of the i^{th} gear mesh, respectively. Assuming that the both gear meshes are subject to same flank modifications yields $\alpha_{1j} = \alpha_{2j}$ [13]. Therefore, the only phase difference between the meshes is Π , which is defined as

$$\Pi = Z_2 (\psi + \gamma), \tag{30.22}$$

where Z_2 is the number of teeth of gear-2, ψ is the angle between the lines connecting the centers of the gears forming the meshes, which is shown in Fig. 30.4. γ is given as

$$\gamma = \begin{cases} 0, & \text{split-torque arrangement} \\ \pi/Z_2, & \text{idler arrangement} \end{cases} \tag{30.23}$$

The same phase relationship is also valid for the mesh stiffness. In addition, tooth deflection is maximum when the mesh stiffness is minimum. Similarly, the minimum tooth deflection corresponds to the maximum mesh stiffness. Thus, there is an out-of-phase relationship between the static transmission error and mesh stiffness of a gear mesh:

$$k_1(t) = \sum_{a=1}^A K_a^{(1)} \sin(a\Omega t + \alpha_{1j} + \pi), \tag{30.24a}$$

$$k_2(t) = \sum_{a=1}^A K_a^{(2)} \sin(a\Omega t + \alpha_{1j} + \pi + a\Pi). \quad (30.24b)$$

Definition of static transmission error e_i and mesh stiffness k_i can be converted to expressions that contain sine and cosine functions as in Eqs. (30.7a) and (30.7b).

30.3 Results and Discussion

A multi-mesh gear train composed of three identical spur gears with the parameters listed in Table 30.1 is considered as the example case. In order to simplify the study, only the first harmonics of the mesh stiffness functions $k_i(t)$ ($i = 1, 2$) and static transmission errors $e_i(t)$ ($i = 1, 2$) are considered. Furthermore, external torque values are taken as constant with no disturbances in the form of pulsations.

Firstly, the period-1 motion solutions found by HBM are compared to the results of the direct numerical integration. Figure 30.5 shows the comparison of the root-mean-square (rms) values of the displacement response in the idler arrangement, whereas the corresponding mean components are plotted in Fig. 30.6. Here, the HBM solution is obtained by assuming three harmonics ($R = 3$ in Eq. (30.8)). The number of teeth of the middle gear Z_2 is taken as even, which results in a phase difference of π between the two meshes.

A characteristic length of $b_c = 20 \mu\text{m}$ is used, which means that each gear has $40 \mu\text{m}$ total backlash. The characteristic frequency $\omega_c = 39667 \text{ rad/s}$ corresponds to the $\bar{\omega}_{11}$ given in Eq. (30.5f-i). With this characteristic frequency, the dimensionless undamped natural frequencies of the corresponding linear system are $\omega_{n1} = 0.71$ and $\omega_{n2} = 1.25$. The rms values are calculated as

Table 30.1 Parameters of the example system

Parameter ($i = 1, 2, 3$)	Numerical value
r_i , [m]	0.0423
Mass, [kg]	1.029
I_i , [kg m ²]	0.00136
k_{1m}, k_{2m} [N/m]	$6 (10^8)$
c_1, c_2 [Ns/m]	3000
T_1, T_2, T_3 in idler arrangement [Nm]	100, 0, -100
T_1, T_2, T_3 in split-torque arrangement [Nm]	100, 200, 100
$K_1^{(1)}, K_1^{(2)}$	0.3
$E_1^{(1)}, E_1^{(2)}$	0.15
ψ	180°

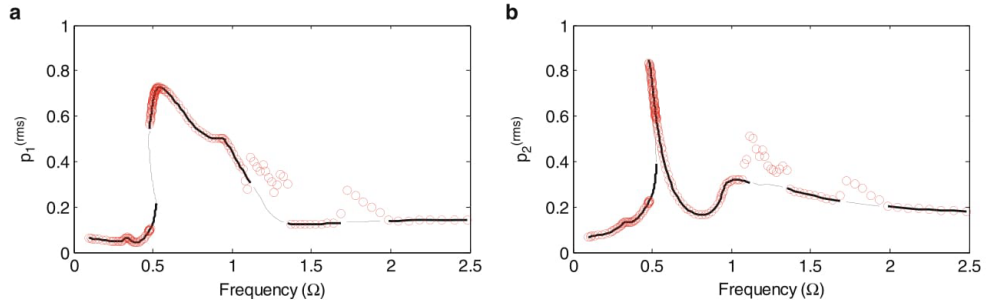


Fig. 30.5 Comparison of rms values of the responses, $p_1(t)$ and $p_2(t)$ predicted by HBM and NI in the idler arrangement with even Z_2 . (straight line) Stable and (dashed line) unstable HBM solution, (circle) NI solutions, (a) $p_1^{(rms)}$ (b) $p_2^{(rms)}$

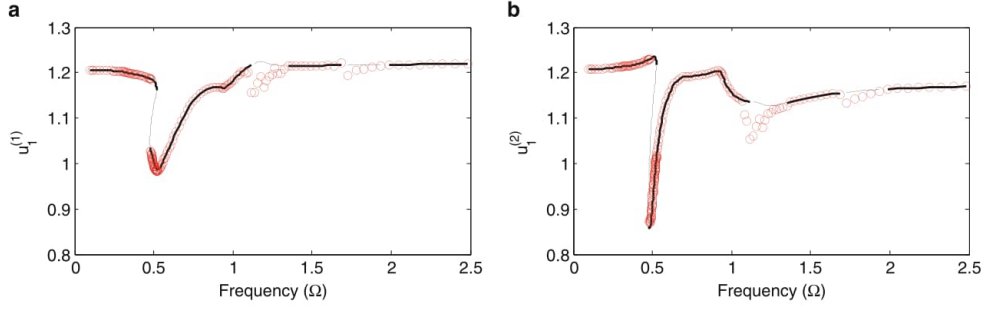


Fig. 30.6 Comparison of the mean components of the responses, $p_1(t)$ and $p_2(t)$ predicted by HBM and NI in the idler arrangement with even Z_2 . (straight line) Stable and (dashed line) unstable HBM solution, (circle) NI solutions, (a) $u_1^{(1)}$ (b) $u_1^{(2)}$

$$p_i^{(\text{rms})} = \left\{ \sum_{r=1}^R [A_r^{(i)}]^2 \right\}^{1/2}, \quad (30.25)$$

where $A_r^{(i)}$ is the amplitude of the r^{th} harmonic of $p_i(t)$ that can be defined as

$$A_r^{(i)} = \left\{ [u_{2r}^{(i)}]^2 + [u_{2r+1}^{(i)}]^2 \right\}. \quad (30.26)$$

In Figs. 30.5 and 30.6, thick solid lines are the stable HBM solutions, while thin dashed lines represent the unstable HBM solutions. It is seen that the solutions of the two methods are in very good agreement except around the unstable frequency ranges observed at $\Omega = [1.13 - 1.33]$ and $\Omega = [1.73 - 1.93]$. This shows the existence of subharmonic motions dictating these ranges, which correspond to the parametric resonances due to the time variation of the mesh stiffness. While the NI solution can converge to these motions depending on the initial condition used, HBM cannot find these motions since the subharmonics are not included in the solutions assumed.

From past studies [1, 3, 4], it is known that spur gears can exhibit both single-sided and double-sided tooth impacts depending on the system parameters. Similar behaviors are also seen here in the results of both HBM and NI. Focusing on Fig. 30.5, gear pairs behave quite linearly with no tooth impact in the low frequency range. As the frequency increases, $p_1^{(\text{rms})}$ and $p_2^{(\text{rms})}$ forced response curves exhibit single-sided tooth impact, which is a softening-type nonlinear behavior due to tooth separation occurring near the primary resonance frequency, $\Omega = \omega_{n1}$. However, the double-sided impact, which is a hardening-type nonlinear behavior due to the additional impact with the preceding tooth, is not observed in the responses, since the vibration amplitudes are small compared to the backlash amount.

Another observation from Fig. 30.5 is that there is a super-harmonic resonance peak at $\Omega \approx 0.5 \omega_{n1} = 0.35$ due to the parametric excitation. This peak can only be observed if sufficient number of harmonics is used in HBM. The nonlinear behavior is also obvious in Fig. 30.6. Mean amplitudes of $p_1(t)$ and $p_2(t)$ remain nearly constant in the case of no tooth separation. However, the values of $u_1^{(1)}$ and $u_1^{(2)}$ vary significantly in the case of tooth separation.

In Fig. 30.7, the response $p_1(t)$ of the split-torque arrangement obtained by HBM and NI is compared. Again, the number of teeth of gear-2 is even; hence, the two meshes are in phase. Due to the symmetry, the responses $p_1(t)$ and $p_2(t)$ are exactly the same; therefore, only $p_1(t)$ is shown here. The gear train in the split-torque arrangement exhibits nonlinear behavior as single-sided impact near the primary resonance frequency at $\Omega = \omega_{n2}$. Contrary to the idler arrangement, anti-resonance occurs near the primary resonance frequency at $\Omega = \omega_{n1}$ in the split-torque case. It is also clear in Fig. 30.7 that HBM and NI solutions are again in very good agreement. In this case, there are no frequency ranges which are dictated by subharmonic motions.

The influence of the out-of-phase relationship between the static transmission error and mesh stiffness in the gear train with even Z_2 is shown in Fig. 30.8. Here, the combined response due to the static transmission error and parametric excitations is compared with the responses of the system, where only one of the excitation sources exists. Split-torque arrangement is considered in Fig. 30.8a while Fig. 30.8b demonstrates the effect in idler case. Focusing on Fig. 30.8a, each excitation alone forms a response peak at the same resonance frequency $\Omega = \omega_{n2}$. However, the out-of-phase relationship results in a decrease

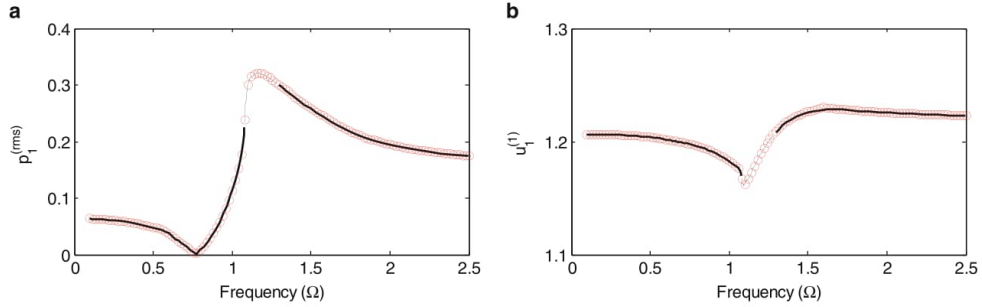


Fig. 30.7 Comparison of rms value and mean component of the response $p_1(t)$ predicted by HBM and NI in the split-torque arrangement with even Z_2 . (straight line) Stable and (dashed line) unstable HBM solution, (circle) NI solutions, (a) $p_1^{(rms)}$ (b) $u_1^{(1)}$

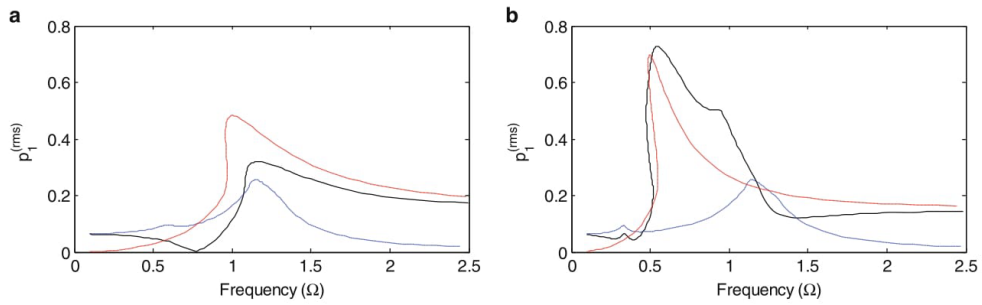


Fig. 30.8 Effect of the out-of-phase relationship between the static transmission error and mesh stiffness. Z_2 is even. (long-short-dashed blue line) Response of the only parametric excitation (dashed red line) Response of the only static transmission error excitation (straight line) Combined response (a) $p_1^{(rms)}$ in split-torque arrangement (b) $p_1^{(rms)}$ in idler arrangement

in the combined response at the resonance frequencies. It is also noted in Fig. 30.8a that the super-harmonic resonance peak at $\Omega \approx 0.5 \omega_{n2} = 0.62$ observed in the response curve of the only parametric excitation vanishes in the combined response. On the other hand, in the idler arrangement, the peak due to each excitation alone appears at different resonance frequency; hence, they do not affect each other significantly.

Figure 30.9 compares the dynamic responses of four different loading conditions: (1) idler arrangement, $Z_2 = even$, (2) idler arrangement, $Z_2 = odd$, (3) split-torque arrangement, $Z_2 = even$, (4) split-torque arrangement, $Z_2 = odd$. As seen from Fig. 30.9, the split-torque arrangement excites the second mode shape at $\Omega = \omega_{n2}$ when $Z_2 = even$ and the first mode shape at $\Omega = \omega_{n1}$ when $Z_2 = odd$. Therefore, a shift in the frequency range occurs due to the change of the excited mode shape. On the other hand, the idler arrangement has always two peaks at both resonance frequencies independent from the number of teeth of gear-2. The amplitudes of the peaks are affected significantly depending on the interaction between the mesh stiffness and static transmission errors in terms of phasing.

Influence of the orientation angles of the end gears around the middle gear is illustrated in Fig. 30.10 for the split-torque arrangement with $Z_2 = 30$. The phase difference between the meshes are found as 0° , 90° and 180° by using Eq. (30.22) corresponding to the orientation angles of 180° , 135° and 90° , respectively. In the configuration with $\psi = 180^\circ$, the peaks in the response curves of both meshes occur at the resonance frequency $\Omega = \omega_{n2}$, while configuration with $\psi = 90^\circ$ triggers the first mode shape at $\Omega = \omega_{n1}$. For $\psi = 135^\circ$, two distinct peaks exist in both $p_1^{(rms)}$ and $p_2^{(rms)}$. This agrees with the results of the linear time-invariant model of multi-mesh helical gear train studied in [13].

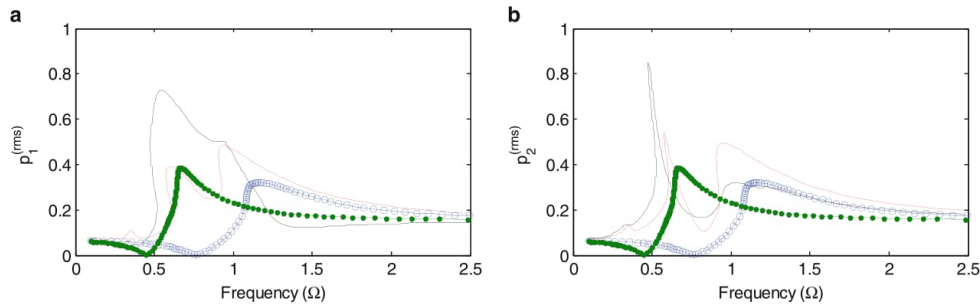


Fig. 30.9 Effect of loading conditions on dynamic response. (straight line) idler arrangement with even Z_2 (dashed red line) idler arrangement with odd Z_2 (blue line with circle) split-torque arrangement with even Z_2 (green line with circle) split-torque arrangement with odd Z_2 (a) $p_1^{(rms)}$ (b) $p_2^{(rms)}$

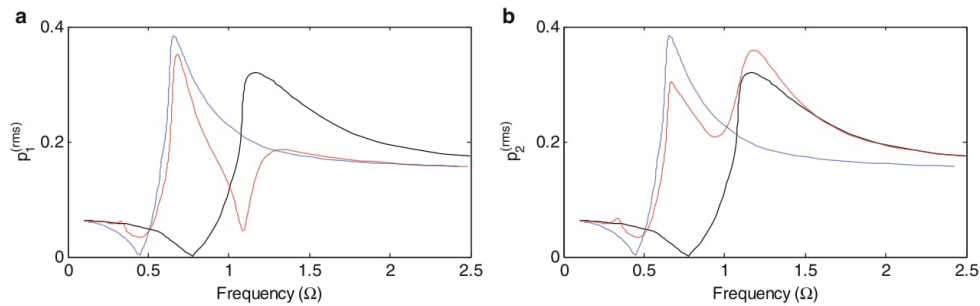


Fig. 30.10 Effect of orientation angle on dynamic response of the split-torque arrangement with $Z_2 = 30$. (straight line) $\psi = 180^\circ$ (dashed red line) $\psi = 135^\circ$ (long-short-dashed blue line) $\psi = 90^\circ$ (a) $p_1^{(rms)}$ (b) $p_2^{(rms)}$

30.4 Conclusion

A nonlinear time-varying dynamic model for a multi-mesh spur gear train consisting of three gears and three shafts is formulated in this study. The resultant dimensionless equations of motion are solved for steady-state period-1 response by using a multi-term Harmonic Balance Method in conjunction with discrete Fourier Transform. The solutions obtained by HBM are compared to ones obtained by direct numerical integration. Floquet theory is applied to determine the stability of the steady state solutions. It is seen from the results that the multi-mesh gear train exhibits nonlinear behavior as single-sided impact with the given system parameters. No back collisions (double-sided impacts) are observed. Solutions obtained by numerical integration also show the existence of the subharmonic motions near the frequencies corresponding to the parametric resonances.

The interaction between the static transmission error and parametric excitations is analyzed by considering the phasing between them. It is shown that the number of teeth of gear-2 has a significant effect on the dynamic response since it directly determines the phase angle between the meshes. Dynamic response is also influenced greatly by the positions of the end gears. Therefore, optimization of these parameters in the design may reduce vibration and noise.

References

1. Kahraman, A., Singh, R.: Non-linear dynamics of a spur gear pair. *J. Sound Vib.* **142**(1), 49–75 (1990)
2. Kahraman, A., Singh, R.: Interactions between time-varying mesh stiffness and clearance non-linearities in a geared system. *J. Sound Vib.* **146**(1), 135–156 (1991)

3. Kahraman, A., Blankenship, G.W.: Steady state forced response of a mechanical oscillator with combined parametric excitation and clearance type non-linearity. *J. Sound Vib.* **185**(5), 743–765 (1995)
4. Kahraman, A., Blankenship, G.W.: Interactions between commensurate parametric and forcing excitations in a system with clearance. *J. Sound Vib.* **194**(3), 317–336 (1996)
5. Kahraman, A., Lim, J., Ding, H.: A dynamic model of a spur gear pair with friction. In: Proceedings of 12th IFTOMM World Congress, Besançon (2007)
6. Shen, Y., Yang, S., Liu, X.: Nonlinear dynamics of a spur gear pair with time-varying stiffness and backlash based on incremental harmonic balance method. *Int. J. Mech. Sci.* **48**, 1256–1263 (2006)
7. Kahraman, A., Blankenship, G.W.: Experiments on nonlinear dynamic behavior of an oscillator with clearance and periodically time-varying parameters. *J. Appl. Mech.* **64**, 217–226 (1997)
8. Kahraman, A., Singh, R.: Non-linear dynamics of a geared rotor-bearing system with multiple clearances. *J. Sound Vib.* **144**(3), 469–506 (1991)
9. Özgüven, H.N.: A non-linear mathematical model for dynamic analysis of spur gears including shaft and bearing dynamics. *J. Sound Vib.* **145**(2), 239–260 (1991)
10. Maliha, R., Doruer, C.U., Ozguven, H.N.: Nonlinear dynamic modeling of gear-shaft-disk-bearing systems using finite elements and describing functions. *J. Mech. Des.* **126**, 534–541 (2004)
11. Gürkan, N.E., Ozguven, H.N.: Interactions Between backlash and bearing clearance nonlinearity in geared flexible rotors. In: Proceedings of IDETC/PTG 2007 ASME 2007 International Design Engineering Technical Conferences and ASME International Power Transmission and Gearing Conference, Las Vegas, pp. 1–10 (2007)
12. Kahraman, A.: Effect of axial vibrations on the dynamics of a helical gear pair. *J. Vib. Acoust.* **115**, 33–39 (1993)
13. Kahraman, A.: Dynamic analysis of a multi-mesh helical gear train. *J. Mech. Des.* **116**, 706–712 (1994)
14. Kubur, M., Kahraman, A., Zini, D.M., Kienzle, K.: Dynamic analysis of a multi-shaft helical gear transmission by finite elements: model and experiment. *J. Vib. Acoust.* **126**(3), 398–406 (2004)
15. Al-shyyab, A., Kahraman, A.: Non-linear dynamic analysis of a multi-mesh gear train using multi-term harmonic balance method: period-one motions. *J. Sound Vib.* **284**, 151–172 (2005)
16. Al-shyyab, A., Kahraman, A.: Non-linear dynamic analysis of a multi-mesh gear train using multi-term harmonic balance method: sub-harmonic motions. *J. Sound Vib.* **279**, 417–451 (2005)
17. Al-shyyab, A., Kahraman, A.: A nonlinear torsional dynamic model of multi-mesh gear trains having flexible shafts. *Jordan J. Mech. Ind. Eng.* **1**(1), 31–41 (2007)
18. Liu, G., Parker, R.G.: Nonlinear dynamics of idler gear systems. *Nonlinear Dyn.* **53**(4), 345–367 (2008)
19. Liu, G., Parker, R.G.: Nonlinear, parametrically excited dynamics of two-stage spur gear trains with mesh stiffness fluctuation. *Proc. Inst. Mech. Eng. C J. Mech. Eng. Sci.* **226**(8), 1939–1957 (2012)
20. Al-shyyab, A., Kahraman, A.: A non-linear dynamic model for planetary gear sets. *Proc. Inst. Mech. Eng. Part K J. Multi-body Dyn.* **221**(4), 567–576 (2007)
21. Sondkar, P., Kahraman, A.: A dynamic model of a double-helical planetary gear set. *Mech. Mach. Theory* **70**, 157–174 (2013)
22. Cigeroglu, E., Samandari, H.: Nonlinear free vibration of double walled carbon nanotubes by using describing function method with multiple trial functions. *Phys. E Low-dimensional Syst. Nanostructures* **46**, 160–173 (2012)
23. Yümer, M.E., Çiğeroglu, E., Özgüven, H.N.: Non-linear forced response analysis of mistuned bladed disk assemblies. In: Proceedings of ASME Turbo Expo 2010: Power for Land, Sea and Air, Glasgow (2010)
24. Von Groll, G., Ewins, D.J.: The harmonic balance method with arc-length continuation in rotor/stator contact problems. *J. Sound Vib.* **241**(2), 223–233 (2001)
25. Cardona, A., Lerusse, A., and Geradin, M.: Fast Fourier nonlinear vibration analysis. *Comput. Mech.* **22**, 128–142 (1998)

Chapter 4

Nonlinear Dynamic Analysis of a Spiral Bevel Geared System

Siar Deniz Yavuz, Zihni Burcay Saribay, and Ender Cigeroglu

Abstract A nonlinear dynamic model of a spiral bevel gear train mounted on flexible shafts and bearings is proposed in this study. The finite element model of shafts is combined with a three-dimensional discrete mesh model of a spiral bevel gear pair. Bearing flexibilities are as well included in the model. Gear backlash is incorporated into the model in the form of clearance-type displacement functions and clearance nonlinearity and stiffness fluctuations of the bearings are neglected. A time-invariant mesh stiffness is assumed for the gear pair to simplify the dynamic model. Eigenvalue solution is used to predict the natural modes of the system. A multi-term Harmonic Balance Method (HBM) is employed for the solution of resulting equations of motion for periodic steady-state response. The results of HBM are validated by comparing them to the solutions obtained by direct numerical integration. Forced response of the system in the form of dynamic mesh force is studied to demonstrate the effects of static mesh force and backlash amount.

Keywords Nonlinear gear dynamics • Spiral bevel gear train • Gear backlash nonlinearity • Time-invariant mesh stiffness • Multi-term Harmonic Balance Method

Nomenclature

b	Half of gear backlash
c_m	Mesh damping coefficient
\mathbf{C}	Damping matrix
e_m	Static transmission error
f_n	Nonlinear displacement function
\mathbf{F}	External force vector
F_m	Dynamic mesh force
\mathbf{F}_N	Nonlinear restoring force vector
\mathbf{h}	Transformation vector
i	Unit imaginary number
\mathbf{J}	Jacobian matrix
\mathbf{K}	Stiffness matrix
k_m	Mesh stiffness
\mathbf{M}	Mass matrix
\mathbf{n}	Line of action (LOA) directional cosine vector
n	Directional cosine
\mathbf{p}	Extended coordinate transformation vectors

S.D. Yavuz
Department of Mechanical Engineering, Middle East Technical University, Universiteler Mahallesi, Dumlupinar Bulvari No:1, 06800,
Cankaya-Ankara, Turkey

Turkish Aerospace Industries, Inc. (TAI), Fethiye Mahallesi Havacilik Bulvari No:17, 06980, Kazan-Ankara, Turkey

Z.B. Saribay
Turkish Aerospace Industries, Inc. (TAI), Fethiye Mahallesi Havacilik Bulvari No:17, 06980, Kazan-Ankara, Turkey

E. Cigeroglu (✉)
Department of Mechanical Engineering, Middle East Technical University, Universiteler Mahallesi, Dumlupinar Bulvari No:1, 06800,
Cankaya-Ankara, Turkey
e-mail: ender@metu.edu.tr

© The Society for Experimental Mechanics, Inc. 2017
D. Di Maio, P. Castellini (eds.), *Rotating Machinery, Hybrid Test Methods, Vibro-Acoustics & Laser Vibrometry, Volume 8*,
Conference Proceedings of the Society for Experimental Mechanics Series, DOI 10.1007/978-3-319-54648-3_4

31

Yavuz, S. D., Saribay, Z. B., and Cigeroglu, E., 2017, "Nonlinear Dynamic Analysis of a Spiral Bevel Geared System," *Rotating Machinery, Hybrid Test Methods, Vibro-Acoustics & Laser Vibrometry, Volume 8*. Conference Proceedings of the Society for Experimental Mechanics Series, D. Di Maio, and P. Castellini, eds., Springer, Cham.

\mathbf{r}	Position vector of the effective mesh point
r	Harmonic index
S	Pinion/gear coordinate system
\mathbf{S}	Nonlinear algebraic equations in vector form
T	Torque
t	Time
\mathbf{U}	Solution vector
\mathbf{u}	Harmonic amplitudes of displacement vector
\mathbf{x}	Displacement vector
β	Rayleigh damping coefficient
δ_d	Dynamic transmission error
λ	Directional rotational radius
ρ	Discrete time interval
θ	Rotational displacement
ω	Frequency

Subscripts

b	Bearing
i	Pinion ($i = p$) and gear ($i = g$)
l	Linear DOFs
n	Nonlinear DOFs
s	Shaft

Superscripts

rms	Root-mean-square value
'	Derivative with respect to time

4.1 Introduction

Dynamic analysis of gear systems has been one of the main topics in power transmission research. Under dynamic conditions, gear systems exhibit much higher gear mesh forces than static forces transmitted. These high frequency dynamic forces are transmitted to the housing and other structures, resulting in excessive noise levels. Moreover, dynamic mesh loads cause increased tooth root and contact stresses and reduce fatigue lives of the driveline components. Therefore, a better understanding of the gear system dynamics is crucial in order to design products with acceptable noise levels and fatigue lives.

There are a large number of studies regarding dynamics of parallel axis gears in the literature. Numerous mathematical models and solution methods are developed in those studies. However, studies related to dynamics of non-parallel axis gears such as hypoid gears and spiral bevel gears are limited due to the complexity of tooth geometry, kinematics and meshing process of these types of gears. A single-point gear mesh-coupling model using the exact spiral bevel gear geometry is developed in [1]. Based on this mesh model, a nonlinear model of a spiral bevel gear pair including time varying mesh stiffness and time-varying directional rotation radius is formulated and solved by using direct numerical integration [2] and HBM [3]. Moreover, the same mesh model is used to develop multiple degrees of freedom (DOFs), lumped parameter model of a spiral bevel geared system and the effects of various gear system parameters on the dynamics of this system are investigated in [4]. Due to the deficiency of this lumped parameter model in representing the shaft-bearing structural characteristics, two different modeling methods, i.e., the finite element model and an enhanced equivalent lumped parameter synthesis, are introduced in [5] for a linear time-invariant (LTI) spiral bevel geared system.

In this study, a nonlinear dynamic model of a spiral bevel gear pair mounted on flexible shafts and bearings is considered. The dynamic model combines the finite element model of shaft-bearing structures with a three-dimensional discrete mesh

model of a spiral bevel gear pair. The resulting differential equations of motion are converted into a set of nonlinear algebraic equations for periodic steady-state response by using multi-term HBM coupled with discrete Fourier transform (DFT). The resulting set of nonlinear algebraic equations is solved by Newton's method with arc-length continuation. The accuracy of the solutions obtained by HBM is demonstrated by comparing them with the solutions obtained by direct numerical integration, which are computationally very expensive. The effects of static mesh force and backlash amount on the dynamic response are studied.

4.2 Dynamic Model Formulation

4.2.1 Physical System and Dynamic Model

The geared system considered in this study consists of a spiral bevel gear pair mounted on flexible shafts and bearings. The shafts including the gear blanks are modeled by using Timoshenko beam formulation, since rotary inertia and shear deformations are expected to be significant. The bearings supporting the gear shafts are represented by linear and torsional springs. Clearance nonlinearity and stiffness fluctuations of bearings due to the alternating number of rolling elements in the loaded zone are neglected.

The stiffness matrix, \mathbf{K}_{sn} , and mass matrix, \mathbf{M}_{sn} , of each individual shaft n ($n = 1, 2$) are formed by assembling the stiffness and mass matrices of each beam element. Overall shaft stiffness and mass matrices of the system are then assembled as $\mathbf{K}_s = \text{Diag}[\mathbf{K}_{s1}, \mathbf{K}_{s2}]$ and $\mathbf{M}_s = \text{Diag}[\mathbf{M}_{s1}, \mathbf{M}_{s2}]$. Both matrices are square matrices of dimension q where $q = 6 \sum_{n=1}^2 (m_n + 1)$ is the total number of degrees of freedom of the system (m_n is the number of beam elements used to model shaft n and each node has 6 DOFs).

In practical applications, each shaft is usually supported by at least two bearings of varying type and size. For a system having a total of n_b bearings, the overall bearing stiffness matrix of the complete system can be obtained by assembling the individual bearing stiffness matrices $\mathbf{K}_{bi} = \text{Diag}[k_{bxi}, k_{byi}, k_{bzi}, k_{b\theta_x i}, k_{b\theta_y i}, k_{b\theta_z i}]$ ($i = 1$ to n_b) as $\mathbf{K}_b = \text{Diag}[\dots \mathbf{K}_{b1} \dots \mathbf{K}_{b1} \dots \mathbf{K}_{bnb} \dots]$. Then, the stiffness matrix of the whole shaft-bearing assembly can be written as $\mathbf{K} = \mathbf{K}_s + \mathbf{K}_b$. Assuming Rayleigh damping for the shafts and bearings for simplicity, the damping matrix of the shaft-bearing assembly is obtained as $\mathbf{C} = \beta \mathbf{K}$ where β is the Rayleigh damping coefficient.

Figure 4.1 shows the mesh coupling between the gears including gear backlash, mesh stiffness, mesh damping and static transmission error, which is along the line of action (LOA), i.e., in the direction of tooth normal. The parameters used to characterize a gear mesh such as gear mesh stiffness, damping, acting point and direction of effective spring-damper element vary substantially for spiral bevel gears due to the tooth geometry as the gear pair rolls. However, they are assumed to remain unchanged under dynamic conditions. A single point mesh model consisting of an effective mesh point and a constant line of action vector for a single spring-damper element is used in this study. Moreover, a time-invariant mesh stiffness is assumed for the gear pair, and gear mesh damping element is assumed not to be subjected to gear backlash nonlinearity in order to simplify the study.

Utilizing six degrees of freedom for each gear, the gear pair has a total of 12 degrees of freedom that defines the coupling between the two shafts holding the gears. The generalized coordinates of the gears are expressed as $\mathbf{x}_i = \{x_i, y_i, z_i, \theta_{xi}, \theta_{yi}, \theta_{zi}\}^T$ ($i = p, g$), which are relative to each local coordinate system S_i ($i = p, g$) whose origin is at the pinion or gear centroid.

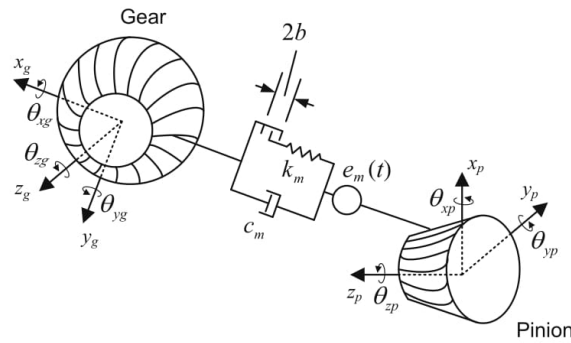


Fig. 4.1 Spiral bevel gear pair dynamic model

The dynamic transmission error along the LOA can be written as follows

$$\delta_d = \mathbf{h}_p \mathbf{x}_p - \mathbf{h}_g \mathbf{x}_g, \quad (4.1)$$

where \mathbf{x}_i ($i = p, g$) is the displacement vector and \mathbf{h}_i ($i = p, g$) is the transformation vector, consisting of the directional cosines and directional rotation radii between the LOA and the respective coordinates of pinion or gear. Transformation vectors can be expressed as

$$\mathbf{h}_i = \{n_{ix}, n_{iy}, n_{iz}, \lambda_{ix}, \lambda_{iy}, \lambda_{iz}\} \quad (i = p, g). \quad (4.2)$$

The directional rotation radii, λ , is defined as

$$\lambda_{ix} = \mathbf{n}_i \cdot (\mathbf{u}_{xi} \times \mathbf{r}_i) \quad (i = p, g), \quad (4.3a)$$

$$\lambda_{iy} = \mathbf{n}_i \cdot (\mathbf{u}_{yi} \times \mathbf{r}_i) \quad (i = p, g), \quad (4.3b)$$

$$\lambda_{iz} = \mathbf{n}_i \cdot (\mathbf{u}_{zi} \times \mathbf{r}_i) \quad (i = p, g), \quad (4.3c)$$

where $\mathbf{r}_i = \{x_{im}, y_{im}, z_{im}\}^T$ is the position vector of the effective mesh point, $\mathbf{n}_i = \{n_{ix}, n_{iy}, n_{iz}\}^T$ is the directional cosine vector of LOA and $\mathbf{u}_{xi} = \{1 \ 0 \ 0\}^T$, $\mathbf{u}_{yi} = \{0 \ 1 \ 0\}^T$ and $\mathbf{u}_{zi} = \{0 \ 0 \ 1\}^T$ are the triad of unit vectors for coordinate system S_i . Subscript $i = p, g$ indicates that the quantity is defined in the local reference frame of the pinion or gear, respectively, in all the above equations.

The dynamic mesh force, F_m , along the LOA can be expressed as

$$F_m(t) = k_m f_n(\delta_d(t) - e_m(t)) + c_m (\dot{\delta}_d(t) - \dot{e}_m(t)), \quad (4.4)$$

where the nonlinear displacement function $f_n(\delta_d(t) - e_m(t))$ is defined as given in the following equation by considering backlash nonlinearity:

$$f_n(\delta_d(t) - e_m(t)) = \begin{cases} \delta_d(t) - e_m(t) - b, & \delta_d(t) - e_m(t) > b \\ 0, & |\delta_d(t) - e_m(t)| \leq b \\ \delta_d(t) - e_m(t) + b, & \delta_d(t) - e_m(t) < -b \end{cases}. \quad (4.5)$$

Here, b denotes the half of the gear backlash.

Rearranging the order of nodes such that mesh nodes are located below the other nodes in the displacement vector, the equation of motion of the whole spiral bevel geared system can be written as

$$\mathbf{M}\ddot{\mathbf{x}}(t) + \mathbf{C}\dot{\mathbf{x}}(t) + \mathbf{K}\mathbf{x}(t) + \mathbf{F}_N(t) = \mathbf{F}(t), \quad (4.6)$$

where $\mathbf{F}(t)$ is the external force vector including the external torques T_i ($i = p, g$) acting on the gears:

$$\mathbf{F}(t) = \mathbf{F} = \{\{0\}, \{0 \ 0 \ 0 \ 0 \ 0 \ T_p\}, \{0 \ 0 \ 0 \ 0 \ 0 \ -T_g\}\}^T. \quad (4.7)$$

In this study, only internal vibratory excitation, i.e., static transmission error, is considered by assuming constant torque values. The only nonzero elements of the forcing vector, \mathbf{F} , are the ones related to rotation of gears about z axis. Due to nonlinearity, the mesh stiffness k_m and the mesh damping c_m are incorporated into the equation of motion through the dynamic mesh force, which forms the nonlinear restoring force $\mathbf{F}_N(t)$ as given in the following equation:

$$\mathbf{F}_N(t) = F_m(t) \mathbf{p}, \quad (4.8)$$

where \mathbf{p} denotes the extended form of the coordinate transformation vectors \mathbf{h}_i ($i = p, g$)

$$\mathbf{p} = \{0, \mathbf{h}_p, -\mathbf{h}_g\}^T. \quad (4.9)$$

4.2.2 Solution Method

4.2.2.1 Multi-Term Harmonic Balance Method with DFT

In order to solve the nonlinear equations of motion for \mathbf{x} , multi-term Harmonic Balance Method coupled with discrete Fourier Transform, which has been successfully applied in [3, 6–10], is used. Since static transmission error excitation is periodic, the solution and the nonlinear displacement function $f_n(\delta_d(t) - e_m(t))$ can also be described periodically [8]. The harmonic expressions for the static transmission error and its derivative with respect to time can be expressed as

$$e_m(t) = \sum_{j=1}^J [\varepsilon_{cj} \cos(j\omega t) + \varepsilon_{sj} \sin(j\omega t)], \quad (4.10a)$$

$$\dot{e}_m(t) = \sum_{j=1}^J [-(j\omega) \varepsilon_{cj} \sin(j\omega t) + (j\omega) \varepsilon_{sj} \cos(j\omega t)]. \quad (4.10b)$$

Given the periodic excitation defined by Eq. (4.10a), the steady-state solution can as well be assumed periodic as

$$\mathbf{x}(t) = \mathbf{u}_0 + \sum_{r=1}^R [\mathbf{u}_{cr} \cos(r\omega t) + \mathbf{u}_{sr} \sin(r\omega t)], \quad (4.11)$$

which can be differentiated to yield

$$\dot{\mathbf{x}}(t) = \sum_{r=1}^R [-(r\omega) \mathbf{u}_{cr} \sin(r\omega t) + (r\omega) \mathbf{u}_{sr} \cos(r\omega t)]. \quad (4.12)$$

Sampling N points within one fundamental mesh period, the time series of the dynamic mesh force can be obtained as

$$F_m(t_n) = k_m f_n(\mathbf{h}_p \mathbf{x}_p(t_n) - \mathbf{h}_g \mathbf{x}_g(t_n) - e_m(t_n)) + c_m (\mathbf{h}_p \dot{\mathbf{x}}_p(t_n) - \mathbf{h}_g \dot{\mathbf{x}}_g(t_n) - \dot{e}_m(t_n)), \quad (4.13)$$

where $t_n = n\rho$ ($n = 0, 1, 2, \dots, N-1$). Here, $\rho = 2\pi/(N\omega)$ and N must be larger than $2R$ where R is the highest harmonic number used in the solution in order to avoid aliasing errors.

Similarly, the dynamic mesh force can be represented by Fourier series as follows

$$F_m(t) = F_{m0} + \sum_{r=1}^R [F_{m(cr)} \cos(r\omega t) + F_{m(sr)} \sin(r\omega t)], \quad (4.14)$$

where, utilizing discrete Fourier Transform,

$$F_{m0} = \frac{1}{N} \sum_{n=0}^{N-1} F_m, \quad (4.15a)$$

$$F_{m(cr)} = \frac{2}{N} \sum_{n=0}^{N-1} F_m \cos\left(\frac{2\pi rn}{N}\right), \quad (4.15b)$$

$$F_{m(sr)} = \frac{2}{N} \sum_{n=0}^{N-1} F_m \sin\left(\frac{2\pi rn}{N}\right). \quad (4.15c)$$

Fourier coefficients of the nonlinear forcing vector $\mathbf{F}_N(t)$ can be obtained by using the extended form of the coordinate transformation vectors, \mathbf{p} , given in Eq. (4.9) as

$$\mathbf{F}_N(t) = \mathbf{F}_{N(0)} + \sum_{r=1}^R [\mathbf{F}_{N(cr)} \cos(r\omega t) + \mathbf{F}_{N(sr)} \sin(r\omega t)], \quad (4.16a)$$

$$\mathbf{F}_{N(0)} = F_{m0} \mathbf{p}, \quad (4.16b)$$

$$\mathbf{F}_{N(cr)} = F_{m(cr)} \mathbf{p}, \quad (4.16c)$$

$$\mathbf{F}_{N(sr)} = F_{m(sr)} \mathbf{p}. \quad (4.16d)$$

Substituting Eqs. (4.11) and (4.16a) into Eq. (4.6) and equating the coefficients of the like harmonic terms, the following nonlinear equations are obtained for $r = 1, 2, \dots, R$

$$\mathbf{S}_0 = \mathbf{K} \cdot \mathbf{u}_0 + (\mathbf{F}_{N(0)} - \mathbf{F}_{(0)}) = 0, \quad (4.17a)$$

$$\mathbf{S}_r = \left(\mathbf{K} - (r\omega)^2 \mathbf{M} + ir\omega \mathbf{C} \right) (\mathbf{u}_{sr} + i \mathbf{u}_{cr}) + (\mathbf{F}_{N(sr)} + i \mathbf{F}_{N(cr)}) - (\mathbf{F}_{sr} + i \mathbf{F}_{cr}) = 0. \quad (4.17b)$$

Equation (4.17a) is a real equation related to the bias terms while Eq. (4.17b) is a complex equation including the sine and cosine terms of the r th harmonic. Therefore, a total of $q \cdot (2R + 1)$ nonlinear real equations are solved in order to obtain the dynamic response of the spiral bevel geared system considered in this study. The solution of this nonlinear equations set, i.e. displacement vector $\mathbf{U} = \{\mathbf{u}_0, \mathbf{u}_{c1}, \mathbf{u}_{s1}, \mathbf{u}_{c2}, \mathbf{u}_{s2}, \dots, \mathbf{u}_{cR}, \mathbf{u}_{sR}\}^T$, is obtained by using Newton's Method with arc length continuation. Application of Newton's method results in the following iterative scheme

$$\mathbf{U}^{(k)} = \mathbf{U}^{(k-1)} - (\mathbf{J}^{-1})^{(k-1)} \mathbf{S}^{(k-1)}, \quad (4.18)$$

where $\mathbf{U}^{(k)}$ denotes the k^{th} iterative solution based on the $(k-1)^{\text{th}}$ solution and $(\mathbf{J}^{-1})^{(k-1)}$ is the inverse of the Jacobian matrix of the nonlinear vector function, \mathbf{S} , estimated at the previous point $(k-1)$. The iteration procedure described by Eq. (4.18) is repeated until the vector norm of $\mathbf{S}^{(k)}$ is below a predefined error limit. Moreover, arc-length continuation method is used in the solution procedure and a new parameter, arc-length, which is the radius of a hypothetical sphere in which the next solution point is searched, is chosen as the continuation parameter instead of frequency in order to follow the solution path even at the turning points. Details of Newton's method with arc-length continuation can be found in [11–13].

4.3 Results and Discussion

A spiral bevel geared system with the parameters listed in Table 4.1 is considered as the example case. In order to simplify the study, a time-invariant mesh stiffness k_m is assumed for the gear pair and only the first harmonic of the static transmission error $e_m(t)$ is considered.

Firstly, the period-1 motion solutions obtained by HBM are compared to the results of the direct numerical integration (NI). Figure 4.2 shows the comparison of the root-mean-square (rms) values of the dynamic mesh force. The response of the corresponding linear system is also shown in Fig. 4.2. The resonance peaks in the linear response observed at $\omega = 1134\text{Hz}$, $\omega = 1744\text{Hz}$, $\omega = 3059\text{Hz}$, $\omega = 3984\text{Hz}$, $\omega = 4911\text{Hz}$ and $\omega = 6608\text{Hz}$ are the 2nd, 4th, 7th, 10th, 11th and 16th natural frequencies of the corresponding linear system. These entire modes exhibit coupled transverse-axial-rotational motions with non-zero relative gear mesh displacements. Three harmonics ($R = 3$ in Eq. (4.11)) are assumed in the HBM solution. The rms values are calculated as

$$F_m^{(rms)} = \left\{ \frac{1}{2} \sum_{r=1}^R (A_r)^2 \right\}^{1/2}, \quad (4.19)$$

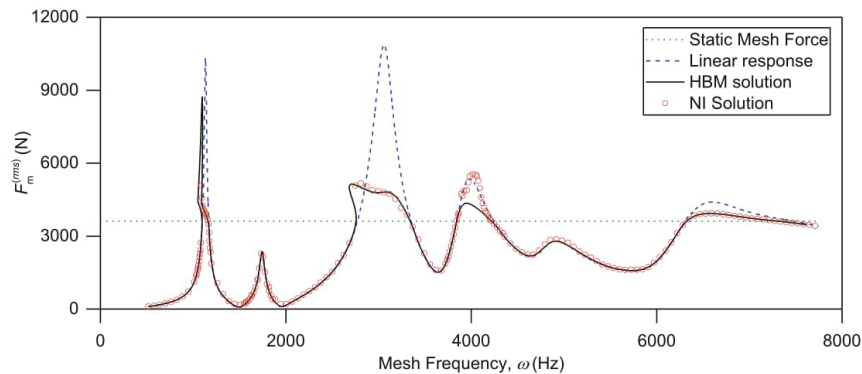
where A_r is the amplitude of the r^{th} harmonic of $F_m(t)$ that can be expressed as

$$A_r = \sqrt{(F_{m(cr)})^2 + (F_{m(sr)})^2}. \quad (4.20)$$

It can be observed from Fig. 4.2 that both HBM and NI solutions agree well with each other except around the resonance peak observed at $\omega = 3952\text{Hz}$. This is due to the existence of subharmonic motions dictating this frequency range, which

Table 4.1 Parameters of the example system

	Pinion	Gear
<i>Shaft parameters</i>		
Outer diameter (mm)	55	70
Inner diameter (mm)	40	50
Length (mm)	202	234
β	$3(10^{-6})$	$3(10^{-6})$
<i>Gear parameters</i>		
Number of teeth	31	39
Spiral angle ($^\circ$)	30	30
Normal pressure angle ($^\circ$)	20	20
Pitch angle ($^\circ$)	38.48	51.52
Pitch radius (mm)	65.1	81.9
Face width (mm)	34	34
Hand	Left	Right
Locations (mm)	172	209
T (Nm)	200	251.61
<i>Bearing parameters</i>		
Locations (mm)	42	74
	127	144
k_b (N/m, Nm/rad)	Diag[$2(10^9)$, $2(10^9)$, $1(10^9)$, $1(10^6)$, $1(10^6)$, 0]	
<i>Gear mesh parameters</i>		
k_m (N/m)	$3(10^8)$	
c_m (Ns/m)	1500	
ε_{s1} (μm)	10	
b (μm)	20	

**Fig. 4.2** Comparison of rms values of the dynamic mesh force $F_m(t)$ predicted by HBM and NI for $T = 200\text{Nm}$ and $b = 20\ \mu\text{m}$

is illustrated in Fig. 4.3 showing the time trace and Fourier spectrum of the response at $\omega = 3952\text{Hz}$ obtained by NI. The response is dominated by the subharmonics with the frequencies of $1/4$ and $3/4$ of the excitation frequency, i.e., the mesh frequency, as well as the fundamental harmonic. While the NI can capture these behaviors depending on the initial condition used, HBM cannot capture since the subharmonics are not included in the solutions assumed.

Past studies [1–4] show that spiral bevel gears can exhibit both single-sided and double-sided tooth impacts depending on the system parameters. Similar behaviors are also seen here in the results of both HBM and NI. It is seen from Fig. 4.4 that gear pair behaves quite linearly with no tooth impact in the low frequency range. When the frequency increases to $\omega = 1095\text{Hz}$, $F_m^{(rms)}$ forced response curve begins to exhibit single-sided tooth impact. Since this is a softening-type nonlinear behavior due to tooth separation, the response curve veers left towards the lower frequency range and continues along the same trajectory as the frequency decreases from $\omega = 1095\text{Hz}$ to $\omega = 1052\text{Hz}$. At $\omega = 1052\text{Hz}$, double-sided tooth impact,

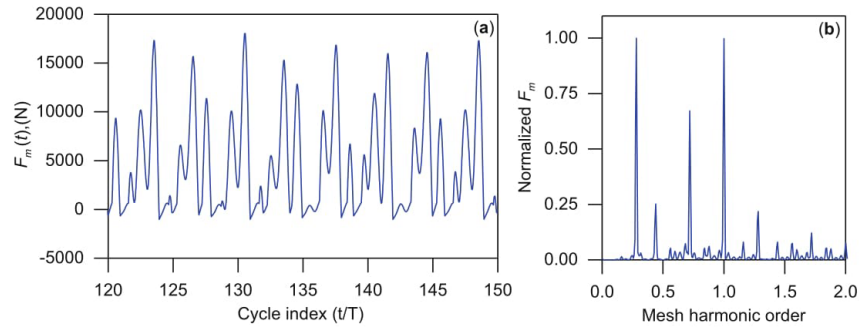


Fig. 4.3 (a) Time trace and (b) corresponding Fourier spectrum of $F_m(t)$ at $\omega = 3952\text{Hz}$ obtained by NI

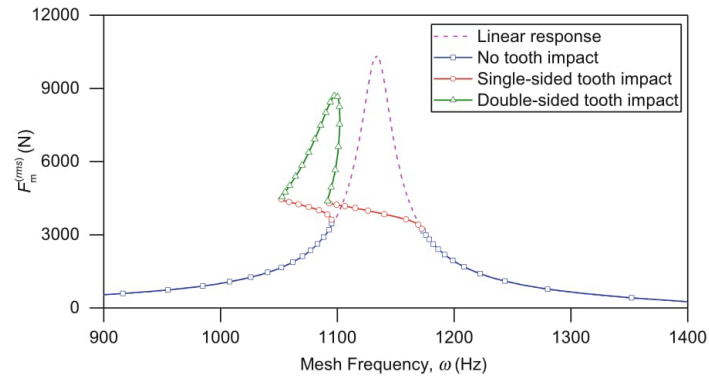


Fig. 4.4 Nonlinear behavior of the spiral bevel geared system

which includes both tooth separation and additional impact with the preceding tooth, begins to emerge. Due to the hardening with respect to single-sided tooth impact, the response curve takes a sharp turn towards the right and begins to climb in both amplitude and frequency. After reaching the peak amplitude at $\omega = 1098\text{Hz}$, the response curve begins to decrease in amplitude as the double-sided tooth impact behavior continues. When the frequency decreases to $\omega = 1092\text{Hz}$, the response changes back to single-sided tooth impact and becomes linear as the frequency increases further.

Returning back to Fig. 4.2, the effect of backlash nonlinearity shows itself as single-sided tooth impact around the 3rd, the 4th and the 6th resonance peaks observed at $\omega \cong 3060\text{Hz}$, $\omega \cong 3950\text{Hz}$ and $\omega \cong 6590\text{Hz}$, respectively. Since the vibration amplitudes at these frequencies are small compared to the backlash amount, double-sided tooth impacts are not observed around these peaks. Another observation from Fig. 4.2 is that the amplitudes of the 2nd and the 5th resonance peaks observed at $\omega = 1744\text{Hz}$ and $\omega = 4911\text{Hz}$, respectively, are smaller than the static mesh force. Therefore, the gear pair behaves linearly around these peaks.

The influence of the static mesh force on the dynamic response of the system due to different external torques is shown in Fig. 4.5 for $b = 20\ \mu\text{m}$. When the pinion torque is increased to $T = 400\text{Nm}$, tooth separation and tooth impact again occur, i.e., backlash nonlinearity is effective, around the 1st and the 3rd resonance peaks while the dynamic behavior of the gear pair around the other peaks is linear. It is also clear from Fig. 4.5 that tooth separation begins to show up at a higher response level compared to the case with $T = 200\text{Nm}$. As the pinion torque is increased further to $T = 800\text{Nm}$, the maximum amplitude of the dynamic mesh force remains below the amplitude of the static mesh force, i.e., dynamic factor is lower than 1, no loss of contact or tooth impact occurs. Therefore, the response of the nonlinear system is exactly the same as the corresponding linear system.

Figure 4.6 shows the influence of backlash amount, which is a significant parameter especially for lightly loaded gear systems. Only the frequency range around the 1st resonance peak is shown in Fig. 4.6, since double-sided tooth impacts are only observed in this range when $T = 200\text{Nm}$. When the backlash amount is increased to $b = 40\ \mu\text{m}$, double-sided tooth

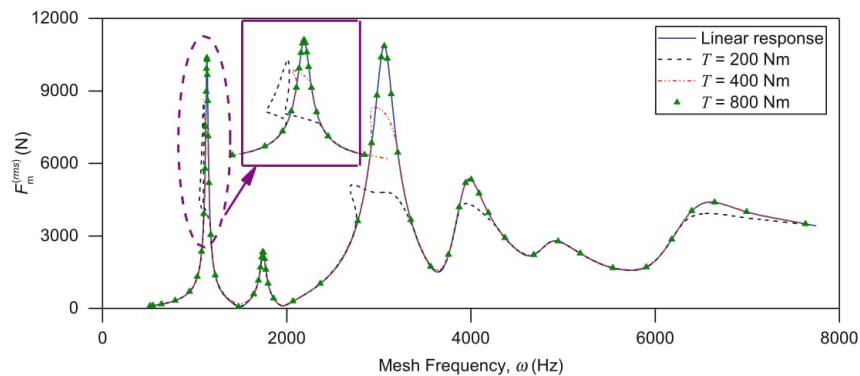


Fig. 4.5 Effect of static mesh force, i.e., external torque, on the dynamic response for $b = 20 \mu\text{m}$

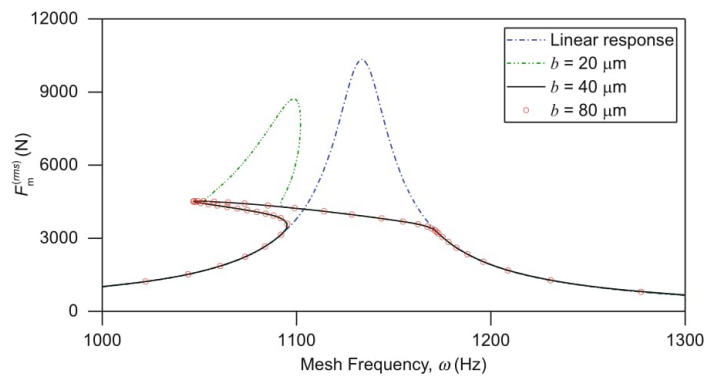


Fig. 4.6 Effect of backlash amount on the dynamic response for $T = 200\text{Nm}$

impact disappears, since the amplitude of the relative mesh displacement is smaller than the total amount of static deflection and backlash. Thus, single-sided tooth impacts dominate the nonlinear response range. As the backlash amount is increased further, since double-sided tooth impacts cannot occur, the nonlinear response of the system is not affected any more.

4.4 Conclusion

A nonlinear dynamic model of a spiral bevel gear train consisting of a finite element model of shaft-bearing assembly combined with a three-dimensional mesh model of a spiral bevel gear pair is formulated in this study. A multi-term Harmonic Balance Method in conjunction with discrete Fourier Transform is used to solve the resultant equations of motion for steady-state period-1 response. The solutions obtained by HBM are validated by comparing them to the solutions obtained by direct numerical integration. The results show that the spiral bevel gear pair exhibits nonlinear behavior as single-sided and double-sided tooth impacts with the given system parameters. Subharmonic motions are also observed in the results of direct numerical integration.

Forced vibration characteristics of the system are studied to demonstrate the influence of static mesh force and backlash amount. There is potential for loss of contact and tooth impact for lightly loaded cases, where the gear backlash is the critical factor for the range and appearance of nonlinear responses. In contrast, for heavily loaded cases, dynamic factor tends to be lower; hence, backlash nonlinearity becomes ineffective.

References

1. Cheng, Y., Lim, T.C.: Vibration analysis of hypoid transmissions applying an exact geometry-based gear mesh theory. *J. Sound Vib.* **240**(3), 519–543 (2001)
2. Wang, J., Lim, T.C., Li, M.: Dynamics of a hypoid gear pair considering the effects of time-varying mesh parameters and backlash nonlinearity. *J. Sound Vib.* **308**, 302–329 (2007)
3. Yang, J., Peng, T., Lim, T.C.: An enhanced multi-term harmonic balance solution for nonlinear period-one dynamic motions in right-angle gear pairs. *Nonlinear Dyn.* **67**(2), 1053–1065 (2011)
4. Peng, T., Lim, T.C.: Coupled multi-body dynamic and vibration analysis of high-speed spiral bevel geared rotor system. In: Proceedings of the SAE Noise and Vibration Conference and Exposition, St. Charles, IL, USA, 2007
5. Hua, X., Lim, T.C., Peng, T., Wali, W.E.: Dynamic analysis of spiral bevel geared rotor systems applying finite elements and enhanced lumped parameters. *Int. J. Automot. Technol.* **13**(1), 97–107 (2012)
6. Kahraman, A., Blankenship, G.W.: Steady state forced response of a mechanical oscillator with combined parametric excitation and clearance type non-linearity. *J. Sound Vib.* **185**(5), 743–765 (1995)
7. Kahraman, A., Blankenship, G.W.: Interactions between commensurate parametric and forcing excitations in a system with clearance. *J. Sound Vib.* **194**(3), 317–336 (1996)
8. Al-shyyab, A., Kahraman, A.: Non-linear dynamic analysis of a multi-mesh gear train using multi-term harmonic balance method: period-one motions. *J. Sound Vib.* **284**, 151–172 (2005)
9. Al-shyyab, A., Kahraman, A.: Non-linear dynamic analysis of a multi-mesh gear train using multi-term harmonic balance method: sub-harmonic motions. *J. Sound Vib.* **279**, 417–451 (2005)
10. Yavuz, S.D., Saribay, Z.B., Cigeroglu, E.: Nonlinear time-varying dynamic analysis of a multi-mesh spur gear train. In: Proceedings of the 34th IMAC, A Conference and Exposition on Structural Dynamics, Orlando, FL, USA, 2016
11. Cigeroglu, E., Samandari, H.: Nonlinear free vibration of double walled carbon nanotubes by using describing function method with multiple trial functions. *Physica E.* **46**, 160–173 (2012)
12. Yümer, M.E., Cigeroglu, E., Özgüven, H.N.: Non-linear forced response analysis of mistuned bladed disk assemblies. In: Proceedings of the ASME Turbo Expo 2010: Power for Land, Sea and Air, Glasgow, UK, 2010
13. Von Groll, G., Ewins, D.J.: The harmonic balance method with arc-length continuation in rotor/stator contact problems. *J. Sound Vib.* **241**(2), 223–233 (2001)

CURRICULUM VITAE

PERSONAL INFORMATION

Surname, Name: Yavuz, Şiar Deniz
Nationality: Turkish (TC)
Date and Place of Birth: 3 November 1985, Ankara
Marital Status: Married
Email: e139371@metu.edu.tr

EDUCATION

Degree	Institution	Year of Graduation
MS	METU Mechanical Engineering	2011
BS	METU Mechanical Engineering	2008
High School	Çankaya Milli Piyango Anadolu High School, Ankara	2003

WORK EXPERIENCE

Year	Place	Enrollment
2013-Present	Turkish Aerospace Industries (TAI)	Senior Structural Analysis Engineer
2008-2013	Bilkent University Acoustics and Underwater Technologies Research Center	Research and Development Engineer
2007 July	Öztrak A.Ş.	Intern Engineering Student
2006 July	MAN Türkiye A.Ş.	Intern Engineering Student

PUBLICATIONS

1. Yavuz, S.D., Saribay, Z.B., Cigeroglu, E.: Nonlinear Time-Varying Dynamic Analysis of a Multi-Mesh Spur Gear Train. In: 34th IMAC, A Conference and Exposition on Structural Dynamics, Orlando, FL, USA (2016)
2. Yavuz, S.D., Saribay, Z.B., Cigeroglu, E.: Nonlinear Dynamic Analysis of a Spiral Bevel Geared System. In: 35th IMAC, A Conference and Exposition on Structural Dynamics, Garden Grove, CA, USA (2017)